Alma Mater Studiorum - Università degli Studi di Bologna

Modeling Hydrothermal System: Deriving Observables and Hydrothermal Instability in Volcanic and non-Volcanic Setting

Presentata da: Antonio Pio Rinaldi

Coordinatore dottorato:

Prof. Michele Dragoni

Tutore:

Dott.ssa Micol Todesco

Referente:

Prof. Maurizio Bonafede

Contents

Introduction

Hydrothermal fluids are a fundamental resource for understanding and monitoring volcanic and non-volcanic systems. This thesis is focused on the study of hydrothermal system through numerical modeling with the geothermal simulator TOUGH2. Several simulations are presented, and geophysical and geochemical observables, arising from fluids circulation, are analyzed in detail throughout the thesis.

In a volcanic setting, fluids feeding fumaroles and hot spring may play a key role in the hazard evaluation. The evolution of the fluids circulation is caused by a strong interaction between magmatic and hydrothermal systems. A simultaneous analysis of different geophysical and geochemical observables is a sound approach for interpreting monitored data and to infer a consistent conceptual model.

After introducing in Chapter 1 the key equations solved by the geothermal simulator TOUGH2 and the basic equations for poro-elasticity, Chapter 2 highlights the effects of hydrothermal fluid circulation on ground displacement. Starting from a well-established approach, based on a conceptual model previously developed for the Campi Flegrei caldera, numerical simulations of multi-phase and multi-component hydrothermal fluid were carried out with the TOUGH2/EOS2 code. According this conceptual model, hydrothermal system is fed by an input of magmatic fluids, and a system instability (unrest event), which may produce changes in the observed signals, correspond to periods of increased magmatic degassing. Ground displacement is then calculated using a mathematical model. The model, based on linear theory of poro-elasticity, was developed in this work and can be used in several studies. In fact, the ground displacement model was applied at Panarea volcano too, as shown in Appendix A.

Ground displacement is not the only observable arising from fluid circulation. Results from Chapter 3, still using the conceptual model for Campi Flegrei, show that circulation obtained varying the input of fluids can generate a wide range of geochemical and geophysical signals. Other analyzed observables are gravity changes, electrical conductivity, amount, composition and temperature of the emitted gases at surface, and extent of degassing area. Results highlight the different temporal response of the considered observables, as well as the different radial pattern of variation.

However, magnitude, temporal response and radial pattern of these signals depend not only on the input of magmatic fluids, but a main role is played by the considered rock properties. Chapter 4 focuses on the effects of rock properties and their spatial distribution on the evolution of selected observables. Numerical simulations highlight differences that arise from the assumption of different permeabilities, for both homogeneous and heterogeneous systems. Rock properties affect hydrothermal fluid circulation, controlling both the range of variation and the temporal evolution of the observable signals.

Results from Campi Flegrei caldera modeling, highlight changes of observables of the same order of magnitude of the observed signals. However, simulations performed on a large scale domain, representing the whole caldera, are unable to properly describe the shallow subsurface. Chapter 5 show a small scale simulation focused on the Solfatara crater, where most of the Campi Flegrei hydrothermal activity is concentrated. A proper choice of the boundary and initial condition results in a detailed modeling of the shallow subsurface, and permits to reproduce the main features of the crater. A more detailed electrical conductivity map is developed, with results comparable with data.

Low temperature fumaroles and low discharge rate may be affected by atmospheric conditions. Continuous monitoring of hydrothermal soil CO_2 flux performed at Furnas volcano (S. Miguel island, Azores) has shown daily and seasonal cycles in time series. Soil degassing well correlates with monitored air temperature and barometric pressure. Chapter 6 show several parametric simulations with TOUGH2/EOS2, aimed to understand the effects of system properties, such as permeability and gas reservoir overpressure, on diffuse degassing when a perturbation is applied to the ground surface. Using a 1D model and changing air temperature and barometric pressure, numerical results are in agreement with observed data and show a strong dependence of the CO_2 degassing on domain permeability and reservoir overpressure.

Hydrothermal circulation, however, is not only a characteristic of volcanic system. Hot fluids may be involved in several mankind problems, such as studies on geothermal engineering, nuclear waste propagation in porous medium, and Geological Carbon Sequestration (GCS). The current concept for large-scale GCS is the direct injection of supercritical CO_2 into deep geological formations which typically contain brine. Upward displacement of such brine from deep reservoirs driven by pressure increases resulting from CO_2 injection may occur through abandoned wells, permeable faults or permeable channels. Brine intrusion into aquifers may degrade groundwater resources. Chapter 7 show simulations, carried out using TOUGH2/EOS7, of upward displacement of warm, salty water into cooler, fresher aquifer. Numerical results show that pressure rise drives dense water up to the conduits, and does not necessarily result in continuous flow. Rather, overpressure leads to new hydrostatic equilibrium if fluids are initially density stratified. If warm and salty fluid does not cool passing through the conduit, an oscillatory solution is then possible. Parameter studies delineate steady-state (static) and oscillatory solutions.

Hydrothermal system and numerical modeling

Contents

1.1 Introduction

Hydrothermal fluid circulation may play a pivotal role in the understanding processes that occur in areas where thermal anomalies are present. Fluids circulating in a hydrothermal system may originate due to the presence of groundwater, meteoric water or seawater. In a volcanic setting, where a magma chamber acts as heat and gases source, fluids feeding fumaroles and hot springs are a fundamental resource for the hazard evaluation. In fact, when a magmatic system approaches a period of activity, changes may affect the hydrothermal system, and then produce variations in fluid conditions. These fluid condition variations may produce measurable changes of geophysical and geochemical observables related to hydrothermal circulation. Hydrothermal fluid circulation, however, is not only a characteristic of volcanic systems. Hot fluids may be involved in several mankind problems, such as studies on geothermal and mining engineering, nuclear waste propagation in porous media, and Geological Carbon Sequestration (GCS).

A hydrothermal system can be summarized as a set of processes with physical, chemical, and biological characteristics. Many reviews of hydrothermal system theory have been produced in the past (e.g. Norton, 1984; Kelley et al., 2002; Pirajno and van Kranendonk, 2005), and this theory is characterized by a complex

mathematical formulation since hydrothermal fluids may coexist in a wide range of temperatures as liquid, gas, two-phase mixture, or supercritical fluids. Then, numerical modeling accuracy of this theory depends on the level of detail we want to investigate, and modeling may range from simple models accounting only for total heat and fluid reserve, to very complex models in which fluid and heat flow are described in detail through space and time.

Ingebritsen et al. (2010) provide a throughout review of the numerical models used in the past 2 decades. Early numerical models of hydrothermal systems were applied for geophysical studies (e.g. Elder, 1967; Norton and Knight, 1977), but a development of multiphase codes is mainly due to application in geothermal engineering (see Stanford Geothermal Program, 1980). Nowadays, multiphase and multicomponent codes, such as TOUGH (Transport of Unsaturated Groundwater and Heat, Pruess, 1988; Pruess et al., 1999), FEHM (Finite Element Heat and Mass Transfer, Zyvoloski et al., 1997), and HYDROTHERM (Hayba and Ingebritsen, 1994), are widely used with applications in many research fields, ranging from environmental restoration to vadose zone hydrology, carbon dioxide sequestration, and mining engineering (O'Sullivan et al., 2001; Pruess, 2008; Oldenburg and Rinaldi, 2011). In the last 2 decades many studies have been focused on hydrothermal fluid circulation in volcanic areas (e.g. Bonafede, 1991; Gaeta et al., 1998, 2003; Reid, 2004) and studies with multiphase and multicomponent code are more and more common (Chiodini et al., 2003; Todesco et al., 2003a,b, 2004, 2010; Todesco and Berrino, 2005; Hurwitz et al., 2007; Todesco, 2009; Hutnak et al., 2009; Rinaldi et al., 2009, 2010, 2011)

Simulations of hydrothermal fluid circulation in this thesis have been carried out with the TOUGH2 code (Pruess et al., 1999). This multi-phase and multi-component geothermal simulator, accounting for coupled flow of heat and fluids, well describes water properties and phase transitions, taking into account the relative permeability of each phase and the effects of capillarity pressure, both calculated as functions of phase volumetric fraction. The continuous mass- and energy-balance equations (described in Sect. 1.2) are discretized in space according to the integral finite difference method, while time is implicitly discretized as a first order finite difference (see Sect. 1.3). Several modules for thermophysical properties (equations of state, EOS) are implemented into TOUGH. In this work we use the module EOS2 (see Sect. 1.3.2 and O'Sullivan et al., 1985), for concurrent presence of water and carbon dioxide, and the module EOS7, an equation of state for saline water and air (see Sect. 1.3.2 and Pruess, 1991). The basic version of TOUGH2 does not account for chemical reaction nor deformation of the rock matrix, although some recent advances of TOUGH family of codes include reactive fluid flow (TOUGHREACT, Xu and Pruess, 2001; Xu et al., 2001) and geomechanics (TOUGH-FLAC, Rutqvist et al., 2002). A program providing inverse modeling capability for TOUGH2 has been also developed recently (iTOUGH2, Finsterle, 2007).

1.2 Fluid, mass, and heat in porous media

1.2.1 Fluid flow

Fluids generally move if subjected to forces, such as pressure and gravity force. An empiric law was established by Henry Darcy (1856), relating fluid flow to the forces causing the motion. Experimentally, fluids move from higher to lower pressure zones. Darcy's experiments show that fluid mass flow rate per unit area (F) depends on pressure variation per unit length, i.e. the pressure gradient (∇p). For three dimensional flow we have:

$$\mathbf{F} = -\kappa \frac{\rho}{\eta} (\nabla p - \rho \mathbf{g}) \tag{1.1}$$

where κ is the absolute permeability, ρ is the fluid density, and η is the fluid viscosity. The vector $\mathbf{g}$ is the gravity acceleration.

The volumetric flow represents the so-called "Darcy velocity", and although it is dimensionally the same of a velocity, it represents the amount of fluid crossing a unit area in a unit time:

$$\mathbf{v} = -\frac{\kappa}{\eta} (\nabla p - \rho \mathbf{g}) \tag{1.2}$$

and it is different from the real velocity at which fluids move in a porous medium ("pore velocity"). Darcy velocity ($\mathbf{v}$) and pore velocity ($\mathbf{w}$) are related by the simple equation:

$$\mathbf{v} = \phi \mathbf{w}$$

where ϕ is the interconnected porosity of the porous medium.

The above formulation is valid for a porous medium filled with single-phase fluid. However, in hydrothermal system both phases (liquid and gas) may coexist inside a pore. Each phase moves because its own pressure gradient and body volume forces, and each phase occupies only a portion of the pore space. This latter effect can be considered introducing a relative permeability $\kappa_{r\beta}$, where β represents the phase (liquid or gas), and Eq. 1.1 turns into (Helmig, 1997):

$$\mathbf{F}_\beta = -\kappa \frac{\kappa_{r\beta} \rho_\beta}{\eta_{r\beta}} (\nabla p_\beta - \rho_\beta \mathbf{g}) \tag{1.3}$$

where ρ_β, η_β and p_β represent the density, viscosity and pressure of phase β, respectively. $p_\beta = p + p_{c\beta}$, where p is a reference pressure (generally taken as the gas phase pressure), and $p_{c\beta}$ (≤ 0) is the capillarity pressure.

1.2.2 Mass balance

Hydrothermal fluids are generally a mixture of several component. Liquid phase is generally water which contain dissolved salt (e.g. NaCl) or non condensible gases (e.g. CO_2, H_2S). Gas phase is usually water vapor, but non-negligible amount of other gases can be present. For a mathematical formulation of multiphase and multicomponent fluid, the mass fraction of each component k in the phase β has to

be taken into account. Mass of each component in a multi-phase, multi-component fluid in a porous medium can be expressed as:

$$M^k = \phi \sum_\beta S_\beta \rho_\beta \chi_\beta^k \tag{1.4}$$

where S_β is the saturation (or volume fraction) of the phase β and χ_β^k is the mass fraction of component k present in phase β. Then the advective mass flow is a sum over the phases:

$$\mathbf{F}_{\text{adv}}^k = \sum_\beta \chi_\beta \mathbf{F}_\beta$$

with $\mathbf{F}_\beta$ as expressed in Eq. 1.3.

Mass transport occurs also by diffusion and hydrodynamic dispersion (Ingebritsen and Sanford, 1998). Diffusive flux can be derived using the Fick's law:

$$\mathbf{F}_{\text{dif}} = -d_w \nabla C$$

where d_w is the coefficient of molecular diffusion in water and C the solute concentration. In a porous medium, however, we have to consider the effects of the porous matrix, such as the reduced volume in which a solute may diffuse and the increase of fluid path tortuosity, and then the diffusion coefficient is:

$$D = \phi \tau d$$

where ϕ is the porosity ad τ is the tortuosity. In case of multiphase mixture the tortuosity ($\tau = \tau_0 \tau_\beta$) should account for both the effects due to porous rock geometry (τ_0) and the effects due to phase saturation ($\tau_\beta = \tau_\beta(S_\beta)$). Mechanical dispersion occurs because of pore velocity fluctuation. Diffusion and mechanical dispersion are generally coupled and cause effects known as hydrodynamic dispersion. Coefficients for hydrodynamic dispersion are defined using a tensor:

$$\bar{D}_{ij} = \alpha_{ijkl} \frac{v_k v_l}{v^2} + D$$

where α_{ijkl} is the porous medium dispersivity, v_k are the component of the Darcy velocity (Eq. 1.2) and D is the diffusivity. For isotropic media, the dispersivity tensor α has only two components: α_L, medium dispersivity along the fluid flow, and α_T, medium dispersivity transverse to the fluid flow. Considering an isotropic medium and a multi-component, multi-phase fluid, diffusive and dispersive mass transport can be written for each component as a sum over the phases (de Marsily, 1986):

$$\mathbf{F}_{\text{dis}}^k = -\sum_\beta \rho_\beta \bar{\mathbf{D}}_\beta^k \nabla \chi_\beta^k$$

where the hydrodynamic dispersion tensor is given by:

$$\bar{\mathbf{D}}_\beta^k = D_{\beta,T}^k \bar{\mathbf{I}} + \frac{(D_{\beta,L}^k - D_{\beta,T}^k)}{v_\beta^2} \mathbf{v}_\beta \mathbf{v}_\beta$$

where

$$\begin{cases} D_{\beta,L}^k = \phi\tau_0\tau_\beta d_\beta^k + \alpha_{\beta,L}v_\beta \\ D_{\beta,T}^k = \phi\tau_0\tau_\beta d_\beta^k + \alpha_{\beta,T}v_\beta \end{cases}$$

are the longitudinal and transverse dispersivity coefficients. d_β^k is the molecular diffusion coefficient for component k in phase β. Mass flow deriving only by molecular diffusion can be taken into account considering $\alpha_T = \alpha_L = 0$ in the previous equations:

$$\mathbf{f}_\beta^k = -\phi\tau_0\tau_\beta d_\beta^k \nabla\chi_\beta^k$$

Mass balance can be applied, for each component, using the equation:

$$\frac{\partial M^k}{\partial t} = -\nabla \cdot (\mathbf{F}^k) + q^k \tag{1.5}$$

where $\mathbf{F}^k = \mathbf{F}_{\text{adv}}^k + \mathbf{F}_{\text{dis}}^k$ and q^k represents the fluid mass contribution due to sinks and source.

1.2.3 Energy balance

Energy changes in a porous medium are due to heat propagation and fluid flow. Considering a porous medium with rock density ρ_R and specific heat C_R filled with a fluid with density ρ_f and specific internal energy u_f, and neglecting viscous dissipation, we can write the energy balance equation as:

$$\frac{\partial}{\partial t}[\phi\rho_f u_f + (1-\phi)\rho_R C_R T] = -\nabla \cdot \mathbf{q} + Q \tag{1.6}$$

where ϕ is the porosity and $\mathbf{q} = \mathbf{q}_c + \mathbf{q}_a$ is the heat flow, which is the sum of conductive and advective contributions. Q represents the energy gain or loss from sinks and sources. Conductive heat flow, using the Fourier law, is associated to a temperature gradient ∇T:

$$\mathbf{q}_c = -\lambda\nabla T$$

where λ is the rock thermal conductivity. Advective contribution are related to heat transport due to fluid motion only:

$$\mathbf{q}_a = h_f\mathbf{F}$$

where $\mathbf{F}$ represents the fluid flow (1.1), and h_f is the specific enthalpy.

Conduction and advection are not the only mechanisms of heat transfer. Heat exchange may occur due to phase changes, such as condensation and evaporation, due to latent heat.

In a multiphase system, we consider a general internal energy per unit volume as accumulation term in Eq. 1.4:

$$M^h = (1-\phi)\rho_R C_R T + \phi\sum_\beta S_\beta\rho_\beta u_\beta \tag{1.7}$$
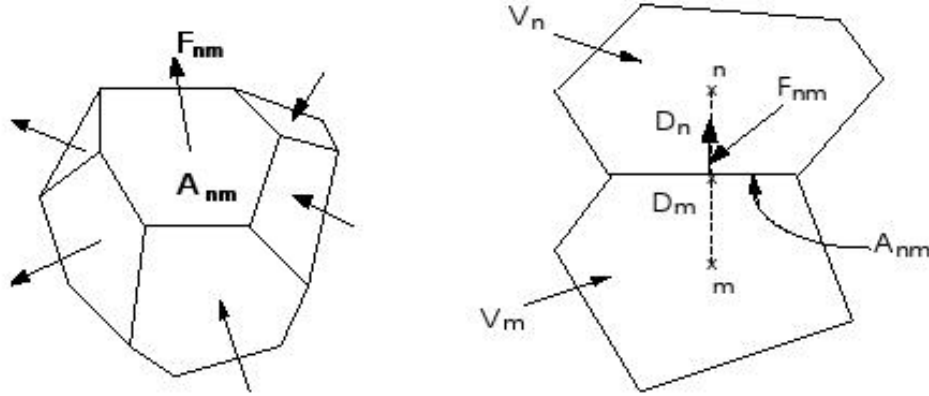
Figure 1.1: Geometry in Integral Finite Difference method as used in TOUGH2 (Pruess et al., 1999)

where u_β is the specific internal energy in phase β. The energy transfer due to fluid flow and conduction is given by:

$$\mathbf{q}^h = -\lambda \nabla T + \sum_\beta h_\beta \mathbf{F}_\beta \tag{1.8}$$

where $\mathbf{F}_\beta$ is the mass flow rate (Eq. 1.3) for the phase β and h_β the corresponding specific enthalpy.

1.3   The TOUGH2 geothermal simulator

1.3.1   Space and time discretization

Mass and energy balance, described in the previous section, can be applied both to the whole system and to a sub-volume or sub-domain. The basic equations solved using TOUGH2 are in a general, integral form:

$$\frac{d}{dt} \int_{V_n} M^k \, dV_n = \int_{\Gamma_n} \mathbf{F}^k \cdot \mathbf{n} \, d\Gamma_n + \int_{V_n} q^k \, dV_n \tag{1.9}$$

integration is over a general volume V_n with a surface Γ_n. Index $k = 1, ..., NK$ (NK is the total number of components) indicates each component that may be present in the system, where $k = NK + 1$ is the index for the "heat component". M^k represents a unit volume mass ($k = 1, ..., NK$, see Eq. 1.4) or a unit volume energy ($k = NK + 1$ with $M^{NK+1} = M^h$, see Eq. 1.7) , for mass or energy balance respectively. $\mathbf{F}^k$ corresponds to mass flow (for $k = 1, ..., NK$, see 1.5) or heat flow ($k = NK + 1$ with $\mathbf{F}^{NK+1} = \mathbf{q}^h$, see Eq. 1.8), and q represents the contribution from sinks and sources. $\mathbf{n}$ is a unit vector, perpendicular to the surface element $d\Gamma_n$, pointing inward into the volume V_n.

Equations 1.9 are discretized in space and time. Space is discretized using the Integral Finite Difference method (IFD, Edwards, 1972; Narasimhan and Witherspoon, 1976) and the terms in Eq. 1.9 can be approximated, introducing appropriate averages, as:

$$\int_{V_n} M^k \; \mathrm{d}V = V_n M_n^k$$

$$\int_{\Sigma_n} \mathbf{F}^k \cdot \mathbf{n} \; \mathrm{d}\Gamma = \sum_m A_{nm} F_{nm}^k$$

where M_n^k is an average value of M^k over a discrete volume V_n, and F_{nm}^k is the average value of the normal component of the vector $\mathbf{F}$ over the surface segment A_{nm} between two volume elements V_n and V_m. Geometry used in IFD is shown in Fig. 1.1. A great advantage of this space discretization technique comes from the fact that there is no reference to a global system, and equations can be used for irregular discretization. However, a high accuracy in evaluating the average conditions in a block is not guaranteed when space discretization is highly irregular, and this results in a low accuracy of the solution.

Solution accuracy depends upon the accuracy by which the various interface parameters can be expressed in terms of average conditions in grid block.

Spatial discretization of Eq. 1.9 results then in a set of first order differential equations in time

$$\frac{dM_n^k}{dt} = \frac{1}{V_n} \sum_m A_{nm} F_{nm}^k + q_n^k \tag{1.10}$$

where basic Darcy's fluxes F_{nm}^k (Eq. 1.3) are discretized based on average parameters for elements V_n and V_m:

$$F_{\beta,nm} = -\kappa_{nm} \left[\frac{\kappa_{r\beta}\rho_\beta}{\eta_\beta} \right]_{nm} \left[\frac{p_{\beta,n} - p_{\beta,m}}{D_{nm}} - \rho_{\beta,nm} g_{nm} \right]$$

where a double index "nm" is related to an average value at the block interface between elements m and n. $D_{nm} = D_n + D_m$ is the distance between nodes for element n and m, and g_{nm} is the component of gravity acceleration along the direction from m to n (Fig. 1.1).

Time changes, considered as a first-order finite difference, are evaluated as a fully implicit calculation, i.e. fluxes are expressed as a function of unknown thermodynamic parameters at time $t^{j+1} = t^j + \Delta t$ (e.g. Peaceman, 1977). Time discretization may be resumed considering a set of algebraic, non-linear equations of the residual $R_n^{k,j+1}$ for the block element n, component k, at time step $j + 1$:

$$R_n^{k,j+1} = M_n^{k,j+1} - M_n^{k,j} - \frac{\Delta t}{V_n} \left\{ \sum_m A_{nm} F_{nm}^{k,j+1} + V_n q_n^{k,j+1} \right\} = 0 \tag{1.11}$$

This is a set of N_{EQ} equations for each block volume V_n, and N_{EQ} is generally equal to NK (number of mass component) plus a further equation for heat ($N_{EQ} = NK + 1$). In a system with N_{EL} elements, the total number of non-linear coupled equations

to be solved is $N_{EQ} \times N_{EL}$. Then at time t^{j+1} the system is completely definided by $N_{EQ} \times N_{EL}$ unknown primary independent variables (x_i; $i = 1, ..., N_{EL} \times N_{EQ}$).

TOUGH2 solves all the equations by Newton/Raphson iteration. Expanding the residual in Eq. 1.11 and introducing an iteration index p, we have:

$$R_n^{k,j+1}(x_{i,p+1}) = R_n^{k,j+1}(x_{i,p}) + \sum_i \left(\frac{\partial R_n^{k,j+1}}{\partial x_i} \right)_p (x_{i,p+1} - x_{i,p}) + \cdots = 0 \quad (1.12)$$

Neglecting terms of high order, and considering only the first-order terms, it results in $N_{EQ} \times N_{EL}$ linear equation for the increments ($x_{i,p+1} - x_{i,p}$):

$$-\sum_i \left(\frac{\partial R_n^{k,j+1}}{\partial x_i} \right)_p (x_{i,p+1} - x_{i,p}) = R_n^{k,j+1}(x_{i,p}) \quad (1.13)$$

where terms $\partial R_n / \partial x_i$ in the Jacobian matrix can be evaluated by numerical differentiations, then Eq. 1.13 is solved by several methods (Duff, 1977; Moridis and Pruess, 1995, 1998). The iteration process lasts until residual are lower than a convergence value:

$$\left\| \frac{R_{n,p+1}^{k,j+1}}{M_{n,p+1}^{k,j+1}} \right\| \leq \varepsilon$$

When a convergence is not reached after an established number of iterations, the time step size Δt is reduced to start a new iteration process.

1.3.2   Equation of State

Thermophysical properties of a multiphase and multicomponent fluid are modeled in TOUGH through the use of several equation-of-state (EOS) modules, depending on the fluid mixture we choose to model (e.g. water and carbon dioxide, or saline water and air). All the thermophysical parameters of an equations of state can be expressed as a function of these primary variables, which are assigned by an EOS module. Furthermore, the EOS module has three additional functions: (i) identify the phase condition through the primary variables for all the volume elements, (ii) recognize the presence of a phase as primary variable during the Newton-Raphson iteration, and (iii) switch and analyze the primary variables when a change of phase occurs.

Although TOUGH2 includes several EOS modules, able to represent several fluid mixtures, one EOS module at a time should be used. For the purposes of this thesis we use only two equations of state, at different time: the EOS2, a module for a fluid mixture with water and carbon dioxide, and the EOS7, which model a saline water with air.

All water properties (density, specific enthalpy, viscosity, saturated vapor pressure), in both EOS2 and EOS7, are calculated from the steam table equations as given by International Formulation Committee (1967). The formulation includes subcooled water below T = 350 °C, super heated stem, and saturation line up to

T = 350 °C. In these regions, density and internal energy are represented within experimental accuracy, while viscosity of liquid water and steam are represented to within 2.5 % by correlations given in the same reference.

EOS2 was originally developed by O'Sullivan et al. (1985) and then modified after Battistelli et al. (1997), and accounts for non-ideal gaseous CO_2, and dissolution of CO_2 in water. EOS2 follows the Henry's law, which states that the partial pressure of CO_2 in gas phase is proportional to the fraction of dissolved CO_2 in aqueous phase:

$$p_{CO_2} = K_h x_{aq}^{CO_2}$$

where K_h is the Henry's law coefficient. K_h strongly depends on temperature, however the correlation is accurate for temperatures in the range 0-350 °C. The viscosity of vapor-CO_2 mixture is accounted following the formulation of Pritchett et al. (1981) and other thermophysical relations follow the model developed by Sutton and McNabb (1977).

EOS7 (Pruess, 1991) is a module for saline water (mixture of pure water and brine) and air mixtures, and follows the approach developed by Herbert et al. (1988). Assuming volume conservation when water and brine are mixed, mixture density ρ_m can be written as:

$$\frac{1}{\rho_m} = \frac{1 - \chi_b}{\rho_w} + \frac{\chi_b}{\rho_b}$$

where χ_b and ρ_b are the brine mass fraction and density, respectively, and ρ_w is pure water density. Compressibility and expansivity of the brine are assumed to be equal to those of the water. Mixture viscosity η_m is modeled taking into account the salinity effects:

$$\eta_m(p, T, \chi_b) = \eta_w(p, T) f(\chi_b)$$

where

$$f(\chi_b) = 1 + v_1 \chi_b + v_2 \chi_b^2 + v_3 \chi_b^3$$

with v_1=0.4819, v_2=-0.2774, and v_3=0.7814 (Herbert et al., 1988). Air dissolution is also taken into account, and modeled by Henry's law. Minor solubility of gases in saline solutions is also considered.

1.4   Elements of poro-elasticity

The presence of fluid in the pores affects the deformation of a porous medium. A pioneer study on deformation in a porous medium was developed by Biot (1941). Several review on poro-elasticity are present in the literature (e.g. Detournay and Cheng, 1993), but for the aim of this thesis we follow the formulation by Rice and Cleary (1976), who accounts for drained and undrained behavior of porous media. A poro-elastic medium can be described by the following parameters:

   a. a tensor of strain e_{ij}, defining the variation of distance between two material points;

b. a tensor of stress τ_{ij}, representing the j-component of surface force applied to i-coordinate plane;

c. the pore pressure p, i.e. the the pressure of the fluid in the pore;

d. the fluid content v, i.e. the volume of fluid in a unit volume of material.

and, moreover, a poro-elastic material must satisfy the following assumptions:

1. isotropy;

2. reversibility of stress-strain relation at equilibrium;

3. linearity of constitutive equations for small deformations;

4. fluid flow in the pores must follow the Darcy law (see Sect. 1.2)

Assuming reversible changes, macroscopic variables such as strain e_{ij} and fluid content v must be functions of stress τ_{ij} and pore pressure p. The elastic relation between strain tensor e_{ij} and stress tensor τ_{ij} is still valid in poro-elasticity, however we need to take into account also the effects on strain deriving from variation in pore pressure p. Effects of pore pressure on deformation can be written as a tensorial relation, and as a function of the identity tensor, due the assumption of isotropy: $e_{ij} = b\Delta p \delta_{ij}$ where b is a constant describing the volume increasing of unit cube of material, due to a change Δp in pore pressure ($b = 1/3H$). Then, the constitutive equations for drained conditions can be written as:

$$e_{ij} = \frac{1}{2\mu}\left(\tau_{ij} - \frac{\nu}{1+\nu}\tau_{kk}\delta_{ij}\right) + \frac{\Delta p}{3H}\delta_{ij} \tag{1.14}$$

where μ and ν are the rigidity module and the Poisson's coefficient of the rock matrix (the so-called "drained" modules). Constant H, known as Biot's constant, can be expressed as a function of the incompressibility coefficient K (drained bulk modulus) and of the incompressibility coefficient K_s for rock matrix only (or K'_s which considers also the presence of insulated pores):

$$\frac{1}{H} = \frac{1}{K} - \frac{1}{K'_s}$$

Fluid content varies proportionally to the pore pressure and the trace of the stress tensor. We can write:

$$v = \frac{1}{3H}\tau_{kk} + \frac{1}{R}\Delta p$$

where R describes the fluid volume increasing (or decreasing) inside the material, due to dilatation (or contraction) of pores induced by changes in pore pressure. When insulated pores are considered, the constant R can be expressed as:

$$\frac{1}{R} = \frac{1}{H} - \frac{v_0}{K''_s}$$

where v_0 is the initial fluid content and K_s'' is an incompressibility coefficient taking into account not only insulated pores, but also that pores are not completely filled by fluid.

In undrained conditions we assume that fluid mass doesn't change during application of stresses. If a fluid is compressible, then its density changes with pore pressure, and the mass variation is:

$$\Delta m = m - m_0 = (\rho_0 + \Delta\rho)(v_0 + \Delta v) - \rho_0 v_0 \sim \rho_0 \Delta v + v_0 \Delta\rho$$

where $\Delta\rho = \rho\Delta p/K_f$ is the density variation, with K_f indicating fluid incompressibility coefficient. Considering the equation for the fluid volume content, mass variations can be then re-written as:

$$\Delta m = \rho_0 \frac{v_0}{K_f}\Delta p + \frac{\rho_0}{3}\left(\frac{1}{K} - \frac{v_0}{K_s''}\right)(\tau_{kk} + 3\Delta p) - \rho_0 \frac{v_0}{K_s''}\Delta p \qquad (1.15)$$

We call "undrained deformation" processes in a short time scale where fluid mass variation is null ($\Delta m = 0$). Applying in such condition a stress τ_{ij} to the material, we will generate a pore pressure (from Eq. 1.15 with $\Delta m = 0$):

$$p = -\frac{1}{3}B\tau_{kk} \quad \text{with } B = \frac{\frac{1}{K} - \frac{1}{K_s'}}{\frac{v_0}{K_f} + \frac{1}{K} - \frac{1}{K_s'} - \frac{v_0}{K_s''}}$$

where B is the so-called Skempton's coefficient. The constitutive equation can be then re-written as a function of an "undrained" Poisson's coefficient:

$$e_{ij} = \frac{1}{2\mu}\left(\tau_{ij} - \frac{\nu_u}{1 + \nu_u}\tau_{kk}\delta_{ij}\right) \qquad (1.16)$$

with ν_u defined as:
$$\nu_u = \frac{3\nu + B(1 - 2\nu)(1 - K/K_s')}{3 - B(1 - 2\nu)(1 - K/K_s')}$$

ν_u values ranges from ν to 0.5. When fluid and rock are incompressible then $B \sim 1$ and we have $\nu_u \sim 0.5$. If we have $K \sim K_s'$ (low compressibility pores) or $B \sim 0$ (high fluid compressibility). then $\nu_u \sim \nu$.

Temperature changes may also affect the elastic response in a porous media. Such effects can be taken into account considering the formulation by McTigue (1986), and the strain due to temperature changes will be:

$$e_{ij} = \frac{\alpha_s}{3}\Delta T\delta_{ij}$$

where ΔT is the temperature variation and α_s represent the volumetric thermal expansion coefficient of the rock matrix.

References

Battistelli, A., Calore, C., Pruess, K., 1997. The simulator TOUGH2/EWASG for Modeling Geothermal Reservoirs with Brines and Non-Condensible Gas. Geothermics 26(4), 437–464.

Biot, M.A., 1941. General theory of three-dimensional consolidation. J. Appl. Phys. 12, 155–164.

Bonafede, M., 1991. Hot fluid migration: an efficient source of ground deformation: application to the 1982-1985 crisis at Campi Flegrei-Italy. J. Volcanol. Geotherm. Res. 48, 187–198.

Chiodini, G., Todesco, M., Caliro, S., Del Gaudio, C., Macedonio, G., Russo, M., 2003. Magma degassing as a trigger of bradyseismic events: the case of Phlegrean Fields (Italy). Geophys. Res. Lett. 30(8), 1434–1437. doi:10.1029/2002GL016790.

de Marsily, G. (Ed.), 1986. Quantitative Hydrogeology: Groundwater Hydrology for Engineers. Academic Press In.c, San Diego.

Detournay, E., Cheng, A.D., 1993. Fundamentals of Poroelasticity, in: Fairhurst, C. (Ed.), Comprehensive Rock Engineering: Principles, Pratice and Projects, vol. II, Analysis and Design Method. Pergamon Press, pp. 113–171.

Duff, I., 1977. MA28 - A Set of FORTRAN Subroutines for Sparse Unsymmetric Linear Equations. AERE Harwell Report R 8730 .

Edwards, A.L., 1972. TRUMP: A Computer Program for Transient and Steady State Temperature Distribution in Multidimensional Systems. National Technical Information Service, National Bureau of Standards, Springfield, VA.

Elder, J., 1967. Transient convection in a porous medium. J. Fluid Mech. 27, 609–623.

Finsterle, S., 2007. iTOUGH2 User's Guide. Paper LBNL-40040. Lawrence Berkeley Natl. Lab., Berkeley, CA, USA.

Gaeta, F.S., De Natale, G., Peluso, F., Mastrolorenzo, G., Castagnolo, D., Troise, C., Pingue, F., Mita, D.G., Rossano, S., 1998. Genesis and evolution of unrest episodes at Campi Flegrei caldera: The role of thermal fluid-dynamical processes in the geothermal system. J. Geophys. Res. 103(B9), 20921–20933.

Gaeta, F.S., Peluso, F., Arienzo, I., Castagnolo, D., De Natale, G., Milano, G., Albanese, C., Mita, D.G., 2003. A physical appraisal of a new aspect of bradyseism: The miniuplifts. J. Geophys. Res. 108(B8). doi:10.1029/2002JB001913.

Hayba, D.O., Ingebritsen, S.E., 1994. The computer model HYDROTHERM, a three-dimensional finite-difference model to simulate ground-water flow and heat transport in the temperature range of 0 to 1,200 °C. U.S. Geol. Surv. Water Resour. Invest. Rep., 94-4045 .

Helmig, R. (Ed.), 1997. Multiphase Flow and Transport Processes in the Subsurface: A Contribution to the Modeling of Hydrosystems. Springer-Verlag, Berlin.

Herbert, A.W., Jackson, C.P., Lever, D.A., 1988. Coupled Groundwater Flow and Solute Transport with Fluid Density Strongly Dependent on Concentration. Water Resour. Res. 24(10), 1781–1795.

Hurwitz, S., Christiansen, L.B., Hsieh, P.A., 2007. Hydrothermal fluid flow and deformation in large calderas: Inferences from numerical simulations. J. Geophys. Res. 112, B02206. doi:10.1029/2006JB004689.

Hutnak, M., Hurwitz, S., Ingebritsen, S.E., Hsieh, P.A., 2009. Numerical models of caldera deformation: Effects of multiphase and multicomponent hydrothermal fluid flow. J. Geophys. Res. 114, B04411. doi:10.1029/2008JB006151.

Ingebritsen, S., Sanford, W.E. (Eds.), 1998. Groundwater in geologic process. Cambridge University Press, New York.

Ingebritsen, S.E., Geiger, S., Hurwitz, S., Driesner, T., 2010. Numerical simulation of magmatic hydrothermal system. Rev. Geophys. 48, RG1002. doi:10.1029/2009RG000287.

International Formulation Committee, 1967. A Formulation of the Thermodynamic Properties of Ordinary Water Substance. IFC Secretariat, Düsseldorf, Germany .

Kelley, D.S., Baross, L.A., Delaney, J.R., 2002. Volcanoes, fluids, and life at mid-ocean ridge spreading centers. Annu. Rev. Earth Planet. Sci. 30, 385–491.

McTigue, D.F., 1986. Thermoelastic response of fluid-saturated porous rock. jgr 91(B9), 9533–9542.

Moridis, G., Pruess, K., 1995. Flow and Transport Simulations Using T2CG1, a Package of Conjugate Gradient Solvers for the TOUGH2 Family of Codes. Paper LBNL-36235. Lawrence Berkeley Natl. Lab., Berkeley, CA, USA.

Moridis, G., Pruess, K., 1998. T2SOLV: An Enhanced Package of Solvers for the TOUGH2 Family of Reservoir Simulation Codes. Geothermics 27(4), 415–444.

Narasimhan, T.N., Witherspoon, P.A., 1976. An Integrated Finite Difference Method for Analyzing Fluid Flow in Porous Media. Water Resour. Res. 12(1), 57–64.

Norton, D.L., 1984. Theory of hydrothermal system. Annu. Rev. Earth Planet. Sci. 12, 155–178.

Norton, D.L., Knight, J., 1977. Transport phenomena in hydrothermal system: cooling plutons. Am. J. Sci. 277, 937–981.

Oldenburg, C.M., Rinaldi, A.P., 2011. Buoyancy Effects on Upward Brine Displacement Caused by CO_2 Injection. Transp. Porous Med. Online First.

O'Sullivan, M.J., Bodvarsson, G.S., Pruess, K., Blakeley, M., 1985. Fluid and Heat Flow in Gas-Rich Geothermal Reservoirs. Society of Petroleum Engineers Journal 25(2), 215–226.

O'Sullivan, M.J., Pruess, K., Lippman, M.J., 2001. State of the art of geothermal reservoir simulation. Geothermics 30, 395–429.

Peaceman, D. (Ed.), 1977. Fundamentals of Numerical Reservoir Simulation. Elsevier, Amsterdam, The Netherlands.

Pirajno, F., van Kranendonk, M.J., 2005. Review of hydrothermal processes and systems on Earth and implications for Martian analogues. Aust. J. Earth Sci. 52, 329–351.

Pritchett, J.W., Rice, M.H., Riney, T.D., 1981. Equation-of-state for Water-Carbon Dioxide Mixtures: Implications for Baca Reservoir. Report DOE/ET/27163-8, Systems, Science and Software, La Jolla, CA.

Pruess, K., 1988. SHAFT, MULKOM, TOUGH: A set of numerical simulators for multiphase fluid and heat flow. Paper LBNL-24430. Lawrence Berkeley Natl. Lab., Berkeley, CA, USA.

Pruess, K., 1991. EOS7, An equation-of-State Module for the TOUGH2 Simulatr for Two-Phase Flow of Saline Water and Air. Paper LBNL-31114. Lawrence Berkeley Natl. Lab., Berkeley, CA, USA.

Pruess, K., 2008. On CO_2 fluid flow and heat transfer behavior in the subsurface following leakage from geologic storage reservoir. Environ. Geol. 54(8), 1677–1686.

Pruess, K., Oldenburg, C.M., Moridis, G., 1999. TOUGH2 User's Guide, Version 2.0. Paper LBNL-43134. Lawrence Berkeley Natl. Lab., Berkeley, CA, USA.

Reid, M.E., 2004. Massive collapse of volcano edifices triggered by hydrothermal pressurization. Geology 32, 373–376.

Rice, J.R., Cleary, M.P., 1976. Some basic stress diffusion solutions for fluid-saturated elastic porous media with compressible constituents. Rev. Geophys. Space Phys. 14, 227–241.

Rinaldi, A.P., Todesco, M., Bonafede, M., 2010. Hydrothermal instability and ground displacement at the Campi Flegrei caldera. Phys. Earth Planet. Int. 178, 155–161. doi: 10.1016/j.pepi.2009.09.005.

Rinaldi, A.P., Todesco, M., Vandemeulebrouck, J., Revil, A., Bonafede, M., 2011. Electrical conductivity, ground displacement, gravity changes, and gas flow at Solfatara crater (Campi Flegrei caldera, Italy): results from numerical modeling. J. Volcanol. Geotherm. Res. Submitted.

Rinaldi, A.P., Vandemeulebrouck, J., Todesco, M., 2009. Modeling of hydrothermal fluid circulation as a tool for volcanic hazard assessment, in: PROCEEDINGS, TOUGH Symposium 2009. Lawrence Berkeley National Laboratory, Berkeley, California, September 14-16, 2009.

Rutqvist, J., Wu, Y.S., Tsang, C.F., Bodvarsson, G., 2002. A modeling approach for analysis of coupled multiphase fluid flow, heat transfer, and deformation in fractured porous rock. Int. J. Rock Mech. 39, 429–442.

Stanford Geothermal Program, 1980. Proceedings of special panel on geothermal model intercomparizon study at 6th Workshop on Geothermal Reservoir Engineering. Stanford University, Stanford, California, December 17, 1980 Stanford Geotherm. Program Rep., SGP-TR-42, Stanford Un., Stanford, CA.

Sutton, F.M., McNabb, A., 1977. Boiling Curves at Broadlands Field, New Zealand. N. Z. J. Sci. 20, 333–337.

Todesco, M., 2009. Signals from the Campi Flegrei hydrothermal system: Role of a "magmatic" source of fluids. J. Geophys. Res. 114, B05201. doi:10.1029/2008JB006134.

Todesco, M., Berrino, G., 2005. Modelling hydrothermal fluid circulation and gravity signals at the Phlegrean Fields caldera. Earth Plan. Sci. Lett. 240, 328–338. doi:10.1016/j.epsl.2005.09.016.

Todesco, M., Chiodini, G., Macedonio, G., 2003a. Monitoring and modelling hydrothermal fluid emission at La Solfatara (Phlegrean Field, Italy). An interdisciplinary approach to the study of diffuse degassing. J. Volcanol. Geotherm. Res. 125, 57–79. doi:10.1016/S0377-0273(03)00089-1.

Todesco, M., Rinaldi, A.P., Bonafede, M., 2010. Modeling of unrest signals in heterogeneous hydrothermal systems. J. Geophys. Res. 115, B09213. doi:10.1029/2010JB007474.

Todesco, M., Rutqvist, J., Chiodini, G., Pruess, K., Oldenburg, C.M., 2004. Modeling of recent volcanic episodes at Phlegrean Fields (Italy): geochemical variations and ground deformation. Geothermics 33, 531–547. doi:10.1016/j.geothermics.2003.08.014.

Todesco, M., Rutqvist, J., Pruess, K., Oldenburg, C.M., 2003b. Multi-phase fluid circulation and ground deformation: a new perspective on bradyseismic activity at Phlegrean Fields (Italy), in: Proceedings of the 28th Workshop on Geothermal Research Engineering. Stanford, CA, USA.

Xu, T., Pruess, K., 2001. Modelling multiphase non-isothermal fluid flow and reactive geochemical transport in variably saturated fractured rocks: 1. Methodology. Am. J. Sci. 301, 16–33.

Xu, T., Sonnenthal, E., Spycher, N., Pruess, K., Brimhall, G., Apps, J., 2001. Modelling multiphase non-isothermal fluid flow and reactive geochemical transport in variably saturated fractured rocks: 1. Methodology. Am. J. Sci. 301, 34–59.

Zyvoloski, G., Robinson, B.A., Dash, Z.D., Trease, L.L., 1997. Summary of models and methods for the FEHM application - A finite-element heat- and mass-transfer code. Rep. LA-13307-MS, Los Alamos, Natl. Lab., Los Alamos, N. M., USA.

Hydrothermal instability and ground displacement at the Campi Flegrei caldera

Contents

2.1 Introduction

Campi Flegrei is a large caldera located west of Naples (Italy). Although the last eruption took place at Monte Nuovo in 1538 AD (Di Vito et al., 1987), activity has been present, especially at the Solfatara volcano, as highlighted by monitoring carried out in the last 40 years (Casertano et al., 1976; Barberi et al., 1984; De Natale et al., 2001; Del Gaudio et al., 2010). An accurate reconstruction of the vertical ground displacement over the last century (Del Gaudio et al., 2010) shows the presence of two major episodes of uplift in 1969-1972 (up to 1.7 m) and 1982-1984 (up to 1.8 m). A slow subsidence begun in 1985 and, since then, only minor uplifts (a few cm each) occurred in the caldera (De Natale et al., 2001). Each uplift phase has been accompanied by seismic activity and gravity changes, and by variation of discharge rate and gas composition in fumaroles. Minor crises were similar to the larger ones in terms of deformation pattern and compositional change. Both large and small unrests have been carefully studied for their actual and potential consequences on the densely inhabited surrounding region.

Early models ascribed the observed deformation to a pressure or volume change inside a magma chamber (Bonafede et al., 1986; Bianchi et al., 1987; De Natale et al., 1991). Casertano et al. (1976) made a pioneer study considering the importance of fluids in bradyseismic events. More recently, other authors recognized the effects of heating and expansion of hydrothermal fluids during an unrest (Bonafede, 1990,

1991; De Natale et al., 1991; Gaeta et al., 1998; Orsi et al., 1999; De Natale et al., 2001). These models describe the maximum uplift (1.8 m) observed in 1982-84, and authors suggest that the following subsidence could be due to lateral diffusion of fluids. Using a 1D model, Gaeta et al. (2003) explain minor uplifts as a consequence of hydrothermal fluid circulation. Although these models provide important conceptual insights, they are based on very simplified descriptions of the fluid dynamics and of the embedding medium.

The use of a more sophisticated model of hydrothermal circulation showed that several aspects of the complex unrest dynamics (including deformation) are related to the intensity of magmatic degassing (Chiodini et al., 2003; Todesco et al., 2003a,b, 2004; Todesco and Berrino, 2005; Hurwitz et al., 2007; Hutnak et al., 2009). In this chapter, we want to quantify the amount of deformation that can be caused by hydrothermal fluids during a generic unrest period at Campi Flegrei. Following a well established approach (Todesco et al., 2003b, 2004; Hurwitz et al., 2007), we first simulate the evolution of the hydrothermal system; then we compute the deformation arising from the simulated changes in pore pressure and temperature.

Our simulation of hydrothermal circulation is based on a conceptual model that was developed for Campi Flegrei in previous papers (Chiodini et al., 2003; Todesco et al., 2003a,b, 2004; Todesco and Berrino, 2005): the hydrothermal system is fed by fluids of magmatic origin, and unrest events correspond to periods of increased magmatic degassing. Pore pressure and temperature changes, arising from a given unrest event, are considered here as axially symmetric distributed sources of deformation, and described in terms of a system of equivalent forces. The resulting displacement of the ground surface is then computed analytically, according to the linear theory of thermo-poro-elasticity. Results show that the simulated unrest period can generate centimeters of vertical displacement at the free surface of an elastic homogeneous half-space. The application of the ground displacement model in a 3D case study can be found in the Appendix A

2.2   The ground deformation model

The mathematical model presented here is based on the linear theory of poro-elasticity, which describes the elastic deformation of a porous medium taking into account the flow of a hot fluid that propagates through the pores. Here we follow the formulation proposed by Rice and Cleary (1976) and, given the high temperatures of the fluid, we also take into account the thermo-elastic response of the rock as described by McTigue (1986). The deformation e_{ij} due to a given change in pore pressure and temperature is:

$$e_{ij} = \frac{1}{2\mu}\left(\sigma_{ij} - \frac{\nu}{1+\nu}\sigma_{kk}\delta_{ij}\right) + \frac{\Delta p}{3H}\delta_{ij} + \frac{\alpha_s}{3}\Delta T\delta_{ij} \tag{2.1}$$

where σ_{ij} is the stress tensor; σ_{kk} is the trace of the stress tensor; μ is the shear modulus; ν is the Poisson's ratio in free-drainage conditions; $1/H = 1/K - 1/K_s'$ is the Biot's constant (K is the isothermal, drained bulk modulus and K_s' is the bulk

modulus of the solid constituent); α_s is the volumetric thermal expansion coefficient for the solid matrix; δ_{ij} is the Kronecker delta. Δp and ΔT are the pore pressure and temperature changes, respectively.

In order to evaluate the displacement field arising from pressure and temperature changes at a given point, we follow the approach proposed by Aki and Richards (1980) to compute the seismic displacement generated by a volume source.

We first consider a porous medium in an initial configuration of vanishing stress and strain. We identify a volume source, with dimensions dx, dy, dz, and remove it from its surrounding, without affecting the porous matrix. We then increase pore pressure and temperature in the source volume by supplying heat and fluid, at constant (vanishing) stress. At this stage (A), the source remains unstressed ($\tau_{ij}^{(A)} = 0$), but its volume is isotropically strained ("*Aki's stress-free strain*") by an amount:

$$e_{ij}^{(A)} = \frac{1}{3}\Delta\theta\delta_{ij}$$

where $\Delta\theta$ is the relative volume change, given by the trace of the strain tensor (2.1)

$$\Delta\theta = \frac{\Delta V}{V_0} = e_{kk}^{(A)} = \frac{\Delta p}{H} + \alpha_s\Delta T$$

In order to place the source back in its original position in the porous medium (stage B), we need to restore its original volume V_0: we apply a stress field $\tau_{ij}^{(B)} = -K\Delta\theta\delta_{ij}$ at constant pore pressure and temperature, to obtain a deformation $e_{ij}^{(B)} = -e_{ij}^{(A)}$:

$$\tau_{ij} = \tau_{ij}^{(A)} + \tau_{ij}^{(B)} = \tau_{ij}^{(B)}, \qquad e_{ij} = e_{ij}^{(A)} + e_{ij}^{(B)} = 0$$

Now the source is back in its place, but a traction discontinuity exists over its surface: the matrix is still unstressed and unstrained while the source is subject to the artificial "stress glut" τ_{ij} applied to restore its initial volume. The difference between the outer and the inner values of traction is then $-\tau_{ij}n_j$. Removal of this traction discontinuity will cause the source to expand again but, this time, the surrounding matrix acts against the expansion and prevents the source from reaching the stress-free volume. The displacement field due to the applied pressure and temperature changes at the source can be expressed in terms of this traction discontinuity (Aki and Richards, 1980):

$$u_i(\mathbf{x}) = \int_V K\Delta\theta(\mathbf{x}')\mathcal{G}_{ik,k}(\mathbf{x},\mathbf{x}')\,\mathrm{d}x'\,\mathrm{d}y'\,\mathrm{d}z' \tag{2.2}$$

where K is the bulk modulus, $\mathbf{x}$ is the observation point, $\mathbf{x}'$ is the source position and $\mathcal{G}_{ik}$ is the Green's Tensor.

In order to evaluate the divergence of the Green's Tensor we use a system of distributed equivalent forces. The isotropic point source can be mathematically described as a system of three equal orthogonal dipoles placed at the source point

(Wang, 2000). The displacement field $\mathcal{G}_{ik}$ arising from a single force in a homogeneous half-space with a traction-free boundary was provided by Mindlin (1936).

In this work, we first calculate the displacement due to a single dipole set along the $\hat{x}$, $\hat{y}$ or $\hat{z}$ axes, and then we sum the single components of each field in order to have the total displacement at the observation point. The vertical component of the displacement for this case is:

$$u_z^{tot} = Fh\frac{(1-2\nu)}{8\pi\mu(1-\nu)}\left[\frac{(z-z')}{R_1^3} - (3-4\nu)\frac{z+z'}{R_2^3} + \frac{2z}{R_2^3} - \frac{6z(z+z')^2}{R_2^5}\right] \qquad (2.3)$$

where F and h are the intensity and arm of each dipole; (x, y, z) is the observation point and (x', y', z') is the source point; R_1 is the distance between the deformation source and the observation point ($R_1^2 = (x - x')^2 + (y - y')^2 + (z - z')^2$) and R_2 is the distance between the mirror-source and the observation point ($R_2^2 = (x - x')^2 + (y - y')^2 + (z + z')^2$).

Since we are using a free surface calculation, the horizontal component of the displacement will be different than the vertical:

$$u_h^{tot} = Fh\frac{(1-2\nu)}{8\pi\mu(1-\nu)}\left[\frac{1}{R_1^3} + (3-4\nu)\frac{1}{R_2^3} - \frac{6z(z+z')}{R_2^5}\right](r - r') \qquad (2.4)$$

where $r^2 = x^2 + y^2$ and $r'^2 = x'^2 + y'^2$ represent the radial distance of the observation point and of the source from the $\hat{z}$ axes, respectively.

2.3 The fluid flow model

Hydrothermal circulation is simulated with the multi-phase and multi-component TOUGH2/EOS2 model (Pruess et al., 1999). The computational domain, two-dimensional and axisymmetric, is 10 km wide and 1.5 km deep (Fig. 2.1 shows the axial region only, since most of changes occur near the symmetry axis).

Bottom and side boundaries are impervious and adiabatic. Atmospheric conditions are fixed along the upper boundary, which is open to heat and fluid flows. The properties of the porous medium are listed in Table 2.1. The shallow hydrothermal circulation is driven by the injection of a hot (ca. 623 K) mixture of water and carbon dioxide. This mixture represents the magmatic component that enters the domain near the symmetry axis (Fig. 2.1).

Initial conditions are obtained by simulating a long-lasting (i.e.: thousands of years) injection of magmatic fluids. The prescribed flow rate at the inlet (1000 tons/day of CO_2 and 2400 tons/day of H_2O) reflects data collected at the Campi Flegrei caldera, and corresponds to a CO_2/H_2O molar ratio of 0.17 (Chiodini et al., 2003). As described in previous works (Chiodini et al., 2003; Todesco et al., 2003a,b, 2004), the prolonged activity of the fluid source generates, at the steady state, a wide two-phase plume, with a shallow and a deep single-phase gas regions (Fig. 2.1a). High temperature characterizes the entire plume (Fig. 2.1b), which is also slightly pressurized with respect to the initial hydrostatic gradient.
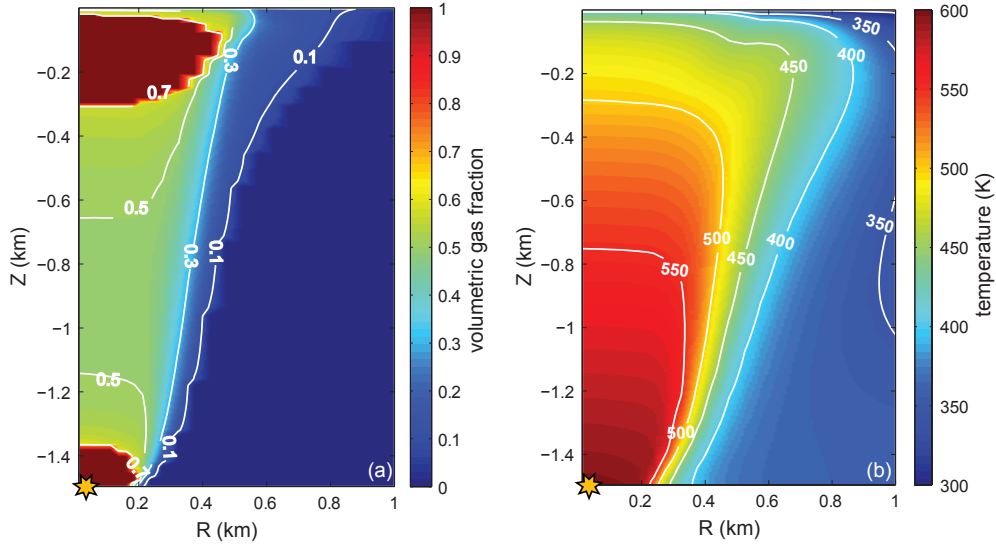
Figure 2.1: Initial conditions: **(a)** volumetric gas fraction and **(b)** temperature (K).The star indicates the inlet of magmatic fluids, which has a radius of 150 m. The computational domain was discretized into 2580 elements, with radial dimensions ranging from 25 to 3196 m and thickness from 5 to 25 m.

Starting from these steady-state initial conditions, the simulation presented here describes an initial unrest phase, provided by a sudden increase of fluid flow, followed by a longer quiet period. The unrest phase lasts 20 months, during which both the input of magmatic fluids and the carbon dioxide content increase (6000 tons/day of CO_2 and 6100 tons/day of H_2O, $CO_2/H_2O=0.4$) at same, constant input temperature (ca. 623 K). During the following quiet phase, flow rate and composition return to the initial values. Inlet conditions corresponding to the different phases are listed in Table 2.2. A sequence of similar unrest and quiet periods was shown to be consistent with observed changes in gas composition and gravity at the Campi Flegrei caldera during the last 30 years (Chiodini et al., 2003; Todesco and Berrino, 2005).

The imposition of a larger discharge rate during the unrest is accompanied by a

Table 2.1: Rock properties considered in the simulation of the hydrothermal system. These properties remain constant during the simulation.

Density	2000 kg m^{-3}
Permeability	10^{-14} m^2
Porosity	0.20
Conductivity	2.80 W m^{-1} K^{-1}
Specific Heat	1000 J kg^{-1} K^{-1}

Table 2.2: Flow rate (ton/day) and CO_2/H_2O molar ratio at the inlet during the unrest and the following quiet. The enthalpy of injected fluids corresponds to a temperature of ca. 623 K and does not change during the simulation.

	CO_2	H_2O	Molar Ratio
Quiet	1000	2400	0.17
Unrest	6000	6100	0.40
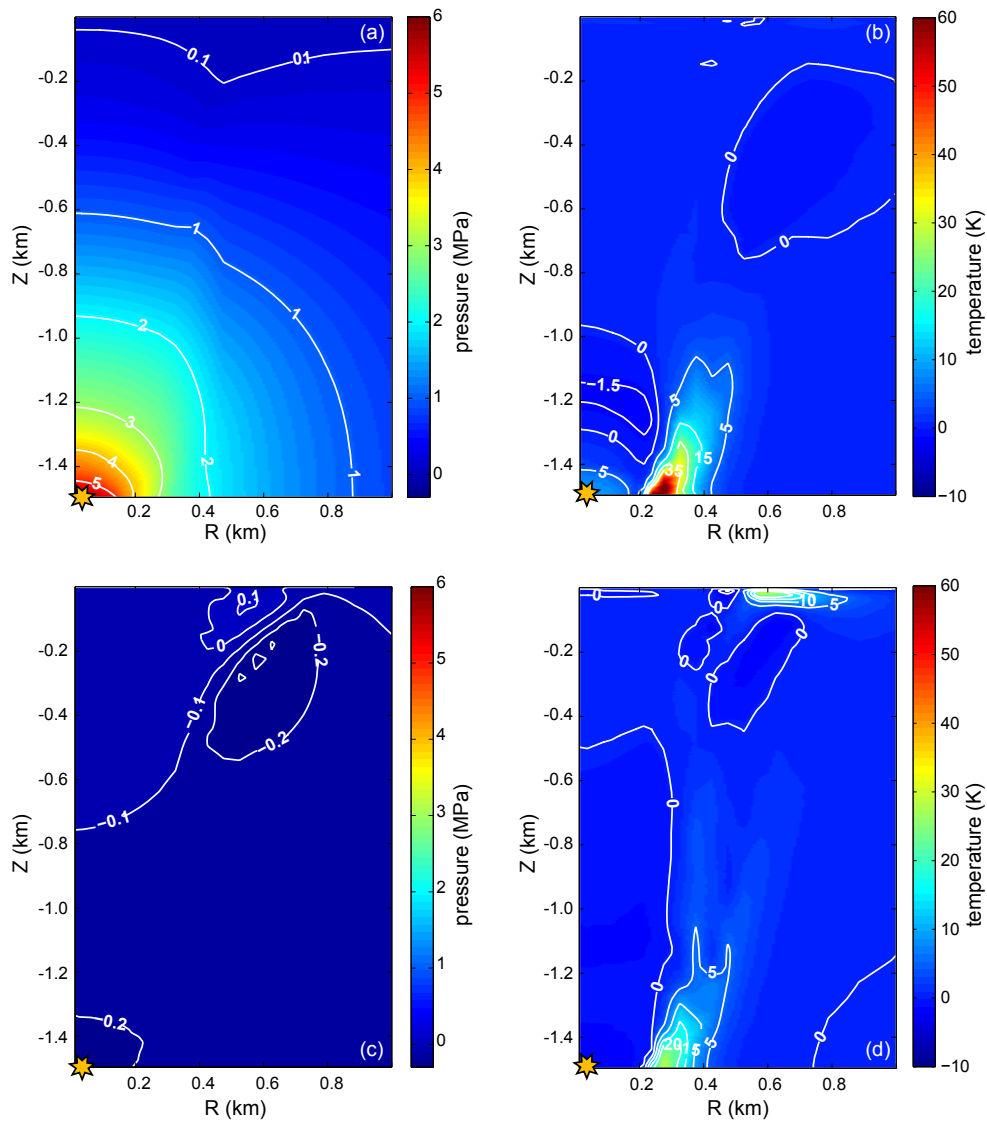
Figure 2.2:   Simulated changes with respect to the initial conditions at different times: (**a,c**) pore pressure (MPa) and (**b,d**) temperature (K) changes at the end of unrest and at the end of simulation, respectively. The figures refer to axial region. The star indicates the inlet of magmatic fluids.

pressure build-up, which gradually spreads out as the fluids propagate through the system. At the end of the unrest, pressure changes range from +5 MPa, near the fluid inlet, to +0.1 MPa near the ground surface (Fig. 2.2a).

The unrest is also associated with temperature changes, even if the specific enthalpy of injected fluids does not change. Temperature changes, up to tens of Kelvin, are mostly confined along the edges of the two-phase plume (Fig. 2.2b) and are related to the lateral spreading of the two-phase region during the unrest. As the hot, gas-rich fluids replace the colder liquid water, temperature may increase up

to 40 K (Fig. 2.3a). Temperature changes within the two-phase plume may occur as well, as a consequence of water phase changes: pressure build-up near the inlet can cause the condensation of water vapor (Fig. 2.3a) and the associated release of latent heat increases the temperature in the region above the fluid source (+5 K). At shallower depths, some fraction of liquid water in the two-phase region evaporates (Fig. 2.3a), subtracting latent heat and causing minor cooling (ca. -1.5 K).

When the unrest is over, pore pressure drops and the two-phase plume begins to shrink gradually. Decompression enhances water evaporation and associated cooling. Fluids entered during the unrest still propagate upwards, affecting shallower portions of the domain during the quiet (Fig. 2.3b). At the end of the simulation, pressure and temperature anomalies persist: localized overpressure (up to +0.1 MPa) is still present at shallow depth (< 200 m), while most of the domain undergoes decompression (up to -0.3 MPa), particularly near the plume border (Fig. 2.2c). Temperature anomalies are mostly confined along the edges of the two-phase plume (Fig. 2.2d). A slow temperature decline occurs at depth, where heating (+20 K) still persists at the end of the simulation. Moderate heating (a few K) takes place at shallower depths, as hot fluids rise toward the surface (Fig. 2.3). The heated region is not uniform along the plume due to the competing effects of fluid displacement and phase changes during the simulation (Fig. 2.2d). It is interesting to note that pressure and temperature changes affect different regions of the domain, which do not necessarily reflect the position of the inlet of magmatic fluids (i.e. the location of the "source" that drives the unrest, Fig. 2.1).
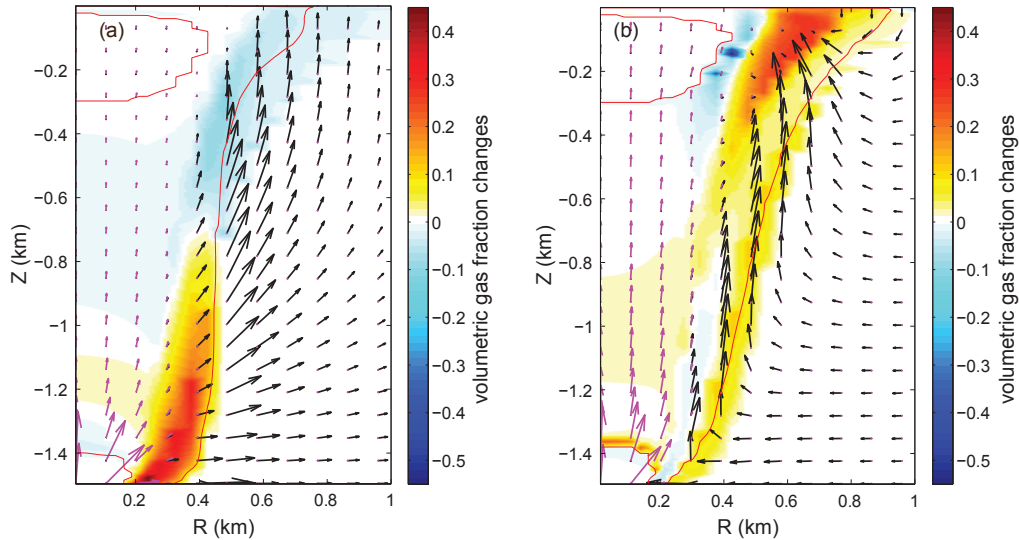
Figure 2.3: Simulated changes with respect to the initial conditions: volumetric gas fraction at the end of unrest (**a**) and at the end of simulation (**b**). Arrows describe the pattern of flow for the liquid (black) and gas phase (magenta). Flow velocity ranges from 0 to 1.25 g s^{-1}.

2.4 Resulting displacement

To compute the ground displacement arising from the simulated evolution, each element of the computational domain is considered as a potential source of deformation. Pressure and temperature changes at different times are calculated with respect to the initial pressure and temperature values in each element. The corresponding vertical and horizontal displacement can be computed from the contribution of each element (el) of the grid:

$$u_z^{el} = -\frac{(1+\nu)}{12\pi(1-\nu)}\Delta\theta^{el}V^{el}\left[\frac{(z-z^{el})}{R_1^3} - (3-4\nu)\frac{z+z^{el}}{R_2^3} + \frac{2z}{R_2^3} - \frac{6z(z+z^{el})^2}{R_2^5}\right]$$

$$u_h^{el} = -\frac{(1+\nu)}{12\pi(1-\nu)}\Delta\theta^{el}V^{el}\left[\frac{1}{R_1^3} + (3-4\nu)\frac{1}{R_2^3} - \frac{6z(z+z^{el})^2}{R_2^5}\right](r-r^{el})$$

where $\Delta\theta^{el} = \left(\Delta p^{el}/H + \alpha_s\Delta T^{el}\right)$ represent the dilatation (compression) of a single element of the grid. V^{el}, z^{el} and r^{el} are the volume, depth and distance from the symmetry axis of the element. R_1 and R_2 are the distance of the observation point from the element and from the image-element. The total displacement is calculated by summing the contributions of all grid block.

Contrary to previous works, our approach for the computation of ground deformation does not require the specification of arbitrary boundary conditions over the boundary of the computational domain, since Mindlin's solutions provide vanishing stress over the free surface and vanishing displacements and stress at remote distance.

As in previous papers (Todesco et al., 2004; Hurwitz et al., 2007), at this time we do not account for the effects of rock deformation back onto fluid propagation (full coupling). Rock deformation is expected to affect fluid circulation by altering the value and distribution of permeability. Nevertheless, major effects are expected only when pore pressure approaches lithostatic values (Zencher et al., 2006).

The temporal evolution of vertical ground displacement, calculated at the surface, on the symmetry axis, is shown in Fig. 2.4a. The values for thermo-poro-elastic parameters are listed in Table 2.3. Uplift begins as soon as the injection rate is increased, at the beginning of the unrest, and reaches the maximum value (10 cm)

Table 2.3: Rock mechanical properties considered in the computation of the ground displacement. μ is the shear modulus, K is the drained bulk modulus, K_s' is the bulk modulus of the solid constituent and α_s is the volumetric thermal expansion coefficient for the solid matrix.

μ	2 GPa
K	5 GPa
K_s'	30 GPa
α_s	10^{-5} K^{-1}
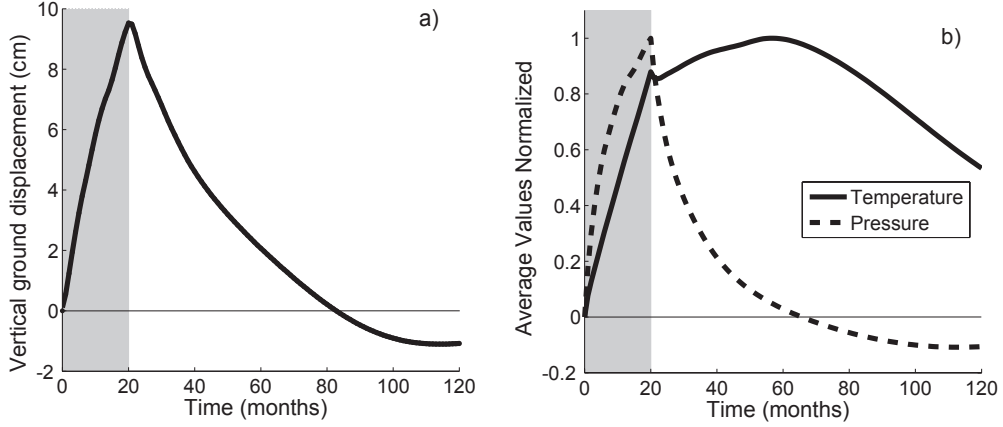
Figure 2.4: (**a**) Temporal evolution of vertical ground displacement at the symmetry axis. (**b**) Temporal variation of the average temperature (solid line) and average pore pressure (dashed line). Values are computed over the entire domain and normalized with respect to the maximum value. Shaded area in both figures highlights the unrest period. Rock mechanical properties: μ=2 GPa; K=5 GPa; K'_s=30 GPa; α_s=10^{-5} K^{-1}

at the end of the crisis. The quiet period is characterized by a slow subsidence that reflects the lower inflow of magmatic fluids. The minimum ground elevation (-1 cm) is attained at the end of the simulation. This trend of deformation arises from the temporal evolution of pressure and temperature anomalies (Fig. 2.4b). The faster uplift phase is due to the combined effects of increasing average pressure and temperature. When the unrest is over, the average pressure quickly declines, but the average temperature keeps increasing until hot fluids begin to discharge at the surface. The effects of fast decompression are therefore mitigated by thermal expansion, and the resulting subsidence rate is slower than the uplift rate. After ca. 60 months of simulation, the average pore pressure drops below its initial value and later on declines at a smaller rate. As a result, the ground level falls below its initial elevation, and then tends to stabilize at the end of the simulation.The pressure drop is associated with an overall decline of fluid density, mainly due to the injection of larger amounts of carbon dioxide during the unrest, and to the evaporation of liquid water associated with decompression. On a larger time scale, the system tends to return to its initial configuration and therefore to restore the initial ground level, which correspond to the steady activity of the fluid source during quiet times.

Fig. 2.5 shows the radial distribution of ground displacement calculated at different times. At the end of the unrest (20 months, solid line in Fig. 2.5a), the pattern of deformation looks like that of a Mogi-type, point source distribution (Mogi, 1958). The maximum uplift is right above the source and deformation vanishes within 4 km from the symmetry axis. Fig. 2.5b shows the radial distribution of the horizontal profile. At the end of the unrest (solid line in Fig. 2.5b), the maximum horizontal displacement (4 cm) is at 1.5 km from the symmetry axis. Also horizontal displace-
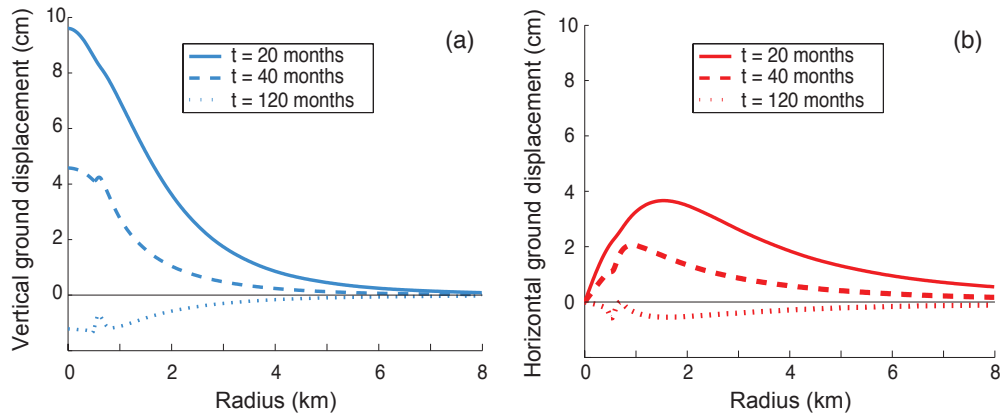
Figure 2.5: Radial distribution of vertical (**a**) and horizontal (**b**) ground displacement, at the end of the unrest and at later times.

ment at the end of the unrest looks like the one produced by a Mogi-type, point source distribution.

A different pattern of deformation characterizes the subsidence. With time, changes in pressure and temperature become shallower and focus at the border of the plume, then some spikes both in vertical and horizontal displacement develop at 500-700 m from symmetry axis (Fig. 2.5, dashed line). At the end of simulation (Fig. 2.5a, dot line), minor subsidence affects the axial region, and vertical displacement is mostly confined within 2 km from the symmetry axis, with negative values. Horizontal displacement has negative values, less than 5 mm, with a maximum at 1.5 km from the symmetry axis (Fig. 2.5b, dot line).

The temporal evolution of vertical (and horizontal, as well) displacement does not depend only on the dynamics of the hydrothermal fluids. The mechanical properties of the porous rock control both the magnitude and the temporal evolution of ground deformation. This is a relevant aspect, as mechanical properties may change significantly with rock type and physical condition, and site-specific values are often poorly constrained. The effects of different values of bulk and shear moduli are shown in Fig. 2.6 for vertical ground displacement. Increasing the bulk modulus reduces the uplift during the unrest, and leads to a slower subsidence during the quiet. For K values above 15 GPa, the initial ground elevation is not restored within the simulation time. Lower bulk moduli lead to larger vertical displacement during the unrest, and drive ground subsidence below the initial elevation. Differences in ground displacement scale quite linearly with increasing bulk modulus during the uplift: 5 GPa changes in bulk modulus produce about 1,5 cm difference in ground displacement (Fig. 2.6a). This linearity is conserved to the end of simulation, although following a different pattern. The shear modulus of the rocks also has a substantial effect on ground deformation. Low rock rigidity leads to larger vertical displacement (up to 18 cm) and faster subsidence during the quiet. In this case, displacements do not scale linearly with increased rigidity (Fig. 2.6b).
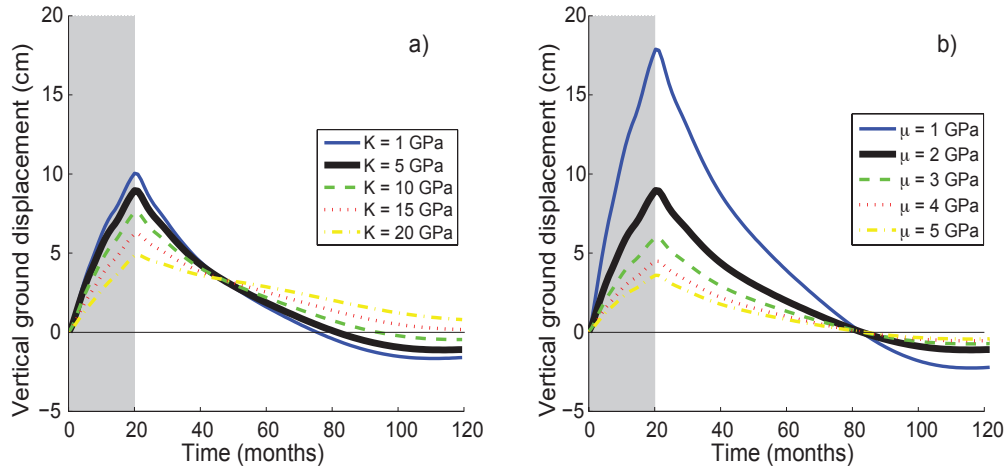
Figure 2.6: Temporal evolution of vertical ground displacement at the simmetry axis for different values of the rigidity (**a**) and bulk modulus (**b**). The other parameters are as listed in Table 2.3. Shaded are in both figures highlights the unrest period.

Bulk modulus K'_s changes, within the range 20-40 GPa, and thermal expansion coefficient changes, within the range 10^{-7}-10^{-5} K^{-1}, have minor effect on the maximum calculated ground displacements.

2.5 Conclusion

In this chapter we present a model of ground deformation based on the linear theory of thermo-poro-elasticity. The model was applied to compute the ground displacement associated with heating and pressurization of hydrothermal fluids during an unrest event at the Campi Flegrei caldera. The evolution of the hydrothermal system was simulated with the TOUGH2 numerical code (Pruess et al., 1999). Then, the corresponding ground deformation was calculated under the assumption of homogeneous mechanical properties of the porous medium. Our approach does not require the definition of boundary conditions for the displacement along the periphery of the computational domain. This is particularly relevant in a small system such as ours, where the presence of a shallow bottom boundary certainly affects the mechanical response of the free surface.

Results show that increasing the fluid injection rate in our system (by a factor 3.5) leads to a maximum uplift of the order of 10 cm, which may double depending on the choice of mechanical properties of the porous rock. A slow subsidence takes place during the quiet phase, when hot fluids reach shallower depths and heating mitigates the effects of pressure drop, leading to a slower evolution.

The evolution of the two-phase region during the quiet is associated with a complex pattern of ground deformation along the surface, with peak values characterizing the edges of the plume. A complex radial pattern of deformation was already emphasized by Todesco et al. (2004)

A direct comparison with previous results (Todesco et al., 2003b, 2004) is not possible, due to a different choice of rock properties and inlet conditions. Nevertheless, results obtained by Todesco et al. (2003b), with a fivefold increase of the flow rate at the inlet, indicate a maximum uplift (15 cm) of the same order of magnitude.

The calculated displacements reflects the flow rate at the inlet, and the permeability of the system, which directly controls the pressure build-up and heat propagation. Stronger inputs of magmatic fluids would cause larger uplifts. Similarly, different choices of rock permeability (or any change in permeability during the unrest) are going to affect system conditions and its response to unrest periods. Higher permeability favors fluid propagation, and hence heating of the system but, at the same time, reduces pressure build up. On the contrary, low permeability hinders fluid propagation and favors the pressure increase, which however would remain confined within a smaller region. The overall outcome in terms of ground displacement is difficult to estimate and further research should focus on this aspect.

Initial conditions also play a role: the deformation depends on pressure and temperature changes with respect to the initial conditions. The same input of magmatic fluids entering a colder region would cause much larger vertical displacement. If the system becomes heated by subsequent unrest events, as in the case of Campi Flegrei, ground deformation is expected to become progressively less pronounced over time, even if the input of magmatic fluids is unchanged. The remarkable difference between the large and the small unrest events at the Campi Flegrei caldera could be due to different sources of deformation acting at different times, but it could also derive from significant changes in rock properties and system conditions after the first major episodes.

With the present choice of initial conditions, feeding rate, and rock properties, based on a sound conceptual model that was developed for Campi Flegrei over time, the calculated displacement is consistent with the deformation observed during the recent, minor uplift events at Campi Flegrei. Our results therefore support the importance of hydrothermal fluids in these recent episodes. The strong influence of system properties and conditions on the calculated deformation pattern should be carefully considered when trying to infer properties of the deformation source from the observed pattern of ground displacement.

References

Aki, K., Richards, P.G. (Eds.), 1980. Quantitative Seismology - Theory and Methods. volume 1. W. H. Freeman & Co., San Francisco, California, USA.

Barberi, F., Corrado, G., Innocenti, F., Luongo, G., 1984. Phlegrean Fields 1982 – 1984: Brief chronicle of a volcano emergency in a densely populated area. Bull. Volcanol. 47, 175–185. doi:10.1007/BF01961547.

Bianchi, R., Coradini, A., Federico, C., Giberti, G., Lanciano, P., Pozzi, J.P., Sartoris, G., Scandone, R., 1987. Modeling of Surface Deformation in Volcanic Areas: The 1970-1972 and 1982-1984 Crises of Campi Flegrei, Italy. jgr 92(B13), 14139–14150.

Bonafede, M., 1990. Axi-symmetric deformation of a thermo-poro-elastic half-space: inflation of a magma chamber. Geophys. J. Int. 103, 289–299.

Bonafede, M., 1991. Hot fluid migration: an efficient source of ground deformation: application to the 1982-1985 crisis at Campi Flegrei-Italy. J. Volcanol. Geotherm. Res. 48, 187–198.

Bonafede, M., Dragoni, M., Quareni, F., 1986. Displacement and stress fields produced by a centre of dilatation and by a pressure source in a viscoelastic half-space. Geophys. J. R. astr. Soc. 87, 455–485.

Casertano, L., Oliveri del Castillo, A., Quagliariello, M.T., 1976. Hydrodynamics and geodynamics in the Phlegrean fields area of Italy. Nature 264, 161–164. doi:10.1038/26416a0.

Chiodini, G., Todesco, M., Caliro, S., Del Gaudio, C., Macedonio, G., Russo, M., 2003. Magma degassing as a trigger of bradyseismic events: the case of Phlegrean Fields (Italy). Geophys. Res. Lett. 30(8), 1434–1437. doi:10.1029/2002GL016790.

De Natale, G., Pingue, F., Allard, P., Zollo, A., 1991. Geophysical and geochemical modelling of the 1982-1984 unrest phenomena at Campi Flegrei caldera (southern Italy). J. Volcanol. Geotherm. Res. 48, 199–222. doi:10.1016/0377-0273(91)90043-Y.

De Natale, G., Troise, C., Pingue, F., 2001. A mechanical fluid-dynamical model for ground movements at Campi Flegrei caldera. J. Geodyn. 32, 487–571. doi:10.1016/S0264-3707(01)00045-X.

Del Gaudio, C., Aquino, I., Ricciardi, C.P., Ricco, C., Scandone, R., 2010. Unrest episodes at Campi Flegrei: A reconstruction of vertical ground movements during 1905-2009. J. Volcanol. Geotherm. Res. 195(1), 48–56. doi:10.1016/j.jvolgeores.2010.05.014.

Di Vito, M., Lirer, L., Mastrolorenzo, G., Rolandi, G., 1987. The 1538 Monte Nuovo eruption (Campi Flegrei, Italy). Bull. Volcanol. 49, 608–615. doi:10.1007/BF01079966.

Gaeta, F.S., De Natale, G., Peluso, F., Mastrolorenzo, G., Castagnolo, D., Troise, C., Pingue, F., Mita, D.G., Rossano, S., 1998. Genesis and evolution of unrest episodes at Campi Flegrei caldera: The role of thermal fluid-dynamical processes in the geothermal system. J. Geophys. Res. 103(B9), 20921–20933.

Gaeta, F.S., Peluso, F., Arienzo, I., Castagnolo, D., De Natale, G., Milano, G., Albanese, C., Mita, D.G., 2003. A physical appraisal of a new aspect of bradyseism: The miniuplifts. J. Geophys. Res. 108(B8). doi:10.1029/2002JB001913.

Hurwitz, S., Christiansen, L.B., Hsieh, P.A., 2007. Hydrothermal fluid flow and deformation in large calderas: Inferences from numerical simulations. J. Geophys. Res. 112, B02206. doi:10.1029/2006JB004689.

Hutnak, M., Hurwitz, S., Ingebritsen, S.E., Hsieh, P.A., 2009. Numerical models of caldera deformation: Effects of multiphase and multicomponent hydrothermal fluid flow. J. Geophys. Res. 114, B04411. doi:10.1029/2008JB006151.

McTigue, D.F., 1986. Thermoelastic response of fluid-saturated porous rock. jgr 91(B9), 9533–9542.

Mindlin, R.D., 1936. Force at a point in the interior of a semi-infinite solid. Physics 7, 39–44.

Mogi, K., 1958. Relations of the eruptions of various volcanoes and the deformations of the ground surface around them. Bull. Earthq. Res. Inst. Tokyo Univ. 36, 99–134.

Orsi, G., Petrazzuoli, S.M., Wohletz, K., 1999. Mechanical and thermo-fluid behaviour during unrest at the Campi Flegri caldera (Italy). J. Volcanol. Geotherm. Res. 91, 453–470. doi:10.1016/S0377-0273(99)00051-7.

Pruess, K., Oldenburg, C.M., Moridis, G., 1999. TOUGH2 user's guide, version 2.0. Paper LBNL-43134. Lawrence Berkeley Natl. Lab., Berkeley, CA, USA.

Rice, J.R., Cleary, M.P., 1976. Some basic stress diffusion solutions for fluid-saturated elastic porous media with compressible constituents. Rev. Geophys. Space Phys. 14, 227–241.

Todesco, M., Berrino, G., 2005. Modelling hydrothermal fluid circulation and gravity signals at the Phlegrean Fields caldera. Earth Plan. Sci. Lett. 240, 328–338. doi:10.1016/j.epsl.2005.09.016.

Todesco, M., Chiodini, G., Macedonio, G., 2003a. Monitoring and modelling hydrothermal fluid emission at La Solfatara (Phlegrean Field, Italy). An interdisciplinary approach to the study of diffuse degassing. J. Volcanol. Geotherm. Res. 125, 57–79. doi:10.1016/S0377-0273(03)00089-1.

Todesco, M., Rutqvist, J., Chiodini, G., Pruess, K., Oldenburg, C.M., 2004. Modeling of recent volcanic episodes at Phlegrean Fields (Italy): geochemical variations and ground deformation. Geothermics 33, 531–547. doi:10.1016/j.geothermics.2003.08.014.

Todesco, M., Rutqvist, J., Pruess, K., Oldenburg, C.M., 2003b. Multi-phase fluid circulation and ground deformation: a new perspective on bradyseismic activity at Phlegrean Fields (Italy), in: Proceedings of the 28th Workshop on Geothermal Research Engineering. Stanford, CA, USA.

Wang, H.F. (Ed.), 2000. Theory of Linear Poroelasticity with Applications to Geomechanics and Hydrology. Princeton University Press, Princeton and Oxford.

Zencher, F., Bonafede, M., Stefansson, R., 2006. Near-lithostatic pore pressure at seismogenic depths: a thermoporoelastic model. Geophys. J. Int. 166, 1318–1334.

Electrical conductivity, ground displacement, gravity changes, and gas flow at Campi Flegrei caldera: results from numerical modeling

Contents

3.1 Introduction

Campi Flegrei features a large hydrothermal system, with manifestations mainly concentrated at the Solfatara crater and characterized by a mud pool, several fumaroles, and strong diffuse degassing. Changes in diffuse degassing and in the size of degassing area were recorded during each unrest (Chiodini et al., 2001, 2003; Chiodini, 2009; Chiodini et al., 2010). Many authors infer that changes in geophysical and geochemical parameters, observed within the Campi Flegrei caldera, are caused by a complex interaction between the deep magmatic system and the shallow hydrothermal fluid circulation (Casertano et al., 1976; Bonafede, 1991; Orsi et al., 1996, 1999; De Natale et al., 2001; Chiodini et al., 2003; Battaglia et al., 2006; Bodnar et al., 2007; Lima et al., 2009). This interaction was also confirmed by further studies using joint inversion of deformation and gravity data to infer the

density of the source of deformation (Gottsmann et al., 2006; Amoruso et al., 2008; Bonafede and Ferrari, 2009).

Several changes in monitored parameters may be associated with the hydrothermal system rather than with the degassing magma, and may occur as the fluids ascend through porous rock. As seen in the previos chapter (2), high temperatures and increase of the pore fluid pressures in undrained conditions can be responsible for ground deformation (see also Bonafede, 1991; Todesco et al., 2004; Hurwitz et al., 2007; Hutnak et al., 2009; Rinaldi et al., 2010). Studies have inferred the role of fluid circulation as a fault lubricant and as a trigger for low-frequency seismic events (Bianco et al., 2004). The distribution of liquid-dominated, two-phase, and gas-dominated regions also determines the subsurface distribution of the fluid mass density. Changes in phase distribution can produce measurable gravity signals (Todesco and Berrino, 2005). The amplitude hydrothermally induced changes mostly depend on the supply rate of magmatic fluids (Todesco, 2009). However, the state and properties of the degassing magma are not the only cause of the evolution of the observable signals. Recent results highlight the role of rock permeability distribution in controlling the evolution of the parameters measured at the surface (Todesco et al., 2010).

Hydrothermal fluids can also influence self-potential and electrical resistivity, since these quantities depend on fluid flow pattern, temperature, and phase saturation (Zlotnicki and Nishida, 2003; Finizola et al., 2006; Aizawa et al., 2009; Revil et al., 2008; Legaz et al., 2009; Richards et al., 2010). Electrical current, either artificially generated or independently existing, may produce surface effects that are detectable by appropriate electrical prospecting. Electrical methods involving direct injection via electrodes at the ground surface are referred to as DC (direct current) or resistivity methods. An apparent electrical resistivity is determined measuring the potentials due to the DC current injected, using several configurations of the electrodes (arrays), and the exploration depth is proportional to the separation between the electrodes (Telford et al., 1990; Dahlin, 2001). Using electromagnetic methods (EM), time-varying currents are made to flow inductively, creating magnetic fields and causing secondary electrical currents which can be measured while the EM equipment is transmitting (frequency domain surveys, FDEM) or when the primay field is switched off (time domain surveys, TDEM) (Fitterman and Stewart, 1986; Telford et al., 1990). Both EM and DC techniques provide results with a good resolution, tough these methods cannot be used to investigate deeper than 500 - 600 m. EM surveys include also magneto-telluric (MT) method, measuring the large scale (low frequency) natural magnetic fields and the electrical current caused by these fields. It is particularly useful to investigate the electrical conductivity distribution up to few kilometers deep, but with low resolution if compared with DC and EM methods (Telford et al., 1990).

The interpretation of observables collected at the surface is not always unequivocally constrained, since magmatic and hydrothermal processes may cause similar effects (Gottsmann et al., 2006; Bodnar et al., 2007; Lima et al., 2009). A simultaneous analysis of different geophysical and geochemical observables is a sound approach

for interpreting monitoring data and to infer a consistent conceptual model. In this chapter, we extend our previous studies and increase the number of observable parameters to include gravity changes, gas temperature, rate of diffuse degassing, and electrical conductivity. As in the previous chapter, we first simulate the evolution of the hydrothermal system and then compute the observables in a postprocess calculation. Using the former large scale simulation (domain 2D-axysimmetric, 10 km wide and 1.5 km deep), with 20 months of increased injection followed by a longer quiet period (see section 2.3 for details), we quantify and compare the evolution of several observable parameters at Campi Flegrei.

3.2 Geophysical and geochemical observables

Some observable parameters are directly related to fluid circulation and appear in the TOUGH2 output. Among these, we take into account the amount and temperature of gas discharged at the surface. For other geophysical observables, such as compositional changes, a simple calculation is required. Gas composition is expressed as the molar ratio CO_2/H_2O, and is evaluated near the surface, where a single-phase gas region forms (see Fig. 2.1a). According to geochemical data, the fumaroles at Solfatara equilibrate within such a shallow dry-gas region before discharging at the surface (Chiodini et al., 2003). Gas composition is computed here by averaging the composition of all the grid blocks that belong to this shallow dry gas region. Other observables can be derived from the TOUGH2 output, but require some postprocess calculation.

3.2.1 Electrical Conductivity

Two main electrical conductivity mechanisms characterize a water-saturated porous medium. The first one is caused by the fluid flow inside the pores, through electro-migration of anions and cations into the connected pore space. A second conduction mechanism occurs at the pore water-mineral interface in the electrical double layer, that is caused by a migration of the weakly adsorbed counterions (usually cations). The electrical double layer forms as charges at mineral surface develop by chemical reactions with water. These charges need to be counterbalanced by weakly adsorbed charges onto the mineral surface in a first layer (Stern layer). The second layer (diffuse layer) comprises the charges only subjected to the Coulomb force (Revil and Florsch, 2010).

In this work, we follow the formulation by Revil et al. (1998) that takes into account the different behavior of different charge carriers: cations and the anions. This formulation is based on the "Hittorf transport numbers", which are the fractions of electrical current carried by the cations and anions in the free electrolyte. These numbers can be established for surface conduction at water/mineral interface. Hittorf numbers are basically related to the ionic mobilities of the ions, and the electrical conductivity is given by combining the definitions of these numbers. Considering a solution with pH range 5-8, the counterions of the electrical diffuse

and Stern layers are mostly cations (Revil and Glover, 1997) and the DC electrical conductivity of the porous rock (σ) is given by:

$$\sigma = \frac{\sigma_f}{F} \left[1 - t_{(+)} + F\xi + \frac{1}{2}(t_{(+)} - \xi) \cdot \left(1 - \frac{\xi}{t_{(+)}} + \sqrt{\left(1 - \frac{\xi}{t_{(+)}}\right)^2 + \frac{4F}{t_{(+)}}\xi} \right) \right]$$

where σ_f is the electrical conductivity of the pore fluid (in Sm^{-1}), which is a function of the salinity of the fluid. F is the electrical formation factor and represents the classical law by Archie (1942), confirmed by several numerical works (Roberts and Schwartz, 1985; Schwartz and Kimminau, 1987; Sen, 1987); $F = \phi^{-m}$ where ϕ is the medium porosity; and m is the cementation exponent, ranging from $3/2$ to $5/2$ and usually set equal to 2 (Waxman and Smits, 1968); $t_{(+)}$ is the Hittorf number for the cation in the electrolyte and represents the electrical current carried by the cations (Revil et al., 1998). ξ is the ratio between the surface electrical conductivity (σ_S) at the water-mineral interface and the pore fluid electrical conductivity (σ_f) in the pores.

The surface electrical conductivity can be written as a function of the density of counterions per pore volume Q_V (in Cm^{-3}), including the charge in both the Stern and the diffuse layer. Assuming that there is no electrical conductivity from the Stern layer in DC electrical formulation, the surface electrical conductivity is a function of the charge density per unit of volume of solution in the medium due to the diffuse layer only $\bar{Q}_V$ (in Cm^{-3}) and of the ionic mobility of the cations in the bulk pore water $\beta_{(+)}$ (in $m^2s^{-1}V^{-1}$) (Revil and Florsch, 2010):

$$\xi = \frac{\sigma_S}{\sigma_f} \approx \frac{\beta_{(+)}\bar{Q}_V}{\sigma_f}$$

In the case of $\xi \ll 1$, as for high-salinity fluids, the DC electrical conductivity for a saturated porous medium can be approximated as follows:

$$\sigma = \frac{1}{F}\left(\sigma_f + \beta_{(+)}\bar{Q}_V\right)$$

Since there is no brine in our modeling of hydrothermal fluid circulation, we assume a constant σ_f=0.1 Sm^{-1}, to account for the salinity of the real fluid. This value, at reference temperature T_0 =300 K, is a good choice in the range of fresh water electrical conductivity (0.01 Sm^{-1}) and water with high salinity (1 Sm^{-1}). In the case of fluid with NaCl, the ionic mobility is $\beta_{(+)} = 5.19 \cdot 10^{-8}$ $m^2s^{-1}V^{-1}$ as shown by Revil et al. (1998). We consider electrically insulated grains, since measures performed on dry samples show negligible values (Revil et al., 2002).

As shown in several papers (Vaughan et al., 1993; Revil et al., 1998; Roberts, 2002), the electrolyte and surface conductivities are temperature dependent. From laboratory measurements (Revil et al., 1998), a linear temperature dependence is valid, both for the ionic mobility and for the brine electrical conductivity:

$$\begin{cases} \sigma_f(T) = \sigma_f(T_0)\left[1 + \alpha_f(T - T_0)\right] \\ \beta_{(+)}(T) = \beta_{(+)}(T_0)\left[1 + \alpha_{(+)}(T - T_0)\right] \end{cases} \tag{3.1}$$

where T_0 is the reference temperature (300 K), and the coefficients $\alpha_f \approx 0.023 \text{ K}^{-1}$, and $\alpha_{(+)} \approx 0.037 \text{ K}^{-1}$ are temperature independent.

For a variety of rock types, there is a strong relationship (Jardani and Revil, 2009) between the charge density per unit pore volume ($\bar{Q}_V$) and the permeability of the medium κ, expressed in m^2:

$$\log_{10} \bar{Q}_V = -9.2 - 0.82 \cdot \log_{10} \kappa$$

a strong connection between these two parameters is valid since there exists a dependence of both on the specific surface area of the porous material. Note that, at this time, we only account for the salinity effects on electrical conductivity, whereas we do not consider its influence on fluid flow.

The above formulation is valid for a saturated medium, but hydrothermal areas are often characterized by multiphase fluids occupying the pore space of the medium. The case we develop below is valid for two-phase fluids: the liquid phase is the electrolyte wetting the mineral grains and the gas-phase is considered an insulating fluid. Considering the formulation for the saturated medium, the influence of the gas-phase upon electrical conductivity can be taken into account introducing the transformation proposed by Waxman and Smits (1968):

$$\begin{cases} \phi^m \rightarrow \phi^m S_w^n \\ \bar{Q}_V \rightarrow \bar{Q}_V / S_w \end{cases}$$

where n is the saturation (or second) Archie exponent (generally $n = m$) and S_w is the pore volume space fraction occupied by liquid phase. A pore completely saturated in the liquid phase will have $S_w = 1$. Considering $m = n = 2$, the electrical conductivity as a function of the water saturation is given by:

$$\sigma = \phi^2 S_w^2 \left(\sigma_f + \beta_{(+)} \frac{\bar{Q}_V}{S_w} \right) \tag{3.2}$$

the presence of a gas phase (like water vapor or CO_2), considered nonwetting and insulating, will increase the electrical conductivity at the pore surface.

3.2.2 Ground Displacement and Gravity Changes

The ground displacement, arising from the simulated pressure and temperature changes, is calculated using the mathematical model analyzed in the previous chapter 2 (see also Rinaldi et al., 2010). Briefly, recalling here the results of the model, the i-th component of the ground displacement on the surface for each block is :

$$u_i^{el} = \frac{1 + \nu}{3\pi} \Delta\theta^{el} V^{el} \frac{(x_i^{el} - x_i^{ob})}{L^3} \tag{3.3}$$

where $\Delta\theta^{el} = \Delta p^{el}/H + \alpha_s \Delta T^{el}$ represents the dilatation (compression) of the grid element with respect to the initial condition (where Δp^{el} and ΔT^{el} are the pressure and temperature changes, respectively). V^{el} and z^{el} are the volume and depth of the element. $L = \sqrt{(x^{el} - x^{ob})^2 + (z^{el})^2}$ is the distance of the observation point (x^{ob}) from the element (x^{el}). We use the following mechanical properties : $1/H = 1/K - 1/K'_s$ is the Biot's constant (where $K = 5$ GPa is the isothermal, drained bulk modulus and $K'_s = 30$ GPa is the bulk modulus of the solid constituent), $\mu = 2$ GPa is the rigidity, $\nu = 0.32$ is the Poisson's ratio in undrained conditions, and $\alpha_s = 10^{-5}$ K^{-1} is the volumetric thermal expansion coefficient of the rock matrix. Other approaches for ground deformation computing can be found elsewhere (Todesco et al., 2004; Hurwitz et al., 2007; Hutnak et al., 2009).

Changes in average fluid density generate a detectable gravity signal, as pointed out by Todesco and Berrino (2005). As in the case of deformation, the overall gravity change at a given time is computed as the sum of the contributions of all the gridblocks of the computational domain, as their average density changes with respect to initial conditions. Todesco and Berrino (2005) calculate the vertical component of gravitational attraction on the surface as:

$$\Delta g_z^{el} = G\phi V^{el}\Delta\rho_f^{el}\frac{z^{el}}{L^3} \tag{3.4}$$

where $G = 6.67 \cdot 10^{-11}$ m^{3}kg^{-1}s^{-1} is the gravitational constant, ϕ is the porosity and $\Delta\rho_f^{el}$ its average fluid density change with respect to the initial condition. If deformation is caused by an isotropic source embedded in a homogeneous medium, the gravity change due to that deformation is zero (Walsh and Rice, 1979), but significant effects could arise if heterogeneous rocks are present (Amoruso et al., 2008)

3.3   Simulated observables

3.3.1   Temporal Changes

Fig. 3.1 show the temporal evolution of vertical ground displacement (solid line) and of the gravity changes(dashed line), both calculated at the surface on the symmetry axis. A detailed description of the vertical displacement has been presented in the Section 2.4. Briefly, displacement presents an uplift at the beginning of the unrest, as soon as the fluid injection rate at the inlet is increased. Uplift reaches the maximum value (~ 10 cm) at the end of the unrest (20 months). The quiet period is characterized by a slow subsidence that reflects the lower inflow of magmatic fluids at the inlet. The minimum ground elevation (-1 cm) is reached at the end of the simulation.

A positive trend characterizes the changes in gravity at the beginning of simulation, as more mass enters the system and pressure build-up increases average fluid density. The maximum value (40 μGal) is reached at the end of the unrest. During the quiet, gravity drops thanks to the combined effects of reduced pore pressure and
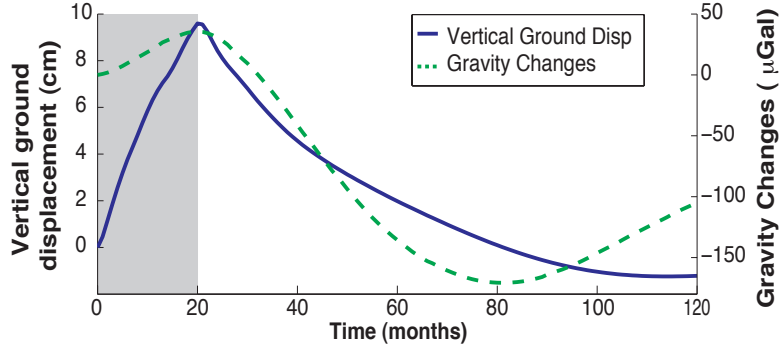
Figure 3.1: Temporal evolution of vertical ground displacement (solid line) and gravity changes (dashed line) at the symmetry axis. Shaded area represents the unrest period.
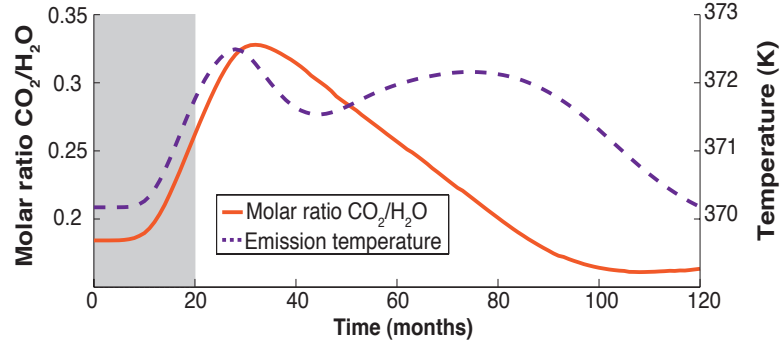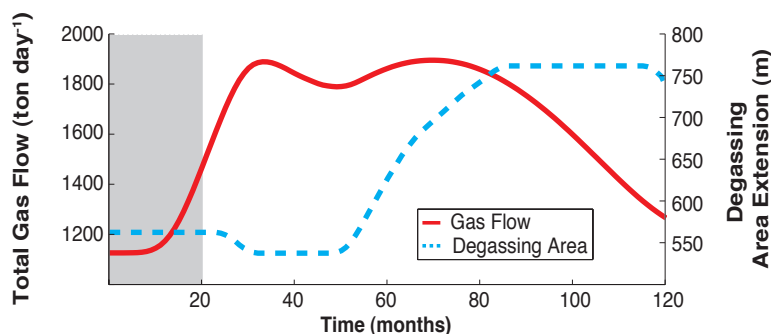

Figure 3.2: Temporal evolution of molar ratio CO_2/H_2O (solid line) and temperature of discharged gas (dashed line). Shaded area represents the unrest period.

ascent of the gas-rich fluids injected during the crisis. The gravity reaches a minimum value of -160 μGal at 80 months. Afterward, pressure drop in source region drives liquid water toward the plume, heading to a new increment of gravity. When the simulation is over, a negative value of -100 μGal is still present.

The temporal evolution of the CO_2/H_2O molar ratio and the emission temperature of the discharged gases at the surface are shown in Fig. 3.2. Since gas composition is monitored near the surface, the effects of the unrest are not recorded immediately at the beginning of the unrest. As new fluids are injected at the base of the system, and ascend toward the surface, older fluids are discharged at the surface first. Therefore, the early evolution of gas composition reflects the composition of the fluids at the beginning of the simulation. The CO_2-rich fluids injected during the high degassing period reach the surface (and modify the observed gas composition) only after a characteristic time, which depends on the flow rate at the source, the system geometry, and the rock permeability (Chiodini et al., 2003; Todesco, 2009; Todesco et al., 2010).

The CO_2/H_2O molar ratio (Fig. 3.2, solid line) reaches its maximum value after 32 months of simulation. Afterward, the CO_2 content declines again, reflecting

Figure 3.3: Temporal evolution of the total gas flow (solid line) and of the radial extent of the degassing area (dashed line). Shaded area represents the unrest period.

lower enrichment during the quiet period. At the end of simulation, the molar ratio reaches a value lower than the initial. The reached maximum value (0.33) is different from the composition of the injected fluids (0.4), indicating a dilution of the fluids moving toward the surface.

Changes in emission temperature of discharged gas are also associated with the unrest. Despite their very low magnitude, they are in agreement with the observed variations, since gases temperature at Campi Flegrei does not change significantly through time. The temporal evolution (Fig. 3.2, dashed line) shows two local maximum. The first one corresponds to fluid arrival at the surface; it occurs at the same time (32 months) as the CO_2/H_2O molar ratio maximum. A second maximum is attained at a later time (about 80 months), corresponding to an average heating of the system (Rinaldi et al., 2010).

Changes in total degassing rate at the surface and in the extent of the degassing area are also associated with the unrest (Fig. 3.3). Here we consider as degassing area the area where the gas flow rate is greater than the 5 % of the maximum value at the surface. The system reaches a first maximum flow rate (1900 ton day^{-1}) several months (32 months) after the end of the unrest (Fig. 3.3, solid line), and a second maximum (1900 ton day^{-1}) is attained after about 70 months. Then the degassing decreases almost to the initial steady state value (1200 ton day^{-1}). The first maximum is due to the arrival of the fluids injected during the unrest, and occurs at the same time of the maximum observed for compositional changes and emission temperature (Fig. 3.2); the second maximum is associated with a larger extent of the degassing area and with lower flow rates per unit area (Fig. 3.3, dashed line). Temporal changes in degassing area extent (Fig. 3.3, dashed line) follow a different trend. When the discharged fluids reach their maximum emission rate, degassing is focused around the symmetry axis (minimum extent at about 40 months is 550 m), then degassing area extent up to ∼750 m when discharged rate decreases. These effects are also associated with the imposed unrest, and they can be explained by looking at the evolution of gas saturation in the two phase plume (Fig. 3.4). During the unrest and later, up to few months after the end of the
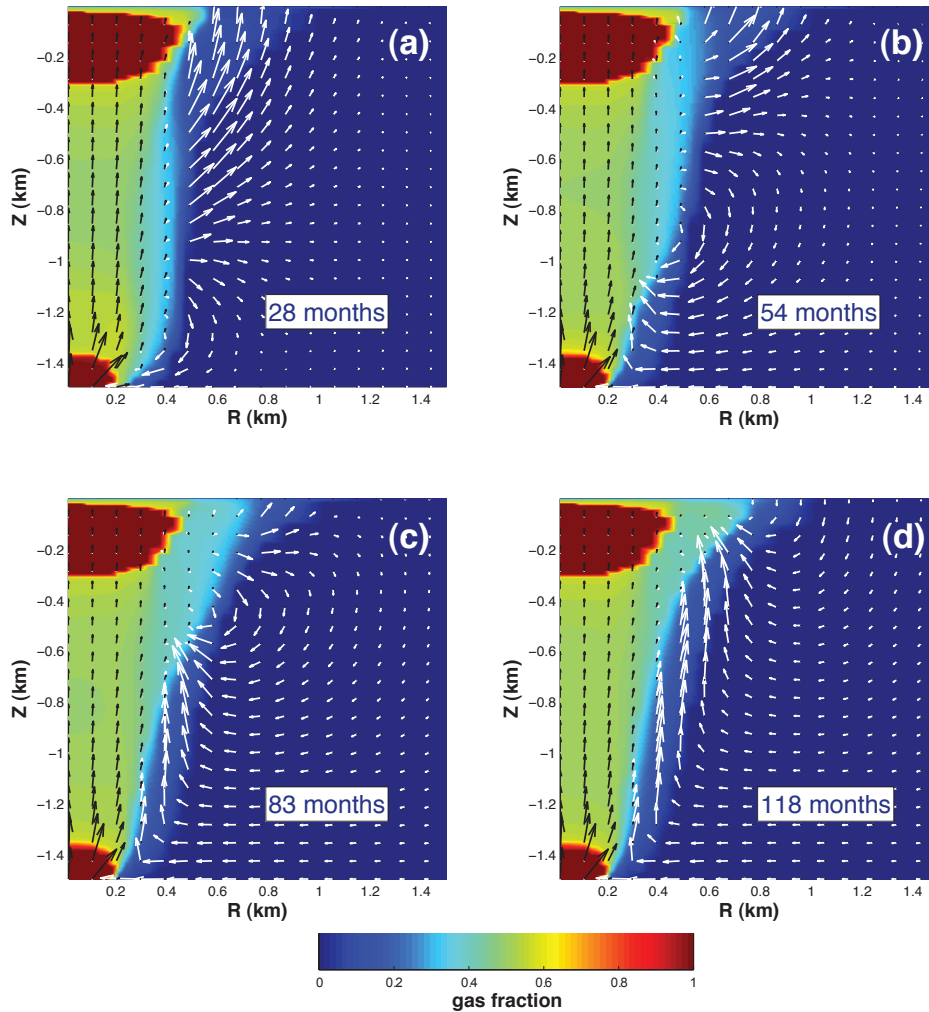
Figure 3.4:   Gas saturation at different times. (**a**) t=28 months, few months after the end of the unrest, when the plume begins to shrink at ground surface. (**b**) t=54 months, decompression during the quiet drives liquid water toward the base of the plume. Hot gases injected during the unrest reach the surface, increasing the emission area. (**c**) t=83 months, the plume has its maximum surface extension. (**d**) t= 118 months, the plume begins to shrink again. Arrows describe the pattern of flow for the liquid (white) and gas phase (black). Flow rates range from 0 to 1.25 g s^{-1}.

crisis, the two phase plume widens near the inlet, and then some water is displaced upward and outward (Fig. 3.4a). This water reaches the surface after some time shrinking the degassing area. When the unrest is over, the two phase plume shrinks at the inlet, and some water is allowed to enter in the plume (Fig. 3.4b). This new water displaces the gases at the plume border (injected during the unrest) toward the surface, and as a consequence the degassing area extends at the surface (Fig. 3.4c). When the system is back to the steady state injection and when the gases

displacement effect is over, the degassing area should return to its initial extent (Fig. 3.4d). Fig. 3.3 shows as the extent of the degassing area decreases after more than 110 months of simulation.

All the observables considered in this section are in agreement with measurements performed at Campi Flegrei. Displacement of the order of centimeters (mini-uplift) are commonly observed during unrests (Gaeta et al., 2003), as well as hundreds μGals of gravity changes (Todesco and Berrino, 2005). Changes in total gas flow rate, composition, and degassing area of the same order of magnitude of the ones simulated, were measured by Chiodini et al. (2010)

3.3.2 Radial Changes

Radial pattern are also important in the observables analysis, since it can provide information on the two-phase plume of ascending gases. The degassing area can be easily related to the amount of discharged gases at the surface, but radial patterns in gravity changes may also play a role in defining the degassing area.

Fig. 3.5a shows the radial distribution of the discharged gases and the gravity changes. after 32 months of simulation. This is the time at which the CO_2/H_2O molar ratio reaches its maximum value. From the amount of gas (Fig. 3.5a, solid line) we infer that the degassing area is about 500-600 m from the symmetry axis.

Gravity changes are computed from fluid density changes. Since these occur mostly at the border of the two-phase plume, a maximum (or minimum) peaks in gravity changes will arise at a radial distance corresponding to the surface extension of the plume. Fig. 3.5a (dashed line) shows a maximum of 150 μGal at a distance of about 600-700 m from the symmetry axis, in good agreement with the same value we can infer from the total gas flow.

The same analysis can be done at the end of the simulation. The results are similar, as shown in Fig. 3.5b. The magnitude of total gas flow is one-half that of the unrest period, and we observe a very strong variation in gravity changes: the minimum value is about -500 μGal, due to arrival of a large quantity of gas near the surface.

In the case where the surface is sealed by an impermeable layer, and then degassing extension is difficult to monitor, the gravity changes would still give the extension of the plume.

3.3.3 Electrical Conductivity

We use Equation 3.2 to compute the electrical conductivity for each gridblock of the computational domain. The result is an electrical conductivity map over the entire system up to a depth of 1.5 km. Even if such a measurement is possible in a real field, for example using a MT surveys, the results are often biased, since the electrical conductivity in a deep layer may be underestimated because the presence of a shallower high conductive layer (such as clay). However, here we focus on the theoretical effects deriving from changes in water saturation and temperature at
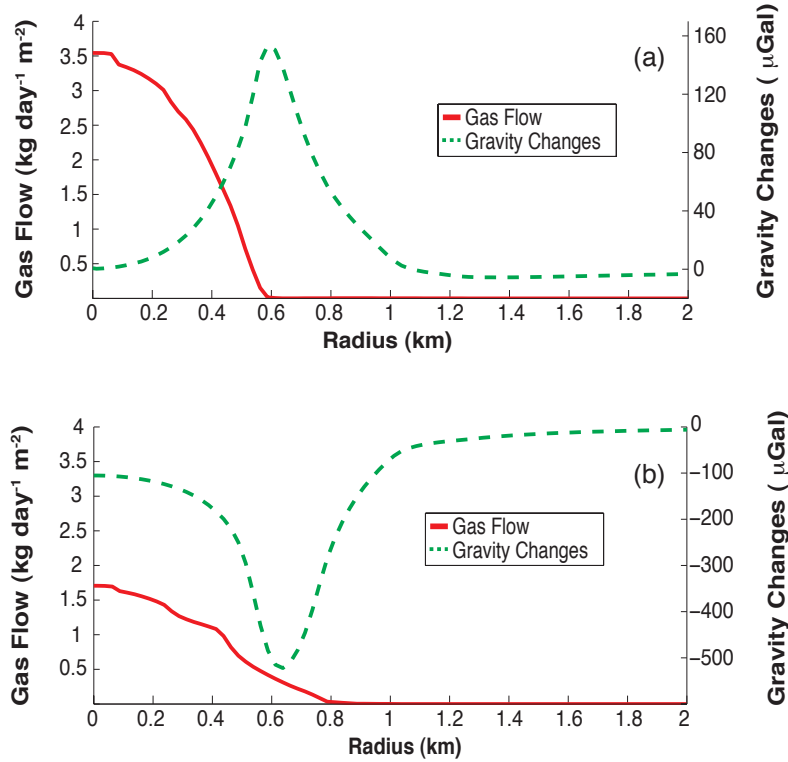
Figure 3.5: Radial distribution of gravity changes (dashed line) and amount of discharged gases at the surface (solid line) at (**a**) t = 32 months, that is when the molar ratio CO_2/H_2O reaches its maximum (Fig. 6), and (**b**) at the end of simulation (120 months). Note the change in gravity scale.

depth.

We want to evaluate if an unrest could cause measurable changes in electrical conductivity. We calculate the electrical conductivity change with respect to the initial steady-state value. Fig. 3.6b shows the electrical conductivity relative changes at the end of the unrest period (20 months of simulation).

The electrical conductivity map presents some negative changes at depth (up to -80 %) near the inlet of magmatic fluids. Here, the gas phase, arising from the increased degassing, replaces the liquid phase (Fig. 3.6a). However, the temperature increases near the fluid source, beyond which there is also little increase in electrical conductivity (5-10 %) at 400 m from the symmetry axis. The displaced fluids move toward the surface, then we observe an increase in electrical conductivity (70 %) at shallower depth. Since most changes in temperature and water saturation happen at the border of the two-phase plume, electrical conductivity changes mainly at that location. Some minute changes occur inside the plume, which can be explained by considering the small front of condensation (for positive changes) or evaporation (negative changes).

The electrical conductivity relative changes at the end of simulation are shown
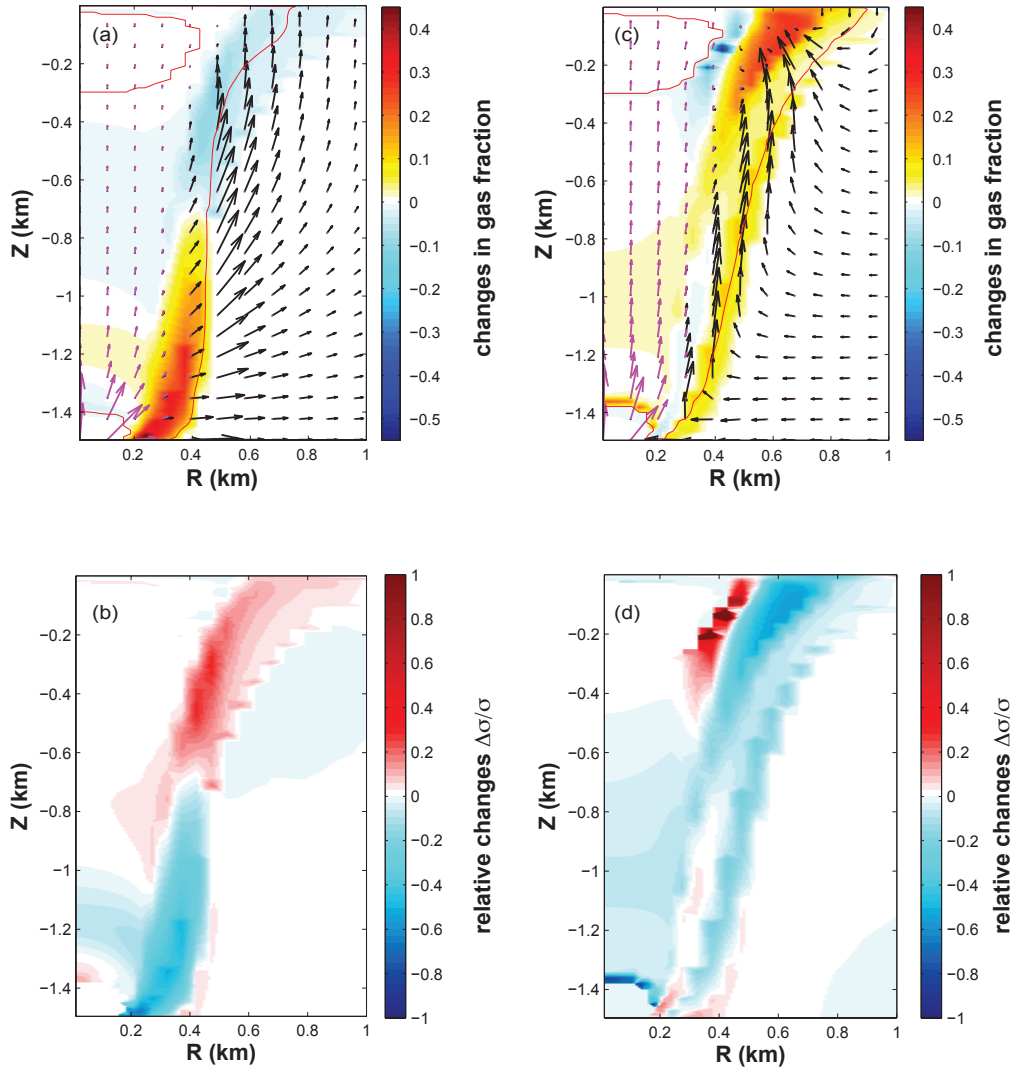
Figure 3.6: Changes in gas saturation and relative changes in electrical conductivity at the end of the unrest period (20 months)(**a,b**) and at the end of the simulation (120 months) (**c,d**). Arrows describe the pattern of flow for the liquid (black) and gas phase (magenta). Flow rates range from 0 to 1.25 g s^{-1}.

in Fig. 3.6d. Also, in this case the changes are mostly confined to the border of the plume; however, at the end of the simulation, the two-phase plume is larger (Fig. 3.6c), and we observe mainly negative changes (up to -100 % near source region). Some positive variations (up to 100 % of the initial value) are still present at shallower depth, caused by fluids movements, and at depth near the inlet, where heating persists at the end of simulation.

3.4 Conclusion

An analysis of several geophysical and geochemical parameters, obtained from numerical simulations of hydrothermal circulation, has been presented. The evolution of these observables after a generic period of unrest has been quantified and compared. Results show that increasing the fluid injection rate in our system (by a factor 3.5) over a period of several months (20 months) results in measurable variations of all parameters.

The simulated unrest leads to a maximum uplift of the order of 10 cm, gravity changes up to 500 μGal and changes in electrical conductivity up to 100% of the initial values. Changes in geochemical parameters were also observed, such as CO_2/H_2O molar ratio, total gas flow at the surface and emission temperature of the discharged gas.

The studied parameters do not show the same temporal evolution. Ground displacement and gravity changes react immediately to the higher fluid injection of magmatic fluids at the inlet. Other signals reach their maximum values after a characteristic time, depending on the flow rate at the source, the system geometry, and the rock permeability. The evolution of the two-phase region over the entire simulation is associated with a complex pattern of variation along the surface, with peak values characterizing the edges of the plume.

Increasing the number of geophysical observables that can be simulated and compared with available observation will improve calibration and contribute to our understanding of volcanic system. Ground displacement, gravity, and gas flow changes can be easily related to the fluid source, whereas a detailed electrical conductivity map reflect changes at very shallow depth and can provide a better description of the phase distribution, as well as the presence of shallow structures focusing the phase distribution.

References

Aizawa, K., Ogawa, Y., Ishido, T., 2009. Groundwater flow and hydrothermal systems within volcanic edifices: Delineation by electric sel-potential and magnetotellurics. J. Geophys. Res. 114, B01208. doi:10.1029/2008JB005910.

Amoruso, A., Crescentini, L., Berrino, G., 2008. Simultaneous inversion of deformation and gravity changes in a horizontally layered half-space: Evidences for magma intrusion during 1982-1984 unrest at Campi Flegrei caldera (Italy). Earth Planet. Sci. Lett. 272, 181–188. doi:10.1016/j.epsl.2008.04.040.

Archie, G.E., 1942. The electrical resistivity log as an aid in determining some reservoir characteristics. Trans. Am. Inst. Min. Metall. Pet. Eng. 146, 54–62.

Barberi, F., Corrado, G., Innocenti, F., Luongo, G., 1984. Phlegrean Fields 1982 – 1984: Brief chronicle of a volcano emergency in a densely populated area. Bull. Volcanol. 47, 175–185. doi:10.1007/BF01961547.

Battaglia, M., Troise, C., Obrizzo, F., Pingue, F., De Natale, G., 2006. Evidence for fluid migration as the source of deformation at Campi Flegrei caldera (Italy). Geophys. Res. Lett. 33, L01307. doi:10.1029/2005GL024904.

Berrino, G., Corrado, G., Luongo, G., Toro, B., 1984. Ground deformation and gravity changes accompanying the 1982 Pozzuoli uplift. Bull. Volcanol. 47, 188–200.

Bianco, F., Del Pezzo, E., Saccorotti, G., Ventura, G., 2004. The role of hydrothermal fluids in triggering the July-August 2000 seismic swarm at Campi Flegrei, Italy: Evidence from seismological and mesostructural data. J. Volcanol. Geotherm. Res. 133, 229–246.

Bodnar, R.J., Cannatelli, C., De Vivo, B., Lima, A., Belkin, H.E., Milia, A., 2007. Quantitative model for magma degassing and ground deformation (bradyseism) at Campi Flegrei, Italy: Implications for future eruptions. Geology 35(9), 791–794. doi:10.1130/G23653A.1.

Bonafede, M., 1991. Hot fluid migration: an efficient source of ground deformation: application to the 1982-1985 crisis at Campi Flegrei-Italy. J. Volcanol. Geotherm. Res. 48, 187–198.

Bonafede, M., Ferrari, C., 2009. Analytical models of deformation and residual gravity changes due to a Mogi source in a viscoelastic medium. Tectonophysics 471, 4–13. doi:10.1016/j.tecto.2008.10.006.

Bruno, P.P.G., Ricciardi, G.P., Petrillo, Z., Di Fiore, V., Troiano, A., Chiodini, G., 2007. Geophysical and hydrogeological experiments from a shallow hydrothermal system at Solfatara Volcano, Campi Flegrei, Italy: Response to caldera unrest. J. Geophys. Res. 112, B06201. doi:10.1029/2006JB004383.

Casertano, L., Oliveri del Castillo, A., Quagliariello, M.T., 1976. Hydrodynamics and geodynamics in the Phlegrean fields area of Italy. Nature 264, 161–164. doi:10.1038/26416a0.

Chiodini, G., 2009. CO_2/CH_4 ratio in fumaroles a powerful tool to detect magma degassing episodes at quiescent volcanoes. Geophys. Res. Lett. 36, L02302. doi:10.1029/2008GL036347.

Chiodini, G., Caliro, S., Cardellini, C., Granieri, D., Avino, R., Baldini, A., Donnini, M., Minopoli, C., 2010. Long term variations of the Campi Flegrei (Italy) volcanic system as revealed by the monitoring of hydrothermal activity. J. Geophys. Res. 115, B03205. doi:10.1029/2008JB006258.

Chiodini, G., Frondini, F., Cardellini, C., Granieri, D., Marini, L., Ventura, G., 2001. CO_2 degassing and energy realease at Solfatara volcano. J. Geophys. Res. 106(B8), 16213–16221. doi:10.1029/2001JB000246.

Chiodini, G., Todesco, M., Caliro, S., Del Gaudio, C., Macedonio, G., Russo, M., 2003. Magma degassing as a trigger of bradyseismic events: the case of Phlegrean Fields (Italy). Geophys. Res. Lett. 30(8), 1434–1437. doi:10.1029/2002GL016790.

Dahlin, T., 2001. The development of DC resistivity imaging techniques. Computers & Geosciences 27, 1019–1029.

De Natale, G., Troise, C., Pingue, F., 2001. A mechanical fluid-dynamical model for ground movements at Campi Flegrei caldera. J. Geodyn. 32, 487–571. doi:10.1016/S0264-3707(01)00045-X.

Del Gaudio, C., Aquino, I., Ricciardi, C.P., Ricco, C., Scandone, R., 2010. Unrest episodes at Campi Flegrei: A reconstruction of vertical ground movements during 1905-2009. J. Volcanol. Geotherm. Res. 195(1), 48–56. doi:10.1016/j.jvolgeores.2010.05.014.

Di Vito, M., Lirer, L., Mastrolorenzo, G., Rolandi, G., 1987. The 1538 Monte Nuovo eruption (Campi Flegrei, Italy). Bull. Volcanol. 49, 608–615. doi:10.1007/BF01079966.

Finizola, A., Revil, A., Rizzo, E., Piscitelli, S., Ricci, T., Morin, J., Angeletti, B., Mocochain, L., Sortino, F., 2006. Hydrogeological insights at Stromboli volcano (Italy) from geoelectrical, temperature and CO_2 soil degassing investigations. Geophys. Res. Lett. 33, L17304. doi:10.1029/2006GL026842.

Fitterman, D.V., Stewart, M.T., 1986. Transient electromagnetic sounding for groundwater. Geophysics 51(4), 995–1005.

Gaeta, F.S., Peluso, F., Arienzo, I., Castagnolo, D., De Natale, G., Milano, G., Albanese, C., Mita, D.G., 2003. A physical appraisal of a new aspect of bradyseism: The miniuplifts. J. Geophys. Res. 108(B8). doi:10.1029/2002JB001913.

Gottsmann, J., Folch, A., Rymer, H., 2006. Unrest at Campi Flegrei: A contribution to the magmatic vers hydrothermal debate from inverse and finite element modelling. J. Geophys. Res. 111, B07203. doi:10.1029/2005JB003745.

Hurwitz, S., Christiansen, L.B., Hsieh, P.A., 2007. Hydrothermal fluid flow and deformation in large calderas: Inferences from numerical simulations. J. Geophys. Res. 112, B02206. doi:10.1029/2006JB004689.

Hutnak, M., Hurwitz, S., Ingebritsen, S.E., Hsieh, P.A., 2009. Numerical models of caldera deformation: Effects of multiphase and multicomponent hydrothermal fluid flow. J. Geophys. Res. 114, B04411. doi:10.1029/2008JB006151.

Jardani, A., Revil, A., 2009. Stochastic joint inversion of temperature and self-potential data. Geophys. J. Int. 179, 640–654. doi:10.1111/j.1365-246X.2009.04295.x.

Legaz, A., Vandemeulebrouck, J., Revil, A., Kemna, A., Hurst, A.W., Reeves, R., Papasin, R., 2009. A case study of resistivity and self-potential signatures of hydrothermal instabilities, Inferno Crater Lake, Waimangu, New Zealand. Geophys. Res. Lett. 36, L12306. doi:10.1029/2009GL037573.

Lima, A., De Vivo, B., Spera, F.J., Bodnar, R.J., Milia, A., Nunziata, C., Belkin, H.E., Cannatelli, C., 2009. Thermodynamic model for uplift and deflation episodes (bradyseism) associated with magmatic–hydrothermal activity at the Campi Flegrei (Italy). Earth-Science Reviews 97, 44–58. doi:10.1016/j.earscirev.2009.10.001.

Mogi, K., 1958. Relations of the eruptions of various volcanoes and the deformations of the ground surface around them. Bull. Earthq. Res. Inst. Tokyo Univ. 36, 99–134.

Orsi, G., Petrazzuoli, S.M., Wohletz, K., 1999. Mechanical and thermo-fluid behaviour during unrest at the Campi Flegri caldera (Italy). J. Volcanol. Geotherm. Res. 91, 453–470. doi:10.1016/S0377-0273(99)00051-7.

Orsi, G., Vita, S.D., Di Vito, M., 1996. The restless, resurgent Campi Flegrei nested caldera (Italy): constraints on its evolution and configuration. J. Volcanol. Geotherm. Res. 74(3-4), 179–214. doi:10.1016/S0377-0273(96)00063-7.

Pruess, K., Oldenburg, C.M., Moridis, G., 1999. TOUGH2 user's guide, version 2.0. Paper LBNL-43134. Lawrence Berkeley Natl. Lab., Berkeley, CA, USA.

Revil, A., Cathles III, L.M., Losh, S., Nunn, J.A., 1998. Electrical conductivity in shaly sands with geophysical application. J. Geophys. Res. 103(B10), 23925–23936.

Revil, A., Finizola, A., Piscitelli, A., Rizzo, E., Ricci, T., Crespy, A., Angeletti, B., Balasco, M., Barde Cabusson, S., Bolève, A., Byrdina, S., Carzaniga, N., Di Gangi, F., Morin, J., Perrone, A., Rossi, M., Roulleau, E., Suski, B., 2008. Inner structure of La Fossa di Vulcano (Vulcano Island, southern Tyrrhenian Sea, Italy) revealed by high-resolution electric resistivity tomography coupled with self-potential, temperature, and CO_2 diffuse degassing measurements. J. Geophys. Res. 113, B07207. doi:10.1029/2007JB005394.

Revil, A., Florsch, N., 2010. Determination of permeability from spectral induced polarization in granular media. Geophys. J. Int. 181, 140–1498. doi:10.1111/j.1365-246X.2010.04573.x.

Revil, A., Glover, P.W.J., 1997. Theory of ionic surface electrical conduction in porous medium. Phys. Rev. B 55, 1757–1773.

Revil, A., Hermitte, D., Spangenberg, E., Cochémé, J.J., 2002. Electrical properties of zeolitized volcaniclastic materials. J. Geophys. Res. 107(B8). doi:10.1029/2001JB000599.

Richards, K., Revil, A., Jardani, A., Henderson, F., Batzle, M., Haas, A., 2010. Pattern of shallow ground water flow at Mount Princeton Hot Springs, Colorado, using geoelectrical methods. J. Volcanol. Geotherm. Res. 198, 217–232. doi:10.1016/j.jvolgeores.2010.09.001.

Rinaldi, A.P., Todesco, M., Bonafede, M., 2010. Hydrothermal instability and ground displacement at the Campi Flegrei caldera. Phys. Earth Planet. Int. 178, 155–161. doi:10.1016/j.pepi.2009.09.005.

Rinaldi, A.P., Vandemeulebrouck, J., Todesco, M., 2009. Modeling of hydrothermal fluid circulation as a tool for volcanic hazard assessment, in: PROCEEDINGS, TOUGH Symposium 2009. Lawrence Berkeley National Laboratory, Berkeley, California, September 14-16, 2009.

Roberts, J.J., 2002. Electrical properties of microporous rock as a function of saturation and temperature. J. App. Phys. 91(3).

Roberts, J.N., Schwartz, L.M., 1985. Grain consolidation and electrical conductivity in porous media. Phys. Rev. B 31, 5990–5997.

Schwartz, L.M., Kimminau, S., 1987. Analysis of electrical conduction in the grain consolidation model. Geophysics 52, 1402–1411.

Sen, P.N., 1987. Electrolytic conduction past arrays of charged insulating spheres. J. Chem. Phys. 87(7), 4100–4107.

Telford, W.M., Geldart, L.P., Sheriff, R.E. (Eds.), 1990. Applied Geophysics - Second Edition. Cambridge University Press.

Todesco, M., 2009. Signals from the Campi Flegrei hydrothermal system: Role of a "magmatic" source of fluids. J. Geophys. Res. 114, B05201. doi:10.1029/2008JB006134.

Todesco, M., Berrino, G., 2005. Modelling hydrothermal fluid circulation and gravity signals at the Phlegrean Fields caldera. Earth Plan. Sci. Lett. 240, 328–338. doi:10.1016/j.epsl.2005.09.016.

Todesco, M., Rinaldi, A.P., Bonafede, M., 2010. Modeling of unrest signals in heterogeneous hydrothermal systems. J. Geophys. Res. 115, B09213. doi:10.1029/2010JB007474.

Todesco, M., Rutqvist, J., Chiodini, G., Pruess, K., Oldenburg, C.M., 2004. Modeling of recent volcanic episodes at Phlegrean Fields (Italy): geochemical variations and ground deformation. Geothermics 33, 531–547. doi:10.1016/j.geothermics.2003.08.014.

Vaughan, P.J., Udell, K.S., Wilt, M.J., 1993. The effects of steam injection on the electrical conductivity of an uncosolidated sand saturated with a salt solution. J. Geophys. Res. 98(B1), 509–518.

Walsh, J., Rice, J., 1979. Local changes in gravity resulting from deformation. J. Geophys. Res 84(B1). doi:10.1029/JB084iB01p00165.

Waxman, M.H., Smits, L.J.M., 1968. Electrical conductivities in oil-bearing shaly sands. Soc. Pet. Eng. J. 8, 107–122.

Zlotnicki, J., Nishida, Y., 2003. Review on morphological insights of self-potential anomalies on volcanoes. Surv. Geophys. 24, 291–338.

Modeling of unrest signals in heterogeneous hydrothermal systems

Contents

4.1 Introduction

The evolution of hydrothermal activity is monitored in many active volcanic areas because of its relation to the magmatic system at depth. A magmatic component is commonly recognized in the fluids discharged in volcanic areas: the abundance, temperature, and composition of this component are expected to change as the volcano approaches eruptive conditions. Significant changes in the magmatic system that feeds the hydrothermal circulation should be accompanied by measurable changes of observable parameters such as gas composition, temperature, flow rate, or the extent of the degassing area. The previous chapters (see Chap. 2 and 3) highlight the dependence of several geophysical parameters on circulating hydrothermal fluids. Changes of these parameters may reflect changes in the magmatic source.

The existence of a relation between the evolution of a magmatic source at depth and different observable parameters is the conceptual base for interpretation of monitoring data and for short-term hazard evaluation. However, different processes,

possibly unrelated to the presence of a degassing magma body, may lead to similar changes, so that the interpretation of monitoring data is not always straightforward (Todesco, 2008, 2009). The properties of the host rocks influence the way in which different signals are generated and transmitted to the surface. This is particularly relevant at Campi Flegrei where seismic data have shown the presence of large heterogeneities at shallow depths, likely to be associated with the presence of fluids (Judenherc and Zollo, 2004; Chiarabba and Moretti, 2006; Tramelli et al., 2006; Bruno et al., 2007; Zollo et al., 2008). Large contrasts between the elastic properties of different rock layers are known to affect the pattern of deformation (Crescentini and Amoruso, 2007; Amoruso et al., 2007) while differences in porosity and permeability are expected to control the propagation of the circulating fluids and the distribution of the fluid phases.

In this chapter, we focus on the effects of rock properties and their spatial distribution on the evolution of selected observables. Numerical simulations run with the same boundary conditions highlight differences that arise from the assumption of different permeabilities, for both homogeneous and heterogeneous systems. Results show that the characteristics of the porous medium substantially control the response of the hydrothermal system to the applied boundary conditions, controlling both the range of variation and the temporal evolution of the observable signals. These results emphasize the importance of a careful definition of in situ rock properties and suggest a great caution when monitored signals are used to infer magmatic conditions.

4.2 The hydrothermal system and the observable parameters

The previous chapter were focused on the effects of a single unrest period on geophysical and geochemical observables. Still using the same conceptual model (Chiodini et al., 2003) and the TOUGH2/EOS2 simulator (Pruess et al., 1999), modeling

Table 4.1: Source activity: mass flow rate and composition of injected fluids during unrest and quiet times. Following Todesco and Berrino (2005), each simulation begins with an unrest phase, and involves 4 unrest and 4 quiet periods. The unrest events last 16, 9, 8, and 3 months, respectively; the following quiet times last 42, 56, 62, and 56 months, respectively. The fluid mixture is injected into the system at constant enthalpy, corresponding to a fluid temperature of ca. 623 K

Injected fluids	Crises	Quiet
CO_2 (tons/day)	6000	1000
H_2O (tons/day)	6100	2400
Total (tons/day)	12100	3400
CO_2/H_2O (molar ratio)	0.40	0.17
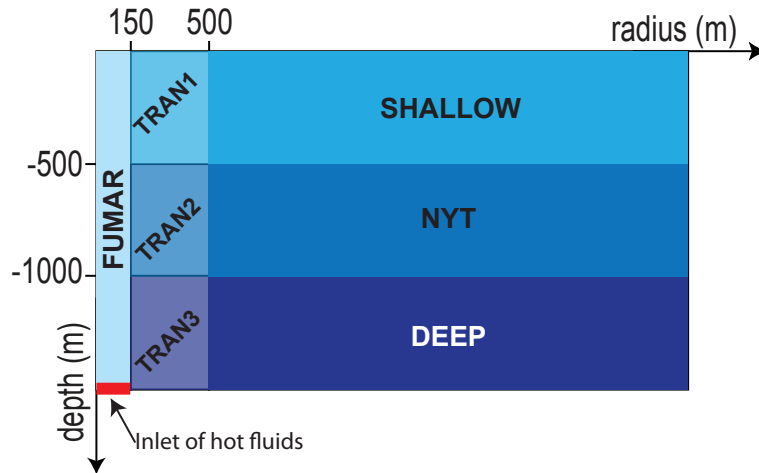
Figure 4.1: Detail of the axial region of the two-dimensional, axisymmetric computational domain. The domain extends radially to 10 km, and reaches a maximum depth of 1.5 km. Bottom and lateral boundaries are impervious and adiabatic, while atmospheric conditions are fixed along the top, which is open to heat and fluid flow. The source of hot, magmatic fluids is indicated in red along the bottom, near the symmetry axis. Flow rate and composition of injected fluids are listed in Table 4.1. Different shades identify the different rock domains used for the simulation of heterogeneous systems, with darker colors associated with lower permeability values. The rock properties used in different simulations are listed in Table 4.3.

results were compared with observed gas composition and gravity data in order to define the source behavior, i.e.: assign the timing, flow rates and gas composition for both the unrest and the quiet periods (Chiodini et al., 2003; Todesco and Berrino, 2005). Following this procedure, and applying the same model, we simulate here the same sequence of unrest and quiet periods, which differ in the amount and composition of magmatic fluids that feed the hydrothermal activity (Table 4.1). In this case, we investigate how heterogeneous rock properties affect the evolution of these observables, compared to results obtained employing a homogeneous domain. The computational domain is the same used in the previous chapters (Chap. 2 and 3).

The different rock domains that characterize the heterogeneous systems are shown in Figure 4.1. Three horizontal layers are chosen to represent the shallow stratigraphy of the Campi Flegrei caldera, where a rather continuous layer of Neapolitan Yellow Tuff separates more permeable shallow rocks from the deeper and older volcanics and marine sediments emplaced after the Campanian Ignimbrite eruption (Orsi et al., 1996; Rosi and Sbrana, 1987). A high-permeability channel is placed at the symmetry axis to represent the feeding system for the fumaroles at Solfatara, the major site of gas discharge in the caldera. The effective heat and fluid transfer underneath Solfatara is likely due to the presence of highly fractured and permeable materials. The permeable channel is as wide as the Solfatara crater. In some simulation, a transition zone with intermediate values of rock permeability is

placed between the vertical channel and the horizontal layers.

The choice of the permeability to assign to the different rock domain in the model is a delicate task. Permeability can vary over orders of magnitude: changes with rock type, with depth and degree of alteration, and evolves through time (Ingebritsen and Manning, 2010; Manning and Ingebritsen, 1999). Some permeability measurements were carried out on different rock samples from Campi Flegrei . According to these data, permeability of the Neapolitan Yellow Tuff ranges from 10^{-14} to 10^{-13} m^2, whereas samples from the Campanian Ignimbrite range from $1.6 \cdot 10^{-16}$ to 10^{-13} m^2 (Peluso and Arienzo, 2007; Vanorio et al., 2002). Some data also derive from the deep geothermal drillings: permeability values were obtained from core samples and well test data but only for the wells in the western portion of the caldera (Mofete area) (Rosi and Sbrana, 1987). These permeability values are scattered over a wide range, regardless to the sampling depth (10^{-17} to 10^{-13} m^2, with most of the value within 10^{-16} and 10^{-14} m^2). Porosity is also characterized by a large variability, ranging from 0.05 to 0.4, with the largest values associated to the shallowest rocks (Rosi and Sbrana, 1987). The choice of rock properties illustrated in Tables 4.2, 4.3, and 4.4 is based on these data, and on modeling results. The four considered permeability distributions do not explore the entire range of possible permeability values, but illustrate the influence of this parameter on the evolution

Table 4.2: Rock properties considered in the simulation of homogeneous system (HO). Rock permeability is isotropic and, unless otherwise specified, is equal to 10^{-14} m^2.

Property	Value
Density (ρ)	2000 kg m^{-3}
Porosity (ϕ)	0.20
Conductivity (λ)	2.80 W m^{-1} K^{-1}
Specific Heat (C)	1000 J kg^{-1} K^{-1}

Table 4.3: Rock properties assigned to the different rock domains shown in Figure 4.1, in all heterogeneous simulations.

	ρ	ϕ	W	C
FUMAR	1800	0.10	1.15	900
TRAN1	1600	0.15	1.15	900
TRAN2	1800	0.15	1.15	900
TRAN3	2000	0.15	1.50	1000
SHALLOW	1600	0.45	1.15	900
NYT	1800	0.35	1.15	900
DEEP	2000	0.15	1.50	1000

Table 4.4: Values of rock permeability (m^2)assigned to each rock domain in the three heterogeneous simulations.

	HE1	*HE2*	*HE3*
FUMAR	10^{-13}	10^{-14}	10^{-14}
TRAN1	$8 \cdot 10^{-14}$	$8 \cdot 10^{-15}$	10^{-14}
TRAN2	$5 \cdot 10^{-14}$	$5 \cdot 10^{-15}$	10^{-14}
TRAN3	10^{-14}	10^{-15}	10^{-14}
SHALLOW	$5 \cdot 10^{-14}$	$5 \cdot 10^{-15}$	$5 \cdot 10^{-15}$
NYT	10^{-14}	10^{-15}	10^{-15}
DEEP	10^{-15}	10^{-16}	10^{-16}

of the hydrothermal circulation.

In each simulation, the initial conditions are obtained by simulating a long-lasting (thousands of years) injection of magmatic fluids, and represent the steady state conditions associated with the specific distribution of rock properties in each considered case. Starting from these initial conditions, the sequence of unrest and quiet periods taken from Todesco and Berrino (2005) is simulated for each considered permeability distribution. The observable parameters calculated from each simulation include fumarole composition, gravity changes, and the ground deformation. Gas composition is expressed again as the molar ratio CO_2/H_2O, and is evaluated near the surface, where a single-phase gas region forms. Gravity changes are calculated using equation 3.4 (Todesco and Berrino, 2005). At this time we focus on the effects associated with the evolving density of hydrothermal fluids, and neglect any contribution arising from the redistribution of rock (or magma) density associated with ground deformation or magma intrusion. Gravity changes arise as fluid density evolves through time, due mainly to a variable distribution of liquid and gas within the system. Rock permeability affects the distribution of the fluid phases, and therefore may affect the gravity changes recorded at the surface. Also in the case of ground displacement, calculated using eq. 3.3 (see also Chap. 2 and Rinaldi et al., 2010, for details), we focus on the effects due to the hydrothermal fluid circulation, but, at this time, we neglect the effects that such deformation may have on the hydraulic properties of the medium: rock permeability and porosity do not change throughout the simulation. This approach assumes that the elastic properties of the rocks, shown in Table 2.3, are homogeneous throughout the system. This assumption implies that heterogeneous systems are composed by rocks that have different permeabilities but the same elastic properties. We are aware that the one-way coupling between hydraulic and mechanical processes and the assumption of homogeneous elastic properties represent a very crude approximation of the natural system that will not provide a realistic description of the expected deformation. Nevertheless, we can use this theoretical exercise to highlight the role of rock permeability on the pattern of deformation caused by the simulated unrest.

4.3 Homogeneous system and associated initial conditions

This section investigates how the value of rock permeability affects the evolution towards steady state conditions in a homogeneous system. Three simulations were run, starting from the same initial geothermal gradient (120 K/km) and hydrostatic pressure profile but with different values of isotropic rock permeability, in the range 10^{-13}-10^{-15} m^2. Other rock properties are listed in Table 4.2. In each case, hot fluids are continuously injected at the base of the system, close to the axis, until the steady state is reached. Flow rate and fluid composition are the same in each simulation and correspond to the quiet-period values reported in Table 4.1. Different values of rock permeability affect the final conditions that characterize the steady

state in each case. The steady-state distribution of volumetric gas fraction and temperature is compared for the three considered cases in Figure 4.2. In all three cases, fluid injection causes the development of a hot, two-phase plume. When the permeability is high (HO1, $\kappa=10^{-13}$ m^2), hot fluids can freely propagate upwards and reach the surface within a few years. The two-phase plume that forms is very narrow (ca. 200 m at the base and 400 m near the surface) and, at its top, a small, dry-gas region forms within ca. 30 years, within which there is no liquid water. At steady-state, the heated region remains close to the symmetry axis, while vigorous convection ensures an effective recharge of cold water through the top of the domain and keeps most of the system at a rather low average temperature (300 K).

In the other two simulations, fluid movement is hindered by lower permeability values. In these cases, the continuous fluid supply at the base is not quickly compensated by a corresponding discharge at the top of the domain. Both pressure and temperature increase in the source region and a wider two-phase zone develops with time. In the intermediate-permeability case (HO2, $\kappa=10^{-14}$ m^2) the plume is 300 m wide at the base and 1000 m near the surface and hosts a larger dry-gas region. In the third case (HO3, $\kappa=10^{-15}$ m^2), the steady state is characterized by a wide two-phase plume (more than 1 km at the surface) and high CO_2 mass fractions are achieved near the top of the domain. However, the single-phase gas region never forms.

In all three cases, the inflow of hot fluids is accompanied by ground deformation associated with an increment in pore pressure and temperature within the system (Figure 4.3). Pressure and temperature changes are faster and smaller for the more permeable system, while greater changes take place more gradually in the less permeable case. These changes deform the porous medium through time. Although these simulations evolve through thousands of years, and therefore transcend the time scale of monitoring systems, we can still compute and compare the ground displacement that arises as each system moves away from its initial linear p,T profiles. The computed ground deformation changes significantly for different values of rock permeability. Figure 4.3a compares the vertical displacement through time for the three considered cases (at the symmetry axis, i.e.: the site of maximum deformation). All simulations begin with a quick uplift phase, which is faster and shorter for higher permeability values: the permeable system reaches ca. 33 cm of vertical displacement after 82 years, whereas the less permeable system totals 1 m of deformation in 2000 years. In the most permeable case (HO1), the vertical displacement undergoes some perturbation due to the onset of small scale convective cells which affect the distribution of pressure and temperature within the system. After a second maximum is reached (34 cm, after 468 yr), the ground level begins to subside, even if the source activity does not vary. At this time, vigorous convection drives cold, surface water toward the deeper portion of the domain, lowering the average temperature of the system (Figure 4.3b). In this simulation, excess fluids entering the system at depth are quickly discharged at the surface, and the average pore pressure does not change significantly throughout the simulation (Figure 4.3c). Subsidence is somewhat slower than the initial uplift, but lasts longer and it drives
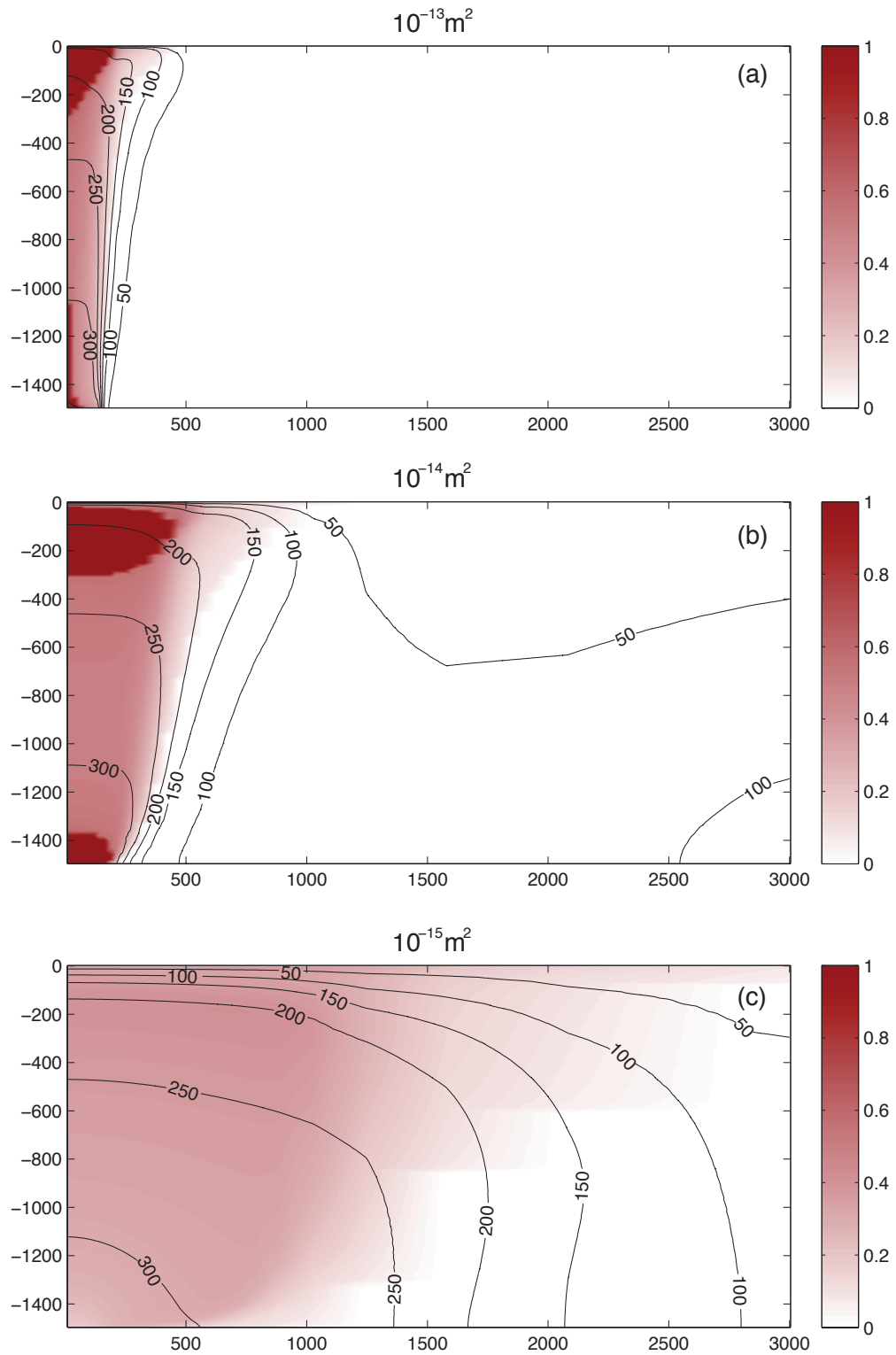
Figure 4.2: Steady state conditions associated with a continued injection of hot fluids at the source for different values of homogeneous and isotropic permeability: (**a**) 10^{-13} m^2; (**b**) 10^{-14} m^2; (**c**) 10^{-15} m^2. Shaded colors indicate the volumetric gas fraction and contour lines refer to temperature (°C). The injected fluids are listed in Table 4.1 (quiet).

the ground surface ca. 50 cm below its initial elevation, where it stands to the end of the simulation. In the case with intermediate permeability, subsidence begins right after the maximum uplift (65 cm in 688 yr) is reached. Subsidence is much slower than the uplift, and by the end of the simulation steady state is not yet reached and the ground level is still ca. 27 cm above its initial elevation. In this case, the system undergoes a minor pressure perturbation that is quickly relieved: the residual displacement at the steady state are due to the very slow temperature decay that maintains some degree of heating and thermal expansion of the system. The average temperature undergoes a very slow decay, but the system remains hotter than the initial conditions throughout the simulation (Figure 4.3b). In the low-permeability case (HO3), permeability is sufficiently low that the system never relaxes: convective cells, which lower the system temperature in the other cases do not form. Pore pressure increases significantly and is not relieved by surface discharge. As a result, no subsidence takes place and the ground level at steady state is still more than 1 m above the initial level. Comparison between the three displacement curves and the corresponding values of average pressure and temperature in the system suggest that the timing of ground displacement, over the long term, is mostly controlled by the system temperature and induced thermal expansion (Hurwitz et al., 2007; Hutnak et al., 2009).

Interesting insights derive from the analysis of the radial pattern of vertical displacement. Figure 4.4a compares the radial profile of ground uplift at the time of maximum deformation for the three simulations. In all cases, the uplift is maximum at the symmetry axis and decays radially, resembling the profile expected for a small spherical source (Mogi, 1958). Only in the most permeable case (HO1) is this profile disturbed by shallow convective cells near the symmetry axis. The radial extent of the uplifted area is largest for the less permeable domain, and reflects the size of the hot plume, which is significantly different in the three cases, although produced by the same fluid source at depth. Even at the time of maximum uplift some subsidence takes place at some distance from the symmetry axis, both for the maximum and for the minimum permeability. Subsidence (negative displacement) reflects the degree of cooling which takes place as the convection draws the cold, shallow water deeper into the system. Figure 4.4 also compares the radial distribution of ground displacement after 1000 years (Figure 4.4b), and at the end of the simulation (Figure 4.4c). Maximum uplift declines with time, and deformation spreads over a wider area, as the system relaxes. In the case of high permeability, most of the deformation is associated with subsidence, which increases as the average temperature declines through time.

The calculated deformations refer to the case of hot gases entering an initially cold and unperturbed system. However, active volcanoes such as Campi Flegrei usually have an active hydrothermal system, characterized by high temperatures and large gas fractions (Chiodini et al., 2001). Our monitoring network must therefore capture signals generated in a system that is already hot and more capable of adjusting to pressure changes than a liquid-dominated system.
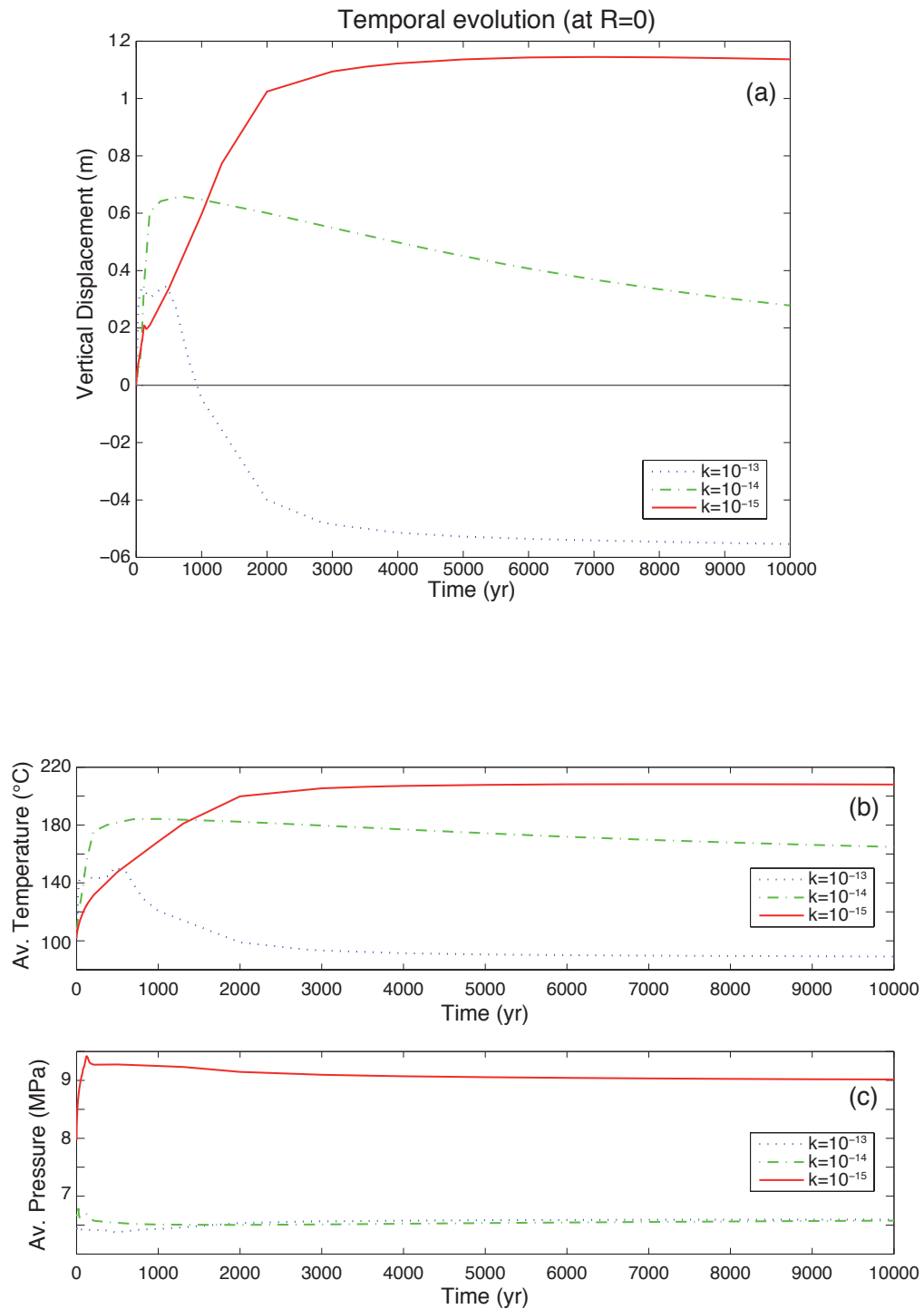
Figure 4.3: (**a**) Temporal evolution of vertical ground displacement during the evolution towards steady state for homogeneous systems with different values of rock permeability. The displacement is calculated at the top of the domain, at the symmetry axis. The corresponding evolution of average temperature and pressure (computed over the entire computational domain) are shown in (**b**) and (**c**), respectively.
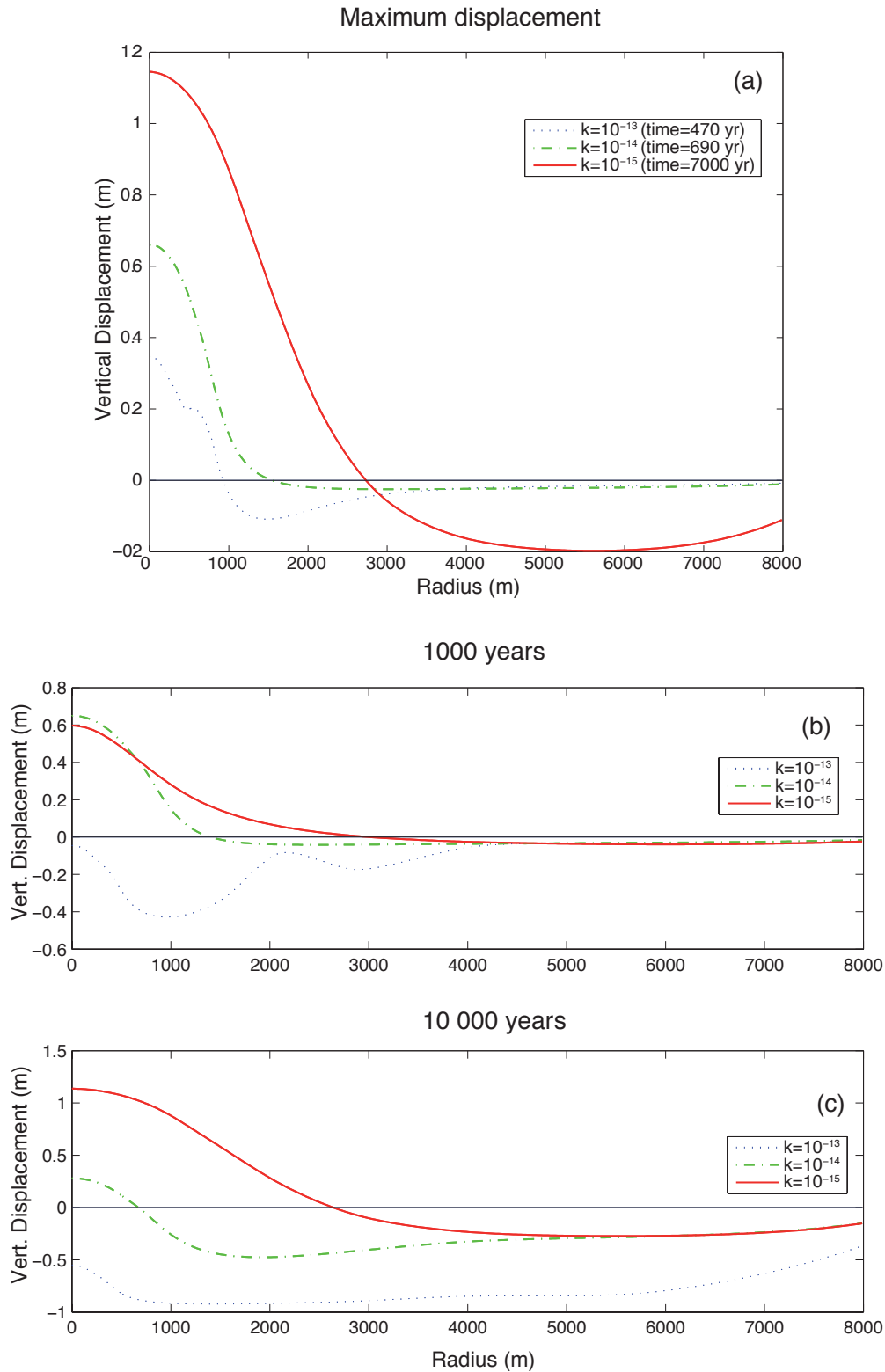
Figure 4.4: Radial distribution of vertical ground displacement for homogeneous systems at different times: (**a**) when the maximum deformation is achieved; (**b**) after 1000 years; (**c**) after 10000 years of simulation.

4.4 Heterogeneous systems

Figure 4.1 illustrates the heterogeneous domain utilized for these simulations. The different rock domains are characterized by specific rock properties (Table 4.3). In all cases, the permeability is higher along the vertical channel and at shallower depth. The three simulations presented below differ in the permeability assigned to each rock domain (Table 4.4): the first case (HE1) is the most permeable; in the second case (HE2), the permeability in each rock domain is one order of magnitude lower than in HE1; while the third case (HE3) maintains the same permeability values assigned to HE2, but with no transition zone and with a wider permeable channel that extends to a radius of 500 m. As in the homogeneous case, the initial conditions are obtained for each domain by simulating a long-lasting injection of hot fluids, according to the flow rate and composition specified in Table 4.1 for the quiet phase. Remarkable differences characterize the steady state attained in the three cases, reflecting the different distribution of rock permeability. Figure 4.5 compares the steady state distribution of temperature and gas fraction obtained with the different permeability distributions. The intermediate-permeability homogeneous case (HO2) described above is also shown for comparison. In the more permeable case (HE1), fluids quickly ascend through the permeable channel and form a thin two-phase plume that is similar to that obtained with the most permeable, homogeneous domain (HO1, Figure 4.2a). In this case, however, the lower permeability of the transition zone (Figure 4.1) confines the flow within the channel, which is thus heated more efficiently. Dry gas forms not only at shallow depths and near the fluid source, as in HO1 and HO2, but extends throughout the channel. Due to the high permeability along the channel, injected fluids ascend quickly toward the surface, while the less permeable transition zone inhibits the recharge of liquid waters from the surrounding region. As a consequence, the gas fraction within the channel remains high and convection takes place only within the shallow, more permeable layer.

When the permeability is lower (HE2), we still observe preferential heating along the vertical channel and the development of a two-phase plume with a shallow dry-gas region. As seen for the homogeneous case, when permeabilities are relatively low, convective cells do not form. The heating due to fluid injection is not compensated by downwelling of cold, shallow waters. The system evolution is much slower, but heating progressively involves a wider portion of the domain, extending to the entire transition zone. The two-phase region is thus much wider than in case HE1, and some gas evolves at depth even within the horizontal layers. The overall gas fraction is lower, with respect to the homogeneous case, and the shallow dry-gas region is thinner and wider. Some pressure build-up occurs in the deepest portion of the domain, near the source region.

The third heterogeneous case (HE3) is characterized by a wider central channel with the same permeability as the homogeneous case. The two-phase plume is hotter, dryer, and slightly less pressurized than in the homogeneous system. The high permeability within the vertical channel concentrates the source effects, favor-
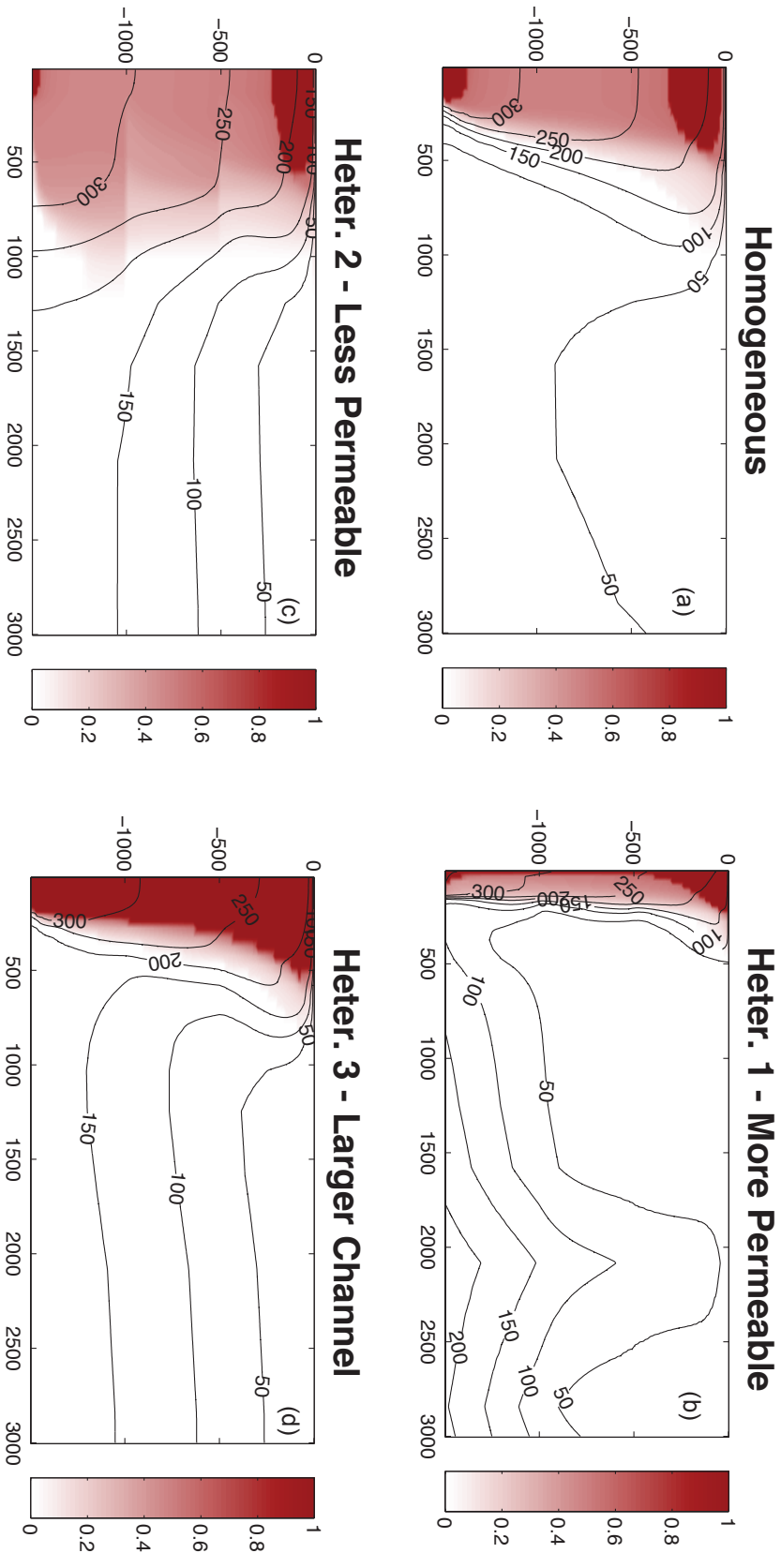
Figure 4.5: Steady state conditions associated with continuous injection of hot fluids. Different plots refer to different permeability distributions within the system: (**a**) homogeneous case (HO2, 10^{-14} m^2); (**b**) heterogeneous domain HE1; (**c**) heterogeneous domain HE2; (**d**) heterogeneous domain HE3. Shaded colors indicate the volumetric gas fraction and contour lines refer to temperature ($^{\circ}$C). The distribution of heterogeneous rock domains is shown in Figure 1, and permeability values used in the three heterogeneous simulations are listed in Table 4.4.

ing hotter temperatures. At the same time, the less permeable surroundings inhibit mitigate the recharge of cold water. As a result, the dry-gas region at steady state occupies most of the channel.

To examine the effects of a pulsating source of fluids on a hot system, the steady state conditions achieved above are taken as initial conditions, and a sequence of unrest and quiet periods are simulated. The case with intermediate homogeneous permeability (HO2) is taken here as the reference case. The temporal evolution of the observables described above is calculated and then compared with results for heterogeneous systems.

4.5 Sequence of unrest

The steady state conditions described above (Figure 4.5) are taken here as initial conditions to simulate a sequence of unrest episodes. Each unrest event is simulated as a period of increased activity of the fluid source at depth, during which both the flow rate and the relative CO_2 content are increased, as discussed in Chiodini et al. (2003). We compare the response of different heterogeneous systems to the same sequence of unrest events described in Todesco and Berrino (2005) for a homogeneous domain, shown in Table 4.1. The system response is evaluated based on the evolution of the three observable parameters introduced above: the composition of the gas in the dry-gas region, gravity changes, and vertical ground displacement.

4.5.1 Gas composition

Figure 4.6 shows the temporal evolution of gas composition, expressed as the average CO_2/H_2O molar ratio. Shaded areas in the figure indicate unrest periods. The temporal evolution of this observable depends on the source properties and distance from the "sampling" point, but also on the initial composition of the gas phase within the system, and on unrest duration (Chiodini et al., 2003; Todesco and Berrino, 2005; Todesco, 2009). In all the simulations presented below, each unrest event increases the CO_2/H_2O molar ratio of the shallow single-phase gas region, whose composition is taken here as a proxy of fumarole composition. The four simulations are characterized by a very different behavior of this parameter. The evolution in the homogeneous case (HO2, Figure 4.6a) is fully described in Todesco and Berrino (2005). The highest CO_2/H_2O molar ratio is reached after the first and longest unrest. Maximum CO_2 enrichment is attained only after the unrest is over. After the peak, the molar ratio declines, at a slightly slower rate. Subsequent peaks are progressively less enriched in CO_2. The minimum value reached between subsequent peaks depends on the length of the quiet period. Over the entire simulation, the unrest periods become progressively shorter, and the overall range of compositional variation becomes narrower and characterized by smoother variations. In this simulation the composition observed at the surface never corresponds to the composition injected by the source at depth (0.17 during the quiet and 0.40 during unrest).
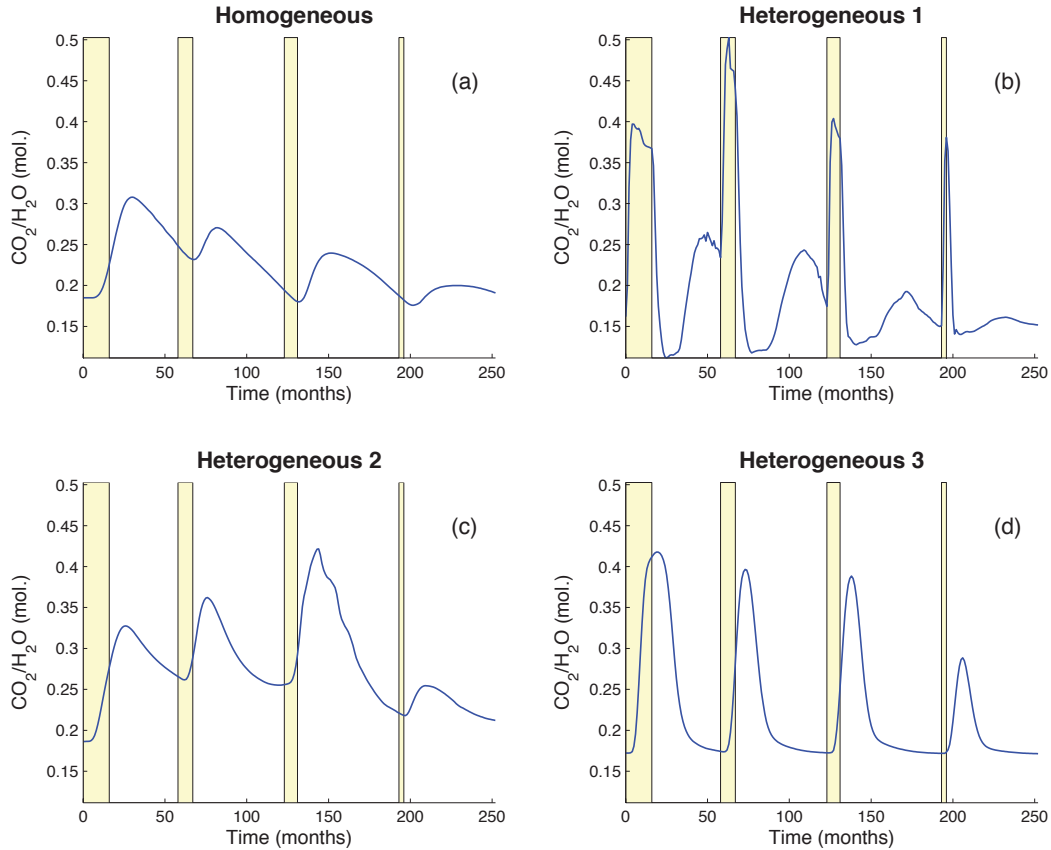
Figure 4.6: Temporal evolution of gas composition corresponding to the sequence of unrest and quiet periods described in Table 4.1. (**a**) Homogeneous domain (HO2); (**b**) heterogeneous domain HE1; (**c**) heterogeneous domain HE2; (**d**) heterogeneous domain HE3. Shaded areas indicate the timing and duration of unrest events.

The first heterogeneous configuration (HE1) is characterized by the highest permeability. Compositional changes at the source are quickly transferred to the surface causing fast compositional variation (Figure 4.6b). In this case, the maximum molar ratio during the unrest reflects the source composition (0.4), as little dilution affects the injected fluids before they reach the surface. The peak values are reached during each crisis, shortly after the beginning of each unrest. After each peak, the molar ratio may decline slightly but only after the end of the crisis does the CO_2 content drop down substantially, below pre-crisis values. The CO_2/H_2O ratio falls somewhat below the composition of the source during quiet periods, reflecting the presence of large amounts of water vapor that form by vaporization of liquid water that reaches the hotter, axial channel from distal regions of the system. Vigorous convection takes place in this case even during quiet periods. When the unrest is over, pore pressure in the axial region decreases and this drives a radial inflow of fluid from the transition region, especially at shallow depths where the permeability is higher. As these fluids enter the permeable channel, they flow upwards and

reach the dry-gas region. As a result, the two-phase plume tends to shrink a little, but significant amounts of CO_2 are driven to the dry-gas region, where they can increase CO_2 content even during the quiet periods. This re-distribution of the fluid components adds to the effects of subsequent unrest events, and contributes to the very high CO_2 enrichments. In this case, the duration of the unrest does not affect the maximum molar ratio: even the shortest unrest yields similar enrichments, and the maximum value is achieved during the second unrest event.

The compositional trends characterizing the second heterogeneous simulation (HE2) are somewhat similar to the homogeneous case (HO2). The rate at which gas composition changes is largely controlled by the permeability of the central channel, which in this case is the same as in the homogeneous case. The presence of the less permeable transition zone focuses the flow within the channel and leads to greater CO_2 enrichments with respect to the HO2 case. Fluid circulation is not as vigorous as in the HE1 case; the dilution of CO_2-enriched fluids associated with convection is limited, and leads to smaller declines during the quiet periods. As a result, gas composition never returns to pre-crisis values, and the effects of subsequent unrest periods cumulate through time and reach a maximum value at the third unrest. This maximum is higher than that achieved in the homogeneous system, and it is larger than some of the peaks obtained with the more permeable HE1 system. This indicates that rock permeability may interact in a complex way with gas composition.

In the third case (HE3) the permeable channel is wider and directly in contact with the less permeable horizontal layers, without a transition region in between. As described above, the dry-gas region occupies most of the channel. In this case, averaging the gas composition over the entire single-phase gas region would include both the composition at the source and at the sampling point, masking the time required by the fluids to migrate from the source to the surface. In the other cases, the single-phase gas zone only developed near the surface and represented a good proxy for fumarole composition. In this case, to obtain a near-surface gas composition, we averaged the CO_2/H_2O ratio over the upper half of the dry-gas zone. Although the rock permeability above the fluid source is similar to the HO2 and HE2 cases, rock properties in this case determine a particular phase distribution that significantly affects the system response to the simulated sequence of unrest and quiet. The absence of a liquid phase within the central channel ensures a quicker response of the system to the changes in the feeding source. The CO_2 enrichment is faster with respect to the homogenous and the HE2 cases, and the maximum CO_2/H_2O ratio is reached shortly after the end of each unrest. The first peak, which follows the longest unrest period, reaches the same CO_2 enrichment (0.4) as the feeding source during the unrest. The post-unrest system reaction is also relatively fast. The CO_2/H_2O ratio rapidly declines to the value that characterizes the feeding source during the quiet periods.
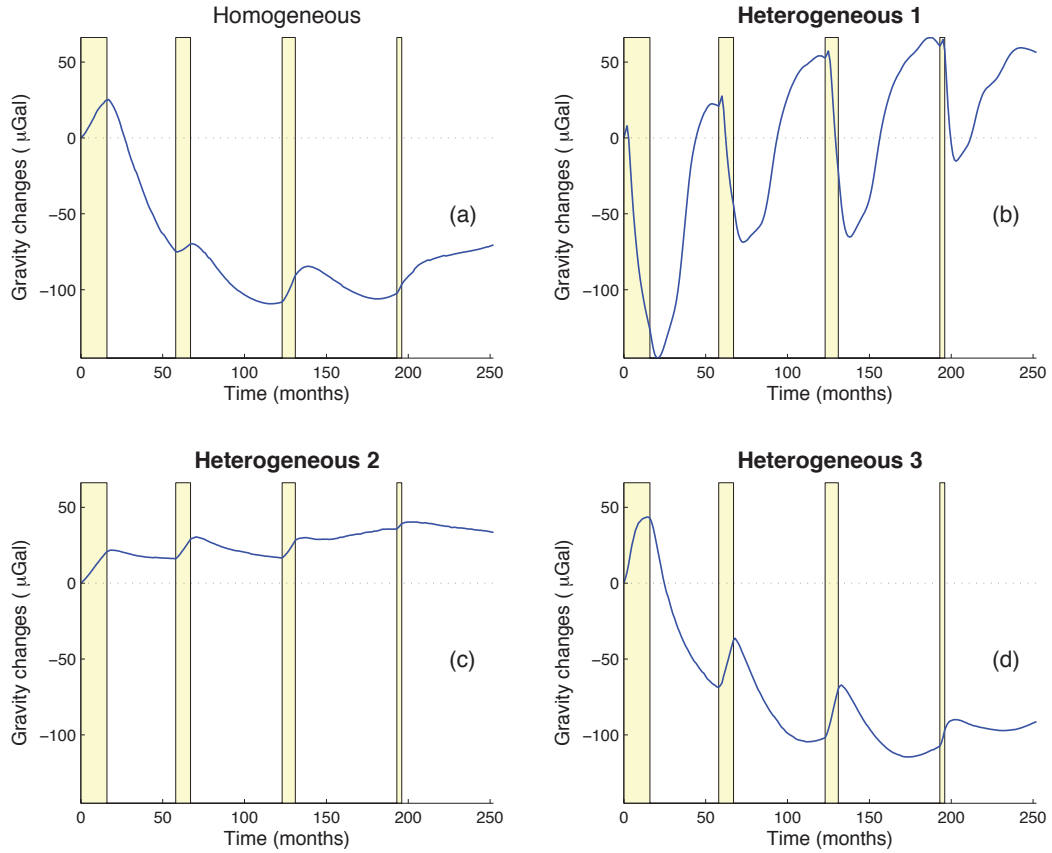
4.5.2 Gravity changes

The temporal variation of surface gravity at the symmetry axis is computed according to equation 1 and is plotted in Figure 4.7, for all the four cases considered. All simulations generate measurable gravity changes, but each case shows a very different temporal evolution and range of variation.

Gravity evolution for the homogeneous case is described in Figure 4.7a. Each unrest period increases the gravitational attraction: larger amounts of fluids enter the system during these periods, and pressure build-up leads to higher fluid densities. When the system relaxes during the quiet, the gravity drops, due to decompression and the upward migration of the gas-enriched fluids injected during the crises. As the simulation proceeds, the gas fraction increases and the two-phase zone progressively enlarges upwards. When the widening of the two-phase zone reaches the surface, the system is more capable of accommodating pressure transients without displacing liquid water. As a result, further unrest events only have minor effects on gravity. The homogeneous case is described with more detail in Todesco and Berrino (2005).

The first heterogeneous system (HE1) is characterized by a rather complex gravity evolution associated with its very fast dynamics (Figure 4.7b). The beginning of each unrest period is signaled by a small, short-lasting peak that is immediately followed by a fast and large gravity drop. As in the homogeneous case, the positive gravity change reflects the addition of fluid, as the unrest begins. In this case, however, the permeability of the central channel is high enough to ensure a prompt system adjustment to the new conditions: the newly injected gases quickly propagate toward the surface, thereby increasing the average gas fraction within the system and causing an overall decline in gravity. When the unrest is over, vigorous convection persists, and drives large amounts of liquid water from the transition zone toward the central channel, causing a marked increase of gravity during the quiet period. This results in a wide range of gravity changes between subsequent unrests. At later times, the overall effect of subsequent crises is to promote convection and movement of liquid water toward the central channel, whereas the excess gas injected during each unrest is quickly discharged at the surface. As a result, the long term trend defined by gravity is positive, while the short-term variations become progressively smaller.

In the second heterogeneous case (HE2), the evolution of gravity is controlled by the lower permeability of the system, which causes widespread pressure build-up during unrest and hinders decompression during quiet periods (Figure 4.7c). The resulting long-term trend is characterized by slow increment and a narrow range of variation.

The gravity evolution associated with the third heterogeneous case (HE3) is broadly similar to the homogeneous case, being characterized by a long-term declining trend, interrupted by sharp increments corresponding to the unrest events (Figure 4.7d). As discussed previously, changes associated with the simulated sequence of unrest events are concentrated in the central channel. Pressure and temperature variations, and associated changes in fluid density, propagate from the fluid

Figure 4.7: Temporal evolution of gravity changes corresponding to the sequence of unrest and quiet periods described in Table 4.1. (**a**) Homogeneous domain (HO2); (**b**) heterogeneous domain HE1; (**c**) heterogeneous domain HE2; (**d**) heterogeneous domain HE3. Shaded areas indicate the timing and duration of unrest events.

source upwards, with only minor diffusion in the radial direction. This emphasizes the gravity changes computed at the surface. In addition, the permeable channel is dominated by the gas phase, which is highly sensitive to pressure perturbation and reacts to the changes in the system conditions. Because of these features, this system exhibits greater gravity changes than the homogeneous case.

During the simulated system evolution, gravity changes not only through time, but also through space: the sequence of unrest and quiet affects the size and shape of the two-phase plume, and this affects the value of gravity at different distances from the symmetry axis. Figure 8 compares the radial distribution of gravity in the four simulations at three different times. Shaded areas in the figure highlight the radial extent of the permeable vertical channel and of the less permeable transition region. At the end of the first unrest (Figure 4.8a), the high-permeability heterogeneous system (HE1) is the only one characterized by negative values. As discussed above, these early, negative values are associated with the very fast dynamic of this permeable system, wherein newly injected fluids quickly reach the surface, reducing
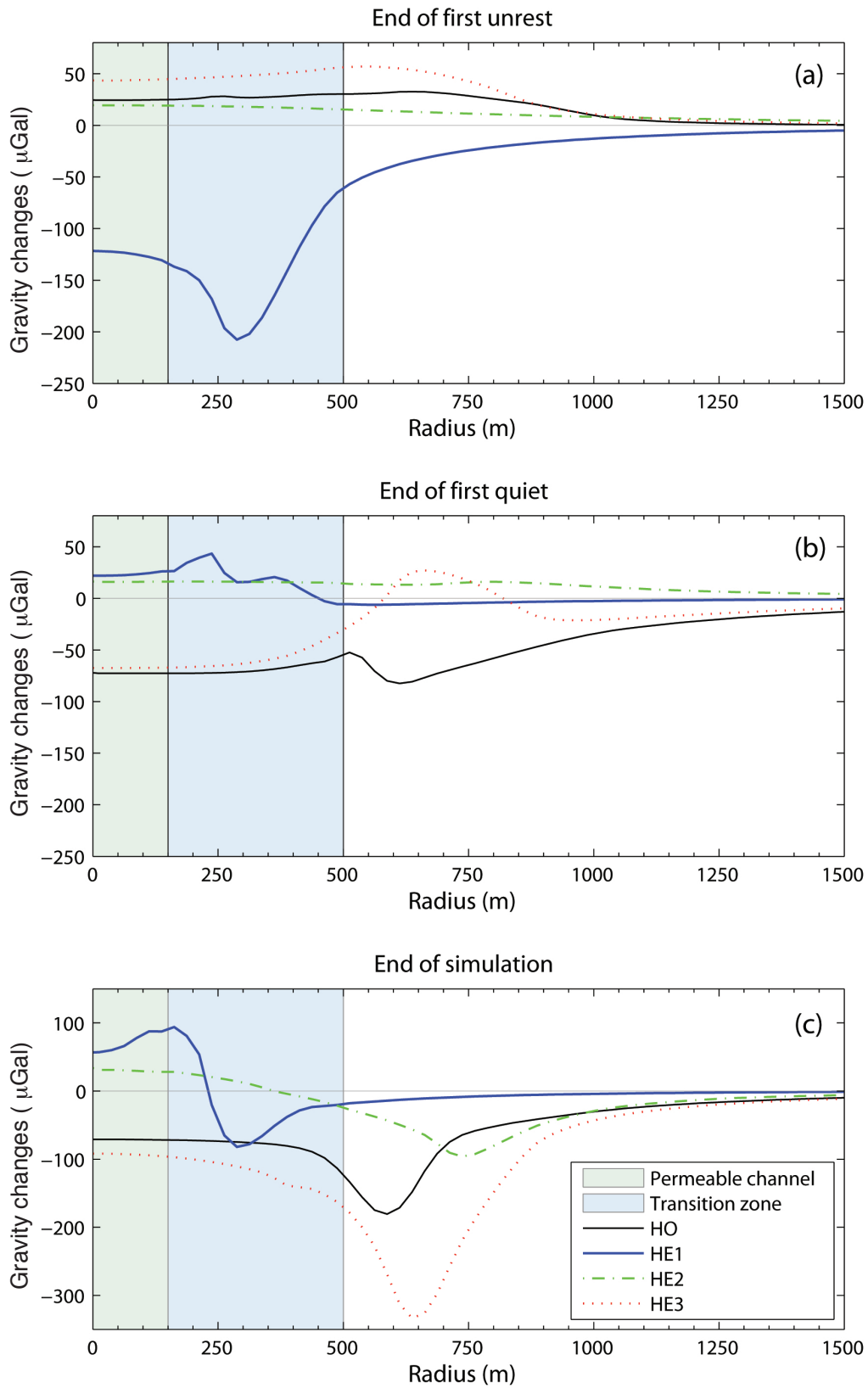
Figure 4.8: Radial distribution of gravity changes at different times: (**a**) end of first unrest event; (**b**) end of first quiet period; (**c**) end of simulation. Shaded areas indicate the radial extent of the permeable channel and transition region.

the liquid fraction at shallow depths. Interestingly, the minimum gravity is reached at some distance (ca. 300 m) from the symmetry axis. The position of this minimum reflects the width of the two-phase plume, which widens as newly injected gases are added during the unrest. In simulation HE1, the two-phase plume is initially confined to the permeable channel. The effects of the first unrest propagate throughout the transition zone, and are small within the distal, horizontal layers. In all the other cases, gravity changes at the end of the first unrest are positive and extend to a maximum distance of less than 1 km. Relative to the homogeneous case (HO2), the less permeable heterogeneous system HE2 shows only minor gravity changes, whereas the third heterogeneous case (HE3) exhibits the largest positive variation. In this case, the less permeable layers around the wide vertical channel confine the horizontal spreading of the ascending fluids and emphasize the effects on the surface gravity value. Figure 8b depicts gravity changes at the end of the first quiet period. At this time, the homogeneous (HO2) and HE3 cases have both relaxed and show negative gravity values in the axial region. In both cases, the edge of the two-phase plume is clearly marked by the presence of a local maximum. This maximum reaches positive values in the HE3 case, where the lower permeability of the horizontal layers hinders radial fluid propagation and thereby prevents effective dissipation of the pore pressure. Positive values characterize the other two cases, with slightly higher values for the more permeable system (HE1), where the inflow of liquid water to the permeable channel creates a complex pattern of fluid density and associated gravity change. Figure 8c shows the radial profiles at the end of the simulation. At this time, the three profiles are substantially different both with respect to peak values and their positions. The more permeable system (HE1) shows a major ($+94$ μGal) positive change, which reflects the inflow of liquid water, with a similarly large (-83 μGal) negative peak nearby associated with the enlargement of the two-phase region within the transition zone. The less permeable system (HE2) is still characterized by a very smooth profile, with positive values ($+34$ μGal) in the axial region, where the overpressure has not yet relaxed completely, and a minimum value (-99 μGal) at ca. 740 m from the axis associated with the enlargement of the two-phase plume, as the excess gases injected during the unrest periods slowly propagate upwards. The homogeneous case (HO2) is characterized at this time by negative gravity changes, with a minimum value (-185 μGal) at ca. 600 m from the axis. The HE3 simulation is characterized by a similar profile, which however reaches a lower minimum (-342 μGal) at a greater distance from the axis.

4.5.3 Vertical ground displacement

The temporal variation of ground displacement at the symmetry axis is shown in Figure 4.9 for the four simulations. In all cases, uplift begins as the injection rate is increased, right at the beginning of each unrest phase, whereas subsidence reflects the lower inflow of hot fluids during quiet times. Ground deformation is driven by changes in pore pressure and temperature, and its evolution is faster for permeable systems, where perturbations propagate faster throughout the system. In the ho-
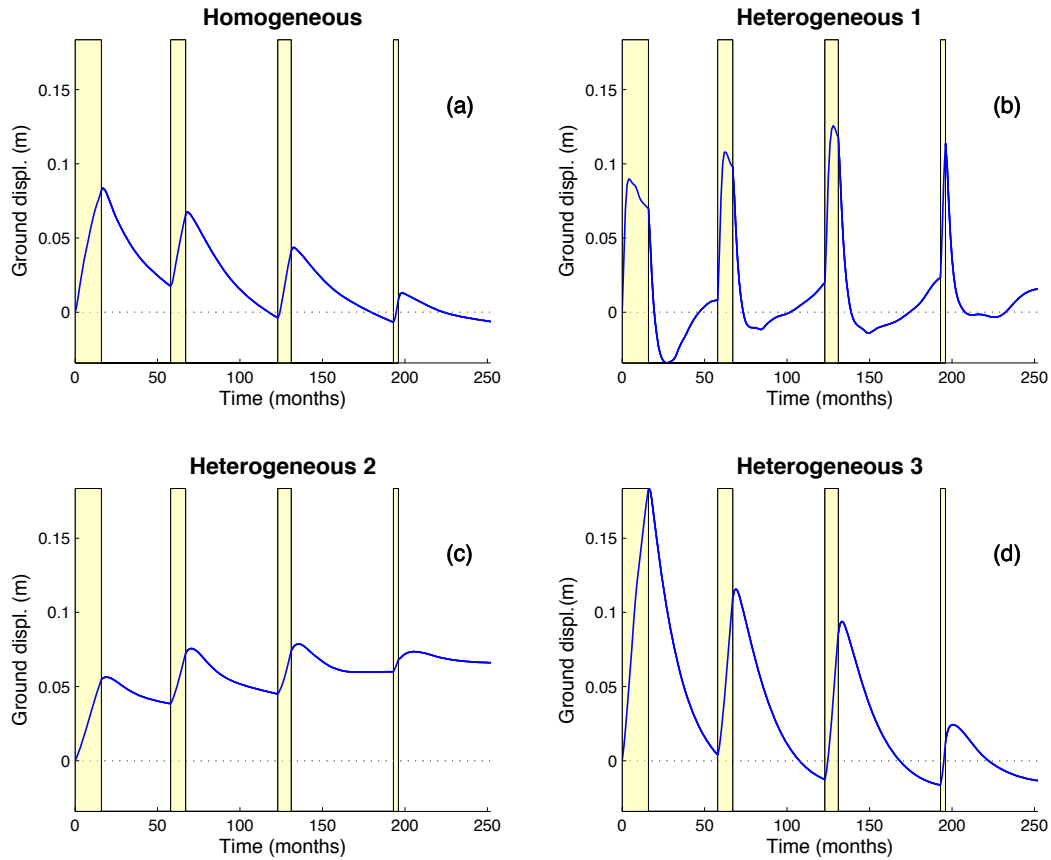
Figure 4.9: Temporal evolution of vertical ground displacement (at the symmetry axis) corresponding to the sequence of unrest and quiet periods described in Table 4.1. (**a**) Homogeneous domain (HO2); (**b**) heterogeneous domain HE1; (**c**) heterogeneous domain HE2; (**d**) heterogeneous domain HE3. Shaded areas indicate the timing and duration of unrest events.

mogeneous case (HO2), the sequence of alternating uplift and subsidence closely reflects the evolution of the fluid source and the duration of the unrest and quiet periods (Figure 4.9a). A local maximum is reached at the end of each crisis, and is followed by slower subsidence during the quiet period. The rate of uplift is similar for the different unrest episodes, and the displacement associated with each crisis depends on its duration. The maximum uplift (ca. 8 cm) is therefore reached at the end of the first unrest period, which is the longest. Subsidence, on the contrary, becomes progressively slower for subsequent quiet periods. At the end of the simulation, the ground level is somewhat below its initial elevation because of the lower pressure and temperature in the system.

In the case of the higher-permeability heterogeneous system (HE1), both uplift and subsidence are very fast (Figure 4.9b). Within a few months, the excess fluid injected during the crisis discharges at the surface, relieving the pore pressure. At the same time, the high permeability favors inflow of cold water towards the deeper

parts of the system, reducing the average temperature. The maximum uplift is therefore reached early in the unrest and subsidence begins before the end of the unrest. At the end of the crisis, the pore pressure drops, driving sudden subsidence that brings the ground level below its original elevation. After a minimum value is reached, a few months after the beginning of the quiet period, pressure and temperature slowly adjust to the new source conditions and the ground level slowly rises again. Because the ground level does not return to its initial value before the onset of a new crisis, the effects of repeated events cumulate and maximum uplift (12 cm) is attained during the third unrest event.

The second heterogenous system (HE2) is the last permeable and shows the smallest changes in vertical ground displacement (Figure 4.9c). Temperature and pore pressure increase significantly, but these changes propagate very slowly from the source region. As a result, only minor deformation is observed at the surface during both the unrest and quiet phases. The low permeability does not allow effective decompression of the system during the quiet and hinders circulation of cold water from the shallow periphery of the system. As a result, the HE2 domain remains pressurized and heated even during quiet periods, and only minor subsidence is recorded at the surface. Repeated unrest events result in a progressive increase in ground elevation, which reaches its maximum value after the third crisis (7.4 cm after 136 months).

The third heterogeneous case (HE3) shows the largest deformation (Figure 4.9d). As in the homogeneous case (HO2), the maximum uplift (17 cm) is reached at the end of the first, longest unrest, while subsequent crises are characterized by less deformation. The subsidence during quiet times reverses the deformation and brings the ground elevation below its initial value. In this case, the presence of less permeable horizontal layers only 500 m from the axis focuses the effects of unrest and quiet periods within the permeable channel, emphasizing the influence of pressure and temperature changes. Pressure and temperature perturbation can effectively propagate to shallow depths but remain concentrated within the axial region, enhancing ground deformation.

The radial distribution of ground displacement at different times also reveals interesting differences among the various cases considered. Figure 4.10a compares the radial distribution of vertical displacement at the end of the first unrest period. In all cases, the maximum uplift is located at the symmetry axis and deformation declines with radial distance, defining a profile similar to that one expected for a small spherical source. As pointed out in Figure 4.9, the maximum uplift is attained in the HE3 case, whereas the minimum deformation is associated with the less permeable HE2 domain. In the homogeneous case (HO), the ground displacement reaches an intermediate value which, however, is maintained over a wide area. In the heterogeneous cases most of the deformation is accomplished within the central portion of the domain. In all cases the uplift decreases below 1 cm, within the first 3.5 km of radial distance. At the end of the first quiet period (Figure 4.10b), deformation is still positive (uplift) for all the simulations, but differences among the various cases emerge. Pressure and temperature perturbations are not easily dissipated in the

End of first unrest

(a)

End of first quiet

(b)

End of simulation

(c)
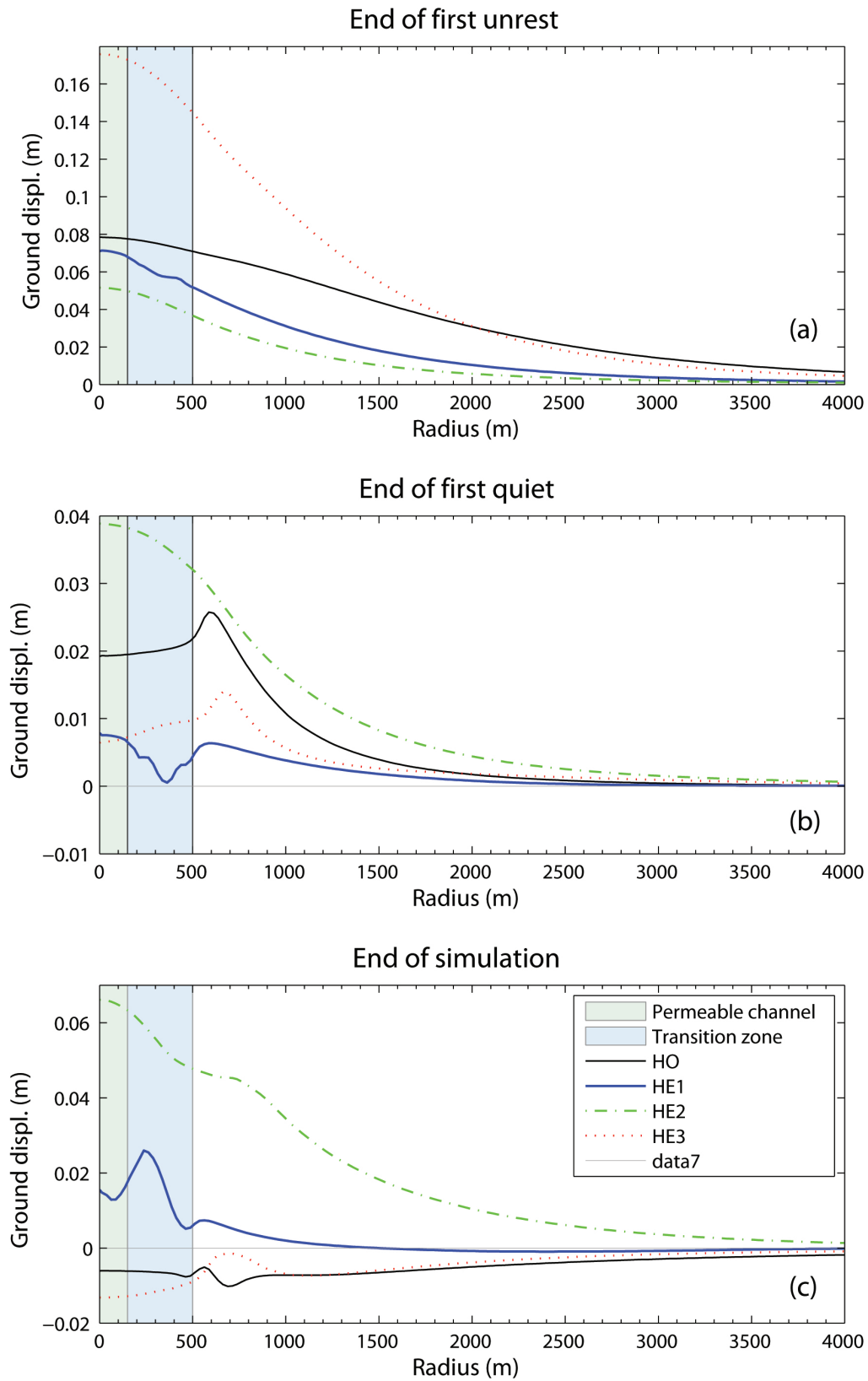
Figure 4.10: Radial distribution of vertical ground displacement at different times: (**a**) end of first unrest event; (**b**) end of first quiet period; (**c**) end of simulation. Shaded areas indicate the radial extent of the permeable channel and of the transition region. Note changes in vertical scale between (**a**), (**b**), and (**c**).

low-permeability HE2 case. As a result, the maximum uplift diminishes, but the radial profile of vertical displacement does not change significantly with respect to the end of the first unrest period. The permeable HE1 system is characterized by a rather complex pattern of deformation, which involves a maximum value at the symmetry axis, a minimum value inside the transition region, and some uplift outside the transition region. This pattern reflects the different behavior of fluid circulation within different rock domains. The homogeneous and HE3 case are characterized by similar patterns, with maximum displacement localized at the edge of the two-phase plume. The low permeability of the horizontal layers in the HE3 simulation confines the fluid circulation within the central channel and accentuates the decompression associated with the quiet period. At the end of the simulation (Figure 4.10c), after four unrest and four quiet periods, the HE2 case is still characterized by the largest amount of uplift, but the radial profile now reflects the presence of the permeable channel and the intermediate transition region. In the more permeable HE1 case, the differences among different domains are larger, and maximum uplift is recorded within the transition region. Both the HO2 and the HE2 cases are characterized by some degree of subsidence, which is larger for the heterogeneous domain. In both cases, a local maximum indicates the edge of the two-phase plume.

4.6 Discussion and Conclusion

In this work we discuss the influence of permeability structure on the evolution of a shallow hydrothermal system fed by magmatic fluids. Starting from the simple conceptual model developed for the Campi Flegrei caldera (Chiodini et al., 2003), we first compared the steady state conditions achieved with different choices of rock permeability, given the same, stationary fluid source at depth. We then studied the effects of periodic unrest events, simulated as periods of increased source activity (in terms of flow rate and CO_2 content). The same sequence of unrest and quiet periods was simulated both for homogeneous and for heterogeneous systems, in which different rock domains are characterized by different rock permeabilities. Although we do not perform a direct comparison with the data from the Campi Flegrei caldera, the rock properties and the spatial distribution of rock types are consistent with available knowledge of the caldera settings (Rosi and Sbrana, 1987; Orsi et al., 1996; Vanorio et al., 2002; Acocella, 2008). The range of values and the spatial distribution of permeability strongly affect the values achieved by state variables under given boundary conditions. When boundary conditions change (as when an unrest event is simulated), rock properties control the system's reaction time, the rate at which system conditions evolve and the time at which they adjust to the new boundary conditions. Hydraulic properties also determine the fraction of the system volume that is affected by the changes, that is the system's sensitivity to external perturbations. High permeability above the fluid source at depth favors the development of a thin, gas-rich plume which quickly reacts to changes in source activity. Wider plumes develop in less permeable systems, which are characterized

by a slower evolution and by lower gas fraction. Low permeability favors heating and pressure build-up near the source region. When a permeable channelway is present in the axial region, and surrounded by less permeable horizontal layers, the effects of source changes are confined within the channel and accentuated, while exchange of heat and fluids with the distal region of the domain is hindered.

These differences in system conditions translate into very different behavior of parameters that can be monitored at the surface. The signals that we record there result from complex interaction between degassing magma at depth, the host rock through which the fluids circulate, and the shallow waters that may permeate the rocks. The value and distribution of rock permeability affect the efficiency of the heat and mass transfer from the deeper region of the volcano toward the surface, control the degree of mixing among different fluid phases, and influence the occurrence of chemical reactions between the fluids and between the fluids and the solid rocks (Todesco, 2008, and ref. therein). A comparison between the variability of gas composition and gravity after an unrest period showed previously that gravity changes are more sensitive to source properties than gas composition (Todesco, 2009). The simulations presented here show that the variability of gas composition is controlled by permeability (being higher for larger permeability values), and that compositional changes are accentuated when fluids are channeled along a permeable zone surrounded by less permeable domains. When all rock domains are relatively permeable (HE1) compositional changes record a very fast reaction to source changes, but also a complex interaction with distal, water-rich fluids that can easily propagate toward the axial region during the quiet. The resulting trend of gas composition is characterized by local minima and maxima which occur during both the unrest and the quiet phases. When rock domains have a lower permeability (HE2), the system reaction speed is reduced. Less vigorous convection hinders the propagation of the CO_2-rich fluids injected during the unrest. As a result, the effects of subsequent crises accumulate through time and lead to higher CO_2 enrichments. When a wider permeable channel is confined by less permeable rocks (HE3), fluids propagate through the channel and reach the surface with little dilution during the unrest. During the quiet period, fluid convection within the channel allows for an effective mitigation of the unrest effects, and gas composition tends to return to its initial value. The other two observables (gravity change and vertical displacement) follow similar trends: more complicated for the more permeable system; slower, with a progressive accumulation of the (minor) effects of subsequent unrests, for the less permeable system; similar to the homogeneous case, but with enhanced effects, in the third heterogeneous case examined. Thus three parameters (gas composition, gravity, and uplift) which are characterized by different temporal evolutions, are affected in a similar way by the permeability distribution. In our simulations, the inflow of external waters in the permeable system modifies the signals generated during and after a crisis. In our simulations all the porous rock is water saturated and therefore the availability of external water may be overestimated with respect to a real system. Nevertheless, the importance of this contribution (both from the thermal and compositional point of view) suggests the need to better define of the

amount of shallow water entering fumarolic conduits in real systems.

At present, given a time series of an observable parameter, it is not possible to filter out the influence of the subsurface rock sequence. Our simulations suggest that it may be important, and particular care should be taken as we try to infer the properties and conditions of the magmatic source from data collected at the surface. Although these simulations are performed assuming no changes in rock properties through time, fracturing or self-sealing processes could also lead to large changes in the observable parameters, even if the deep source remains unchanged. In this case, the departure of monitored signals from their baseline values (i.e., the apparent unrest) would not reflect the state of the magmatic system at depth, but rather the evolution of the shallower portion of the volcanic edifice. This once again invites us to use great caution while deciphering the meaning of unrest events.

References

Acocella, V., 2008. Activating and reactivating pairs of nested collapses during caldera-forming eruptions: Campi Flegrei (Italy). Geophys. Res. Lett. 35(17), L17304. doi:10.1029/2008GL035078.

Allard, P., Maiorani, A., Tedesco, D., Cortecci, G., Turi, B., 1991. Isotopic study of the origin of sulfur and carbon in Solfatara fumaroles, Campi Flegrei caldera. J. Volcanol. Geotherm. Res. 48(1-2), 139–159. doi:10.1016/0377-0273(91)90039-3.

Amoruso, A., Crescentini, L., Linde, A.T., Sacks, I.S., Scarpa, R., Romano, P., 2007. A horizontal crack in a layered structure satisfies deformation for the 2004–2006 uplift of Campi Flegrei. Geophys. Res. Lett. 34, L22313. doi:10.1029/2007GL031644.

Barberi, F., Corrado, G., Innocenti, F., Luongo, G., 1984. Phlegrean Fields 1982 – 1984: Brief chronicle of a volcano emergency in a densely populated area. Bull. Volcanol. 47, 175–185. doi:10.1007/BF01961547.

Battaglia, M., Troise, C., Obrizzo, F., Pingue, F., De Natale, G., 2006. Evidence for fluid migration as the source of deformation at Campi Flegrei caldera (Italy). Geophys. Res. Lett. 33, L01307. doi:10.1029/2005GL024904.

Berrino, G., Corrado, G., Luongo, G., Toro, B., 1984. Ground deformation and gravity changes accompanying the 1982 Pozzuoli uplift. Bull. Volcanol. 47, 188–200.

Bodnar, R.J., Cannatelli, C., De Vivo, B., Lima, A., Belkin, H.E., Milia, A., 2007. Quantitative model for magma degassing and ground deformation (bradyseism) at Campi Flegrei, Italy: Implications for future eruptions. Geology 35(9), 791–794. doi:10.1130/G23653A.1.

Bruno, P.P.G., Ricciardi, G.P., Petrillo, Z., Di Fiore, V., Troiano, A., Chiodini, G., 2007. Geophysical and hydrogeological experiments from a shallow hydrothermal system at Solfatara Volcano, Campi Flegrei, Italy: Response to caldera unrest. J. Geophys. Res. 112, B06201. doi:10.1029/2006JB004383.

Casertano, L., Oliveri del Castillo, A., Quagliariello, M.T., 1976. Hydrodynamics and geodynamics in the Phlegrean fields area of Italy. Nature 264, 161–164. doi:10.1038/26416a0.

Chiarabba, C., Moretti, M., 2006. An insight into the unrest phenomena at the Campi Flegrei caldera from Vp and Vp/Vs tomography. Terra Nova 18, 373–379. doi:10.1111/j.1365-3121.2006.00701.x.

Chiodini, G., 2009. CO_2/CH_4 ratio in fumaroles a powerful tool to detect magma degassing episodes at quiescent volcanoes. Geophys. Res. Lett. 36, L02302. doi:10.1029/2008GL036347.

Chiodini, G., Caliro, S., Cardellini, C., Granieri, D., Avino, R., Baldini, A., Donnini, M., Minopoli, C., 2010. Long term variations of the Campi Flegrei (Italy) volcanic system as revealed by the monitoring of hydrothermal activity. J. Geophys. Res. 115, B03205. doi:10.1029/2008JB006258.

Chiodini, G., Frondini, F., Cardellini, C., Granieri, D., Marini, L., Ventura, G., 2001. CO_2 degassing and energy realease at Solfatara volcano. J. Geophys. Res. 106(B8), 16213–16221. doi:10.1029/2001JB000246.

Chiodini, G., Todesco, M., Caliro, S., Del Gaudio, C., Macedonio, G., Russo, M., 2003. Magma degassing as a trigger of bradyseismic events: the case of Phlegrean Fields (Italy). Geophys. Res. Lett. 30(8), 1434–1437. doi:10.1029/2002GL016790.

Corey, A., 1954. The interrelation between gas and oil relative permeabilities. Producers Monthly 19(1), 38–41.

Crescentini, L., Amoruso, A., 2007. Effects of crustal layering on the inversion of deformation and gravity data in volcanic areas: An application to the Campi Flegrei caldera, Italy. Geophys. Res. Lett. 34, L09303. doi:10.1029/2007GL029919.

De Natale, G., Pingue, F., Allard, P., Zollo, A., 1991. Geophysical and geochemical modelling of the 1982-1984 unrest phenomena at Campi Flegrei caldera (southern Italy). J. Volcanol. Geotherm. Res. 48, 199–222. doi:10.1016/0377-0273(91)90043-Y.

De Natale, G., Troise, C., Pingue, F., 2001. A mechanical fluid-dynamical model for ground movements at Campi Flegrei caldera. J. Geodyn. 32, 487–571. doi:10.1016/S0264-3707(01)00045-X.

Hurwitz, S., Christiansen, L.B., Hsieh, P.A., 2007. Hydrothermal fluid flow and deformation in large calderas: Inferences from numerical simulations. J. Geophys. Res. 112, B02206. doi:10.1029/2006JB004689.

Hutnak, M., Hurwitz, S., Ingebritsen, S.E., Hsieh, P.A., 2009. Numerical models of caldera deformation: Effects of multiphase and multicomponent hydrothermal fluid flow. J. Geophys. Res. 114, B04411. doi:10.1029/2008JB006151.

Ingebritsen, S., Manning, C., 2010. Permeability of the continental crust: dynamic variations inferred from seismicity and metamorphism. Geofluids 10(1–2), 193–205. doi:10.1111/j.1468-8123.2010.00278.x.

Judenherc, S., Zollo, A., 2004. The Bay of Naples (southern Italy): Constraints on the volcanic structures inferred from a dense seismic survey. J. Geophys. Res. 109(B10). doi:10.1029/2003JB002876.

Lima, A., De Vivo, B., Spera, F.J., Bodnar, R.J., Milia, A., Nunziata, C., Belkin, H.E., Cannatelli, C., 2009. Thermodynamic model for uplift and deflation episodes (bradyseism) associated with magmatic–hydrothermal activity at the Campi Flegrei (Italy). Earth-Science Reviews 97, 44–58. doi:10.1016/j.earscirev.2009.10.001.

Manning, C., Ingebritsen, S., 1999. Permeability of the continental crust: Implications of geothermal data and metamorphic systems. Rev. Geophys. 37(1), 127–150. doi:10.1029/1998RG900002.

Mogi, K., 1958. Relations of the eruptions of various volcanoes and the deformations of the ground surface around them. Bull. Earthq. Res. Inst. Tokyo Univ. 36, 99–134.

Newhall, C., Dzurisin, D., 1988. Historical unrest at large calderas of the world. USGS Bull. (1855), 1108.

Orsi, G., Petrazzuoli, S.M., Wohletz, K., 1999. Mechanical and thermo-fluid behaviour during unrest at the Campi Flegri caldera (Italy). J. Volcanol. Geotherm. Res. 91, 453–470. doi:10.1016/S0377-0273(99)00051-7.

Orsi, G., Vita, S.D., Di Vito, M., 1996. The restless, resurgent Campi Flegrei nested caldera (Italy): constraints on its evolution and configuration. J. Volcanol. Geotherm. Res. 74(3-4), 179–214. doi:10.1016/S0377-0273(96)00063-7.

Peluso, F., Arienzo, I., 2007. Experimental determination of permeability of Neapolitan Yellow Tuff. J. Volcanol. and Geotherm. Res. 160(1-2). doi:10.1016/j.jvolgeores.2006.09.004.

Pruess, K., Oldenburg, C.M., Moridis, G., 1999. TOUGH2 user's guide, version 2.0. Paper LBNL-43134. Lawrence Berkeley Natl. Lab., Berkeley, CA, USA.

Rinaldi, A.P., Todesco, M., Bonafede, M., 2010. Hydrothermal instability and ground displacement at the Campi Flegrei caldera. Phys. Earth Planet. Int. 178, 155–161. doi:10.1016/j.pepi.2009.09.005.

Rosi, M., Sbrana, A., 1987. The Phlegrean Fields. Quaderni de La Ricerca Scientifica 114. Consiglio Nazionale delle Ricerche, Roma ,Italy.

Sorey, M., McConnell, V., Roeloffs, E., 2003. Summary of recent research in Long Valley Caldera, California. J. Volcanol. Geotherm. Res. 127(3-4), 165–173. doi:10.1016/S0377-0273(03)00168-9.

Tedesco, D., 1994. Chemical and isotopic gas emissions at Campi Flegrei: Evidence for an aborted period of unrest. J. Geophys. Res. 99(B8). doi:doi:10.1029/94JB00465.

Tedesco, D., Allard, P., Sano, Y., Wakita, H., 1990. Helium-3 in subaerial and submarine fumaroles of campi flegrei caldera, italy. Geochimica et Cosmochimica Acta 54, 1105–1116. doi:10.1016/0016-7037(90)90442-N.

Todesco, M., 2008. Hydrothermal fluid circulation and its effects on caldera unrest, in: Gottsmann, J., Marti, J. (Eds.), Caldera Volcanoes: Analysis, Modeling and Response, Dev. Volcanol.. Elsevier, Amsterdam. volume 10, pp. 393–416.

Todesco, M., 2009. Signals from the Campi Flegrei hydrothermal system: Role of a "magmatic" source of fluids. J. Geophys. Res. 114, B05201. doi:10.1029/2008JB006134.

Todesco, M., Berrino, G., 2005. Modelling hydrothermal fluid circulation and gravity signals at the Phlegrean Fields caldera. Earth Plan. Sci. Lett. 240, 328–338. doi:10.1016/j.epsl.2005.09.016.

Todesco, M., Chiodini, G., Macedonio, G., 2003. Monitoring and modelling hydrothermal fluid emission at La Solfatara (Phlegrean Field, Italy). An interdisciplinary approach to the study of diffuse degassing. J. Volcanol. Geotherm. Res. 125, 57–79. doi:10.1016/S0377-0273(03)00089-1.

Todesco, M., Rutqvist, J., Chiodini, G., Pruess, K., Oldenburg, C.M., 2004. Modeling of recent volcanic episodes at Phlegrean Fields (Italy): geochemical variations and ground deformation. Geothermics 33, 531–547. doi:10.1016/j.geothermics.2003.08.014.

Tramelli, A., Del Pezzo, E., Bianco, F., Boschi, E., 2006. 3D scattering image of the Campi Flegrei caldera (Southern Italy): New hints on the position of the old caldera rim. Phys. Earth Planet. Int. 155, 269–280. doi:10.1016/j.pepi.2005.12.009.

Troise, C., De Natale, G., Pingue, F., Obrizzo, F., De Martino, P., Tammaro, U., Boschi, E., 2007. Renewed ground uplift at Campi Flegrei caldera (Italy): New insight on magmatic processes and forecast. Geophys. Res. Lett. 34, L03301. doi:10.1029/2006GL028545.

Vanorio, T., Prasad, M., Patella, D., Nur, A., 2002. Ultrasonic velocity measurements in volcanic rocks: correlation with microtexture. Geophys. J. Int. 149(1), 22–36. doi:10.1046/j.0956-540x.2001.01580.x.

Villemant, B., Hammouya, G., Michel, A., Semet, M., Komorowski, J.C., Boudon, G., Cheminée, J.L., 2005. The memory of volcanic waters: Shallow magma degassing revealed by halogen monitoring in thermal springs of La Soufrière volcano (Guadeloupe, Lesser Antilles). Earth and Plan. Sci. Lett. 237(3-4), 710–728. doi:doi:10.1016/j.epsl.2005.05.013.

Walsh, J., Rice, J., 1979. Local changes in gravity resulting from deformation. J. Geophys. Res 84(B1). doi:10.1029/JB084iB01p00165.

Zollo, A., Maercklin, N., Vassallo, M., Dello Iacono, D., Virieux, J., Gasparini, P., 2008. Seismic reflections reveal a massive melt layer feeding Campi Flegrei caldera. Geophys. Res. Lett. 35(12). doi:10.1029/2008GL034242.

Small scale simulation at the Solfatara crater

Contents

5.1 Introduction

$\mathbf{A}$ctivity of Campi Flegrei caldera is mainly concentrated at Solfatara volcano, a 180 m tuff-cone located NE of Pozzuoli. Using stratigraphic and geochronological data, Di Vito et al. (1999) infer that Solfatara formed between 3.8 ad 4.1 ka. Deposits are mainly hydrothermally altered breccia, covered by accretionary lapilli-rich, dune-bedded ash, and lapilli beds, lying over an area of about 0.8 km^2 (Rosi and Sbrana, 1987). The crater is characterized by a roughly sub-rectilinear rims, with subvertical inner walls (dip > 70°). Rims are cut by two main fault with strike in NW-SE direction, and two NW-SE striking fault are also present on the eastern part of the cone (Bianco et al., 2004). Subvertical fracture filled by hydrothermal minerals are also present at Solfatara.

Hydrothermal system at Solfatara crater features mud pools (Fangaia), several fumaroles (main vents named as Bocca Grande and Bocca Nuova) and a strong diffuse degassing 5.1. CO$_2$ degassing amounts to about 1500 ton/day at Solfatara (Chiodini et al., 2001). Soil degassing is associated with high temperatures over an area of 0.5 km^2 and high thermal energy released by degassing ($\sim$ 100 MW), a value much higher than both the conductive heat flux over the entire caldera (90 km^2) and the seismic and deformation energy released during the major unrests (Chiodini et al., 2001, 2007). The highest temperatures are registered at the two main fumarolic vents (Bocca Grande e Bocca Nuova), where values reach $\sim$160 °C (Caliro et al., 2007).

Figure 5.1: Large view of the Solfatara crater. All the white zones are hydrothermally altered and characterized by diffuse degassing. Position and enlargement of both the Fangaia mud pool and the two main fumaroles are also highlighted.

Following the conceptual model proposed by Chiodini et al. (2003) for Campi Flegrei caldera, the previous chapters (Chap. 2, 3, 4) shows as a source of magmatic fluids, with period of higher injection, may control the evolution of several geophysical and geochemical observables (see also Todesco et al., 2004; Todesco and Berrino, 2005; Rinaldi et al., 2009, 2010, 2011), although hosting rocks and fluid source play a main role (Todesco, 2008, 2009; Todesco et al., 2010). However, simulations were performed on large scale domain representing the whole caldera and centered at Solfatara, with a depth up to 1.5 km. Using this domain, we were unable to represent the shallow subsurface of the Solfatara crater. Moreover, simulations result as fully water saturated and do not take into account unsaturated regions (vadose zone) at shallow depths and far from the degassing zone, hence a comparison between computed and observed electrical conductivity is biased. Studies at Solfatara volcano (Campi Flegrei caldera) highlight the presence of an unsaturated layer at depth and allow to determine the position of the water table (Bruno et al., 2007). In order to produce a more detailed electrical conductivity map, in this chapter we focus on the Solfatara crater and simulate a small scale (3 km wide and 0.4 km deep) hydrothermal fluid circulation at shallow depth, using a new, refined meshgrid and taking into account the real topography of the crater.

5.2   Buondary and initial conditions

In order to represent the subsurface below the crater and the presence of the unsaturated level we designed a small scale simulation, using a new computational 2D mesh, with appropriate initial and boundary condition to perform a more detailed computation of electrical conductivity, and taking into account the real topography (Fig. 5.2).

The new grid is 2D non-axisymmetric, 3000 m long and only 400 m deep, reaching a depth of 250 m below the sea level, and follow the real topography of a profile of the Solfatara crater (red line in Fig. 5.2a). We want to reproduce two main features

of the crater: the Fangaia mud pool and the Bocca Grande fumarole (see Fig. 5.1).
The profile has been chosen passing through these two points, and ending out of the
crater on west side and at the sea level on east side. The topography of the chosen
profile is shown in Fig. 5.2b. Fig. 5.2c shows the grid mesh and the initial phase
distribution: an unsaturated layer (brown), a water layer (blue) and a gas reservoir
(cyan) at a depth of 200 m. The gray color indicates a low permeability seal, initially
saturated with a two-phase fluid. The reservoir conditions (p, T, p_{CO_2}) are taken
from the former simulation and correspond to the conditions of the shallow dry gas
region (Fig. 2.1 or 3.3a). We choose homogeneous rock properties, listed in Table
5.1, with the exception of the low permeability layer whose permeability is much
lower (10^{-18} m^2). Temperature and pressure distribution are initially stratified over
the entire domain. The east side boundary is set to low temperature (300 K) to
represent the sea in the upper part, and to high temperature in the low permeability
layer and in the gas reservoir. Both sides and bottom boundaries, and ground surface
are open to fluid flow.

We set the presence of two preferential pathways for fluid ascent, representing
the fault ring around the crater. On the eastern portion of the crater, diffuse de-
gassing and minor fumarolic vents are obtained introducing a permeable region (40
m wide) connecting the reservoir to the groundwater. On the western side of the
crater the Bocca Grande fumarole is simulated as a channel (4 m wide) connecting
the reservoir to the ground surface. The channel boundaries are impervious and
adiabatic, and allow a fast ascent of reservoir fluids. This is obtained by assigning
low permeability (10^{-18} m^2) and high heat capacity to a thin rock layer around the
channel. The emission temperature of the discharged gas at the channel was set
to 450 K. We also set boundary conditions for the Fangaia mud pool, here repre-
sented as a two-phase zone at ground surface with a temperature of 350 K. Instead
of placing a fluid source as in the former simulation (Chap. 2, 3, 4), in this case
we simulate the ascent of fluids imposing an overpressure at the base of the domain
(Fig. 5.2).

Table 5.1: Rock properties considered in the simulation of the small scale hydrothermal sys-
tem system. Rock properties are homogeneous, with the exception of the low permeability
layer whose permeability is 10^{-18} m^2.

Property	Value
Permeability (κ)	10^{-14}, 10^{-18} m^2
Density (ρ)	2000 kg m^{-3}
Porosity (ϕ)	0.20
Conductivity (λ)	2.80 W m^{-1} K^{-1}
Specific Heat (C)	1000 J kg^{-1} K^{-1}
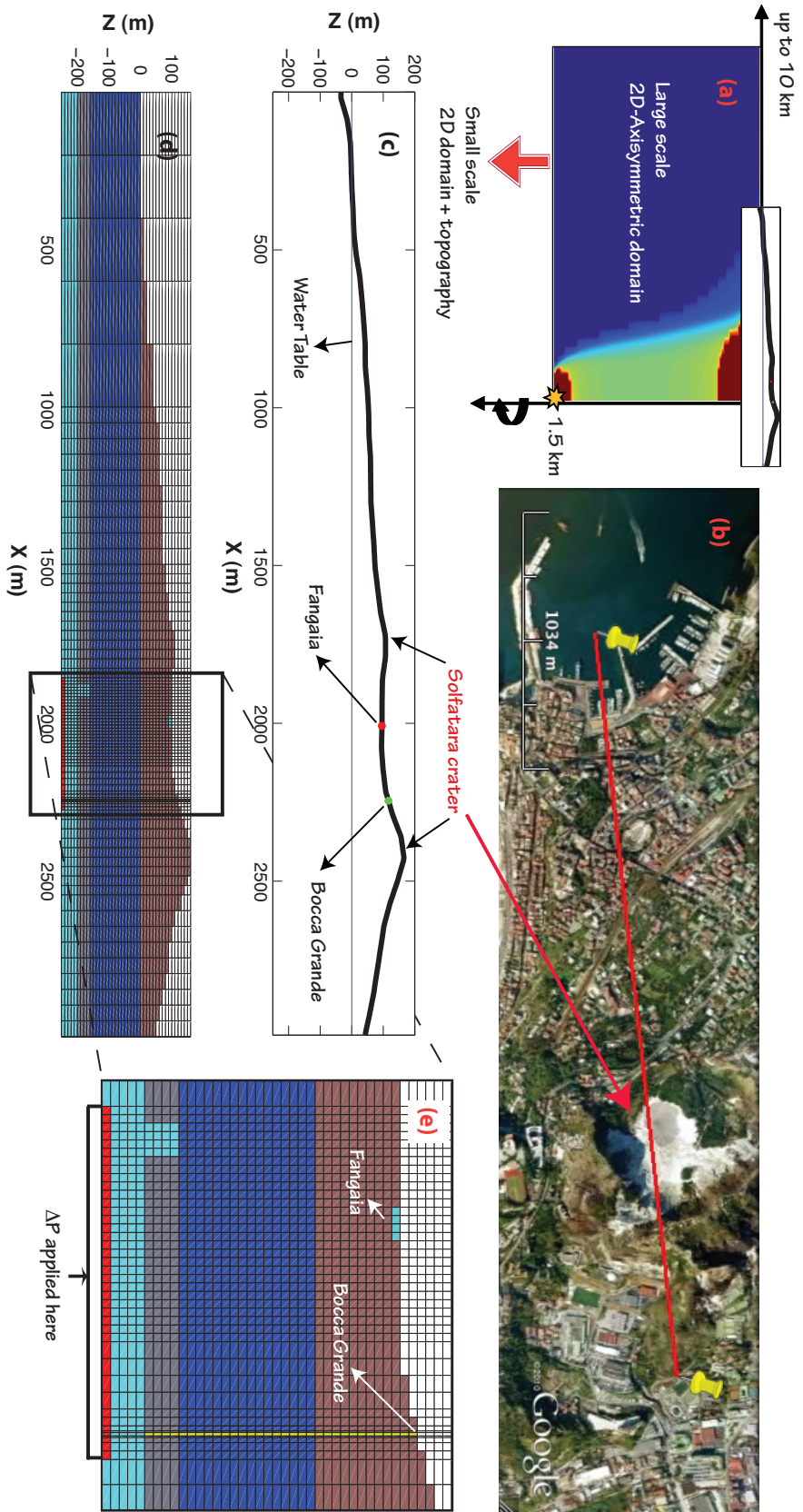
Figure 5.2: (a) Comparison between the large computational domain and the small mesh used to reproduce the groundwater at Solfatara crater. (b) Profile for the new mesh (red line, Google Earth picture), (c) profile topography. Red point indicates the location of Fangaia mud pool. Green point indicates the position of the Bocca Grande fumarole. The water table set as initial condition (blue line) is here at sea level. (d) 2D meshgrid and initial phase distribution condition. Brown: unsaturated domain filled by CO_2. Blue: water layer. Gray: low permeability layer, interrupted below Solfatara crater where fractures are supposed to feed surface emission at Fangaia and Bocca Grande (wide opening in cyan and channel in yellow). Cyan: two-phase and two-component gas reservoir. (e) Enlargement of the Solfatara crater. Overpressure is set for the red grid blocks. Two different kinds of fracture are simulated at each crater wall. Fangaia mud pool is set as a two-phase fluid with a fixed temperature of 350 K and Bocca Grande fumarole is set as a single-phase gas with the reservoir composition and a degassing temperature of 450 K.

5.3 Steady-state simulation

A very long simulation , at steady-state (i.e. after hundred thousands of year), using the TOUGH2/EOS2 simulator described previously (see Chap. 1 and Pruess et al., 1999), produces the gas saturation and the temperature distribution shown in Fig. 5.3.

We set the boundary conditions in order to get the water table almost everywhere at the sea level and at the ground surface below the Solfatara crater (Fig. 5.3a). Such a distribution is in agreement with the description by Bruno et al. (2007). Two separate plumes develop at shallow depth, corresponding to the two different fractures. The opening in the low permeability layer below the east crater wall enables the generation of a wide two-phase plume. The channel simulating the Bocca Grande fumarole generates a narrow plume, characterized by a small single phase zone at very shallow depth. Liquid water occupies the inner portion of the crater and feeds the Fangaia mud pool. The gas reservoir at bottom is characterized by a wide single phase zone, extending as much as the Solfatara crater in length and up to a depth of -150 m. The gas in the two phase plume, along the fumarole and in the reservoir have the same composition (molar ratio CO_2/H_2O=0.4). Heating of the Bocca Grande fracture induces boiling of all the groundwater and creates the single-phase zone.

Temperature distribution, shown in Fig. 5.3b, presents temperature up to 530 K, where the overpressure is imposed, and high gradient in correspondence to the two plumes. Surface temperature is shown in Fig. 5.3c (red line). It is characterized by three peaks representing (from East to West) the plume at the western crater edge, the Fangaia mud pool, and the Bocca Grande fumarole where temperature reaches approximately 460 K (from East to West). Fig. 5.3c also shows the degassing rate at the ground surface. Surface degassing only occurs above the two plumes, and this is not in agreement with the observation at Solfatara, where high diffuse degassing is observed over the whole crater. Moreover, the degassing values at the fractures are very low if compared with real data. For example at Bocca Grande we simulate an emission of 3000 g day^{-1} m^{-2}, instead of the tons by day registered at the fumarole.

Still using the equation 3.2 (see Chap. 3; Revil et al., 1998; Revil and Florsch, 2010; Rinaldi et al., 2011, for detail), we calculate an electrical conductivity map of the Solfatara crater (Fig. 5.4). A high electrical conductivity body (up to 0.05 Sm^{-1} in the deeper and hotter parts) characterizes the zone underneath the central part of the crater. Areas where gases are rising, i.e. fractured zones, have low electrical conductivity (0.01 to 0.015 Sm^{-1}). Single phase gas zones and the gas reservoir show a very low electrical conductivity (less than 0.01 Sm^{-1}). Temperature effects on electrical conductivity (Eq. 3.1) play a big role in the computation (Vaughan et al., 1993; Revil et al., 1998; Roberts, 2002), and may enhance the results up to 0.03 Sm^{-1} in case of very high temperature as in the area close to the impermeable layer when water is present.
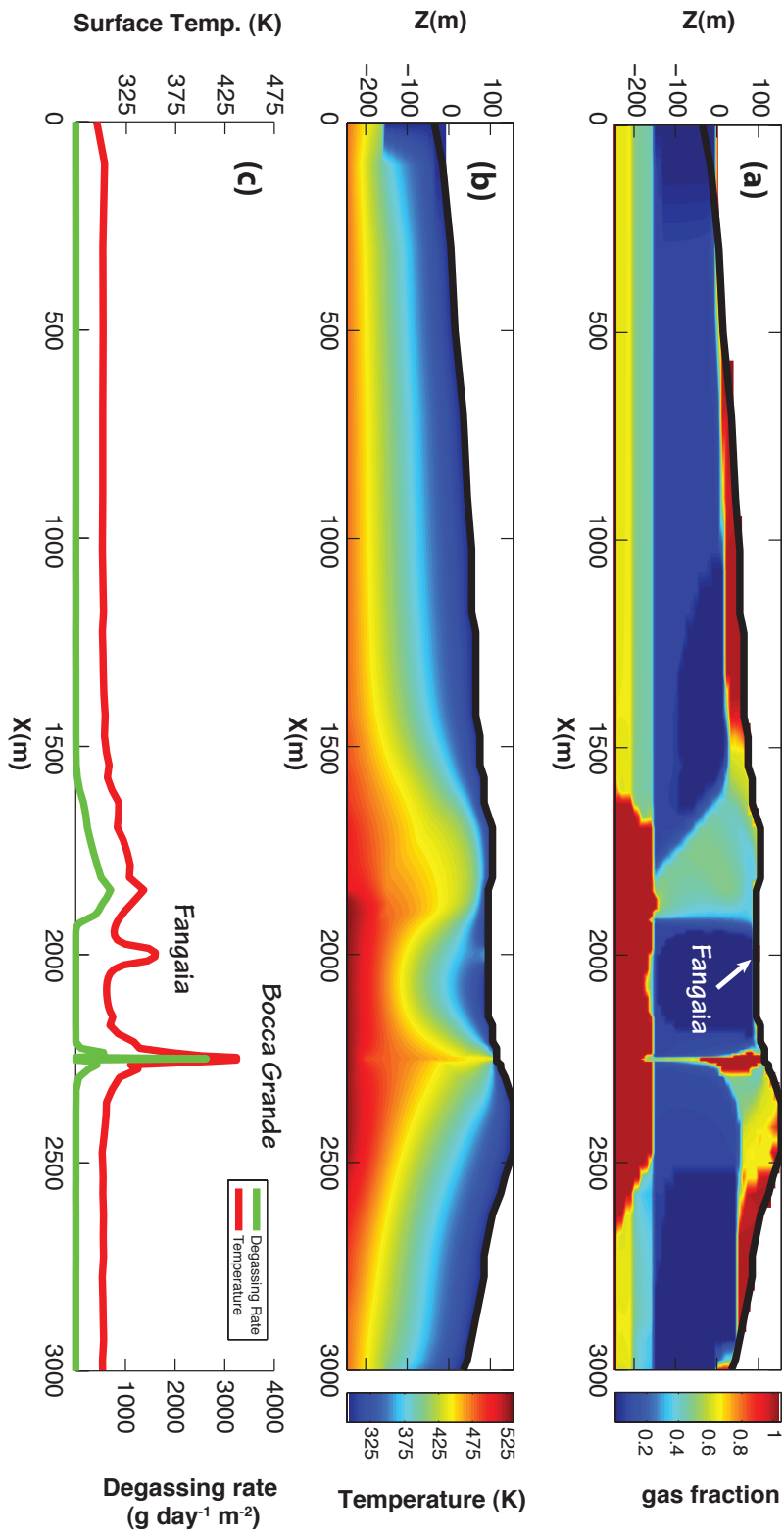
Figure 5.3: (a) Gas saturation. The water table reaches the surface at the crater, and the effects of the two different fractures are well identifiable. (b) Temperature distribution. (c) Temperature at ground surface (red) and degassing rate (green) along the profile.
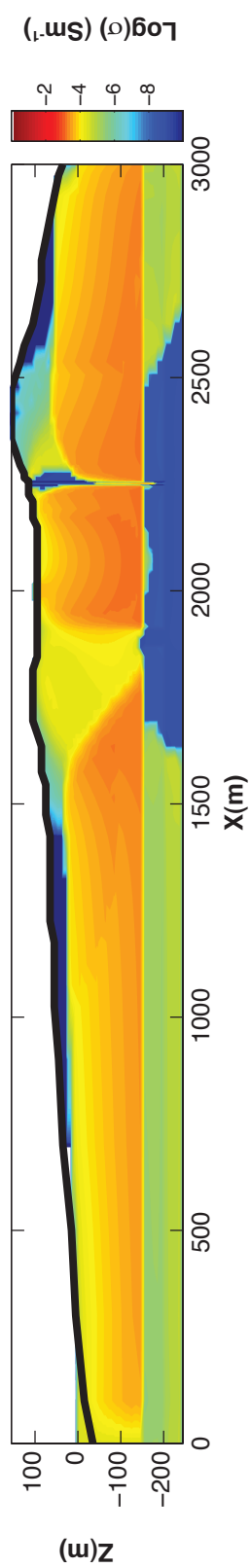
Figure 5.4: Electrical conductivity map (Sm^{-1}) for the unsaturated system. A very conductive body characterizes the domain below the Fangaia mud pool. Red line represents the topography.

5.3.1   Comparison with data

The results here obtained might be compared with electrical resistivity measurements performed at Solfatara crater. Bruno et al. (2007) performed profiles both in SW-NE direction (profiles ER1 and ER2 in Fig. 5.5) and NW-SE direction (profiles ER3 and ER4 in Fig. 5.5). They found a resistive layer "A" standing over a conductive (1-15 Ω m) body "B" (Fig. 5.5). Layer "A" disappears below the mud pools area. They associate the high electrical resistivity in zone "A" to an unsaturated argillitic zone with alteration affected by CO_2 degassing, and the low electrical resistivity zone "B" to the hydrothermal aquifer recharged by natural condensates.

Within conductive zone "B", Bruno et al. (2007) found three higher resistivity areas (Fig. 5.5): (1) a round body "C" (25-50 Ωm), located at the southeastern end of electrical profile ER4 and at the northwestern end of profile ER2, beneath the main fumaroles; (2) an elongated body "D" (15-30 Ωm) imaged along profiles ER4 (Fig. 5.5); and finally (3) a resistive body "E" (20-70 Ωm) visible as a round area along electrical profiles ER1 and ER2, and associated by Bruno et al. (2007) to a NW-SE striking fault cutting Solfatara crater.

The conductivity profile, calculated in this work, is supposed to be in E-W direction, then it is difficult to perform a direct comparison with the data provided by Bruno et al. (2007). However, we can compare the magnitude of the calculated electrical resistivity ($\rho = 1/\sigma$) in the mud pools zone and fumarolic region. Assuming a very high conductivity for the fluid phase ($\sigma_f = 1$ S/m in Eq. 3.2), we calculated and electrical resistivity map near the Fangaia mud pool at shallower depths (up to 80 m below the ground surface). We found values in agreement with measurements performed at Solfatara crater (Fig. 5.6): electrical resistivity lower than 5 Ωm in mud pools zone (comparable with body "B" in figure 5.5); a resistive layer ($\rho > 10$ Ωm) at shallow depth disappearing at mud pool (layer "A" in figure 5.5); values of electrical resistivity in the range 10-20 Ωm where diffuse degassing occurs on the left of Fangaia mud pool (associable with body "C" in profiles ER4 and ER2 in figure 5.5); and finally a resistive body ($\rho > 30$ Ωm) when a fracture is presents, i.e. at Bocca Grande fumarole (comparable with the body "E" in profile ER2 and ER1 in figure 5.5, associated by Bruno et al. (2007) to a striking fault).

5.4   Effects of unrest

Simulations of an unrest period, lasting for 20 months, has been carried out for this new, small scale simulation. In the previous chapter (see Chap, 2, 3, 4), unrest were simulated as a priod during which both the amout and CO_2 content were increased at the fluid source. However, in this small scale simulation we chose to reproduce the source as a gas reservoir over-pressurized with respect to hydrostatic conditions (see red blocks in Fig. 5.2 and Sect. 5.2), hence the unrest period has been simulated changing the properties (p, T, p_{CO_2}) in the gas reservoir. We changed in turn the gas reservoir properties and simulated several different unrest (see Table ??). The unrest phase is followed by a longer quiet period, during which the gas reservoir
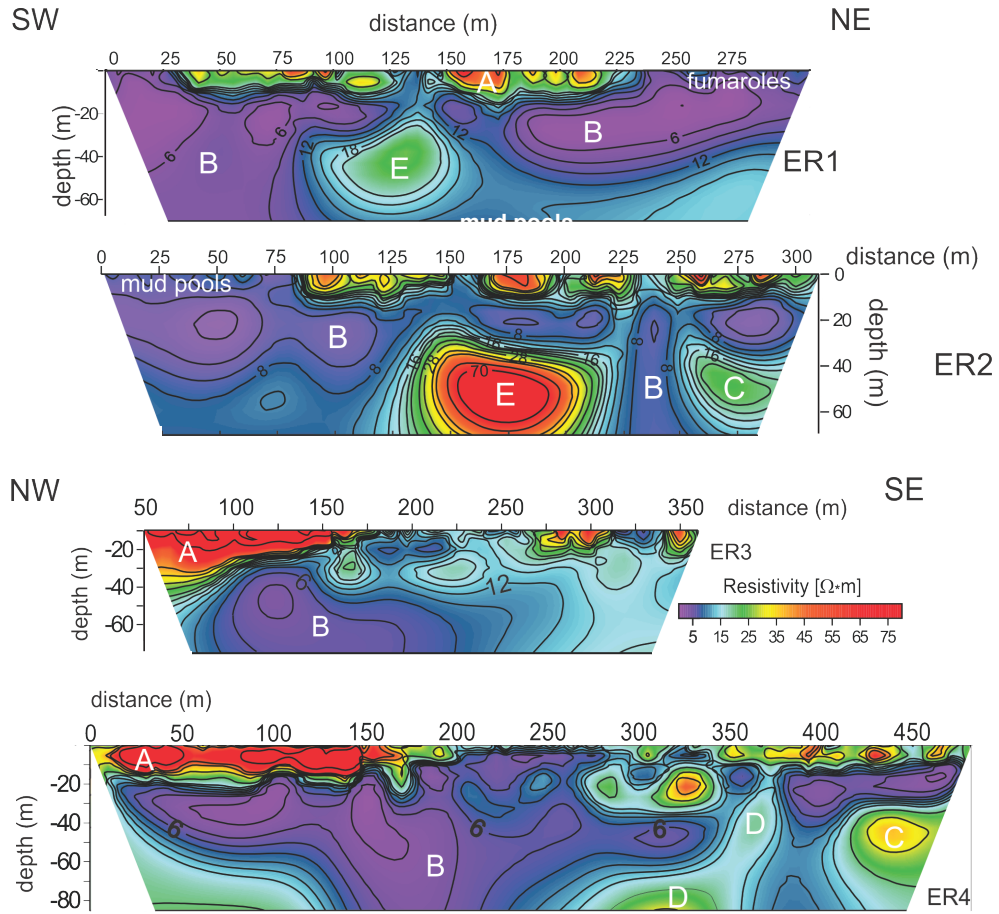
Figure 5.5: Electrical resistivity profiles carried out by Bruno et al., 2007. Geophysical and hydrogeological experiments from a shallow hydrothermal system at Solfatara Volcano, Campi Flegrei, Italy: Response to caldera unrest, J. Geophys. Res., 112, B06201. Copyright [2007] American Geophysical Union. Modified by permission of American Geophysical Union. Profiles ER1 and ER2 are in SW-NE direction. Profiles ER3 and ER4 were carried out in NW-SE. Numerical simulations of the small scale system considered in this work are in E-W direction. For letters see the text.
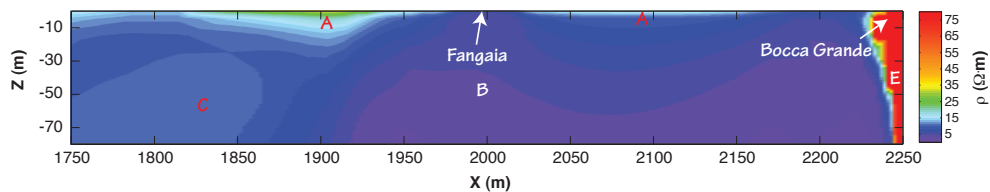
Figure 5.6: Simulated electrical resistivity (Ωm) near the surface at Solfatara crater, assuming $\sigma_f = 1$ Sm^{-1}. Fangaia mud pool and Bocca Grande fumarole are also indicated. For letters see the text.

Table 5.2: Conditions in the gas reservoir for the simulated unrests and steady state conditions.

	p (MPa)	T (°C)	p_{CO_2} (MPa)
Steady state	2.87	260	0.81
Unrest 1 (**U1**)	4	260	2
Unrest 2 (**U2**)	4	300	2
Unrest 3 (**U3**)	6	260	2
Unrest 4 (**U4**)	4	260	3

returns at steady state conditions.

Unrest effects has been examined analyzing ground displacement and gravity changes that occur because of changes in pore pressure, temperature, and fluid density. Again we calculated ground displacement and gravity changes at the crater surface using Eq. 2.3 (Rinaldi et al., 2010) and Eq.2.4 (Todesco and Berrino, 2005) respectively.

Results of the unrest simulations are shown in Fig. 4.7. All the simulations show the same radial pattern of deformation (Fig. 4.7a, b, c, d). Slightly differences in magnitude occur when a higher pore pressure in the gas reservoir is considered (U3). Small peaks develops in the bell-shape curve of vertical displacement, both at the end of the unrest period and at the end of simulation (Fig. 5.7a, b). These peaks can be related to small changes in pressure and temperature at very shallow depth, and are also notifiable in horizontal ground displacement (Fig. 5.7c, d). However, magnitude of the calculated displacement is very low (less than 1 mm), and are in the noise level of the instruments generally used for displacement measurements. Gravity changes also occur (Fig. 5.7e, f), but with a magnitude of the order of few μGal, then again in the noise level.

These results on geophysical observables were partially expected, since we simulated a very small part of the entire hydrothermal system, and highlight the importance of the changes at large deep during the unrest, which produce observables of the same order of magnitude of the observed signals (see Chap. 2, 3, 4).

5.5   Conclusion

Simulation of the shallow, unsaturated region has been performed to provide a better description of electrical conductivity and groundwater beneath the Solfatara crater. Our simulation, thanks to the choice of boundary conditions, reproduces two of the main features of the crater: the Bocca Grande fumarole and the Fangaia mud pool. Using an overpressure as instability in the gas reservoir at the base of the simulated system we were able to represent the water table beneath the Solfatara and the rise of the aquifer up to the ground surface at the mud pool. However, the values we
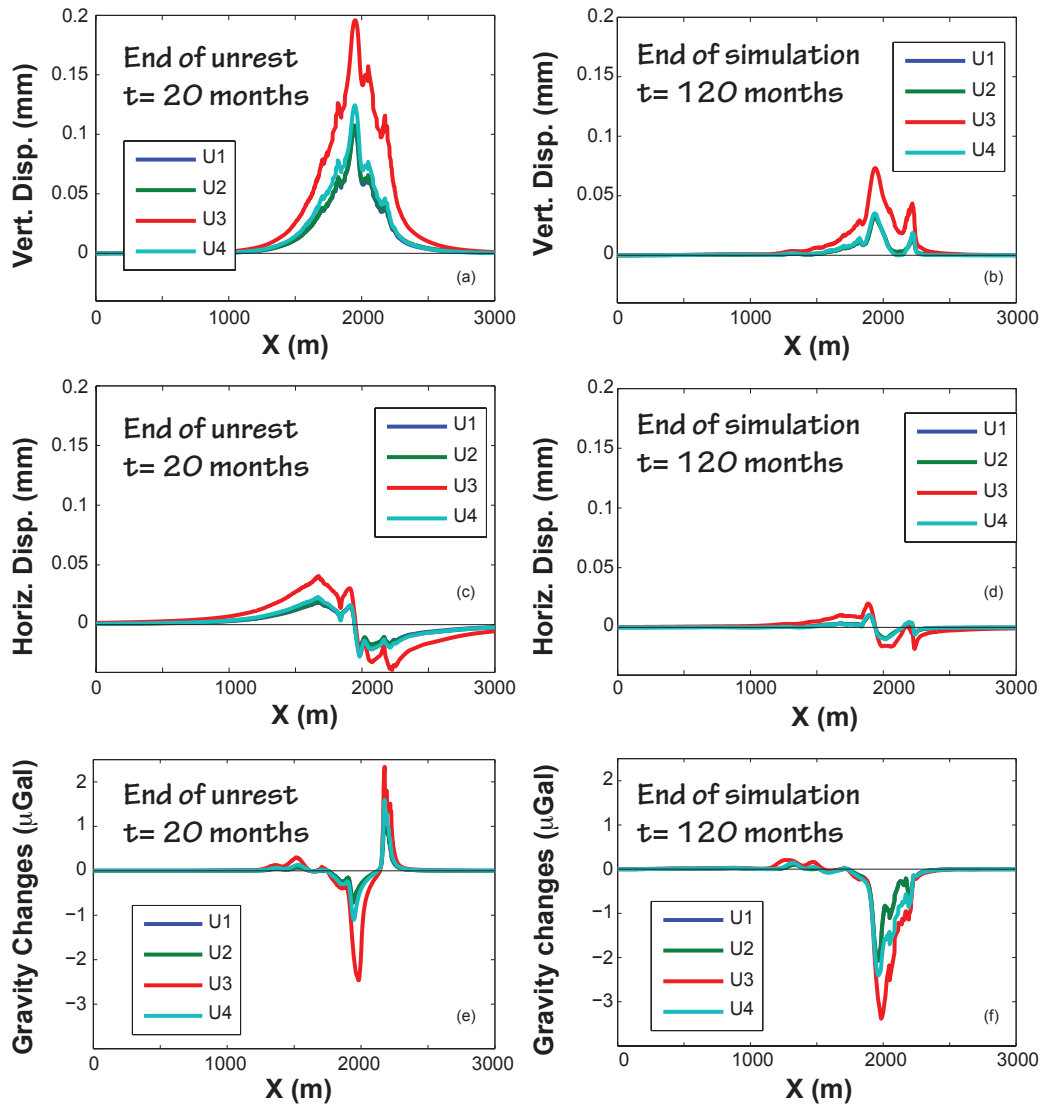
Figure 5.7: Effects of unrest in the small scale domain. (**a,b**) Vertical ground displacement, (**c,d**) Horizontal ground displacement, (**e,f**) Gravity changes.

found for the gas flow in this small scale simulation are underestimated with respect to the data. A new electrical conductivity map was developed, which presents a conductive body below the crater surrounded by two less conductive zones where gases ascend toward the surface. A comparison in magnitude with measurements performed at Solfatara at very shallow depth is possible assuming a high salinity for the fluids circulating in the crater ($\sigma_f = 1$ S/m). Calculated values for the several features of the crater (mud pools, diffuse degassing, and fractures) are in agreement with the data provided by Bruno et al. (2007).

A detailed electrical conductivity map reflect changes at very shallow depth and can provide a better description of the phase distribution, as well as the presence

of shallow structures focusing the phase distribution. In addition, electrical conductivity is a fundamental parameter required to calculate other electrical-related geophysical observables, such as the self-potential: a very common parameter studied in volcanic regions. In the future, numerical simulations of hydrothermal fluid circulation should allow to compute self-potential and its relation with other observables.

Unrest in this small scale simulation does not reproduce remarkable ground displacement and gravity, and the very small effects are mostly related to changes at very shallow depth. These results were partially expected, and highlight ever more the importance of the deep part of the hydrothermal system in affecting the geophysical and geochemical observables.

References

Bianco, F., Del Pezzo, E., Saccorotti, G., Ventura, G., 2004. The role of hydrothermal fluids in triggering the July-August 2000 seismic swarm at Campi Flegrei, Italy: Evidence from seismological and mesostructural data. J. Volcanol. Geotherm. Res. 133, 229–246.

Bruno, P.P.G., Ricciardi, G.P., Petrillo, Z., Di Fiore, V., Troiano, A., Chiodini, G., 2007. Geophysical and hydrogeological experiments from a shallow hydrothermal system at Solfatara Volcano, Campi Flegrei, Italy: Response to caldera unrest. J. Geophys. Res. 112, B06201. doi:10.1029/2006JB004383.

Caliro, S., Moretti, G.C.R., Avino, R., Granieri, D., Russo, M., Fiebig, J., 2007. The origin of the fumaroles of La Solfatara (Campi Flegrei, South Italy). Geochim. Cosmochim. Acta 71, 3040–3055. doi:10.1016/j.gca.2007.04.007.

Chiodini, G., Frondini, F., Cardellini, C., Granieri, D., Marini, L., Ventura, G., 2001. CO_2 degassing and energy realease at Solfatara volcano. J. Geophys. Res. 106(B8), 16213–16221. doi:10.1029/2001JB000246.

Chiodini, G., Todesco, M., Caliro, S., Del Gaudio, C., Macedonio, G., Russo, M., 2003. Magma degassing as a trigger of bradyseismic events: the case of Phlegrean Fields (Italy). Geophys. Res. Lett. 30(8), 1434–1437. doi:10.1029/2002GL016790.

Chiodini, G., Vilardo, G., Augusti, V., Granieri, D., Caliro, S., Minopoli, C., Terranova, C., 2007. Thermal monitoring of hydrothermal activity by permanent infrared automatic stations: Results obtained at Solfatara di Pozzuoli, Campi Flegrei (Italy). J. Geophys. Res. 112, B12206. doi:10.1029/2007JB005140.

Di Vito, M.A., Isaia, R., Orsi, G., Southon, J., de Vita, S., D'Antonio and L. Pappalardo and M. Piochi, M., 1999. Volcanism and deformation since 12,000 years at the Campi Flegrei caldera (Italy). J. Volcanol. Geotherm. Res. 91, 221–246.

Pruess, K., Oldenburg, C.M., Moridis, G., 1999. TOUGH2 user's guide, version 2.0. Paper LBNL-43134. Lawrence Berkeley Natl. Lab., Berkeley, CA, USA.

Revil, A., Cathles III, L.M., Losh, S., Nunn, J.A., 1998. Electrical conductivity in shaly sands with geophysical application. J. Geophys. Res. 103(B10), 23925–23936.

Revil, A., Florsch, N., 2010. Determination of permeability from spectral induced polarization in granular media. Geophys. J. Int. 181, 140–1498. doi:10.1111/j.1365-246X.2010.04573.x.

Rinaldi, A.P., Todesco, M., Bonafede, M., 2010. Hydrothermal instability and ground displacement at the Campi Flegrei caldera. Phys. Earth Planet. Int. 178, 155–161. doi:10.1016/j.pepi.2009.09.005.

Rinaldi, A.P., Todesco, M., Vandemeulebrouck, J., Revil, A., Bonafede, M., 2011. Electrical conductivity, ground displacement, gravity changes, and gas flow at Solfatara crater (Campi Flegrei caldera, Italy): results from numerical modeling. J. Volcanol. Geotherm. Res. Submitted.

Rinaldi, A.P., Vandemeulebrouck, J., Todesco, M., 2009. Modeling of hydrothermal fluid circulation as a tool for volcanic hazard assessment, in: PROCEEDINGS, TOUGH Symposium 2009. Lawrence Berkeley National Laboratory, Berkeley, California, September 14-16, 2009.

Roberts, J.J., 2002. Electrical properties of microporous rock as a function of saturation and temperature. J. App. Phys. 91(3).

Rosi, M., Sbrana, A., 1987. The Phlegrean Fields. Quaderni de La Ricerca Scientifica 114. Consiglio Nazionale delle Ricerche, Roma ,Italy.

Todesco, M., 2008. Hydrothermal fluid circulation and its effects on caldera unrest, in: Gottsmann, J., Marti, J. (Eds.), Caldera Volcanoes: Analysis, Modeling and Response, Dev. Volcanol.. Elsevier, Amsterdam. volume 10, pp. 393–416.

Todesco, M., 2009. Signals from the Campi Flegrei hydrothermal system: Role of a "magmatic" source of fluids. J. Geophys. Res. 114, B05201. doi:10.1029/2008JB006134.

Todesco, M., Berrino, G., 2005. Modelling hydrothermal fluid circulation and gravity signals at the Phlegrean Fields caldera. Earth Plan. Sci. Lett. 240, 328–338. doi:10.1016/j.epsl.2005.09.016.

Todesco, M., Rinaldi, A.P., Bonafede, M., 2010. Modeling of unrest signals in heterogeneous hydrothermal systems. J. Geophys. Res. 115, B09213. doi:10.1029/2010JB007474.

Todesco, M., Rutqvist, J., Chiodini, G., Pruess, K., Oldenburg, C.M., 2004. Modeling of recent volcanic episodes at Phlegrean Fields (Italy): geochemical variations and ground deformation. Geothermics 33, 531–547. doi:10.1016/j.geothermics.2003.08.014.

Vaughan, P.J., Udell, K.S., Wilt, M.J., 1993. The effects of steam injection on the electrical conductivity of an uncosolidated sand saturated with a salt solution. J. Geophys. Res. 98(B1), 509–518.

Effects of atmospheric conditions on soil diffuse degassing

Contents

6.1 Introduction

Secondary manifestations of volcanism in the Azores archipelago (Fig. 6.1) include low temperature fumaroles (maximum temperature around 100 °C), hot springs, CO$_2$ cold springs and several diffuse degassing areas . Continuous monitoring of hydrothermal soil CO$_2$ flux started at Furnas volcano (S. Miguel island) in October 2002 with the installation of a permanent gas station coupled with several meteorological sensors (barometric pressure, air temperature, wind speed and direction, air relative humidity, rainfall, soil temperature and soil water content). Daily and seasonal cycles have been observed in the time series of soil CO$_2$ flux. From all the monitored variables, air temperature and barometric pressure are the ones that best correlate with the soil CO$_2$ flux cycles. Air temperature and soil CO$_2$ flux are inversely correlated: the higher soil CO$_2$ flux values are registered early in the morning (lower air temperature) and lower soil CO$_2$ flux values in the afternoon (higher air temperature). Barometric pressure shows higher correlation with the CO$_2$ cycles during winter months and in bad weather conditions. From these correlations become evident that CO$_2$ flux released in hydrothermal areas behaves
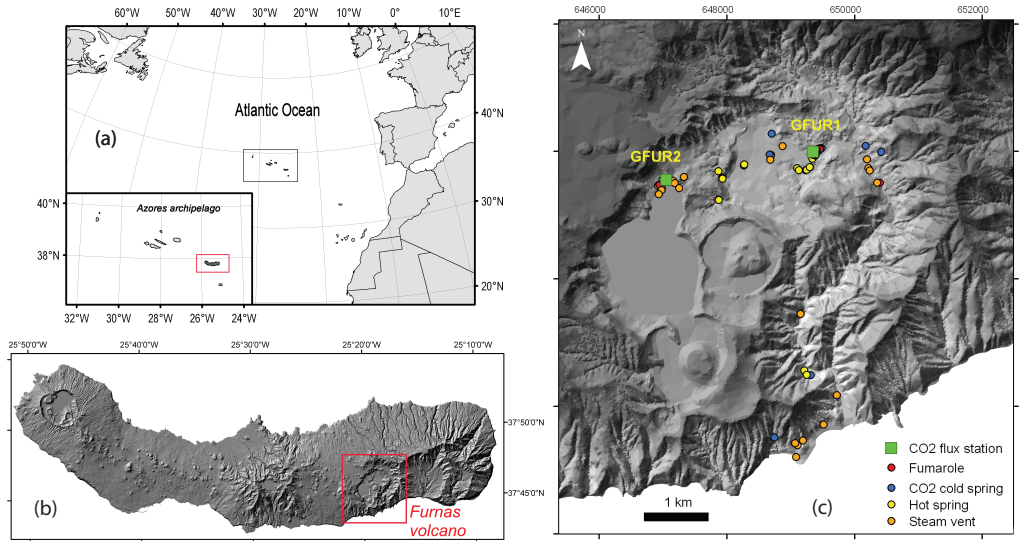
Figure 6.1: **(a)** Azores archipelago location highlighting S. Miguel Island; **(b)** Digital Elevation Model of the S. Miguel Island; (**c**) Hydrothermal manifestations and location of the permanent soil CO_2 stations at Furnas volcano.

oppositely of areas where the only source of CO_2 is biogenic, since in biogenic areas CO_2 production is dependent on the temperature and the CO_2 oscillations are positively correlated with the air/soil temperature changes (Witkamp, 1969; Bajracharya et al., 2000; Nakadai et al., 2002). In fact, in the case of the data acquired by the Furnas volcano permanent stations, the magnitude of the diurnal variations on the soil CO_2 flux (usually from 50 to 100 g m^{-2} d^{-1}) exclude the possibility that the variations of CO_2 are of biogenic origin. Works published in biogenic environments (e.g. Nakadai et al., 2002) refer daily amplitudes for CO_2 flux of about 5 - 6 g m^{-2} d^{-1}, which is low when compared with data showed in this study, clearly dominated by volcanic-hydrothermal environment. Very few papers were found in the literature that analyzed diurnal variations for the soil CO_2 flux in hydrothermal environments. Granieri et al. (2003) identified 24 h cycle in CO_2 fluxes from Solfatara volcano between 1998-2002 and Padrón et al. (2008) recognized diurnal and semidiurnal fluctuations in the gas flux acquired during 2004 in a station located at El Hierro (Canary Islands).

In order to understand the influence of atmospheric and soil conditions on the gas release, several simulations with TOUGH2 geothermal simulator were performed. We used the TOUGH2/EOS2 module to describe a CO_2 in gas phase fluid. Using a 1D model, a parametric study was performed to understand the physical mechanisms producing the observed variations. In this simplified model, only the air temperature and barometric pressure were changed. Numerical results, in agreement with the observed data, show that the CO_2 fluxes are strongly dependent on domain permeability, reservoir pressure and temperature and pressure changes applied at the surface.

Figure 6.2: **(a)** Monitoring site showing the accumulation chamber in up and down positions; **(b)** Shelter of GFUR2 with the solar panel. Several meteorological sensors are coupled to the station.

6.2 Furnas permanent soil CO$_2$ flux stations

Two permanent soil CO$_2$ flux stations are presently installed inside Furnas volcano caldera (S. Miguel Island, Azores archipelago) (Fig. 6.1). *GFUR1* station was running between October 2001 and July 2006 and it was placed in a garden of the Furnas thermal baths, close to Furnas village fumarolic field. Values measured of CO$_2$ flux were $\sim$260 g m^{-2} d^{-1}. The station was reinstalled (and renamed as *GFUR3*) in January 2008 closer to Furnas village main fumaroles, in a thermally anomalous zone (average soil temperature is 38 °C at 30 cm depth) with a soil CO$_2$ flux $\sim$650 g m^{-2} d^{-1}. A soil CO$_2$ flux station (named *GFUR2*) was also installed inside Furnas caldera in the vicinity of Furnas Lake fumarolic ground in October 2004, where soil CO$_2$ flux values around 350 g m^{-2} d^{-1} were measured.

The permanent flux stations perform measurements based on the accumulation chamber method (Chiodini et al., 1998) (Fig. 6.2a). Every hour a chamber is lowered on the ground and the gas released at the ground surface is pumped into an infrared gas analyzer (IRGA).

The soil CO$_2$ flux value is computed as the linear best fit of the flux curve during a predefined period of time. Measurements have a reproducibility within 10% for the CO$_2$ range between 10 and 20000 g m^{-2} d^{-1} (Chiodini et al., 1998). The automatic stations have also coupled meteorological sensors (Fig. 6.2b) and acquire simultaneously with the gas flux measurements information related to the barometric

pressure, air temperature, air relative humidity, wind speed and direction, rainfall, soil water content and soil temperature.

6.3 Spectral analysis applied to CO_2 flux data

Seasonal periodicities and diurnal variations are observed on the CO_2 time series concomitant with the periodicity observed in some meteorological variables (e.g. air temperature and air relative humidity). Soil CO_2 flux is inversely correlated wind speed and air temperature, and

6.3.1 GFUR1 station

In order to evaluate the existence of seasonal variations, spectra of winter and summer months were calculated. Daily cycles are observed in the soil CO_2 flux time series (Figs. 6.3 and 6.4). Two dominant spectral peaks are observed for the 24 h (S1) and for the 12 h components (S2), even if some lower energy peaks (3, 4 and 5 cycles per day, cpd) also appear in spectrum of Fig. 6.3.

Air temperature, air relative humidity and wind speed spectra also show daily fluctuations, usually with S1 > S2. Similarly diurnal variations are observed for the barometric pressure, however S2 > S1.

In order to understand the physical processes that rule soil diffuse degassing cyclic behavior transfer function with 256 block size was applied between each of the meteorological variables (that show daily cycles) and soil CO_2 flux (Tab. 6.1 and 6.2). The correlation coefficient between the monitored variables and the time delays between them were calculated, for the S1 and S2 peaks. Only correlation coefficients higher than 0.5 were included in the tables. For the winter period (Tab. 6.1) the correlations between the soil CO_2 flux and the barometric pressure are the most significant ($r>0.8$ for 2 cpd), with time delays of about 8 and 5 h for S1 and S2 peaks, respectively. During the summer period (Tab. 6.2), soil CO_2 flux show a delay of about 10-11 h with respect to air temperature, relatively to the S1 peak. Air relative humidity shows an insignificant delay with respect to the soil CO_2 flux for 1 cpd. These observations are in agreement with higher soil CO_2 fluxes registerd

Table 6.1: Correlation and time delay between each of the meteorological variables and the soil CO_2 flux at GFUR1 for the winter months (n.a. - not applicable).

	Corr. (r)		Delay (h)	
	1 cpd	2 cpd	1 cpd	2 cpd
Humidity	<0.5	0.584	n.a.	∼5 h
Temp.	<0.5	0.745	n.a.	∼2 h
Pressure	0.645	0.862	∼8 h	∼5 h
Soil Temp.	<0.5	<0.5	n.a	n.a

Table 6.2: Correlation and time delay between each of the meteorological variables and the soil CO_2 flux at GFUR1 for the summer period (n.a. - not applicable).

	Corr. (r)		Delay (h)	
	1 cpd	2 cpd	1 cpd	2 cpd
Humidity	0.569	0.696	1-2 h	∼4 h
Temp.	0.764	0.791	10 h	∼3 h
Pressure	0.855	0.879	∼9 h	∼6 h
Soil Temp.	0.691	<0.5	0 h	n.a.
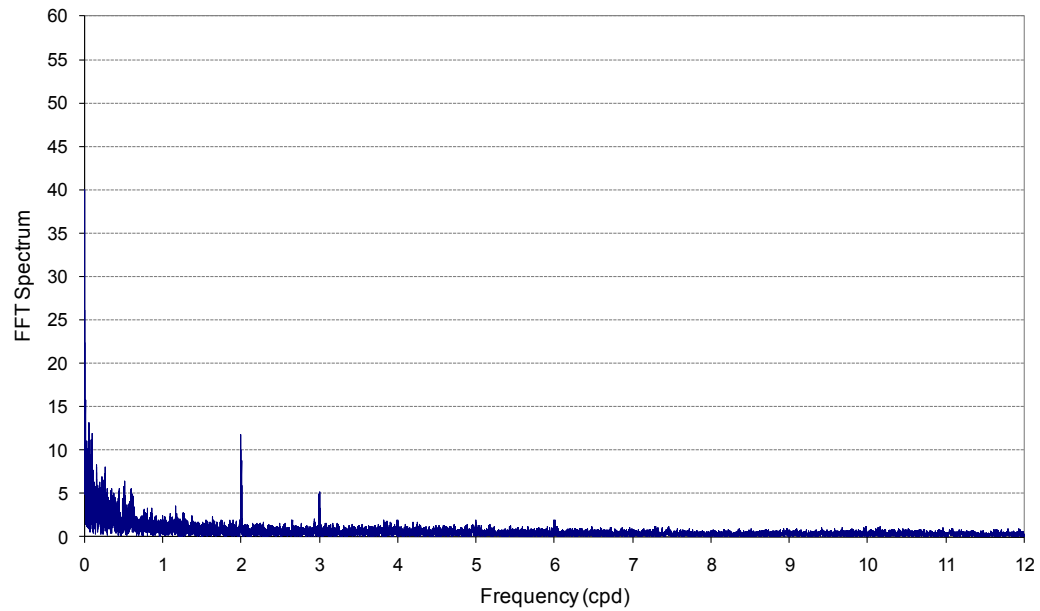
Figure 6.3: Amplitude spectrum of the soil CO$_2$ flux data at GFUR1 during winter months (from November to April).
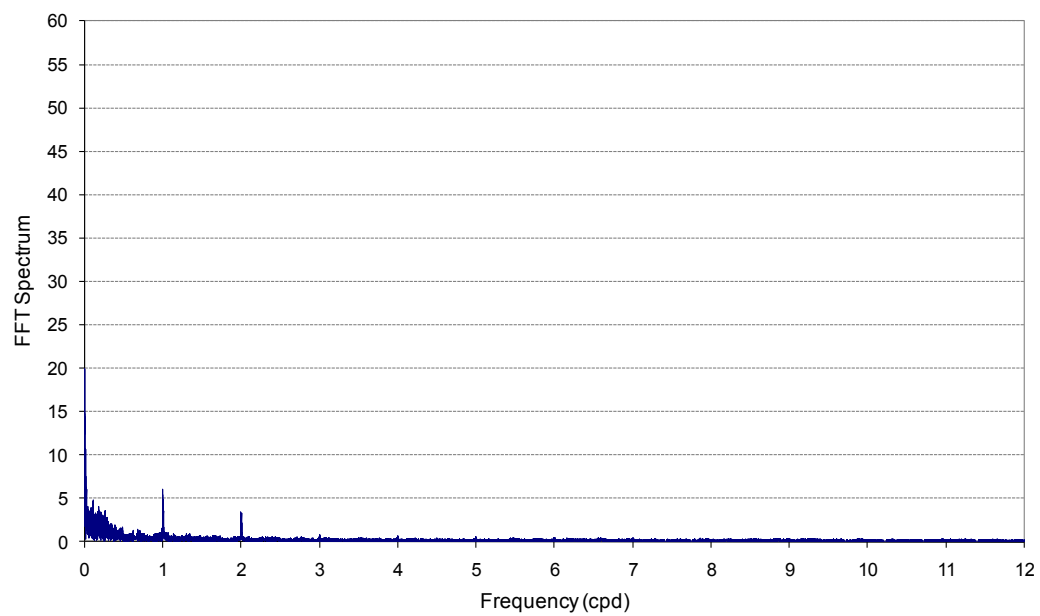
Figure 6.4: Amplitude spectrum of the soil CO$_2$ flux data at GFUR1 during summer months (from May to September).

in the early morning and lower values in the afternoon.

6.3.2　GFUR2 station

Several technical problems affected GFUR2 station during the monitored period and, for this reason, data were split in four intervals to calculate the spectra:

Period 1: 01-01-2005 to 09-02-2007

Period 2: 03-05-2007 to 20-10-2007

Period 3: 01-03-2008 to 09-01-2009

Period 4: 14-04-2009 to 30-06-2009

Daily cycles (1 and 2 cpd) are observed in the soil CO_2 flux time series, with S1 significantly stronger than S2. Air temperature, air relative humidity and wind speed recorded at GFUR2 site show as well daily fluctuations.

Spectra of winter and summer months were calculated in order to evaluate the existence of seasonal variations on the soil CO_2 flux daily cycles. Diurnal variations are lower during winter months (where only 1 cpd peak emerges) (Fig. 6.5) and larger during summer period (with both 1 and 2 cpd identified) (Fig. 6.6).

Transfer functions calculated for winter and summer months are shown in Tables 6.3 and 6.4. The highest correlations appear for summer periods with wind speed, air temperature and air relative humidity showing the best correlations with soil CO_2 flux for the 24 h component. Relatively to the 12h component, air temperature and wind speed are the meteorological variables that correlate best with the CO_2 flux. For what concerns the delay between variables, air relative humidity shows no delay with the soil CO_2 flux for 1 cpd (Tables 6.3 and 6.4). Air temperature and wind speed show 10 - 11 h delay with CO_2 flux, similarly to the observed at GFUR1 site. This means that also at GFUR2 monitoring site higher soil CO_2 fluxes are registered in the early morning and lower values in the afternoon. Barometric pressure shows low correlation with soil CO_2 flux, when compared with GFUR1 station.

Table 6.3: Correlation and time delay between each of the meteorological variables and the soil CO_2 flux at GFUR2 for the winter months (n.a. - not applicable).

	Corr. (r)		Delay (h)	
	1 cpd	2 cpd	1 cpd	2 cpd
Humidity	0.592	<0.5	0 h	n.a.
Temp.	0.541	<0.5	12 h	n.a.
Pressure	<0.5	<0.5	n.a.	n.a.
Wind	0.559	<0.5	11 h	n.a

Table 6.4: Correlation and time delay between each of the meteorological variables and the soil CO_2 flux at GFUR2 for the summer period (n.a. - not applicable).
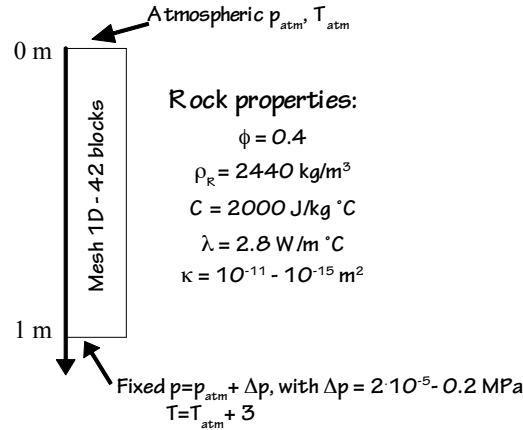
	Corr. (r)		Delay (h)	
	1 cpd	2 cpd	1 cpd	2 cpd
Humidity	0.880	0.686	0 h	0 h
Temp.	0.890	0.721	11 h	~6 h
Pressure	0.533	0.683	~6 h	~4 h
Wind	0.904	0.727	10 h	~6 h
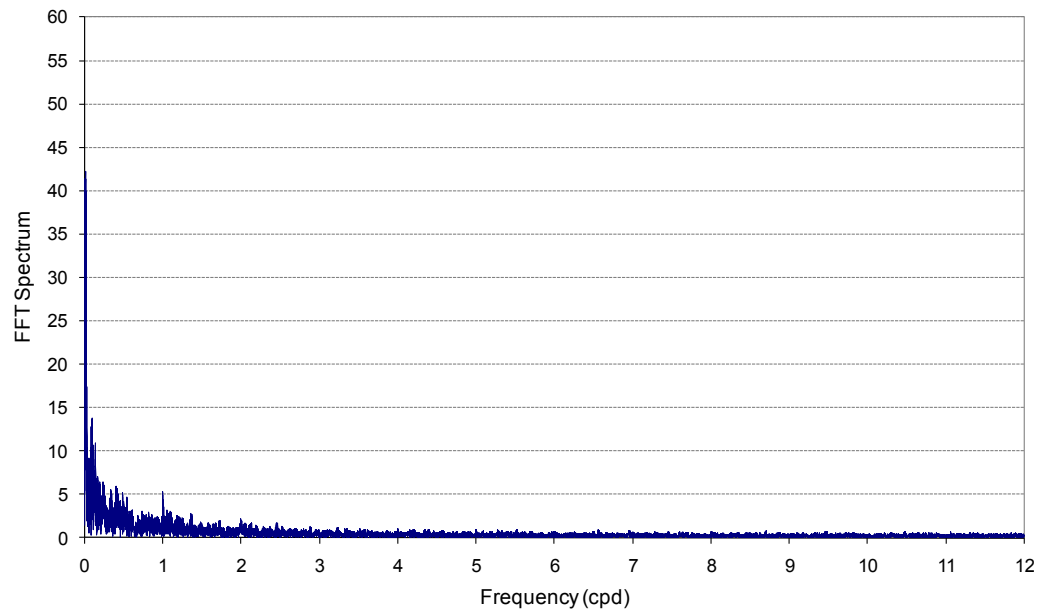
Figure 6.5: Amplitude spectrum of the soil CO$_2$ flux data at GFUR2 during winter months (from November to April).
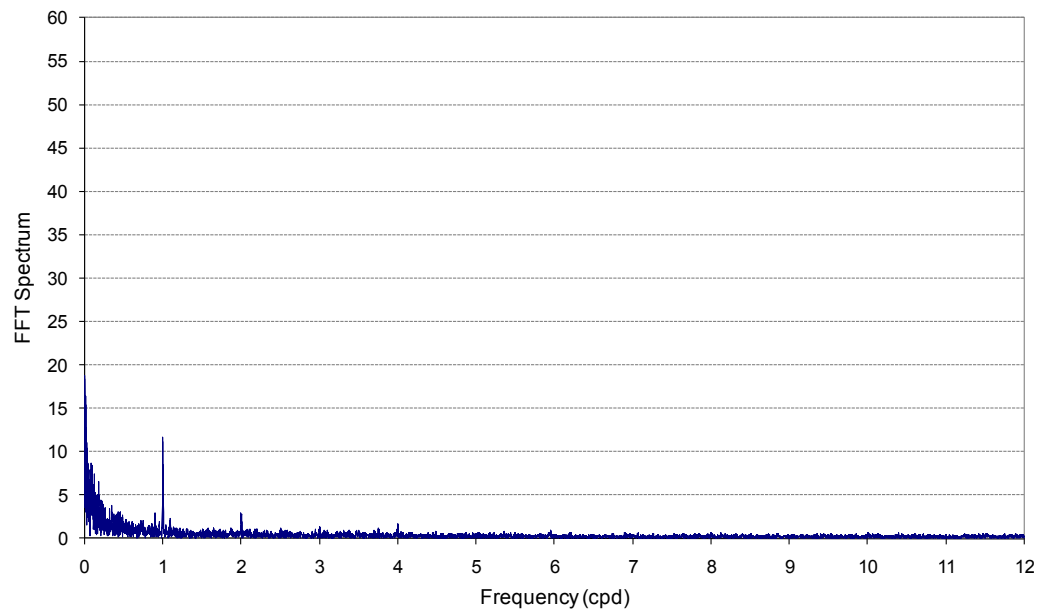
Figure 6.6: Amplitude spectrum of the soil CO$_2$ flux data at GFUR2 during summer months (from May to September).

Figure 6.7: Numerical 1D domain and rock properties. ϕ is the porosity, ρ_R is the rock density, C is the specific heat, and λ is the thermal conductivity. These properties were kept constant during all the simulations. κ is the range of variation for the rock permeability. Atmospheric pressure and temperature depend on the considered simulation. When a temperature change only is applied to the ground surface $p_{atm} = 0.1 MPa$ and $T_{atm} = T_0$ where T_0=17.5 °C is the initial value of the applied temperature time series. When a pressure change only is applied to the ground surface T_{atm}=20 °C and $p_{atm} = p_0$ where p_0=0.09927 MPa is the initial value of the applied pressure time series. In case of application of both temperature and pressure time series at surface $T_{atm} = T_0$ and $p_{atm} = p_0$. Δp at the bottom is the range of variation for the reservoir overpressure.

6.4   Numerical simulation

In order to compute the CO_2 flux changes that arise from variations in atmospheric pressure and temperature conditions and to understand the role played by the rock permeability and by the reservoir overpressure on observed delay, parameter studies of fluid circulation were carried out with the TOUGH2/EOS2 simulator (see Chap. 1 and Pruess et al., 1999). Fig. 6.7 show the 1D domain, 1 m deep, with the rock properties. The domain was discretized into 42 elements of 2.5 cm. The bottom (reservoir) is open to fluid flow, and has a fixed temperature, 3 °C/m above the atmospheric temperature, and fixed reservoir pressure, which is higher than atmospheric pressure. The value of reservoir overpressure depends on the considered simulation. The top boundary is open and at fixed atmospheric pressure and temperature, which in turn or both change following the observed temporal variation. Before applying top boundary changes, steady state conditions were reached after a long simulation, which produced a linear pressure and temperature gradient in the medium. We chose to simulate a medium fully saturated with CO_2 in gas phase.

We simulated a two days variation of the air temperature and barometric pressure, modifying the boundary condition at the top of the domain. The changes were chosen from data collected at the GFUR2 station (Fig. 6.8). Here we show only variations during two days in the summer period.
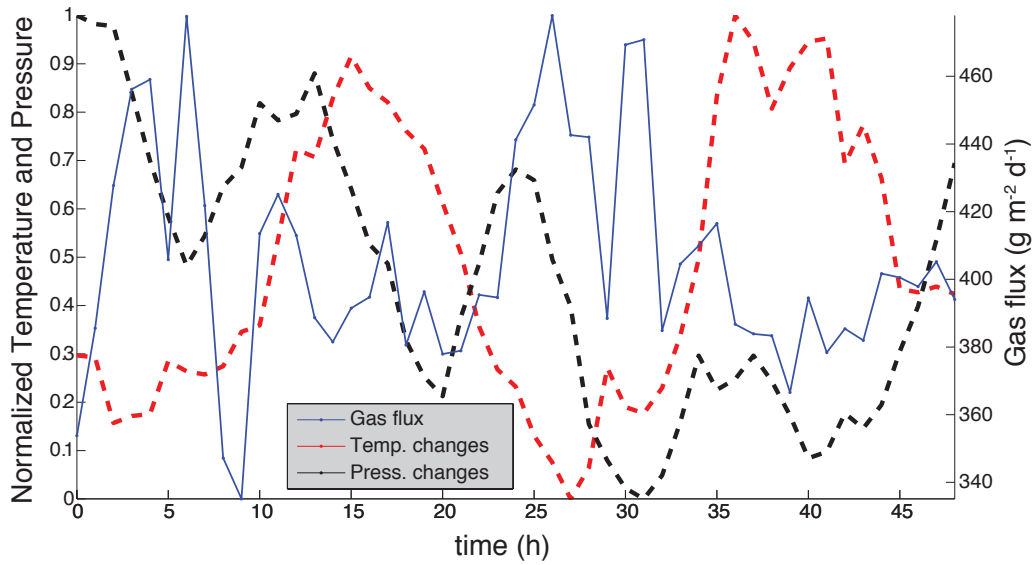
Figure 6.8: Applied atmospheric air temperature (red) and barometric pressure (black) variations. Blue line represents the measured CO_2 flux. Temperature and pressure are normalized in this figure.

6.4.1 Effects of domain permeability

A parameter study has been carried out changing the permeability of the medium in the range $\kappa=10^{-11} - 10^{-15}$ m^2. We applied in turn the temperature and the pressure changes at the surface, in order to understand the effects which may be produced by a single variable. Then temperature and pressure functions have been applied simultaneously to analyze the coupled effects as well.

In order to analyze the effects of the permeability when a temperature variation is applied to the top boundary, we set a steady state simulation with fixed atmospheric pressure (0.1 MPa), and a reservoir overpressure $\Delta p = 0.07$ MPa. After reaching a steady state for each considered permeability, we started the two days simulation. Results for high, medium and low permeability are shown in Fig. 6.9a, c, and e, respectively. The calculated CO_2 flux changes when a perturbation is applied to the surface, as we expected from measurements performed at Furnas caldera. However the calculated CO_2 flux has a temporal trend which depends on permeability. In fact, for high permeability, temperature and CO_2 flux trend are inversely correlated, which means that we observe the maximum degassing when the temperature is at minimum value, i.e. the observed delay is ~ 12 h (Fig. 6.9a). Time delay is defined as the time between a minimum in temperature time series and a minimum in CO_2 flux time series. These changes observed at the surface propagate quickly through the system, then at the bottom of the domain we observe exactly the same variation in CO_2 flux as observed at the surface (Fig. 6.9b). Lowering the permeability by two orders of magnitude, will increase the time delay up to $\sim$16 h between the two
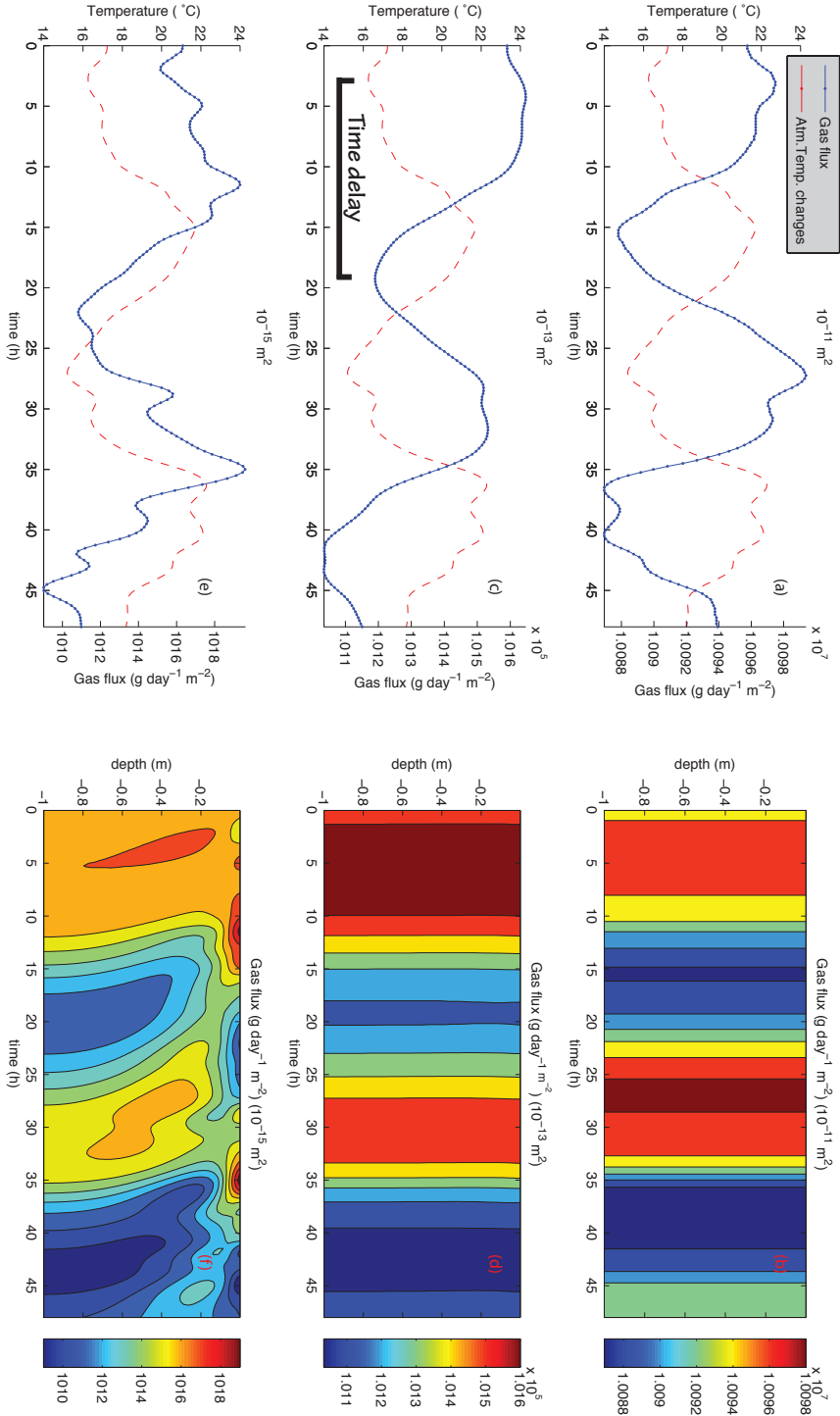
Figure 6.9: (**a,c,e**) Simulated temporal CO$_2$ flux changes (blue line) at the surface due to the application of a temperature variation (red line) for permeability 10^{-11}, 10^{-13}, and 10^{-15} m^2 respectively. (**b,d,f**) CO$_2$ flux in time and depth for permeability 10^{-11}, 10^{-13}, and 10^{-15} m^2 respectively. Time delay (the time between minimum temperature and CO$_2$ flux) is indicated for fig. (c).
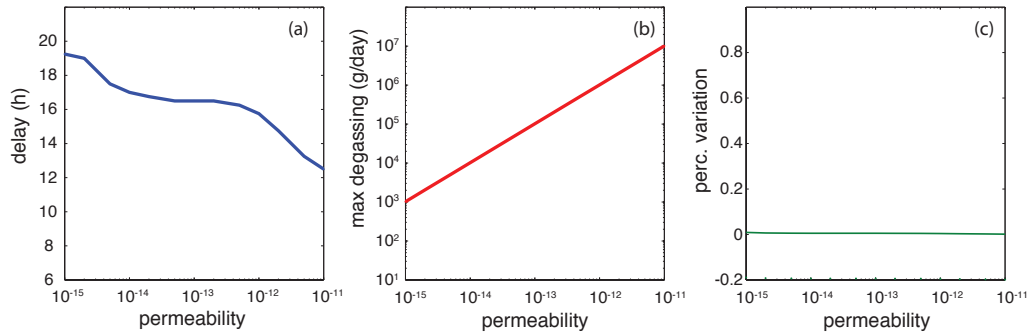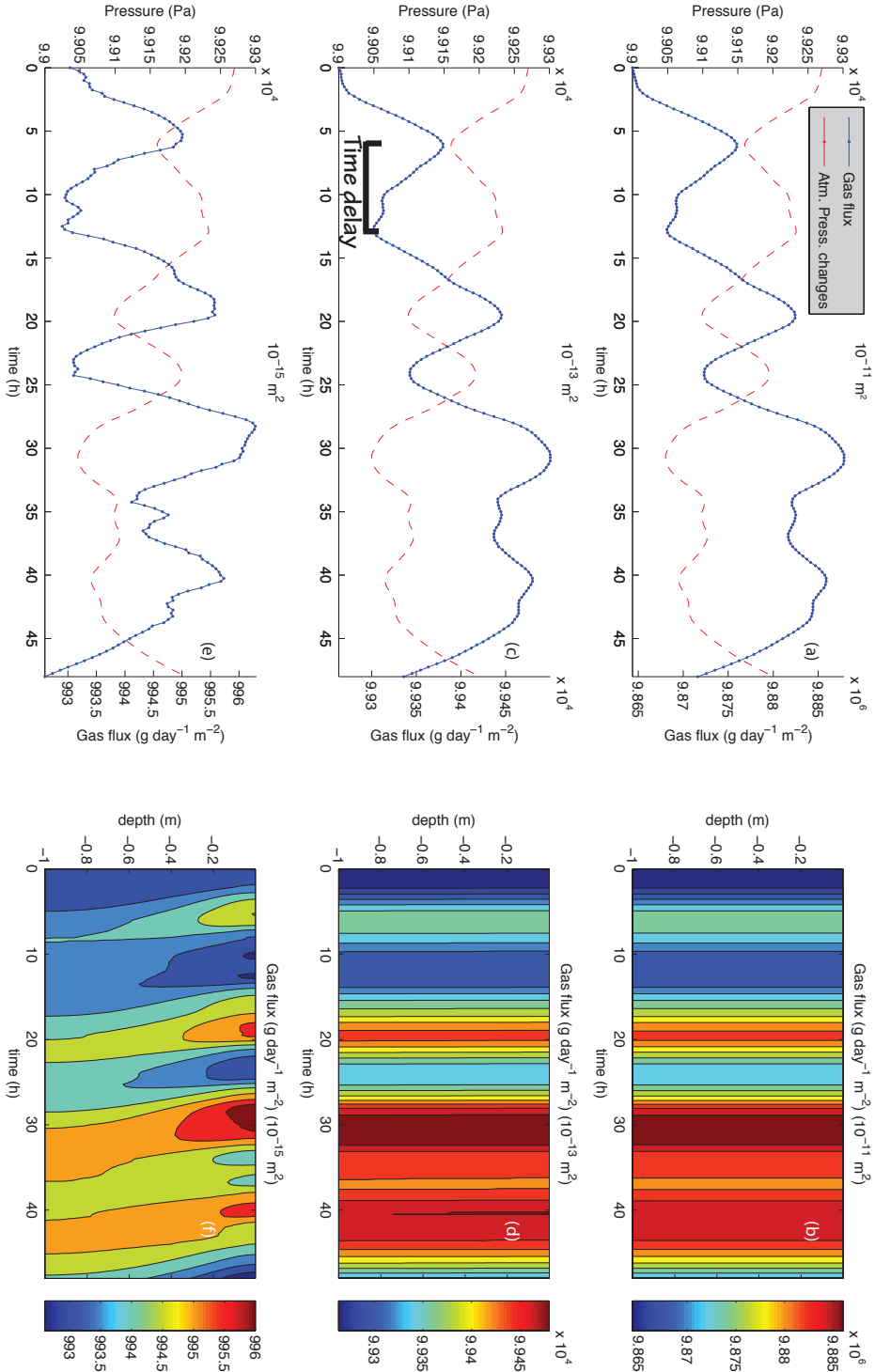
Figure 6.10: (**a**) Time delay with respect to the temperature time series as a function of permeability, due to the temperature variation only. (**b**) Maximum degassing as a function of permeability. (**c**) Percentage variation as a function of permeability. Percentage variation is calculated as the ratio between the maximum amplitude of changes and the maximum degassing.

minima of CO_2 flux and temperature (Fig. 6.9c,d). For low permeability (10^{-15} m^2) the time delay is very high ($\sim$20 h) and several small peaks are present in the CO_2 flux temporal trend (Fig. 6.9e). This effects is due to the slow propagation of the fluid in the system. Fig. 6.9f shows as CO_2 flux at the bottom behave as in the case of higher permeability, however, fluids slowly propagate, thus we observe a different behavior, i.e. a higher time delay, at very shallow depth.

Time delay as a function of permeability is shown in Fig. 6.10a. For low permeability the time delay is high due to very shallow depth effects, in the medium permeability range (10^{-14} – 10^{-12} m^2) delay is almost constant ($\sim$16 h), and for high permeability the time delay drops to a value of $\sim$12 h, i.e. similar to the observed delay at Furnas. However, simulated maximum degassing is very high with respect the measured values, and it ranges from 10^3 g/day for very low permeability to a maximum of 10^7 g/day in case of high permeability (Fig. 6.10b). Moreover, the temperature function produces very small percentage variations in CO_2 flux (Fig. 6.10c). Percentage variation are calculated as a ration between the maximum amplitude of variation and the maximum degassing.

Keeping constant the overpressure in the gas reservoir and the temperature at the top boundary (20 °C), in a second set of simulations we applied a barometric pressure variation at the surface (see Fig. 6.8, black line). Results are shown in Fig. 6.11. Permeability parameter study does not show any changes in time delay (Fig. 6.11a,c,d), although very shallow depth effects may be present for very low permeability (Fig. 6.11f).

Time delay, here calculated as the delay between the simulated CO_2 flux minimum and the minimum in the applied pressure variation, does not change as a function of the permeability (Fig. 6.12a) and remains constant at $\sim$6 h. Also in this case, as shown in Fig. 6.12b and c, simulated maximum degassing is very high and the percentage variation in CO_2 flux is very small (less than 1 %).
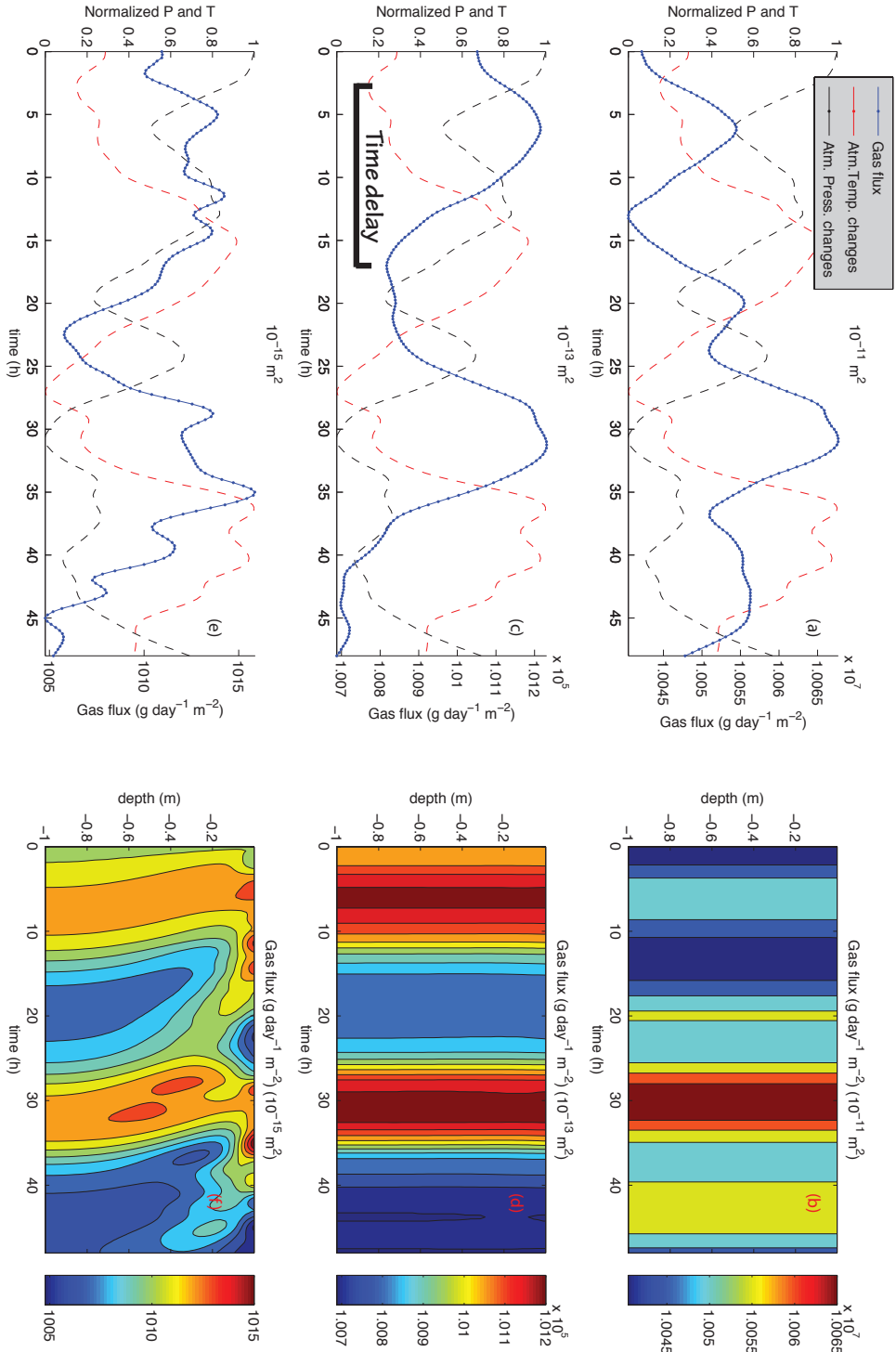
Figure 6.11: Simulated temporal CO_2 flux changes (blue line) at the surface due to the application of a pressure variation (red line) for permeability 10^{-11}, 10^{-13}, and 10^{-15} m^2 respectively. **(b,d,f)** CO_2 flux in time and depth for permeability 10^{-11}, 10^{-13}, and 10^{-15} m^2 respectively.Time delay (the time between minimum pressure and CO_2 flux) is indicated for fig. (c).
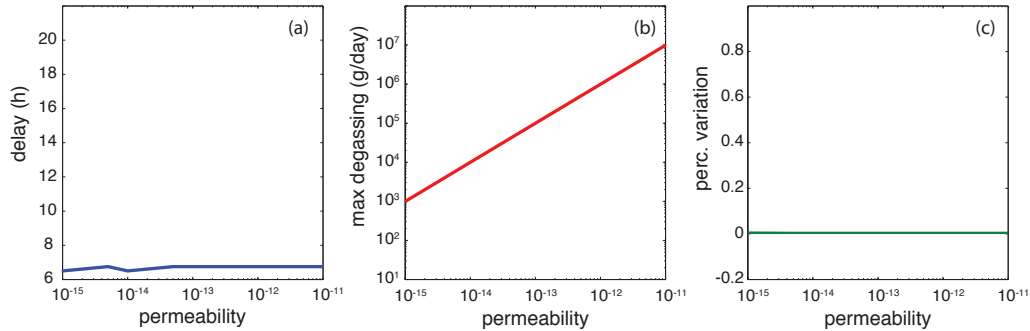
Figure 6.12: (**a**) Time delay with respect to the pressure time series as a function of permeability, due to the pressure variation only. (**b**) Maximum degassing as a function of permeability. (**c**) Percentage variation as a function of permeability. Percentage variation is calculated as the ratio between the maximum amplitude of changes and the maximum degassing.

In the last set of simulations, both temperature and pressure variations have been applied simultaneously, keeping a constant overpressure in the gas reservoir (0.07 MPa). The applied pressure and temperature changes at the surface does not always produce the same range of variation. For high permeability pressure, effects are predominant (Fig. 6.13a), i. e. the simulated CO_2 flux temporal trend is very similar to the one due to pressure variation only (Fig. 6.10). Lowering the permeability, the effects due to the applied temperature become larger than pressure effects (Fig. 6.13c), i.e. the resulting CO_2 flux is very similar to the one produced when a temperature variation only is applied. When the permeability is very low, CO_2 flux temporal trend is influenced by very shallow depth effects, and is then impossible to recognize the effects of a single variable changes (Fig. 6.13e and f).

The time delay of the CO_2 flux with respect the temperature time series as a function of the permeability is shown in Fig. 6.14a. The coupled effects of temperature and pressure applied results, for high and medium permeabilities, in a time delay lower than values obtained after the application of temperature changes at surface (Fig. 6.11), although the temporal trend is similar. The minimum delay ($\sim$10 h) occurs for a permeability of 10^{-11} m^2, then time delay increases to a constant value of $\sim$14 h for permeability in the range $5{\cdot}10^{-14} - 10^{-12}$ m^2. For permeability lower than $5{\cdot}10^{-14}$ m^2, very shallow depth effects occur, and then the time delay changes up to values greater than 20 h. Applying both the temperature and pressure perturbation at surface we observe a very high maximum degassing (Fig. 6.14b), and the simulated percentage variation is still less than 1% (Fig. 6.14c).

Figure 6.13: Simulated temporal CO_2 flux changes (blue line) at the surface due to the application of both pressure (black line) and temperature variation (red line) for permeability 10^{-11}, 10^{-13}, and 10^{-15} m^2 respectively. **(b,d,f)** CO_2 changes in time and depth for permeability 10^{-11}, 10^{-13}, and 10^{-15} m^2 respectively. Time delay (the time between minimum temperature and CO_2 flux) is indicated for fig. (c).
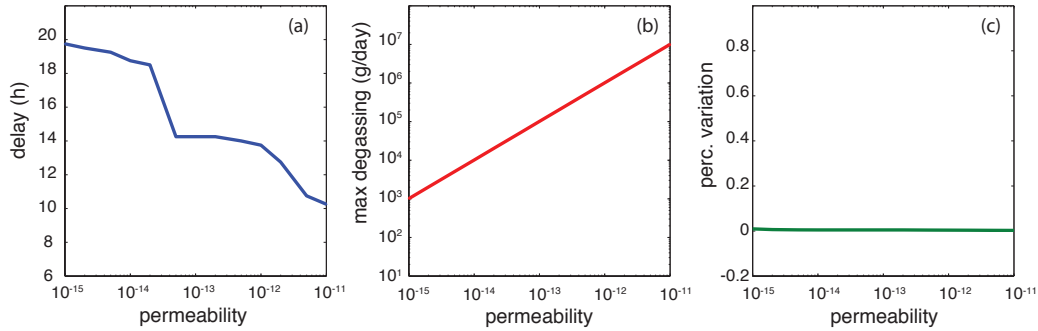
Figure 6.14: (**a**) Time delay with respect to the temperature time series as a function of permeability due to the application of both temperature and pressure variation. (**b**) Maximum degassing as a function of permeability. (**c**) Percentage variation as a function of permeability. Percentage variation is calculated as the ratio between the maximum amplitude of changes and the maximum degassing.

6.4.2   Effects of reservoir overpressure

In this section we considered a constant permeability (10^{-13} m^2) and carried out parameter studies changing the overpressure in the gas reservoir in the range $2 \cdot 10^{-5}$ MPa – 0.2 MPa. As in the previous section, we first applied a temperature or pressure variation only at the surface, then we studied the effects of a coupled variation.

The first set of simulations has been computed for the temperature variation, with a fixed atmospheric pressure (0.1 MPa). Results are shown in Fig. 6.15. For very low overpressure, changes of atmospheric temperature produce very shallow depth effects (Fig. 6.15a,b), which cause a high time delay. For higher overpressure, these shallow depth effects effects disappear (Fig. 6.15c, d, e, and f) and the temperature variation produces a CO_2 flux time series similar to the one observed previously (Fig. 6.9).

Time delay as a function of the reservoir overpressure is shown in Fig. 6.16a. Time delay is high ($\sim$22 h) in the low pressure region, affected by very shallow depth effects, but an increase in the reservoir pressure will result in a lowering of the time delay between CO_2 flux and temperature time series. Maximum degassing varies from tens of g/day to hundreds of kg/day when a high overpressure is considered (Fig. 6.16b). Percentage variation of CO_2 flux is very high for low overpressure, and becomes suddenly much smaller when a higher pressure gradient is taken into account. It drops from a value of 100% of variation for $2 \cdot 10^{-5}$ MPa to less than 20% for hundreds of Pa, then it is very small (less than 1%) for higher overpressure (Fig. 6.16c).

The second set of simulation has been computed applying the pressure variation only, with a fixed atmospheric temperature (20 °C). The system does not present any relevant variation in the overpressure range considered, and having a fixed medium
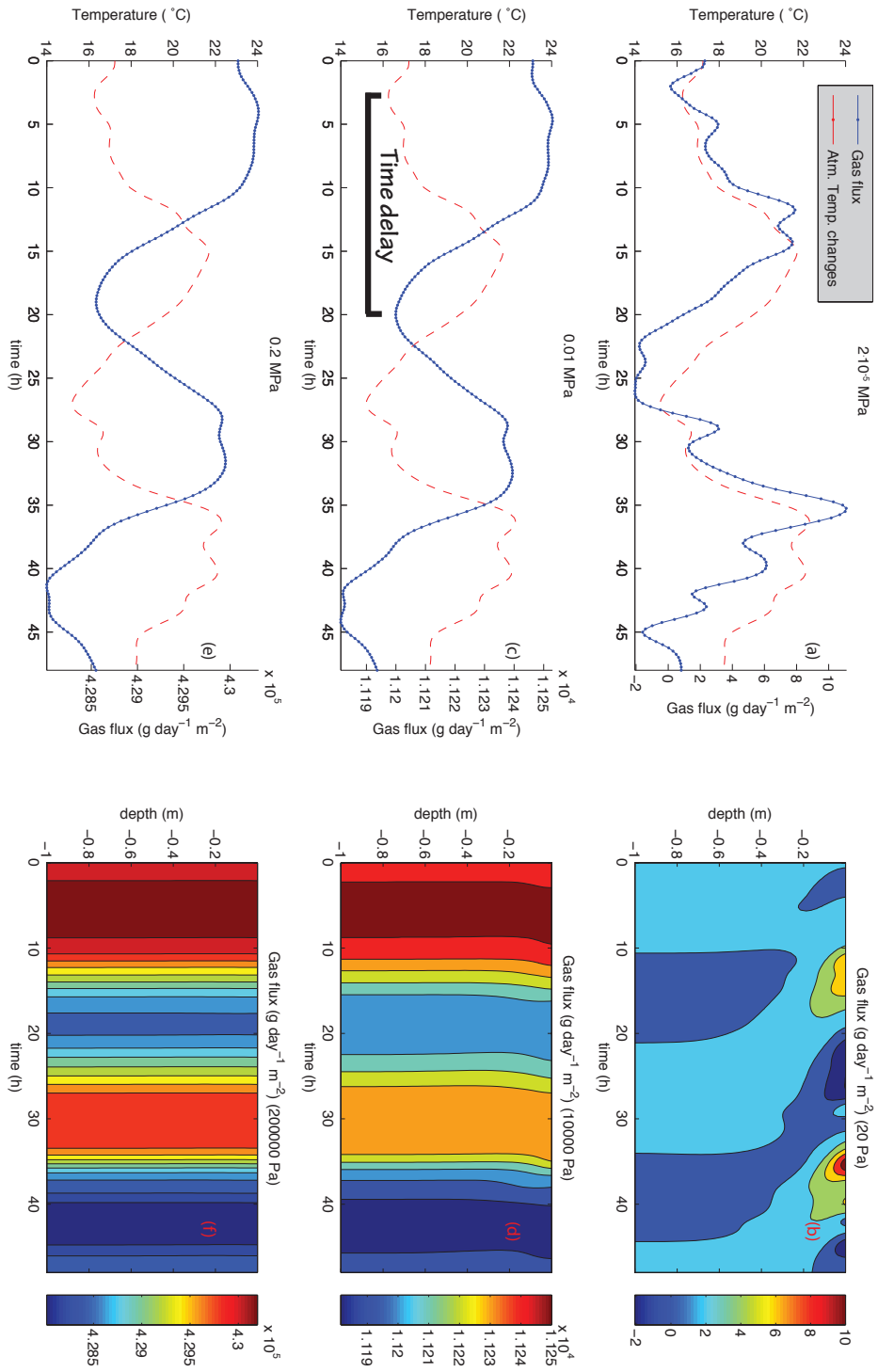
Figure 6.15: Simulated temporal CO_2 flux changes (blue line) at the surface due to the application of a temperature variation at surface (red line) for reservoir overpressure $2 \cdot 10^{-5}$, 0.01, and 0.2 MPa respectively. (**b,d,f**) CO_2 changes in time and depth for reservoir overpressure $2 \cdot 10^{-5}$, 0.01, and 0.2 MPa respectively. Time delay (the time between minimum temperature and CO_2 flux) is indicated for fig. (c).
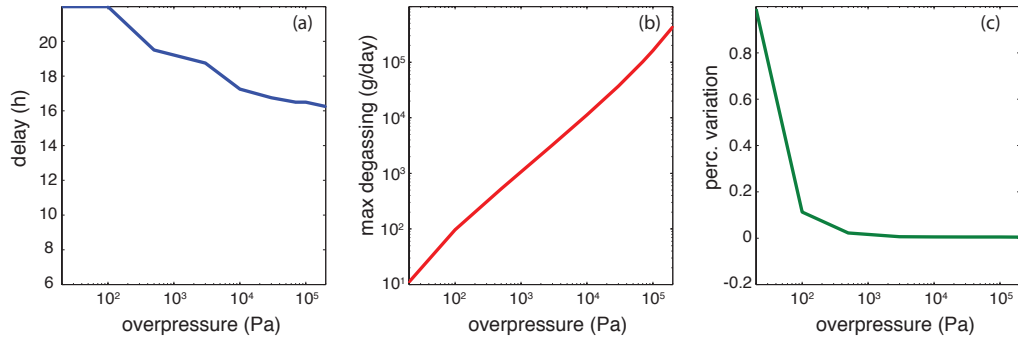
Figure 6.16: (**a**) Time delay with respect to the temperature time series as a function of reservoir overpressure due to the application of temperature variation only. (**b**) Maximum degassing as a function of reservoir overpressure. (**c**) Percentage variation as a function of reservoir overpressure. Percentage variation is calculated as the ratio between the maximum amplitude of changes and the maximum degassing.
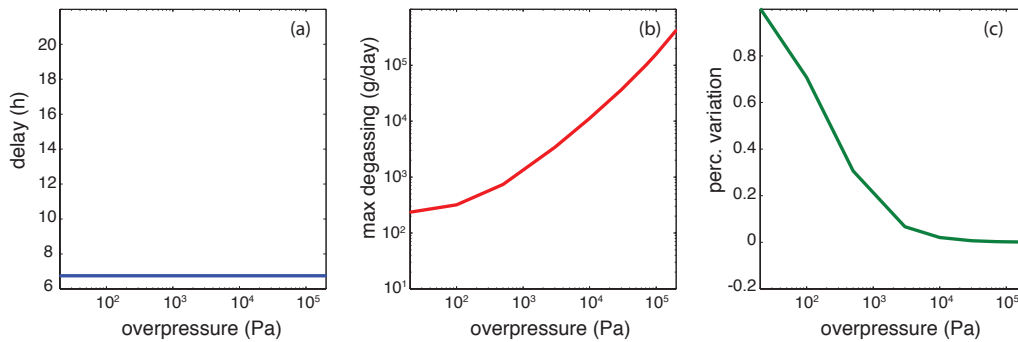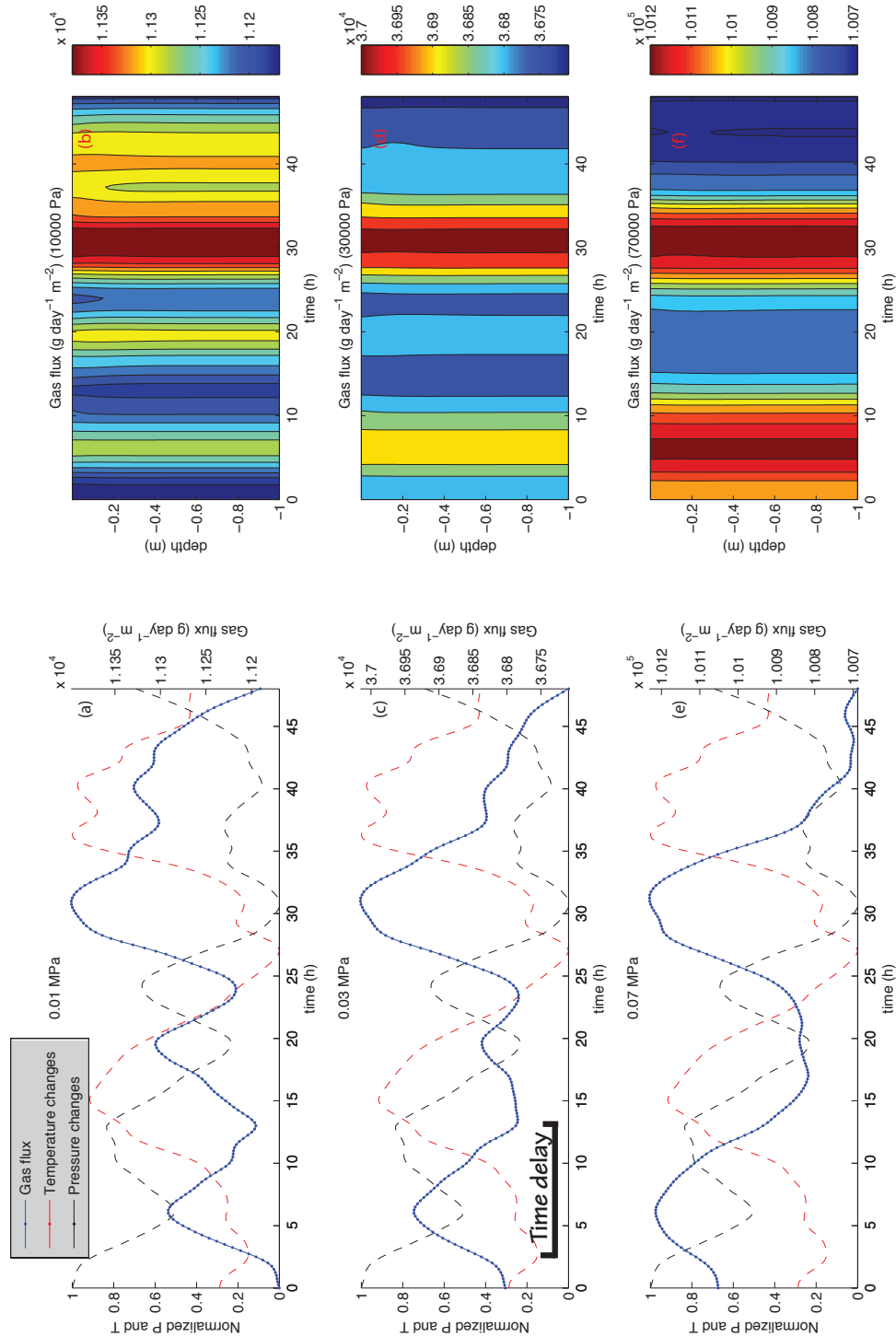

Figure 6.17: (**a**) Time delay with respect to the temperature time series as a function of reservoir overpressure due to the application of pressure variation only. (**b**) Maximum degassing as a function of reservoir overpressure. (**c**) Percentage variation as a function of reservoir overpressure. Percentage variation is calculated as the ratio between the maximum amplitude of changes and the maximum degassing.

value of permeability (10^{-13} m^2). Time delay between pressure and CO_2 flux time series is constant at $\sim$6 h (Fig. 6.17a). Maximum degassing for low overpressure is much higher (order of hundreds g/day) if compared with flux deriving from the application of a temperature variation only (Fig. 6.17b). This behavior is due the application of pressure variations at the surface with a magnitude (order of hundreds Pa) comparable with the overpressure fixed at the gas reservoir. This results also in a higher percentage variation of gas flux for pressure up to thousands of Pa (Fig. 6.17c). However, when high values of overpressure are taken into account, maximum degassing and percentage variation of degassing are comparable with values due to the applied changes of the atmospheric temperature only (see Figs. 6.16b,c and 6.17b,c for high overpressure).

The last set of simulations has been carried out applying at the same time both
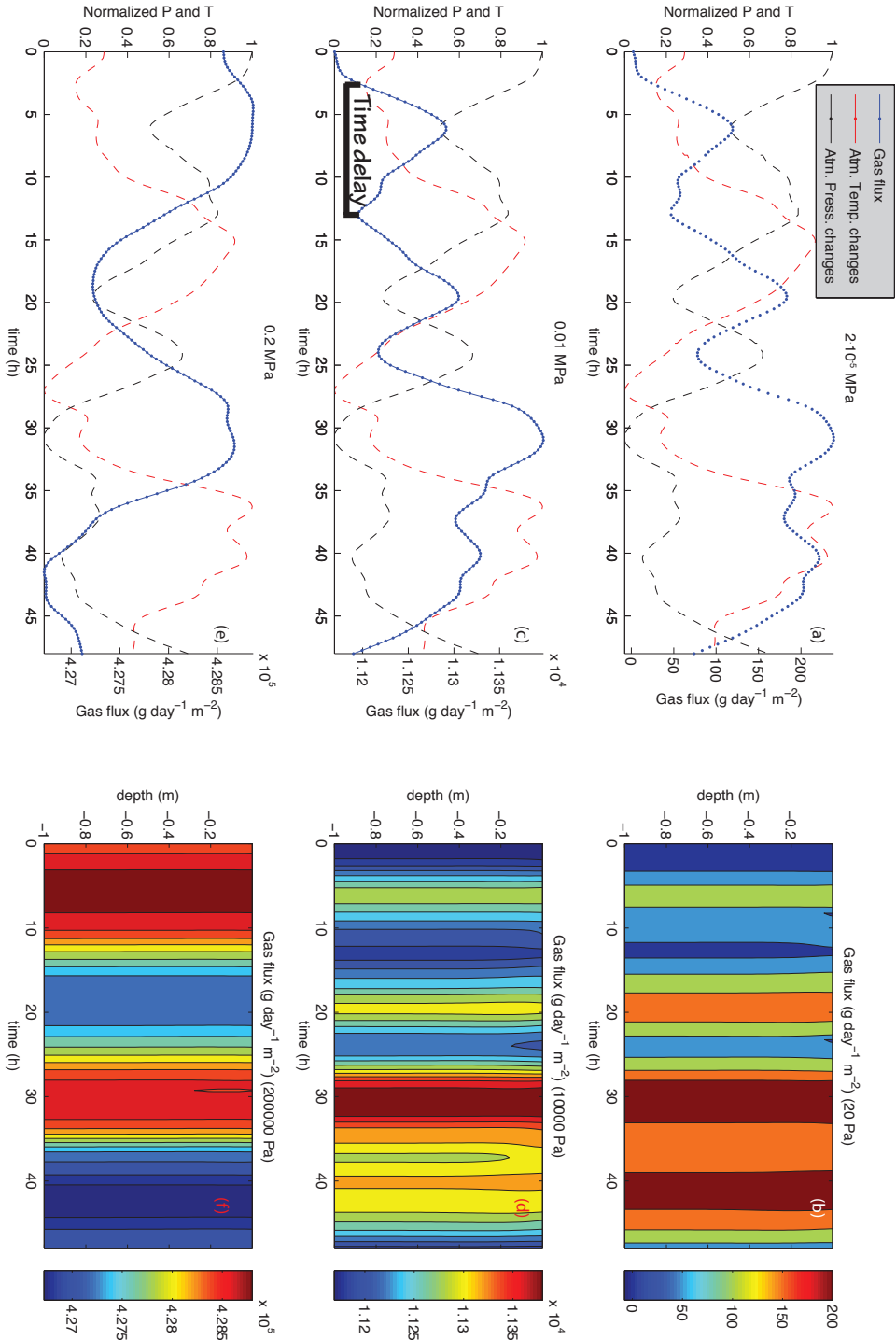
Figure 6.18: Simulated temporal CO_2 flux changes (blue line) at the surface due to the application of both pressure (black line) and temperature variation (red line) for reservoir overpressure $2\cdot10^{-5}$, 0.01, and 0.2 MPa respectively. (**b,d,f**) CO_2 changes in time and depth for reservoir overpressure $2\cdot10^{-5}$, 0.01, and 0.2 MPa respectively. Time delay is indicated for fig. (c).

Figure 6.19: Simulated temporal CO_2 flux changes (blue line) at the surface due to the application of both pressure (black line) and temperature variation (red line) for reservoir overpressure 0.01, 0.03 and 0.07 MPa respectively. (**b,d,f**) CO_2 changes in time and depth for reservoir overpressure 0.01, 0.03 and 0.07 MPa respectively. Time delay (the time between minimum temperature and CO_2 flux) is indicated for fig. (c).
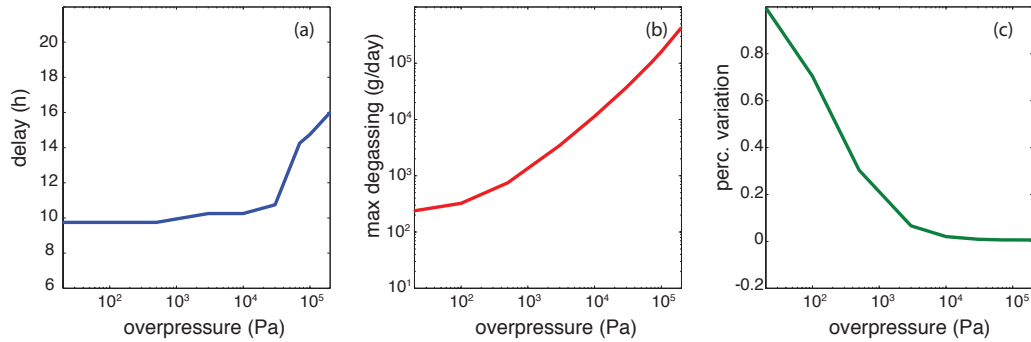
Figure 6.20: (**a**) Time delay with respect to the temperature time series as a function of reservoir overpressure due to the application of both temperature and pressure variation. (**b**) Maximum degassing as a function of reservoir overpressure. (**c**) Percentage variation as a function of reservoir overpressure.

the pressure and temperature variation at the surface. Results, shown in Fig. 6.18, highlight a pressure dominated behavior when the reservoir overpressure is in the low-medium range (Fig. 6.18a,c), i.e. the CO_2 flux time series looks like the one observed when atmospheric pressure changes only are applied, however when a high overpressure is applied to the gas reservoir, the CO_2 flux time series is mainly affected by the temperature variation, i.e. CO_2 flux time series is similar to the one observed when temperature changes only are applied. A detailed analysis in the medium range overpressure is shown in Fig. 6.19. The effects of pressure and temperature variation are comparable for an intermediate overpressure (Fig. 6.19b). CO_2 flux gradually changes from a pressure-dominated time series for an overpressure of 0.01 MPa (Fig. 6.19a) to a temperature-dominated time series for an overpressure of 0.07 MPa (Fig. 6.19c). The simultaneous application of temperature and pressure variation, and the choice of a medium permeability (10^{-13} m^2), do not allow the formation of very shallow depth effects (Figs. 6.18b,d,e and 6.19b,d,e).

Fig. 6.20a shows the time delay with respect to temperature changes as a function of the reservoir overpressure. When the CO_2 flux is pressure-dominated, the time delay is constant at ∼10 h (i.e. for low and medium reservoir overpressure). However time delay will increase for high overpressure (up to ∼16 h), when the CO_2 flux is temperature-dominated. Maximum degassing and percentage variation (Fig. 6.20b,c) presents the same variation simulated when a pressure variation only is applied at the surface.

Fig. 6.21 shows the time delay as a function of both permeability and reservoir overpressure. The dark red zone represents the region in permeability-overpressure plane where very shallow depth effects occur (low permeability-low overpressure). The blue zone is the region where CO_2 flux time series is pressure dominated, i.e. where time delay is constant at ∼10 h (high permeability-low overpressure). When overpressure is higher than 0.07 MPa, CO_2 time series is affected mainly by the temperature variation at the surface (red zone in Fig. 6.21) and time delay changes
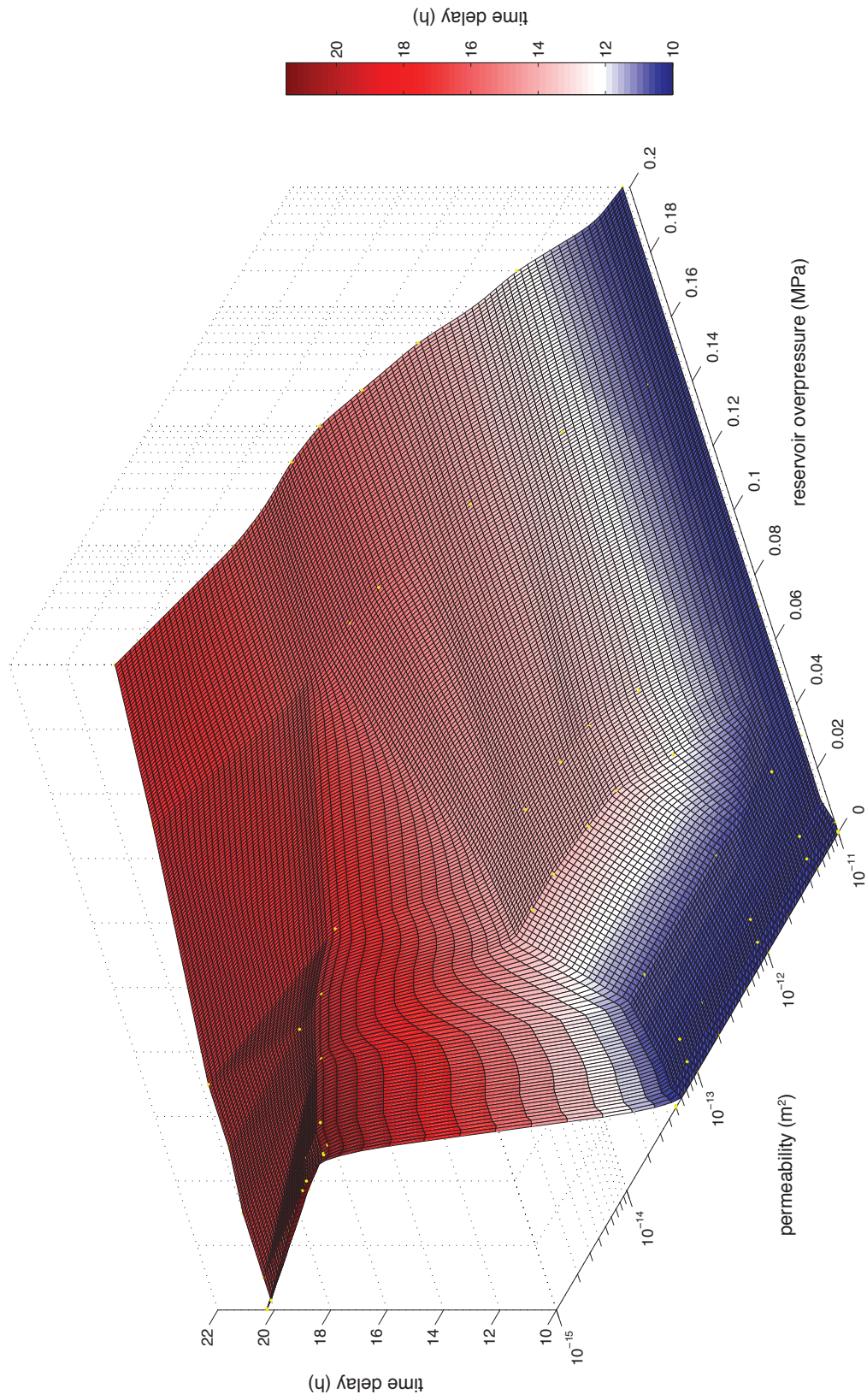
Figure 6.21: Dual parameters simulations. Dark red zones represents very high delay affected by very shallow depth effects. Blue zones are the regions where pressure effects are prevalent. Red zones are characterized by a temperature-dominated behavior. In order to have time delay comparable with the observed value at Furnas, and to have at same time pressure and temperature effects we should use permeability and overpressure in the white zones.

between 13 h and 20 h. To obtain a delay of order of 11-12 h, similar to the delay observed at Furnas (see Tab. 6.3 and 6.4), corresponding permeability and reservoir overpressure are in the white zone in Fig. 6.21, i.e. a permeability in the range $5 \cdot 10^{-12}$–$5 \cdot 10^{-13}$ and a reservoir overpressure in the range 0.03–0.07 MPa.

6.4.3   Sealed ground surface

In the previous sections a detailed dual parameter analysis has been presented. Results highlight as time delay between the applied temperature variation at surface and the CO_2 flux time series highly depends on both the domain permeability and the overpressure in the gas reservoir. A time delay comparable with the observation at Furnas (see Tab. 6.3 and 6.4) is possible assuming a permeability in the range $5 \cdot 10^{-12}$–$5 \cdot 10^{-13}$ with a reservoir overpressure in the range 0.03–0.07 MPa. However, the maximum degassing with this choice of permeability and reservoir overpressure (Figs. 6.14b and 6.20b) is very high compared with the observed degassing. To prevent these high values we can assume that the ground surface is sealed by a low permeability layer, which also allows to confine the pressure perturbation at shallow depth. Because of the low permeability layer, degassing is much lower than a homogeneous case and with a confined pressure perturbation we can choose a reservoir overpressure lower than 0.03 MPa without entering in the pressure-dominated region (blue zone in Fig. 6.21).

Using a domain permeability $\kappa = 10^{-12}$ m^2, a reservoir overpressure $\Delta p = 0.005$ MPa, and a low permeability layer $\kappa_s = 6 \cdot 10^{-16}$ with thickness $h = 10$ cm, we were able to simulate a CO_2 flux time series with a time delay of ~ 10 h (Fig. 6.22a). Fig. 6.22b shows as temperature changes propagate through time and depth. Pressure changes are confined at shallow depth up to 10 cm (Fig. 6.22c).

The resulting CO_2 flux time series depends on both temperature and pressure variations, and fluxes are in good agreement with data observed at Furnas (see Fig. 6.8). However, the maximum amplitude of variation in the simulated flux (~ 25 g m^{-2} d^{-1}) is small if compared with the observed data (~ 120 g m^{-2} d^{-1})

6.5   Conclusion

This chapter focused on the effects of the atmospheric conditions on soil diffuse degassing. Spike-like oscillations are observed on the soil CO_2 flux time series at Furnas volcano in S. Miguel island in the Azores archipelago, and these variations are mainly correlated with monitored meteorological variables on the permanent stations, mainly barometric pressure and air temperature. In order to understand the role played by the rock permeability and by an overpressure driving gas ascent, a dual parameters study was performed by numerical simulation with TOUGH2/EOS2 simulator, applying the observed air temperature and barometric pressure changes at surface.

Numerical results show that the CO_2 flux changes when temperature and pressure change, and presents a time delay in agreement with data observed at Furnas.
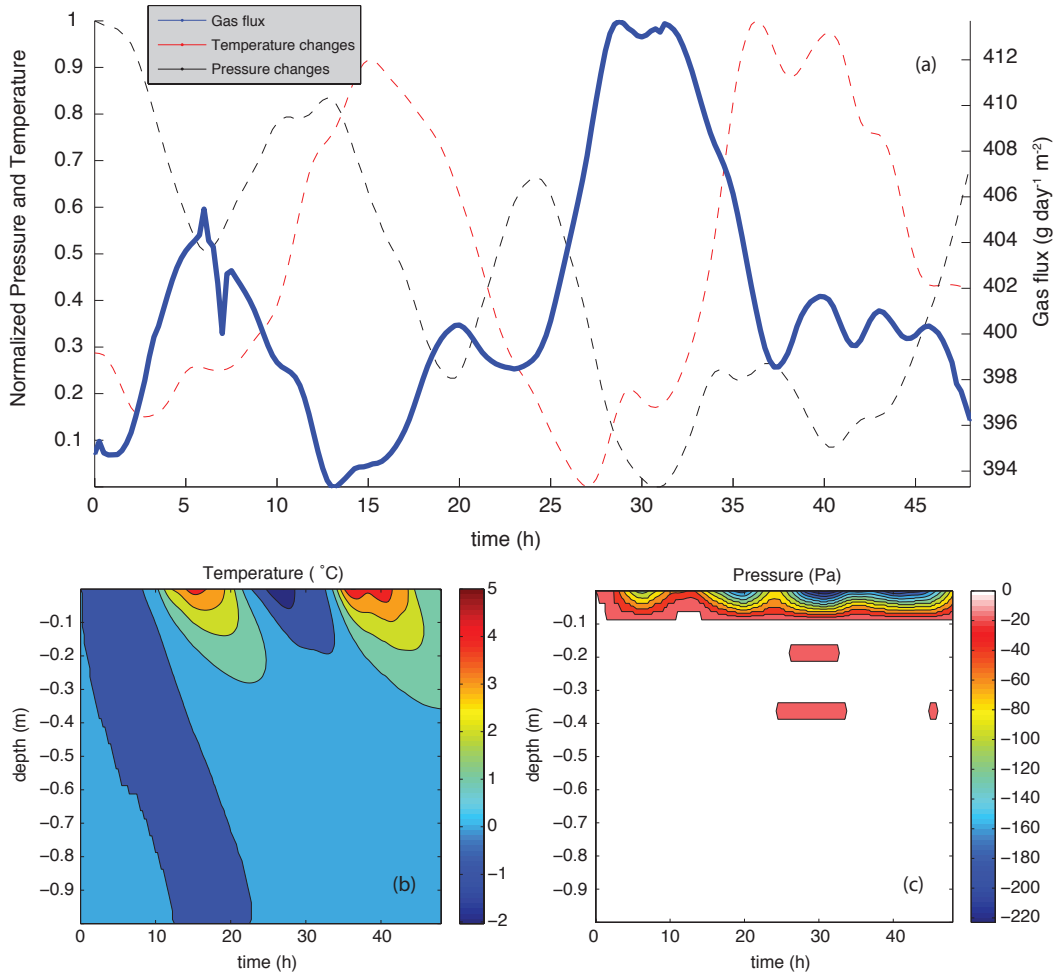
Figure 6.22: (**a**) CO_2 flux time series (blue line) for sealed degassing. Applied barometric pressure (black line) and air temperature (red line) at surface are also showed. (**b**) Temperature changes as a function of time and depth. (**c**) Pressure changes as a function of time and depth.

However, CO_2 flux time series highly depend on both the domain permeability and the overpressure in the gas reservoir. The dual parameters study highlights several different behaviors for CO_2 flux: (1) very shallow depth effects may occur when low permeability and low overpressure are considered, and the time delay reaches very high value (~ 22 h); (2) CO_2 is pressure-dominated for high permeability and low overpressure with a low time delay (~ 10 h) and (3) for overpressure greater than 0.07 MPa, CO_2 time series is affected mainly by the temperature variation at the surface, with a time delay in the range 13-20 h. A time delay comparable with the observed data at Furnas (11-12 h) is possible considering a permeability in the range $5 \cdot 10^{-12}$–$5 \cdot 10^{-13}$ with a reservoir overpressure in the range 0.03–0.07 MPa.

However, considering these ranges of variation, the maximum CO_2 degassing

is still high (thousands of g/day) if compared with data (hundreds of g/day). To prevent these high flux we assumed that degassing is sealed by a low permeability layer, which also permits to lower the range of reservoir overpressure. Considering a low permeability layer ($6 \cdot 10^{-16}$ m^2) with thickness of 10 cm, an overpressure of 0.005 MPa, and a domain permeability of 10^{-12} m^2, time delay and degassing rate are in good agreement with measured values, although simulated CO_2 flux amplitude is lower than data observed at Furnas.

References

Bajracharya, R.M., Lal, R., Kimble, J.N., 2000. Diurnal and seasonal CO_2-C flux from soil as related to erosion phases in central Ohio. Soil Sci. Soc. Am. J. 64, 286–293.

Chiodini, G., Cioni, R., Guidi, M., Raco, B., Marini, L., 1998. Soil CO_2 flux measurements in volcanic and geothermal areas. Applied Geochemistry 13, 543 – 552.

Granieri, D., Chiodini, G., Marzocchi, W., Avino, R., 2003. Continuous monitoring of CO_2 soil diffuse degassing at Phlegrean Fields (Italy): influence of environmental and volcanic parameters. Earth and Planetary Science Letters 212, 167–179.

Nakadai, T., Yokozawa, M., Ikeda, H., Koizumi, H., 2002. Diurnal changes of carbon dioxide flux from bare soil in agricultural field in Japan. App. Soil Ecol. 19, 161–171.

Padrón et al., 2008. Diffuse CO_2 emission rate from Pululahua and the lake-filled Cuicocha calderas, Ecuador. J. Volcanol. Geotherm. Res. 176, 163–169.

Pruess, K., Oldenburg, C.M., Moridis, G., 1999. TOUGH2 user's guide, version 2.0. Paper LBNL-43134. Lawrence Berkeley Natl. Lab., Berkeley, CA, USA.

Witkamp, M., 1969. Environmental effects on microbial turnover of some mineral elements: Part II–Biotic factors. Soil Biology and Biochemistry 1(3), 177 – 184. doi:10.1016/0038-0717(69)90017-0.

Contents

7.1   Introduction

The current global dependence on fossil fuels for over 80% of mankind's primary energy supply (IEA, 2010) is causing atmospheric CO_2 concentrations to rise resulting in climate change (IPCC, 2007a). To avoid the most serious effects of climate change, measures need to be taken now to reduce net CO_2 emissions by at least one-half (IPCC, 2007b). A combination of approaches has the best chance of reducing CO_2 emissions at the scale and rate needed to avoid the most serious effects of climate change (Pacala and Socolow, 2004) . Of the six most feasible options proposed by Pacala and Socolow (2004), capture of CO_2 from fossil-fuel power plants and other stationary industrial sources with Geologic Carbon Sequestration (GCS) is the only option that permits a bridging from current carbon-based energy sources to an energy-supply future that uses only low-carbon energy sources. The current concept for large-scale GCS is the direct injection of supercritical CO_2 into deep geologic formations which typically contain brine (IPCC, 2005).

In order to inject CO_2 into deep brine-filled aquifers, over-pressure must be applied to drive the CO_2 into the formation and displace the brine outward to

accommodate the injected CO_2. By this process, injection of CO_2 causes pressure increases in the brine formations (e.g., Nicot, 2008; Birkholzer and Zhou, 2009; Birkholzer et al., 2009; Zhou et al., 2010). Because brine and the porous matrix are not very compressible, pressure will propagate rapidly to large distances away from the injection well (e.g., Zhou et al., 2008). The resulting pressure gradients provide a driving force for brine flow, which may be upwards if there are vertical conduits. Potential conduits for this upward flow could be (1) an open well, (2) poorly cemented well annulus, (3) permeable faults or fracture zones, etc. Although such conduits are not expected to be present, this paper addresses the question of the dynamics of upward brine flows assuming a conduit exists. We note that the conduit does not convey CO_2 upward as the injected CO_2 may be many kilometers away, but rather it conveys over-pressured brine that results from CO_2 injection some distance away.

The issue of brine upflow into groundwater resources is critically important for environmental risk assessment of GCS. The context for upward brine flow in GCS systems involves several key features that make the process interesting:

1) Pressures in deep systems are nearly hydrostatic, so small over- or under-pressures can cause brine flow provided there is sufficient permeability.

2) Brine flow can be continuous and steady, or it can be short-lived and end with establishment of a new hydrostatic equilibrium, or it can be transient or oscillatory.

3) Brine flow is affected not only by pressurization or depressurization, but also by buoyancy of the brine relative to surrounding groundwater.

4) Buoyancy of the brine is controlled by both compositional (salinity) and thermal effects.

5) Thermal and salinity effects operate very differently in porous media due to thermal conduction into solid grains of the matrix, resulting in the process known as thermal retardation.

6) Diffusion of heat is much faster than diffusion of dissolved salt in brine.

7) Salinity generally increases with depth as does temperature, tending to compensate each other with respect to fluid density.

In this chapter, we illustrate some of the features above through numerical modeling of the dynamics of upward brine flow. In so doing, we illuminate key parameters that control upward brine flow allowing an estimate of behavior of various systems based on their site-specific parameter values. The model system is highly idealized to focus attention on the thermal and solutal effects.

The conceptual model for the system considered here is shown in Fig. 7.1, which shows a conduit assumed to be a leaky well. In fact, the system we model is more generic and models upward flow through a 5 m-wide conduit with the same
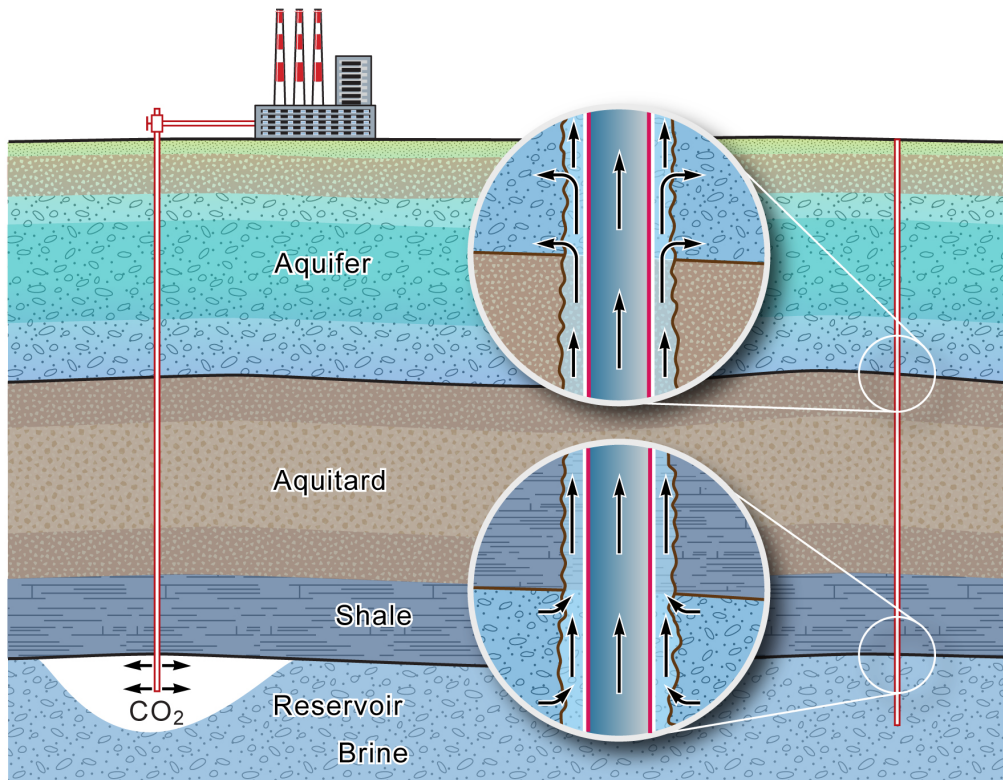
Figure 7.1: Conceptualization of CO_2 injection causing pressure rise that leads to brine up flow in an abandoned well.

permeability as the reservoir rocks. As such, the model is not site-specific nor is it representative of any actual GCS site. Instead the purpose of the modeling presented here is to demonstrate concepts of the establishment of a new hydrostatic equilibrium upon reservoir pressurization, sustained flow, and oscillatory dynamic solutions in the brine up flow system. The use of an idealized model is made purely as an end-member case to examine the potentially interesting dynamics that could arise in some special circumstances. Although it is necessary to understand what might happen if brine upflow occurs, in general, highly conductive features such as those assumed here will not be present in any GCS system.
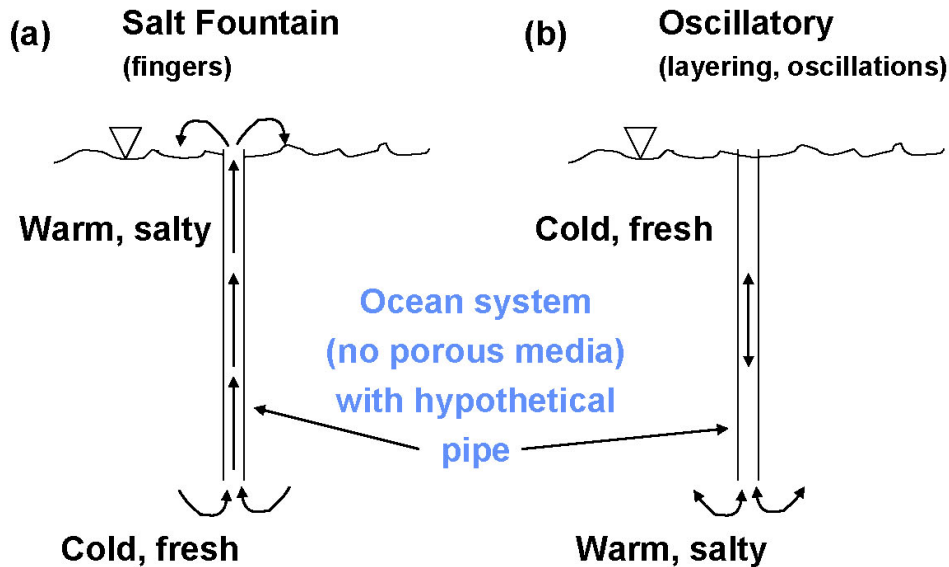
7.2 Prior Work

The structure of deep sedimentary basins and associated flow of groundwater has been studied in the context of understanding deep hydrologic systems (e.g., Bethke, 1985; Gupta and Bair, 1997), geothermal resources (Bachu and Burwash, 1991), ore deposits (Garven and Freeze, 1984; Bethke, 1986), oil migration (e.g., Hindle, 1997), and GCS (Ginter et al., 2004). In the case of GCS, upward migration of CO_2 has been studied extensively through various combinations of overburden and conduc-

tive and non-conductive features by analytical (e.g., Silin et al., 2009; Hayek et al.,
2009) and numerical approaches (e.g., Pruess, 2008; Doughty and Meyer, 2009).
The large potential for upward vertical flow (i.e., leakage) through fast paths such
as abandoned wells was pointed out by Nordbotten et al. (2004) who also provided
semi-analytical approaches to estimating the magnitude of such leakage. While
much of the early focus of potential impacts of GCS was on upward CO_2 leakage
into groundwater resources, more recently concern is being focused on upward brine
displacement and associated degradation of groundwater. One reason for this inter-
est is that pressure increases due to injection can extend tens of km or more, making
it difficult to characterize the area thoroughly enough to guarantee absence of con-
duits capable of conveying brine upward. The hazard is that up-flowing deep brines
will increase Total Dissolved Solids (TDS) and potentially other components such
as heavy metals (e.g., lead, arsenic, etc.) in shallower aquifers potentially leading
to degradation of groundwater quality (Apps et al., 2010; Zheng et al., 2009).

The overall topic of well-bore integrity relative to upward leakage is an area of
ongoing research critical to GCS safety and effectiveness (e.g., Gasda et al., 2004;
Carey et al., 2007). The potential for brine flowing upward in wells was analyzed by
Nicot et al. (2009a,b) who considered density effects and drilling mud in the wellbore
in a hydrostatic context as possible mitigating features for upward brine flow. While
the properties of faults remain even more enigmatic than that of well bores, recent
efforts have used percolation theory and fuzzy rules to estimate connectivity of fault
networks that could give rise to a connected flow path if the individual faults are
conductive (Zhang et al., 2010).

When deep brine flows upward into cooler regions along the geothermal gradi-
ent, both thermal and solutal effects of buoyancy come into play. The advection
of heat and salt by flowing brine in viscous liquid systems (e.g., Turner, 1973) is
very different from the flow of heat and salt in porous media (e.g., Nield, 1968).
Specifically, solute is transported at the pore velocity in porous media whereas heat
is transported approximately at the Darcy velocity due to thermal conduction into
the solid grains of the matrix (Phillips, 1991). This interesting behavior gives rise to
plume separation (Oldenburg and Pruess, 1999), that is, the solute plume tends to
advance ahead the thermal plume when a parcel of hot, salty water moves through
cooler, fresher porous media, a phenomenon that will be observed in some of the
results presented below.

Finally by analogy to viscous liquid systems (no porous media) such as the
oceans, we note that researchers have identified the different kinds of behavior that
can be expected depending on the stratification of heat and salt. Shown in Fig. 7.2
are two conceptual depictions of configurations borrowed from early oceanographic
work in this area (e.g., see reviews in Turner, 1973) that lead to very different
forms of natural convection. Specifically, as a thought experiment consider the
situation when cold, fresh water is displaced upward in a hypothetical flexible pipe
that exchanges heat but not salt with its surroundings. In this case, the flow is
unstable and accelerates upwards as seen in Fig. 7.2a. In contrast, warm, salty water
displaced upward in the hypothetical pipe tends to return to its original location

(a) Salt Fountain
(fingers)

(b) Oscillatory
(layering, oscillations)

Warm, salty

Cold, fresh

**Ocean system
(no porous media)
with hypothetical
pipe**

Cold, fresh

Warm, salty

Figure 7.2: Conceptual depictions of double-diffusive convection in the finger regime (**a**) and the oscillatory regime (**b**). Note that differences in diffusivity between heat and salt mean that the pipe is not necessary to develop fingers (**a**) and layered or oscillatory convection (**b**).

as it cools but remains salty at higher levels in the system. These behaviors were observed by Stommel and Federov (1967) and related topics were covered in depth by Turner (1973). One interesting feature of these thought experiments is that because thermal diffusivity is much greater than solutal diffusivity (giving rise to so-called double-diffusive convection), the pipe does not have to be present for these fingering or oscillatory convective patterns to develop. We mention these previously recognized aspects of double-diffusive convection in viscous liquid systems simply to point out the importance of multiple sources of buoyancy and the interesting convective phenomena that they can cause in viscous liquid and in porous media systems (e.g., layering, as described in Oldenburg and Pruess, 1998). In the geologic carbon sequestration case, warm, salty water can potentially be pushed upwards by CO_2 injection into cooler, fresher aquifers as will be discussed in detail below.

7.3   Methods

We have simulated the upward single-phase flow of deep brine into a shallower aquifer using the non-isothermal reservoir simulation model TOUGH2 with the EOS7 equation-of-state module (Pruess et al., 1999) for single-phase conditions and three components (water, brine, and air).

The brine component in EOS7 is defined as a concentrated NaCl brine, a more convenient choice than solid NaCl and water components because the brine and
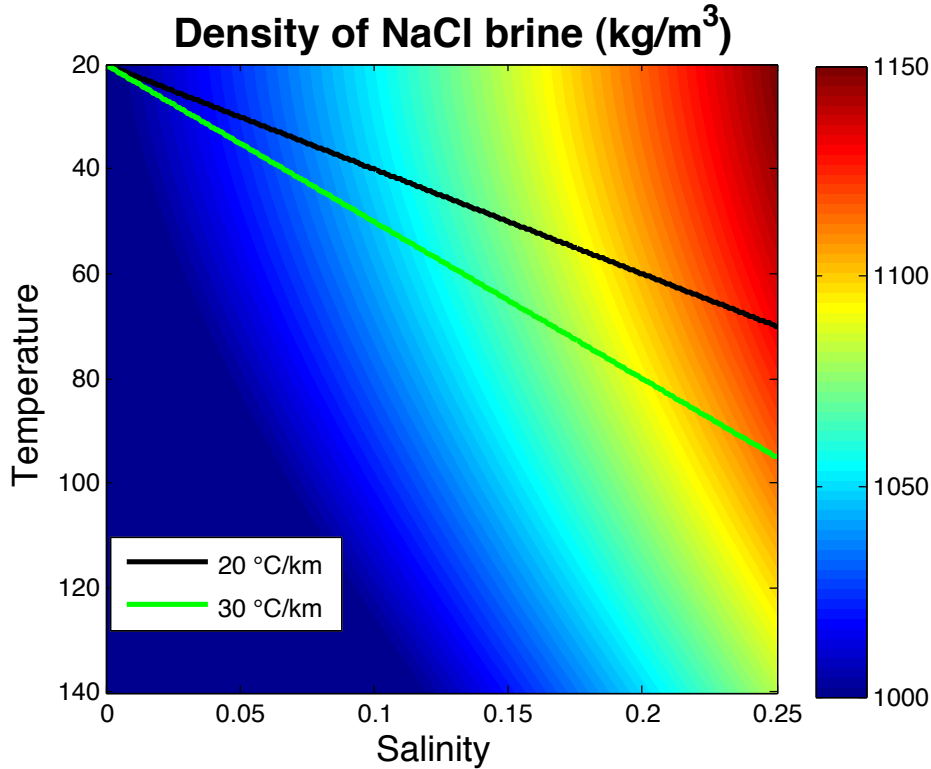
Figure 7.3: Variation of density of NaCl brine as a function of temperature and salinity as calculated in TOUGH2/EOS7 with some typical geothermal gradients shown assuming zero salinity at the ground surface and salinity of 0.25 at a depth of 2.5 km.

water volumes are approximately linearly additive whereas NaCl and water volumes are not linearly additive. The density of pure water as a function of temperature is calculated using the results of the IFC (1967). Under natural conditions, temperature and salinity both tend to increase with depth, with opposite impacts on density. The net effect is that density of brine increases with depth. Given that ρ_{H_2O} (1 bar, 15 °C) = 999 kg m^{-3}, and the densest brine considered is 1150 kg m^{-3} which is assumed to correspond to a brine with 25% salinity, we approximate salinity for any reference brine density by the formula

$$s = \frac{(\rho_{ref\ brine} - 999)}{(1150 - 999)}0.25 \tag{7.1}$$

Which gives salinities of 0.25, 0.17, and 0.08 for the reference brines of density 1150, 1100, and 1050 kg m^{-3}, respectively. The density as calculated in EOS7 of brine-water mixtures with maximum density of 1150 kg m^{-3} are shown in Fig. 7.3 as a function of temperature and salinity.

The conceptual model of the multilayered hydrologic system with GCS underway was shown in Fig. 7.1. The sub-system that we consider is taken to be far away

Table 7.1: Properties used in the brine upflow model.

	Lower and upper aquifers and conduit
Temperature (T)	Variable (geothermal gradient)
Porosity (ϕ)	0.30
Permeability (κ)	Variable $(10^{-11}, 10^{-13}, 10^{-13} \text{ m}^2)$
Thermal conductivity (λ)	2.51 W m^{-1} K^{-1}
Molec. diffusivity coefficients $(d_\beta K)$	Liquid: 10^{-10} m^{2}s^{-1}
Tortuosity (τ_0)	1.0

(laterally displaced) from the CO_2 injection well and addresses only the upward flow of brine (no CO_2 present) through a conduit such as a well that cuts through a thick aquitard into an upper shallow aquifer. Some properties of the system are listed in Table 7.1. The model system consists of a lower reservoir (brine formation) with closed boundaries and a grid block at the lower left-hand corner at which the pressure is raised impulsively to represent CO_2 injection at a large distance away from the conduit. The boundary conditions at the top of the system are open (constant T = 20 °C, 1 bar) and the sides of the system are closed (no flow). The system was discretized as shown in Fig. 7.4 with a 5 m-wide conduit. The choice of closed boundaries on the lower reservoir was made to ensure a significant pressure rise. As for the upper aquifer, the closed side boundaries represent a system with lateral compartmentalization. We also ran some cases with open side boundaries in the upper reservoir as discussed below.
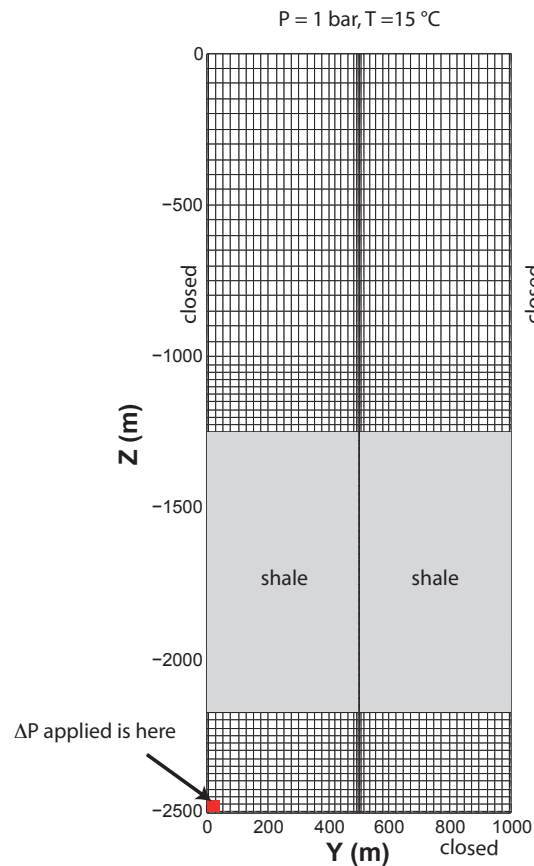
Figure 7.4: Idealized model system showing boundary conditions and discretization.

7.4   Results

7.4.1   Overview

Before showing the details of the results, we summarize the overall behavior of the
system. First, the initial condition consists of hydrostatic brine linearly stratified
in salinity and temperature from the top to the bottom. The overpressure applied
at the lower left-hand corner of the system propagates rapidly through the lower
reservoir and serves to drive warm, salty brine up the conduit. If the brine density
is high enough or the overpressure low enough, the warm brine moves only part way
up the conduit and finds a new hydrostatic equilibrium.

   If the brine density is low or the overpressure is high, the warm brine flows
all the way up the conduit and into the upper aquifer. With closed boundaries
500 m away on each side of the well in the model, the brine cannot flow laterally
for very long, and ponds in the upper aquifer increasing hydrostatic pressure and
eventually finding a new hydrostatic equilibrium. If the lateral boundaries are open
or the upper aquifer lateral extent were very large, brine exiting the conduit into the

upper aquifer would flow laterally along the lower-most regions of the upper aquifer as controlled by buoyancy; this flow can be sustained for as long as the lateral flow occurs. In the hypothetical case that brine ponds in the upper aquifer and cools, the brine can become dense enough to overcome the original overpressure of the lower reservoir that drove it up the conduit. The result is that the brine is sufficiently dense to flow back down the conduit. Once in the lower reservoir, it heats up again and the cycle continues. This is the essential mechanism of the oscillatory solutions to be discussed below.

7.4.2 Base Case

We present first the details of the simulation result for the case of the highest salinity brine we considered, approximately 25% salinity (sea water has a salinity of approximately 3.5%) and a geothermal gradient of 30 °C/km. Shown in the Fig. 7.5 are temperature, salinity, and brine density in contour form and profiles along the conduit after 500 yr of a pressure perturbation of 0.2 MPa and permeability (κ) equal to 10^{-12} m^2. As shown, the resulting system is nearly static with the dense brine from the lower aquifer positioned part way up the conduit. Note the temperature field remains equal to the initial geothermal gradient while the salinity becomes higher in the conduit. This is due to the well-known effect of thermal retardation during the initial upward displacement whereby the solute front moves out ahead of the thermal front in the porous medium (e.g., Oldenburg and Pruess, 1999) and then the solute anomaly persists for a very long time as controlled by the slow diffusion of salinity. This effect is reflected in the density profile which shows fluid density in the conduit reflecting anomalous brine concentration.

In Fig. 7.6 we show details of results for the case of brine salinity equal to 17% and pressure perturbation 0.2 MPa for $\kappa=10^{-12}$ m^2. As shown, in this case the 0.2 MPa pressure rise is able to push the warm brine up the conduit and into the lower part of the upper aquifer where it spreads out at t = 500 yrs. This spreading will occur in this system until the brine ponds to a depth sufficient to match the pressure perturbation supporting the column of brine in the conduit. If the model domain were laterally much larger in the upper aquifer, the upward flow could be sustained for a long time with dense brine underplating the upper aquifer as controlled by buoyancy. Note the vertical profile of density shows an inversion in the conduit resulting from nearly uniform salinity during upflow with geothermal-gradient-controlled temperature. This profile shows the system is still evolving at t = 500 yrs.

The case with all properties the same as in Figs. 7.5 and 7.6 except the maximum salinity is 8% is shown in Fig. 7.7. Here the brine up flow into the upper aquifer is correspondingly stronger, and the system is dynamic at t = 500 yrs as brine underplates the upper aquifer. As in Fig. 7.6, the salinity in the conduit as shown in Fig. 7.7 is relatively uniform resulting in a density inversion.
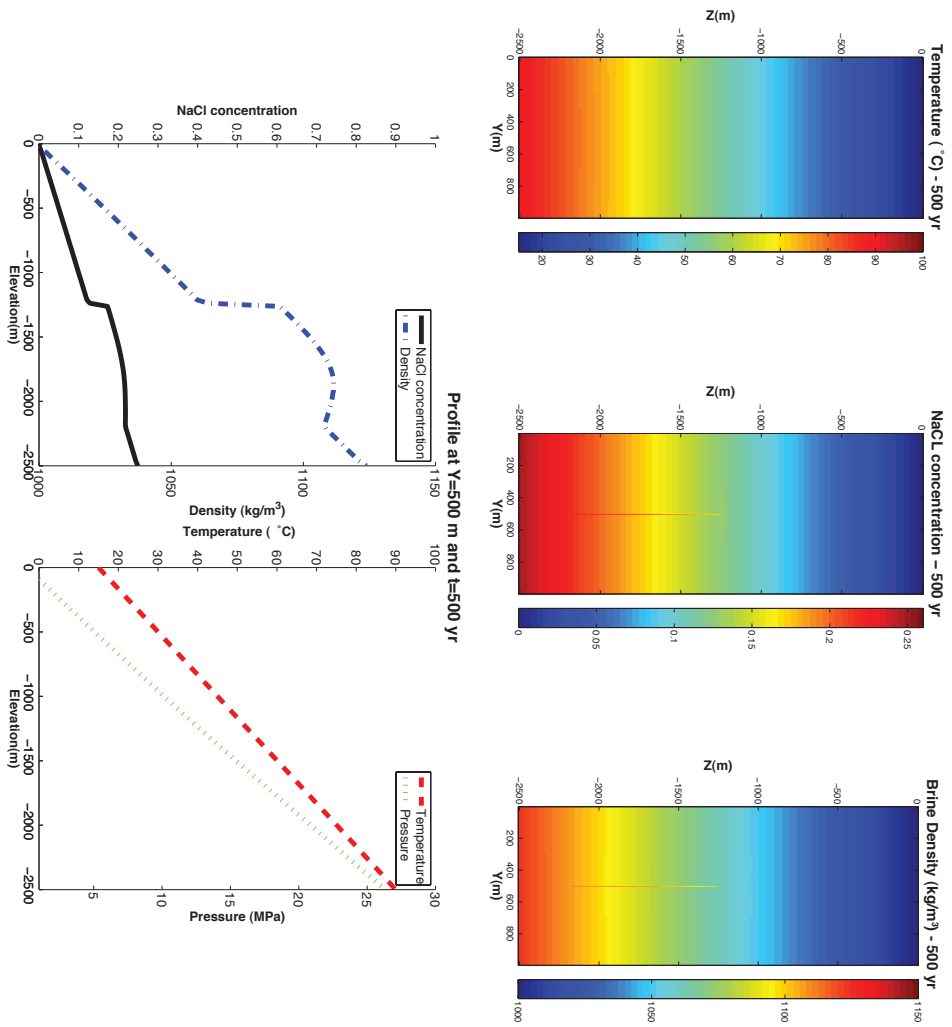
Figure 7.5: High-salinity brine is displaced up into the conduit where it is held in a static equilibrium due to pressure rise of 0.2 MPa.
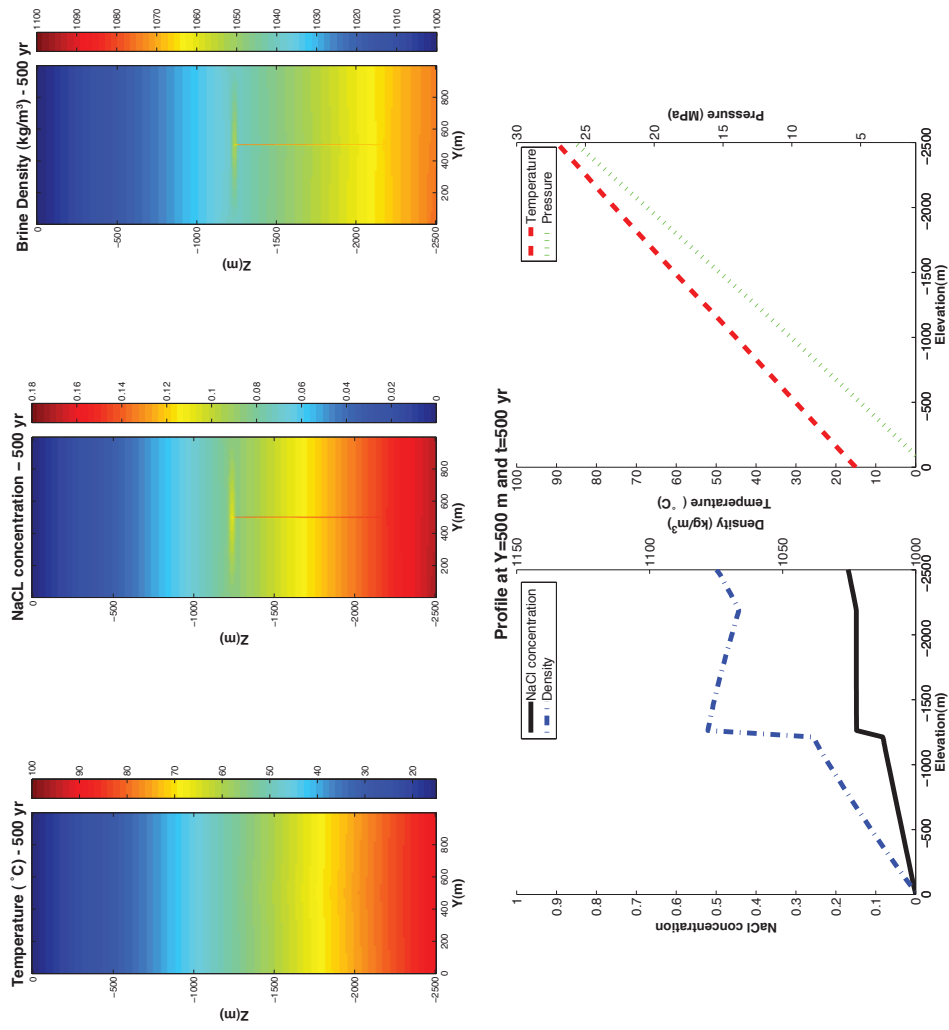
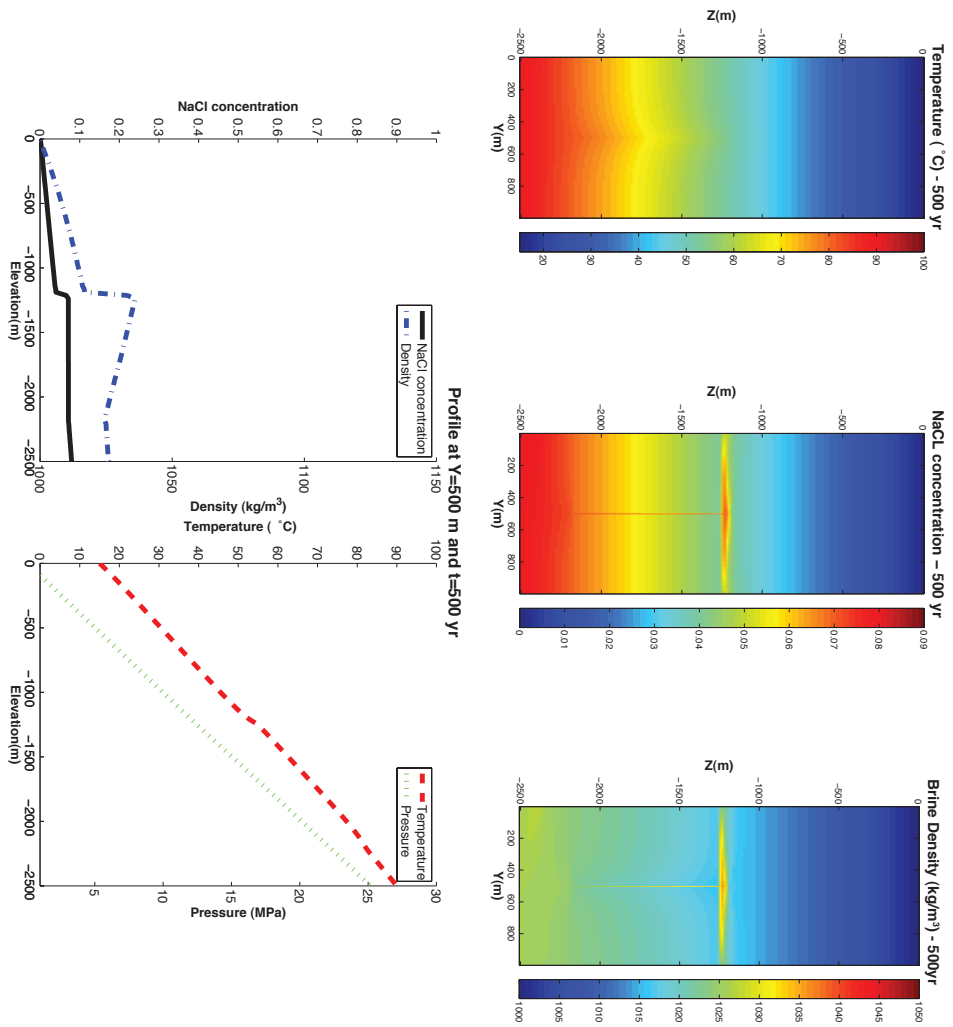Figure 7.6: Medium-salinity brine flowing up the conduit due to pressure rise of 0.2 MPa.

Figure 7.7: Low-salinity brine flowing up the conduit due to pressure rise of 0.2 MPa.

7.4.3 Oscillatory Solutions

In the interest of examining all possible situations, we study next the consequences of a hypothetical situation not generally expected in sedimentary basin systems but potentially relevant in systems with varying geothermal gradients with depth. The situation is illustrated in Fig. 7.8 which shows details of results for a system in which the conduit is thermally insulated from the shale, an effect achieved by removing the shale layer from the simulation, causing warm brine to arrive at the upper aquifer. In this case, the simulation shows a very strong density inversion in the vertical profile along the conduit. This arises from the hot brine entering the upper aquifer and undergoing significant cooling. During this cooling process, the density increases strongly, and can become so large that the fluid overcomes the over-pressure that drove it upward to the upper aquifer. The result is that the brine begins to move back down the conduit and into the lower aquifer as it cools. Once in the lower aquifer, the brine heats up again and rises up the conduit. This oscillatory behavior appears to go on indefinitely with time scales of oscillation on the order of thousands of years but dependent on system properties.

We show in Fig. 7.9 some oscillatory behavior by plotting the height of the brine layer in the upper aquifer versus time for various combinations of parameters and $\kappa=10^{-12}$ m^2. Note the long time scales for this oscillation. Note also that this is a hypothetical situation in which no heat transfer occurs from the fluid to the walls of the conduit, and in which the geothermal gradient in the upper aquifer is not maintained but rather is controlled by fluid up- and down-flow and the top boundary condition. Nevertheless, we believe this behavior is worth noting and may be relevant in some situations with anomalous geothermal gradients.

7.4.4 Parameter Study of Oscillatory and Static Solutions

For the case in which no heat transfer occurs between fluid and conduit, and the geothermal gradient in the upper aquifer is controlled by fluid flow, we mapped out oscillatory and steady static solutions for 27 combinations of the parameters including (1) pressure perturbation (ΔP), (2) salinity as given by brine density at standard conditions, and (3) permeability. Values used were ΔP=0.03, 0.1, and 0.2 MPa, ρ_{brine}=1050, 1100, and 1150 kg m^{-3}, and $\kappa=10^{-13}$, 10^{-12}, and 10^{-11} m^2. We present in Fig. 7.10 results showing that oscillatory solutions tend to occur for large ΔP, small salinity, and large permeability. Again we emphasize that this mapping of parameter space corresponds to hypothetical conditions of heat transfer that are not likely to occur, but that are consistent with the trend that static steady states are the expected result of weak upflow of dense brine in low permeability conduits.
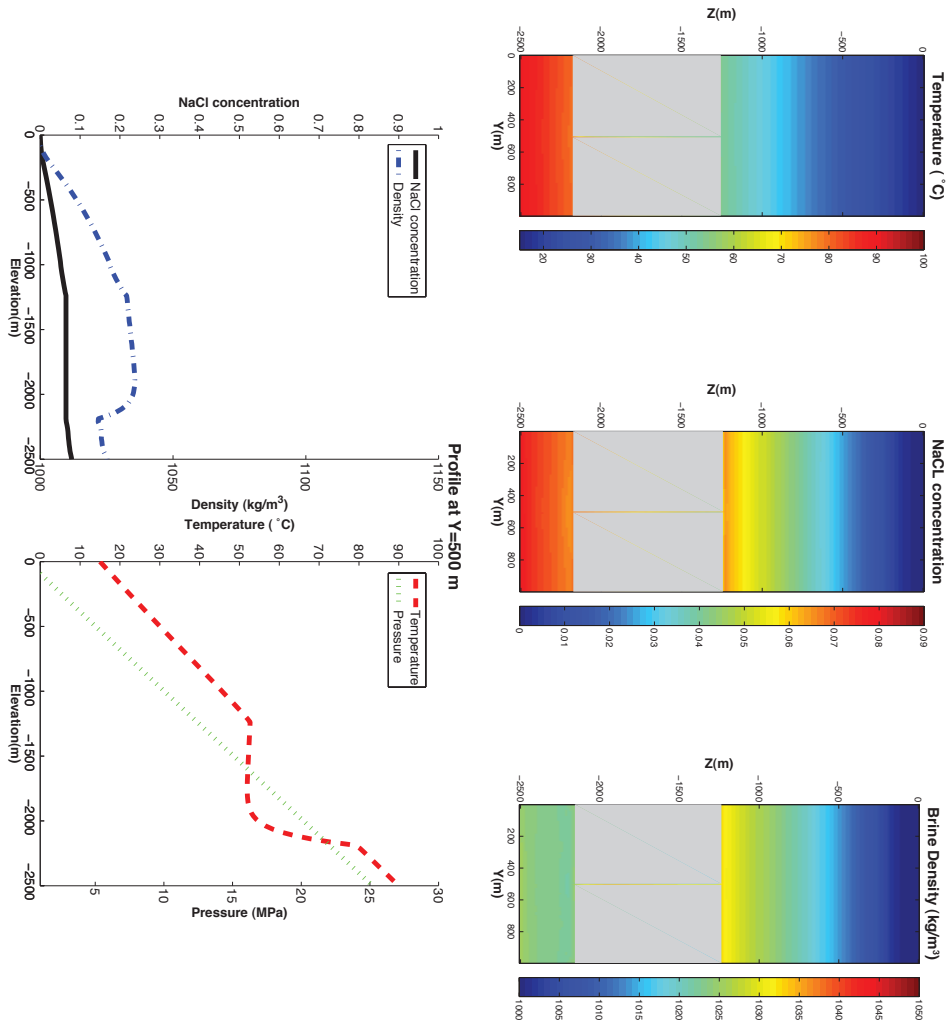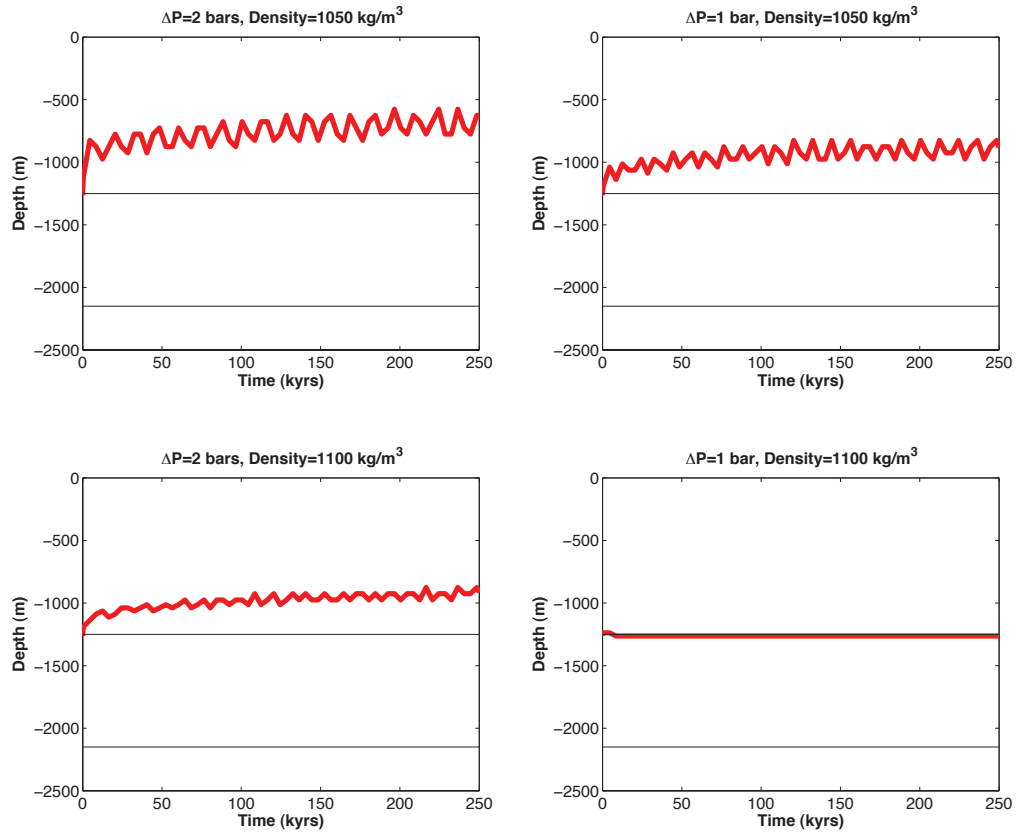
Figure 7.8: Dynamic change of height of brine intrusion with time showing oscillatory behavior.

Figure 7.9: Oscillatory and static solutions shown by the height of the brine layer in the upper aquifer as a function of time.

7.5 Conclusions

The injection of large quantities of CO_2 for geologic carbon sequestration will increase pressure in brine formations and tend to displace brine upwards if high-permeability conduits (e.g., permeable fracture zones or faults) are present. The extent of upward flow of warm brine in the conduit will be affected by overpressure and the density of the upward-displaced fluid. Fluid density in saline systems is controlled by both temperature and salinity. Because of the large difference in thermal diffusivity relative to salt diffusivity, porous media double-diffusive convective effects may arise. In addition, the porous medium alone tends to cause plume separation due to thermal retardation. For high salinity or low over-pressure, brine tends to move up a vertical conduit until it finds a new hydrostatic equilibrium. For low salinity or high overpressure, brine tends to move up the conduit and out into the upper aquifer. In the hypothetical case that the conduit has very low thermal conductivity, warm brine may move up the conduit into an upper aquifer where it
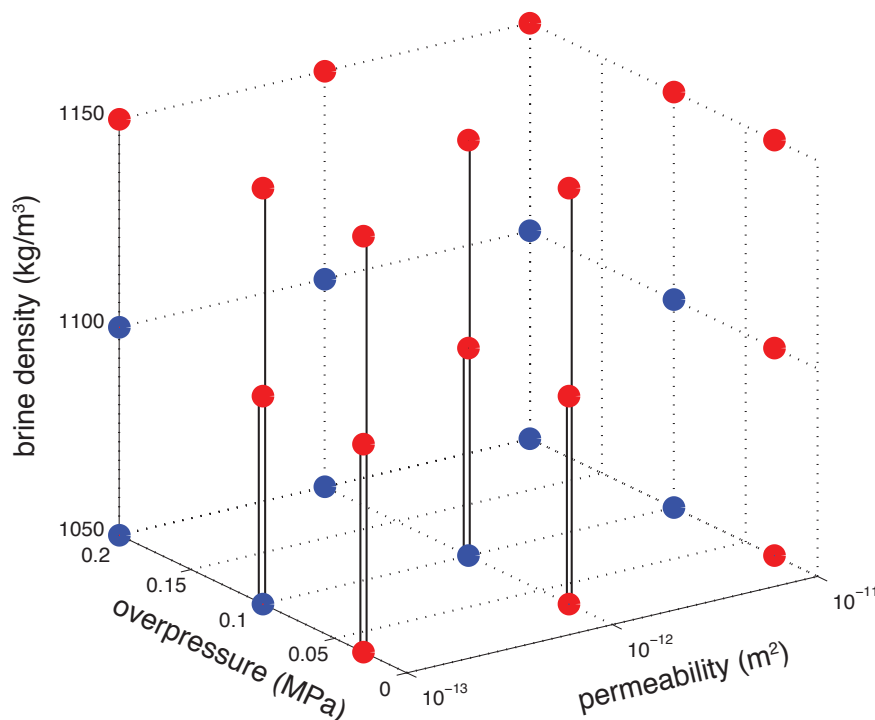
Figure 7.10: Regions of steady-state static (red dots) and oscillatory (blue dots) solutions for the upward brine displacement as a function of pressure rise, salinity, and permeability.

will cool. Once the brine cools, its density may be sufficient to overcome the overpressure and cause brine to flow back down the conduit. Once in the warm lower aquifer, heating will occur again and the cycle may repeat itself. Our simulations show the existence of oscillatory solutions in which this cycle repeats itself at least for hundreds of thousands of years.

References

Apps, J.A., Zheng, L., Zhang, Y., Xu, T., Birkholzer, J.T., 2010. Evaluation of potential changes in groundwater quality in response to CO_2 leakage from deep geologic storage. Transp. Porous Media 82(1), 215–246.

Bachu, S., Burwash, R.A., 1991. Regional-scale analysis of the geothermal regime in the western canada sedimentary basin. Geothermics 20(5–6), 387–407.

Bethke, C.M., 1985. A numerical model of compaction-driven groundwater flow and heat transfer and its application to the paleohydrology of intracratonic sedimentary basins. J. Geophys. Res 90, 6817–6828.

Bethke, C.M., 1986. Hydrologic constraints on genesis of the Upper Mississippi Valley Mineral District from Illinois Basin brines. Econ. Geol. 81, 233–249.

Birkholzer, J.T., Zhou, Q., 2009. Basin-scale hydrogeological impacts of CO_2 storage: regulatory and capacity implications. Int. J. Greenh. Gas Control 3(6), 645–756.

Birkholzer, J.T., Zhou, Q., Tsang, C.F., 2009. Large-scale impact of CO_2 storage in deep saline aquifers: a sensitivity study on pressure response in stratified systems. Int. J. Greenh. Gas Control 3(2), 181–194.

Carey, W.J., Wigand, M., Chipera, S.J., WoldeGabriel, G., Pawar, R., Lichtner, P.C., Wehner, S.C., Raines, M.A., Guthrie, G.D.J., 2007. Analysis and performance of oil well cement with 30 years of CO_2 exposure from the SACROC Unit, West Texas, USA. Int. J. Greenh. Gas Control 1(1), 75–85.

Doughty, C., Meyer, L.R., 2009. Scoping calculations on leakage of CO_2 in geologic storage: the impact of overburden permeability, phase trapping, and dissolution, in: McPherson, B.J., Sundquist, E.T. (Eds.), Carbon Sequestration and Its Role in the Global Carbon Cycle, Geophysical Monograph Series. American Geophysical Union, Washington, DC. volume 183, p. 350.

Garven, G., Freeze, R.A., 1984. Theoretical analysis of the role of groundwater flow in the genesis of stratabound ore deposit. 1. Mathematical and numerical model. Am. J. Sci. 284, 1085–1124.

Gasda, S.E., Bachu, S., Celia, M.A., 2004. Spatial characterization of the location of potentially leaky wells penetrating a deep saline aquifer in a mature sedimentary basin. Environ. Geol. 46, 707–720.

Ginter, W.D., Bachu, S., Benson, S., 2004. The role of hydrogeological and geochemical trapping in sedimentary basins for secure geological storage of carbon dioxide. Geol. Soc. Lond. Special Publ. 233, 129–145.

Gupta, N., Bair, E.S., 1997. Variable-density flow in mid-continent basins and Arches Region of the United States. Water Resour. Res. 33(8), 1785–1802.

Hayek, M., Mouche, E., Mügler, C., 2009. Modeling vertical stratification of CO_2 injected into a deep layered aquifer. Adv. Water Resour. 32, 450–462.

Hindle, A.D., 1997. Petroleum migration pathways and charge concentration: a three-dimensional model. AAPG Bull. 81, 1451–1481.

Intergovernmental Panel on Climate Change (IPCC). Special report on CO_2 capture and storage, IPCC, 2005, in: Metz, B., Davidson, O., de Conick, H., Loos, M., Meyer, L. (Eds.), 431 pp. Ca,mbridge University Press, UK, 2005.

Intergovernmental Panel on Climate Change (IPCC). Fourth Assessment Report: Climate Change 2007 (AR4), in: Solomon, S., Qin, D., Manning, M., Chen, Z., Marquis, M., Averyt, K.B. (Eds.), Contribution of Working Group I. Cambridge University Press, Cambridge, United Kingdom and New York, NY, USA, 2007a.

Intergovernmental Panel on Climate Change (IPCC). Fourth Assessment Report: Climate Change 2007 (AR4), in: Metz, B., Davidson, O.R., Bosch, P.R., Dave, R., Meyer, L.A. (Eds.), Contribution of Working Group III. Cambridge University Press, Cambridge, United Kingdom and New York, NY, USA, 2007b.

International Energy Agency (IEA). Statistics for world total primary energy supply, 2010.
    http://www.iea.org/stats/graphresults.asp?COUNTRY_CODE=29 .

International Formulation Committee (IFC). A Formulation of the Thermodynamic Prop-
    erties of Ordinary Water Substance. IFC Secretariat, Düsseldorf, Germany, 1967 .

Nicot, J.P., 2008. Evaluation of large-scale CO_2 storage on fresh-water sections of aquifers:
    an example from Texas Gulf Coast Basin. Int. J. Greenh. Gas Control 2(4), 582–593.

Nicot, J.P., Hovorka, S.D., Choi, J.W., 2009a. Investigation of water displacement following
    a large CO_2 sequestration operations. Energy Procedia 1(1), 4411–4418.

Nicot, J.P., Oldenburg, C.M., Bryant, S.L., Hovorka, S.D., 2009b. Pressure perturbations
    from geologic carbon sequestration: area-of-review boundaries and borehole leakage driv-
    ing forces. Energy Procedia 1(1), 47–54.

Nield, D.A., 1968. Onset of thermohaline convection in a porous medium. Water Resour.
    Res. 4(3), 553–560.

Nordbotten, J.M., Celia, M.A., Bachu, S., 2004. Analytical solutions for leakage rates
    through abandoned wells. Water Resour. Res. 40, W04204.

Oldenburg, C.M., Pruess, K., 1998. Layered thermohaline convection in hypersaline geother-
    mal system. Transp. Porous Media 33, 26–63.

Oldenburg, C.M., Pruess, K., 1999. Plum separation by transient thermohaline convection
    in porous media. Geophys. Res. Lett. 26(19), 2997–3000.

Pacala, S., Socolow, R., 2004. Stabilization wedges: solving the climate problem for the
    next 50 years with current technologies. Science 13305(5686), 968–972.

Phillips, O.M. (Ed.), 1991. Flow and Reactions in Permeable Rocks. Cambridge University
    Press, UK.

Pruess, K., 2008. On CO_2 fluid flow and heat transfer behavior in the subsurface following
    leakage from a geologic storage reservoir. Environ. Geol. 54(9), 1677–1686.

Pruess, K., Oldenburg, C.M., Moridis, G., 1999. TOUGH2 User's Guide, Version 2.0. Paper
    LBNL-43134. Lawrence Berkeley Natl. Lab., Berkeley, CA, USA.

Silin, D., Patzek, T., Benson, S., 2009. A one-dimensional model of vertical gas plume
    migration through a heterogeneous porous medium. Int. J. Greenh. Gas Control 3, 300–
    310.

Stommel, H., Federov, K.N., 1967. Small scale structure in temperature and salinity near
    Timor and Mindanao. Tellus 19, 306–325.

Turner, J. (Ed.), 1973. Buoyancy Effects in Fluids. Cambridge University Press, Cambridge.

Zhang, Y., Oldenburg, C.M., Finsterle, S., 2010. Percolation-theory and fuzzy rule-based
    probability estimation of fault leakage at geologic carbon sequestration sites. Env. Earth
    Sci. 59(7), 1447–1459.

Zheng, L., Apps, J.A., Zhang, Y., Xu, T., Birkholzer, J., 2009. Reactive transport simulations to study groundwater quality changes in response to CO_2 leakage from deep geological storage. Energy Procedia 1(1), 1887–1894.

Zhou, Q., Birkholzer, J., Mehnert, E., Lin, Y., Zhang, K., 2010. Modeling basin- and plume-scale process of CO_2 storage for full-scale deployment. Ground Water 48(4), 494–514.

Zhou, Q., Birkholzer, J., Tsang, C., Rutqvist, J., 2008. A method for quick assessment of CO_2 storage capacity in closed and semi-closed saline formations. Int. J. Greenh. Gas Control 2(4), 626–639.

Conclusion

Detailed conclusion and discussion for the single parts of this thesis can be found at the end of each chapter. Here the main conclusions are briefly summarized. The work has been focused on numerical modeling hydrothermal fluid circulation in volcanic systems and on the signals which may arise from circulating fluids.

Following a conceptual model developed for Campi Flegrei caldera (Italy), hydrothermal system is fed by an input of magmatic fluids, and a system instability corresponds to a period with increased magmatic degassing. A simulation is then composed by a period of instability (unrest), followed by a longer period during which the degassing returns to its initial value. The first two chapters were focused on the effects produced by the system instability on several geophysical and geochemical observables, such as: ground displacement, gravity changes, electrical conductivity, amount, composition and temperature of emitted gases, and extent of the degassing area.

Particular attention was focused on ground displacement, which is calculated following a mathematical model of poro-elasticity developed in this work. Results show that an increasing in degassing rate of a factor 3.5 may produce up to tens of cm of vertical displacement, in a model such as the one developed for Campi Flegrei. The ground displacement model was also applied to the case of Panarea island (Aeolian islands, Italy), as a 3D case study (Appendix A).

Gravity changes derives from changes in average fluid density, and results showed that the instability may lead to changes up to hundreds of μGal. Electrical conductivity, because highly dependent on gas saturation, also shows high variation in a system where a large amount of hot fluids is involved. To produce a more detailed electrical conductivity map of the Solfatara crater, where most of the activity of Campi Flegrei is concentrated, a numerical simulation at shallow depth was performed, modeling the main features of the crater, such as mud pools and fumaroles (Chapter 5). Amount, composition and temperature of the emitted gases, as for the other observables, presented measurable variation of the same order of magnitude of the observed signals. Temporal and radial pattern of variation were also analyzed. The studied parameters do not show always the same temporal evolution, and the evolution of fluid circulation is associated with a complex pattern of variation along the surface.

Numerical simulations run with the same boundary conditions have highlighted differences that arise from the assumption of different porous medium permeabilities, for both homogeneous and heterogeneous systems, as showed in Chapter 4. Rock properties affects the timing and magnitude of simulated changes in the considered observables, controlling the long-term trend in a complex way. High permeability and channeling favor faster and larger changes of all the observables.

Low temperature volcanic system, such as the case of Furnas volcano (S. Miguel island, Azores), has been also modeled to study the effects of atmospheric conditions

on diffuse degassing. Applying time-dependent boundary conditions (air temperature and barometric pressure) at the surface, a dual parameters study was performed changing the rock permeability and the reservoir overpressure, which allow fluids to rise. Results show as a time delay develop between CO_2 flux and temperature (or pressure) time series, in agreement with data observed at Furnas, and this time delay changes as a function of both rock permeability and reservoir overpressure.

Although hydrothermal system can be often related to a volcanic system, hot fluids are involved in many mankind applications, such the geological carbon sequestration, i.e. the direct injection of supercritical CO_2 into deep geological formations containing brine. The injection may displace this brine upward through a conduits (abandoned well or permeable faults,) and then degrade the groundwater. Results from numerical simulations show as the overpressure due to a far injection may drive the brine up conduits. Pressure rise does not necessarily result in continuous flow, rather the pressure changes leads to a new hydrostatic equilibrium if fluids are initially stratified. Moreover, in a hypothetical case where warm and salty fluid is allowed to cool in the groundwater, it becomes denser than it was originally and flows back down the conduits where it warms up again only to repeat the process. Parameter studies delineate steady-state (static) and oscillatory solutions and reveal the character and period of oscillatory solutions.

# Modeling vertical ground displacement at Panarea volcano

Contents

A.1 Introduction

Between November 2nd and 3rd 2002 an intense submarine gas eruption started about 2 km in the offshore (Fig. A.1), east of Panarea island (Aeolian islands, Italy). Gas emission was accompanied by ground deformation, and GPS data show an uplift of ∼4 cm at Panarea islands (Esposito et al., 2006, 2010). To investigate the coupling between hydrothermal fluids and ground deformation we simulated a 3D model, representing a first-step approximation of Panarea volcano. Starting from our experience on Campi Flegrei, we applied here the ground deformation mathematical model discussed in Chapter 2 (see also Rinaldi et al., 2010), simulating three different unrest scenarios. This work represents a good theoretical exercise and test in a 3D modeling of the ground displacement model.

Panarea island is a volcano located in the Aeolian volcanic arc between the Calabrian arc and the Southern Tyrrhenian sea (Fig. A.1). The Aeolian volcanic arc is an archipelago that comprises 7 main islands (Alicudi, Filicudi, Salina, Lipari, Vulcano, Panarea, and Stromboli), and several sea-mounts. Aeolian archipelago features an active volcanism, with high and low temperature fumaroles over each island, and ongoing magmatic eruption events at Stromboli volcano. Volcanism is mainly associated to the subduction of the Ionian lithosphere beneath the Calabrian arc (Faccenna et al., 2005), where the slab deepening produces shallow and deep seismicity (Chiarabba et al., 2005). Active structural deformation is also associated to the subduction process (Anzidei, 2000; Serpelloni et al., 2005; Tallarico et al., 2003).
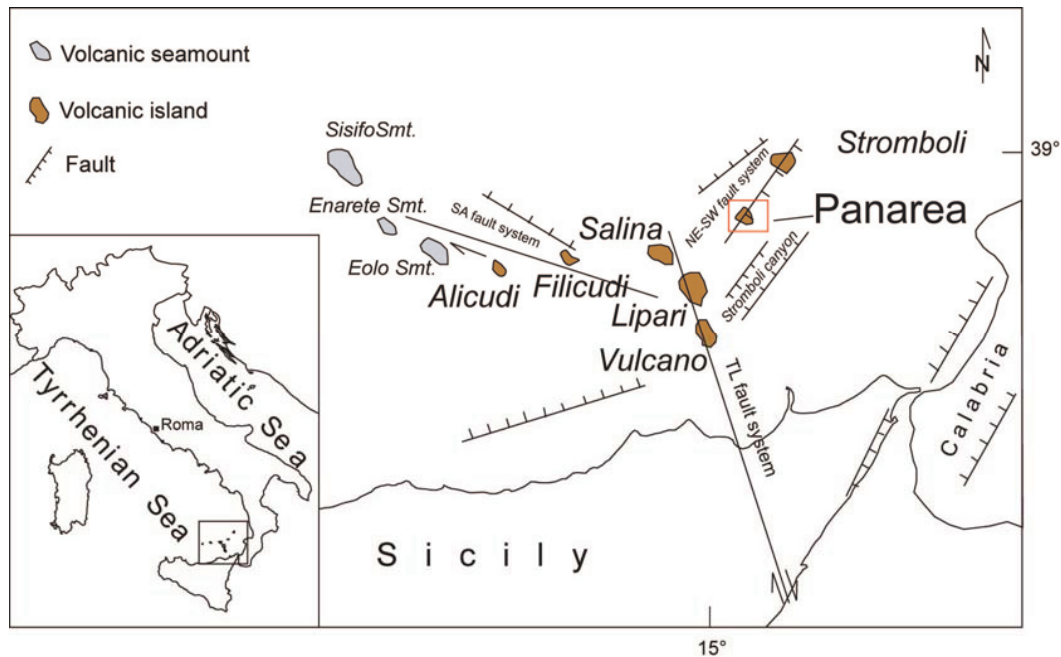
**Figure A.1**: Location and structural sketch map of the Aeolian volcanic arc.

Panarea island is the emergent portion of a $\sim$1.6 km high and $\sim$18 km wide submarine stratovolcano located on the eastern active sector of the Aeolian volcanic arc (Favalli et al., 2005; Esposito et al., 2010). The submarine volcano features a large platform at $\sim$ 100 m under the sea level, and the emergent portion of this platform forms, in addition to Panarea island, a small archipelago with several small islets (Basiluzzo, Dattilo, Panarelli, Lisca Bianca, Bottaro, Lisca Nera, and Le Formiche) at East of Panarea.

Effusive and explosive volcanic eruptions occurred at Panarea volcano between about 150 ka and 8 ka (Dolfi et al., 2007). Before 2002 the activity of Panarea volcano was characterised by mild degassing of hydrothermal fluids due to cooling of magma reservoir, and degassing activity is well known at Panarea since historical times (Calanchi et al., 1995; Anzidei, 2000).

The gas emission of November 2002 was accompained by a low magnitude ($<$1.8 M) earthquake (Saccorotti et al., 2003). The most intense gas vent was recognized west of the islet Bottaro (Fig. A.2), with a rate of 10^8-10^9 lt/day (Caliro et al., 2004), i.e. two order of magnitude greater than average total gas flux measured previously in the Panarea area (Italiano and Nuccio, 1991). Average temperature of sea water rose up to 22-23 °C, and direct measurements showed temperatures up to 50 °C (Capaccioni et al., 2003). Maximum temperature (110 °C) was reached in April 2003 (Caramanna et al., 2003). The gas flow rate gradually reduced, and reached normal condition in September 2003. Compositional analysis of gas emitted at Panarea shows that the hydrothermal system is fed by a source of magmatic fluids (Italiano and Nuccio, 1991; Caliro et al., 2004; Chiodini et al., 2006), which may
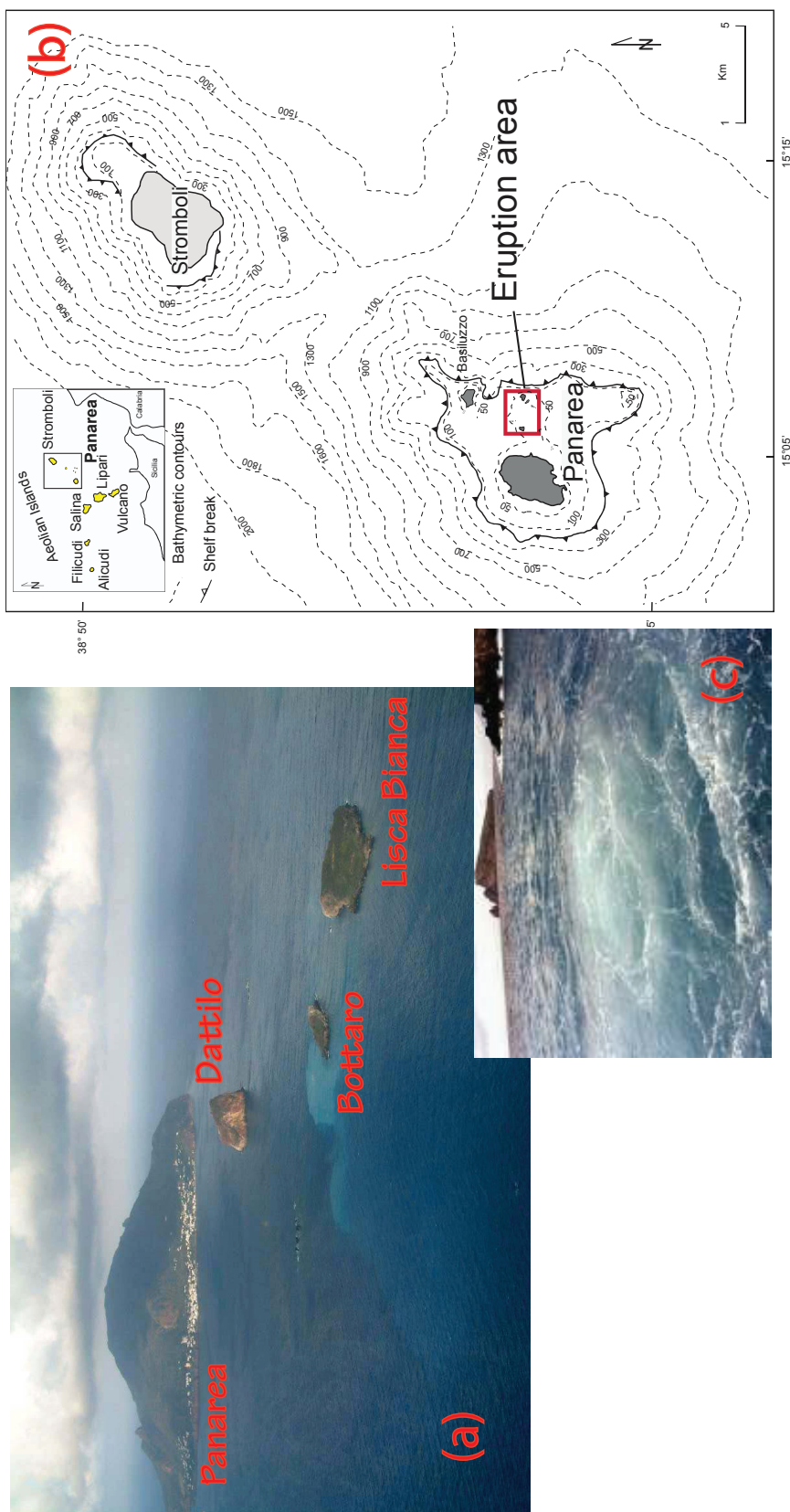
Figure A.2: (**a**) aerial view of Panarea island and islets. (**b**) Bathymetry of Panarea and Stromboli volcano. (**c**) The gas rose to the sea surface forming bubbles some meters in diameter (Photo by L. Lodato, INGV-Catania).
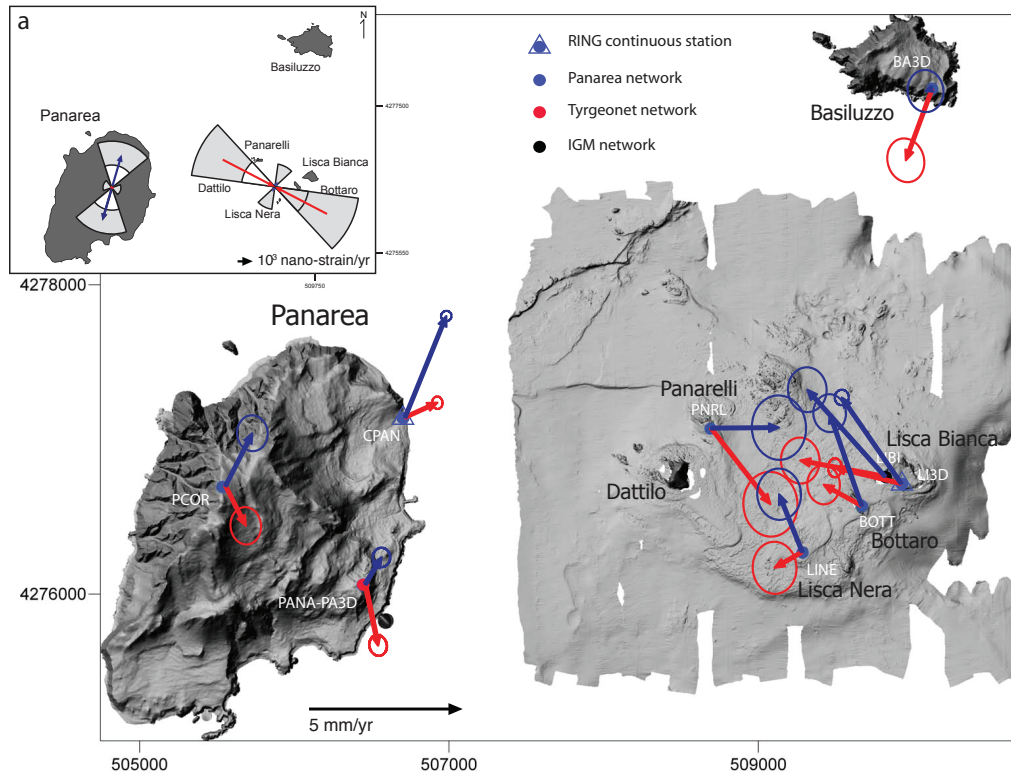
Figure A.3: DEM and MDEM of Panarea volcano (Esposito et al., 2006). GPS velocities fields in blue with respect to EURASIA_ITRF05; in red with respect to Panarea volcano rigid motion. (**a**) principal axes of horizontal strain rate tensor and associate 1σ error. Blue arrows indicate extension; red arrows indicate shortening.

produce an overpressure able to overcome tensional strength of the confining rock, allowing the rise of gases (Esposito et al., 2006).

A.2   GPS data

GPS monitoring was performed by A. Esposito and M. Anzidei of the "Istituto Nazionale di Goefisica e Vulcanologia", section of Rome. The local GPS Panarea network consists of 8 non permanent stations located on the Panarea island and on Basiluzzo, Lisca Bianca, Bottaro, Lisca Nera, and Panarelli islets (PANA; PA3D; PCOR, BA3D, LIBI, BOTT, LINE, PNRL) (Fig. A.3) (Anzidei et al., 2005). Most stations were established after the 2002 gas eruption, while a few stations belong to already existent networks: IGM and Tyrgeonet (Anzidei et al., 1995). GPS data analysis was performed combining the episodic campaigns of Panarea and other local networks located in the Aeolian area, carried out between 1995 and 2006, and data of 200 continuous European and Italian sites. For each campaign daily loosely constrained solutions were generated using Bernese GPS software 5.0 (Dach et al., 2007) and later combined with about 10 years of daily loosely constrained
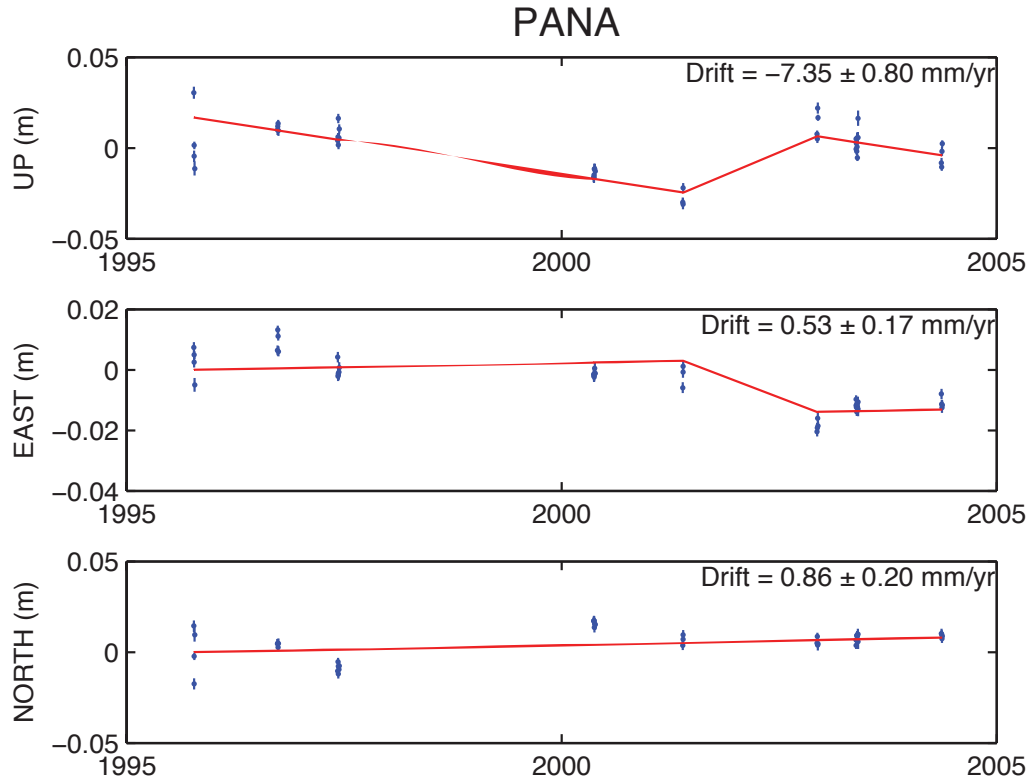
Figure A.4: Coordinate time series of PANA station relative to Eurasia

solutions of the large network (Serpelloni et al., 2007): to perform the combination, 9 of these stations, belonging to the IGS network and included in the ITRF05 solution (Altamini et al., 2007), were also included in all campaign processing. The combination was performed by a rigorous strategy, based on the complete covariance matrices and a convenient handling of constraints.

The results show at Panarea volcano two distinct crustal domains characterized by different kinematics and styles of deformation (Fig. A.3). Extension is recognized between Panarea island and its archipelago. Shortening WNW-trending of the order of 10^{-6}, is present in the islets area. The time series of all sites in the Panarea network show presently a general subsidence; the site of PANA (Fig. A.4) shows an uplift of 4.2±0.5 cm in correspondence of gas eruption event, apparently not affecting the general subsidence pattern before and after December 2002.

A.3 Modeling hydrothermal system at Panarea

In order to investigate the coupling between hydrothermal fluids and ground displacement, we have set a simulation using the TOUGH/EOS2 geothermal simulator (see Chap. 1 and Pruess et al., 1999). The 3D mesh grid has been built taking into account the bathymetry of Panarea submarine volcano (Fig. A.5). Computational
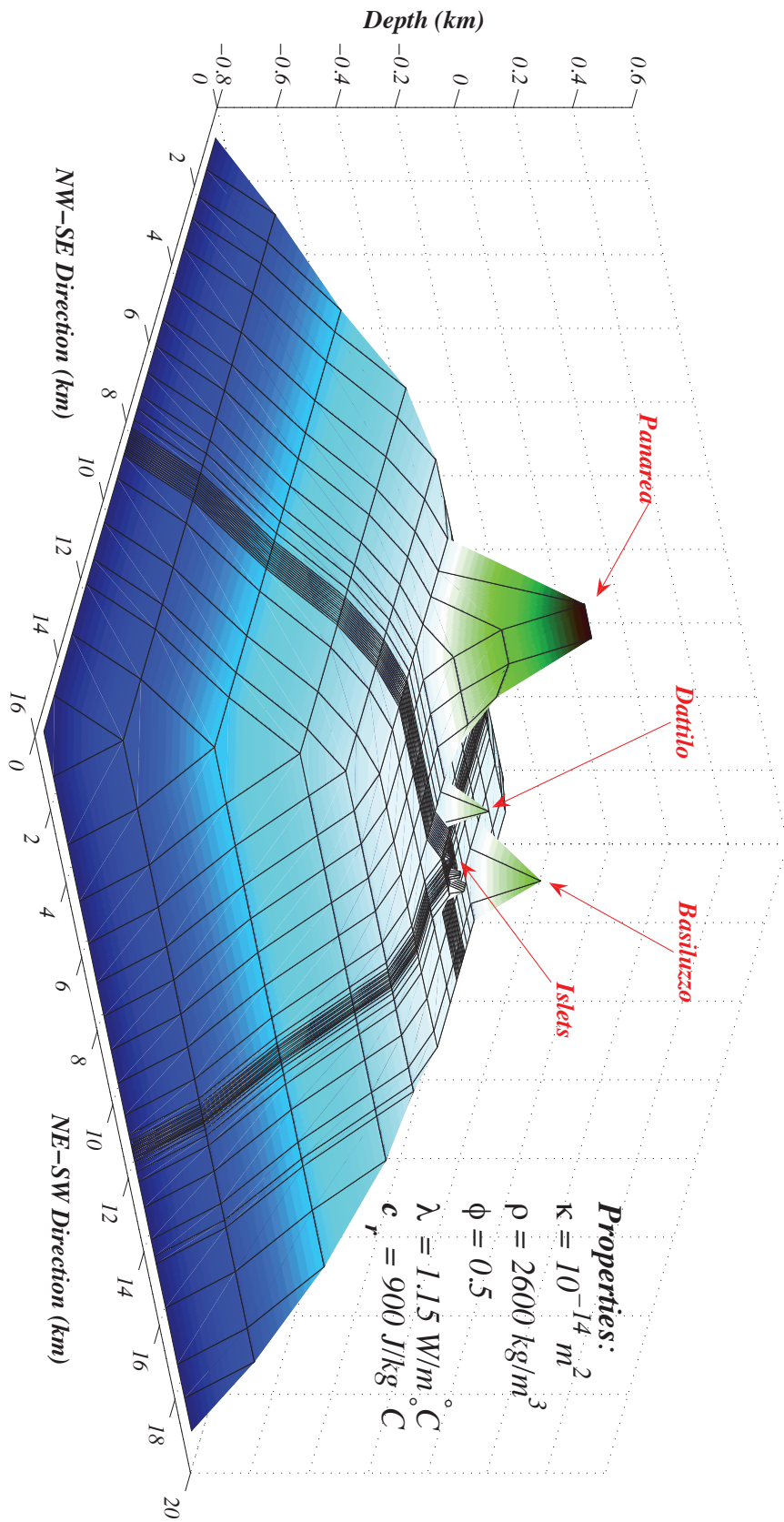
Figure A.5: Meshgrid used in TOUGH2/EOS2 simulations. Main islands and rock properties used in the simulation are also indicated. κ is the permeability, ρ is the rock density, ϕ is the porosity, λ is the thermal conductivity, and c_r is the rock specific heat.

Properties:
$\kappa = 10^{-14} \ m^2$
$\rho = 2600 \ kg/m^3$
$\phi = 0.5$
$\lambda = 1.15 \ W/m \cdot {}^{\circ}C$
$c_r = 900 \ J/kg \cdot {}^{\circ}C$

Table A.1: Fluid source activity: mass flow rate and enthalpy of injected fluids.

| Injected fluids	Amount (tons/day)	Enthalpy (kJ/kg)
CO_2	600	290
H_2O	1200	2800

domain is 20 km wide in the NE-SW direction and 16 km wide in NW-SE direction. It reaches a depth of -800 m below the sea level, and the maximum height is at Panarea island, where altitude reaches 420 m above the sea level. Top boundary is open to fluid flow, and side and bottom boundaries are impervious and adiabatic. We set atmospheric condition (p,T, p_{CO_2}) at surface, while bottom boundary has fixed temperature (180 °C) and pressure (8.7 MPa). We have placed an inlet of hot fluids at the bottom boundary, exactly below the islets. The fluid source discharges hot water and CO_2 at fixed enthalpy, over an area of 7500 m^2. Mass flow rate has been chosen based on our experience on Campi Flegrei caldera, and are listed in Table A.1.

Steady state conditions have been created simulating a long lasting (thousands of years) injection of hot fluid. The gas distribution produced during the injection is shown in Fig. A.6. A single phase plume develops in the domain below the islets, where the inlet of fluid is placed (Fig. A.6a,b). Plume has two components (water and carbon dioxide) with a CO_2 fraction of 0.4 (Fig. A.6c,d). Temperature distribution is characterized by high temperature (up to 300 °) where the plume is present, below the islets (Fig. A.7c,d). Convective cells develop in the rest of the domain. Fig. A.6a,b shows the temperature distribution below the Panarea island. A linear pressure gradient characterizes the whole domain (Fig. A.7a,b), and a high overpressure (greater than 14 MPa) forms in the region near the fluid inlet, allowing the rise of gases toward the islets, where gas emission was recognized during November 2002 crisis.

A.4   Unrest and vertical ground displacement

Starting from the steady-state conditions described previously, we have carried out simulations of three different unrest scenarios. The unrest is considered as a period during which the amount of injected fluids is increased with respect the steady state condition. Unrests, here simulated, have different length and intensities, and are followed by a longer period of quiet during which mass flow rate either returns to steady state conditions or no injection is considered. Unrest and quiet condition are listed in Table A.2.

High fluid injection during unrest produces a pressure build up near the inlet of fluids (Fig A.9a,b,c). An unrest period of 1 yr, as in the case 1 (see Tab. A.2),
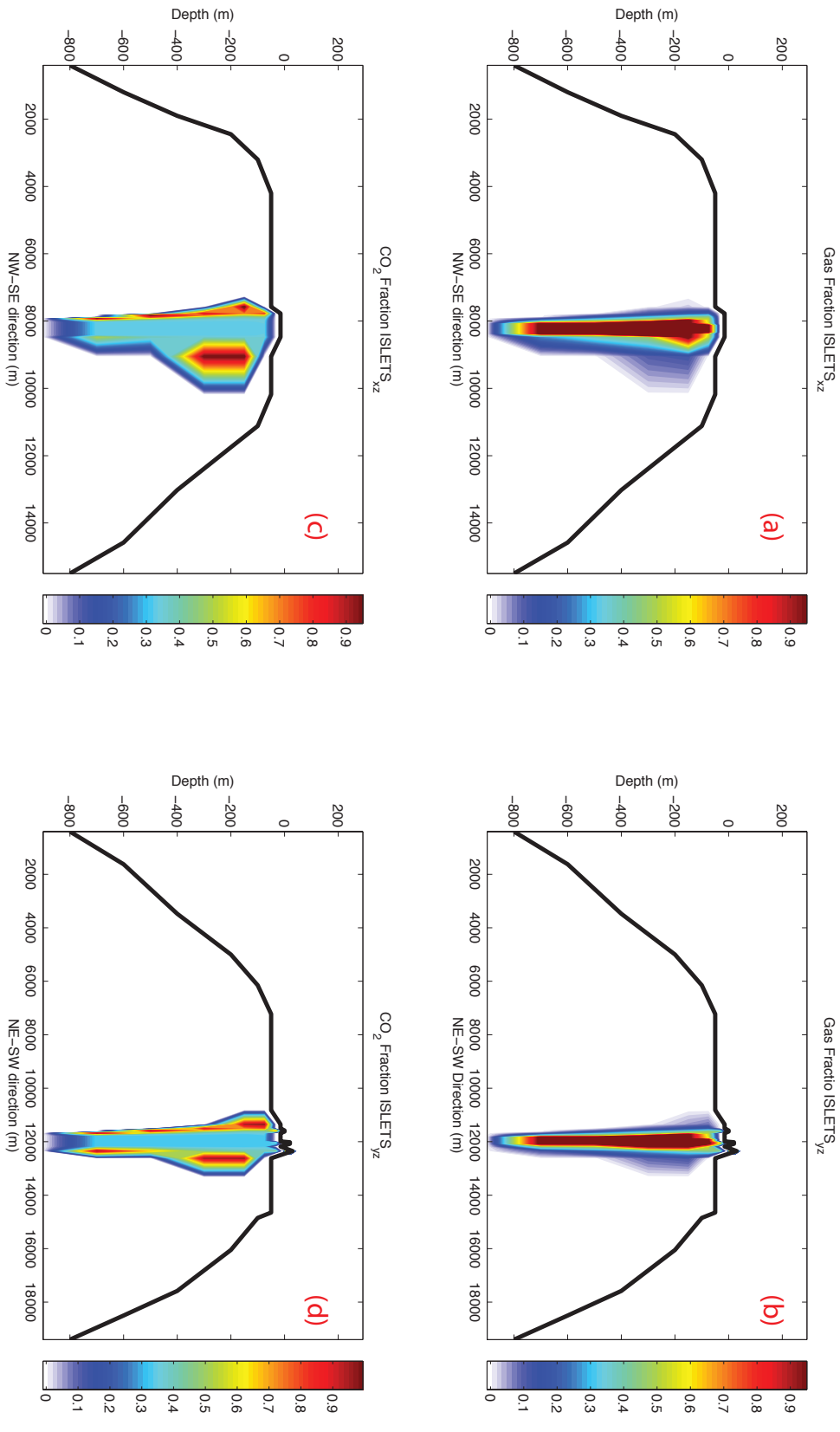
Figure A.6: **(a,b)** Gas fraction in the region below the islets in XZ- and YZ-plane respectively. **(c,d)** CO_2 fraction in the region below the islets in XZ- and YZ-plane respectively.
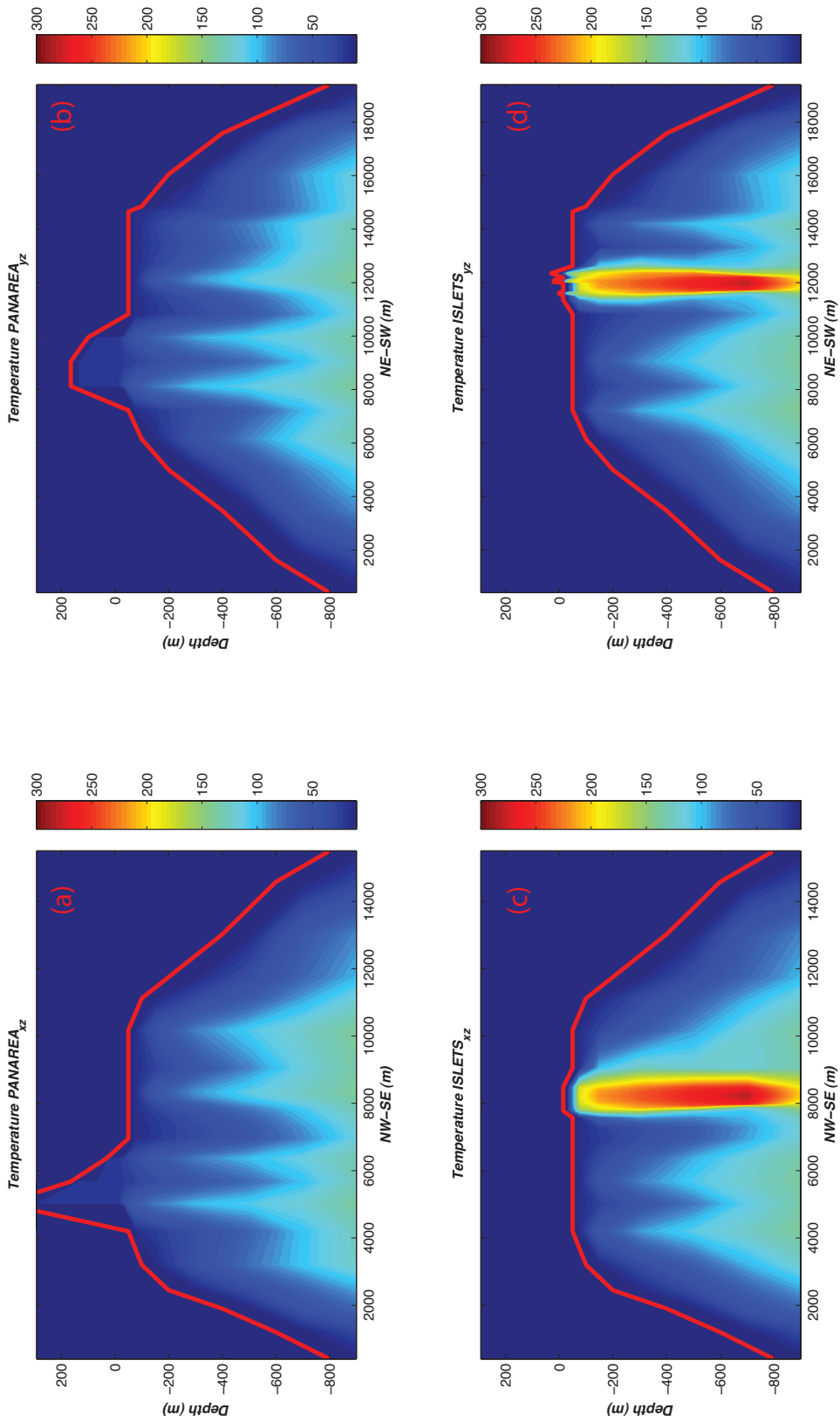
Figure A.7: (**a**,**b**) Temperature distribution below Panarea island in XZ- and YZ-plane, respectively. (**c**,**d**) Temperature distribution below the islets in XZ- and YZ-plane, respectively.
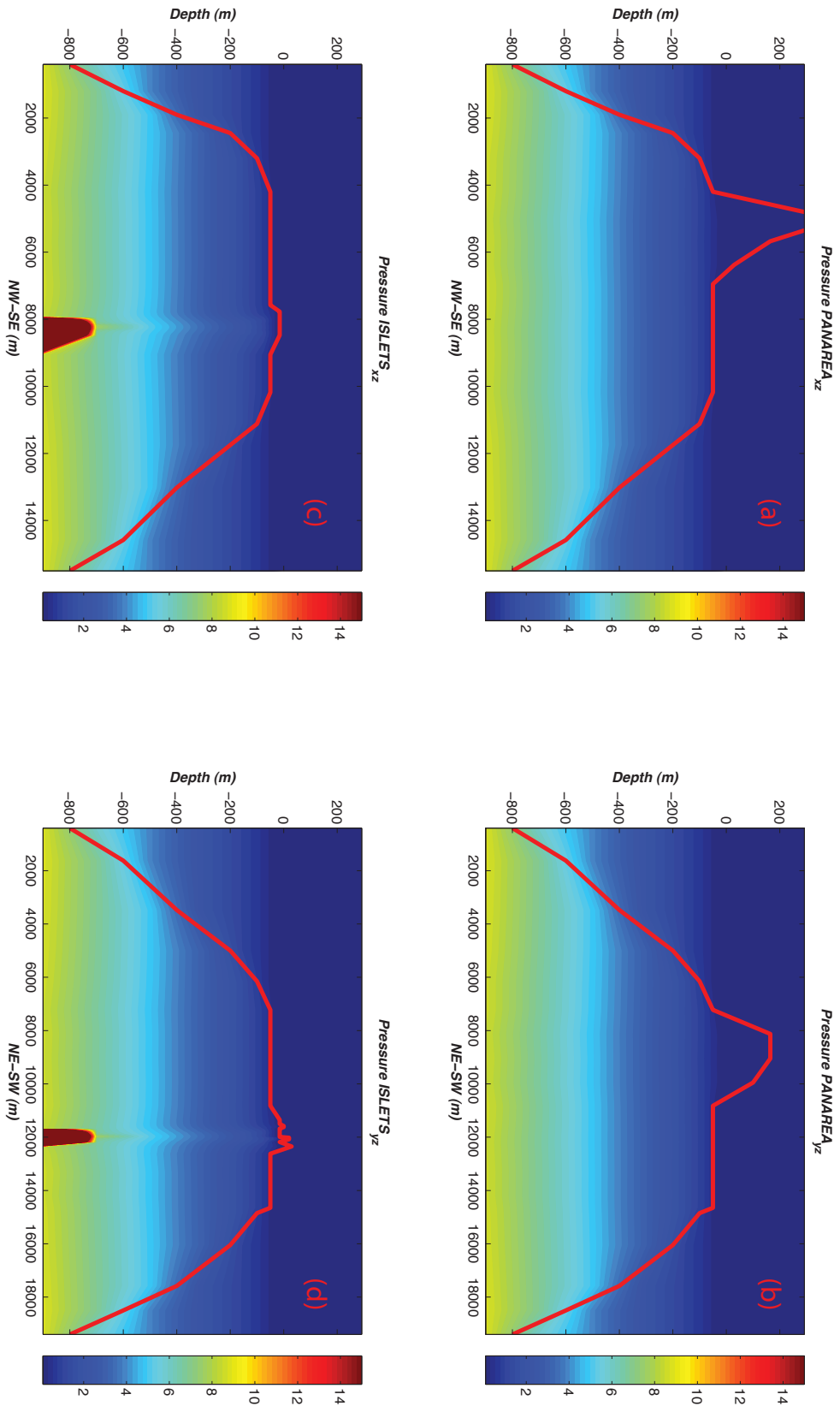
Figure A.8: (**a,b**) Pressure distribution below Panarea island in XZ- and YZ-plane, respectively. (**c,d**) Pressure distribution below the islets in XZ- and YZ-plane, respectively.

Table A.2: Unrest and quiet period: duration and injection rate.

	UNREST	QUIET
Case 1	1 yr (10x)	4 yr (1x)
Case 2	5 yr (10x)	45 yr (1x)
Case 3	5 yr (10x)	45 yr (-)

produces pressure changes up to 9 MPa (Fig. A.9a), whereas a longer injection (5 yrs), as in the cases 2 and 3, produce pressure changes up to 12 MPa (Fig. A.9b,c), even if the same amount of gases is injected in each case. Temperature changes are also associated to the high injection during an unrest, as shown in Fig. A.9d,e,f. Temperature varies mostly at inlet and in the gas plume, and temperature change reaches a value of 50 °C during short unrest (Fig. A.9d) and values up to 100 °C when a long unrest is simulated (Fig. A.9e,f). Pressure returns almost at steady state value (Case 1 and 2, Fig. A.10a,b), however if the injection is null as in the Case 3, we observe a pressure drop of few MPa (Fig. A.10c). The system is still at higher temperature with respect to steady state when a low level injection is present during quiet period (Case 1 and 2, Fig. A.10d,e). When we stop injecting fluid at inlet during quiet period (Case 3), we observe a temperature lowering at inlet, with value up to -80 °C near the fluid source.

Pressure and temperature changes can be used as a source of deformation. Using a mathematical model by Rinaldi et al. (2010), described also in Chap. 2, we calculated the ground displacement at different points of the considered domain (Fig. A.5). In this chapter we only considered the vertical component of the ground displacement, since it can be mainly affected by changes in hydrothermal system, rather than horizontal component, which is biased by the large tectonic component present in the Aeolian area. Recalling here the equation for vertical ground displacement, we have for each element considering the observation point at sea level:

$$u_z^{el} = \frac{(1+\nu)}{3\pi}\Delta\theta^{el}V^{el}\frac{z^{el}}{R^3}$$

with:

$$\begin{cases} \Delta\theta^{el} = \dfrac{\Delta p^{el}}{K} + \alpha_s\Delta T^{el} \\[2mm] R = \sqrt{(x^{el}-x^{ob})^2 + (y^{el}-y^{ob})^2 + (z^{el})^2} \end{cases}$$

we consider an effective bulk modulus K=10 GPa and a rigidity μ=5 GPa (then a Poisson's coefficient ν=0.25). α_s=3·10^{-5} °C^{-1} is the volumetric expansion coefficient of the solid matrix.

Resulting vertical ground displacement for the Case 1 is shown in Fig. A.11. In this first case, where the unrest lasts for 1 yr, vertical displacement reaches a value of
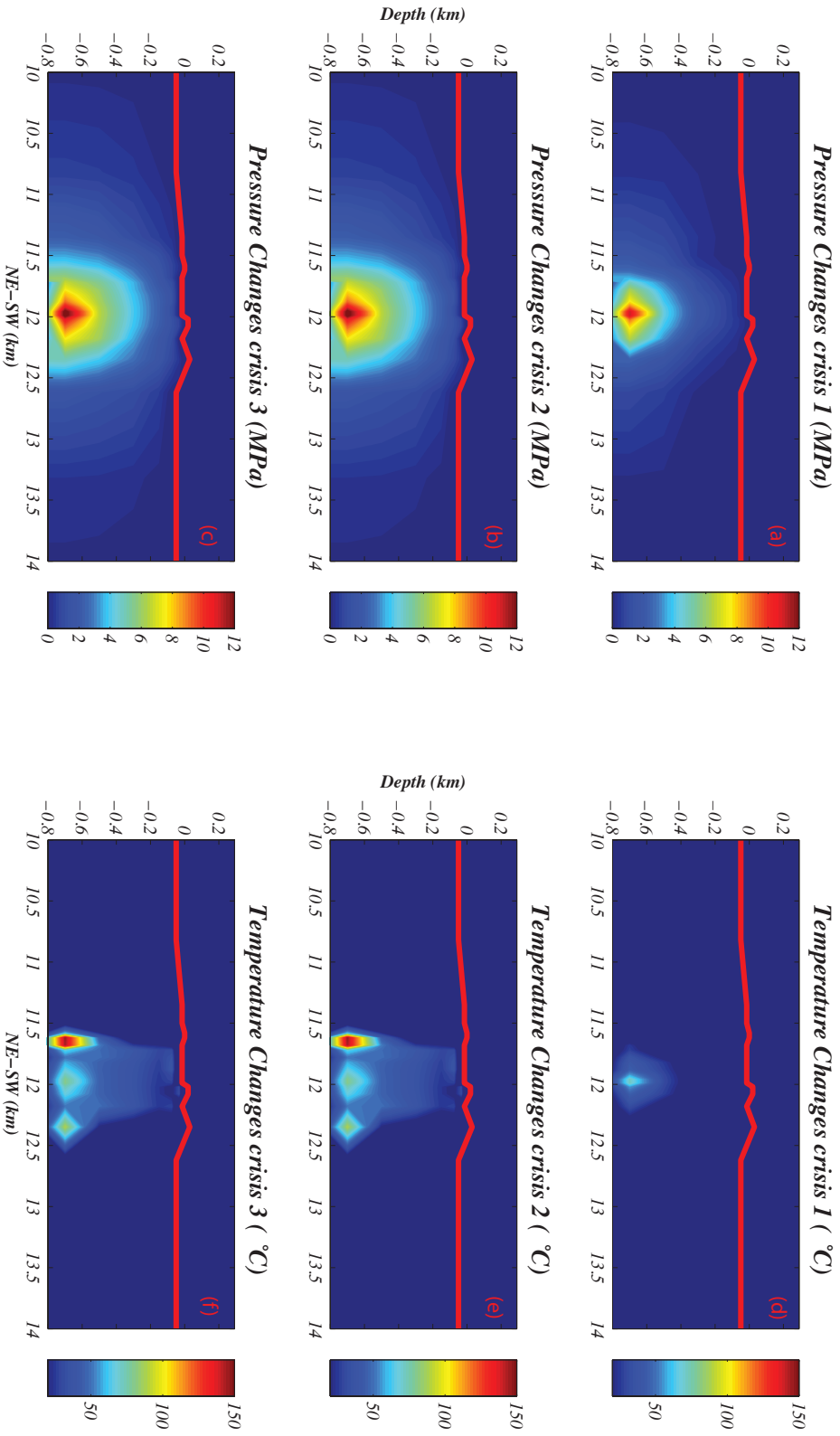
Figure A.9: **(a,b,c)** Pressure changes at the end of the unrest for the three cases below the islets YZ-plane, respectively. **(d,e,f)** Temperature changes at the end of the unrest for the three different cases below the islets in YZ-plane.
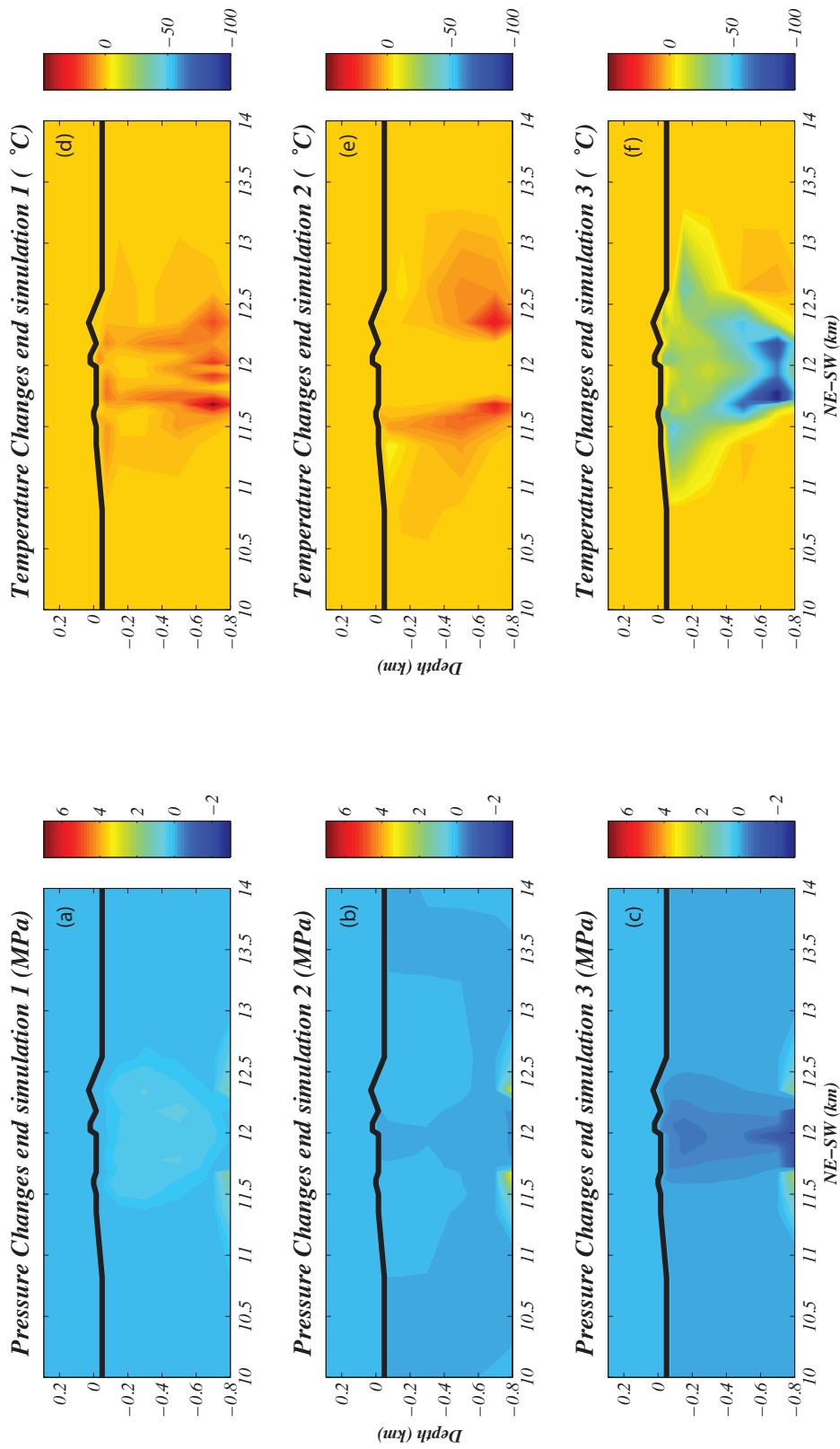
Figure A.10: (**a,b,c**) Pressure changes at the end of the simulation for the three cases below the islets YZ-plane, respectively. (**d,e,f**) Temperature changes at the end of the simulation for the three different cases below the islets in YZ-plane.
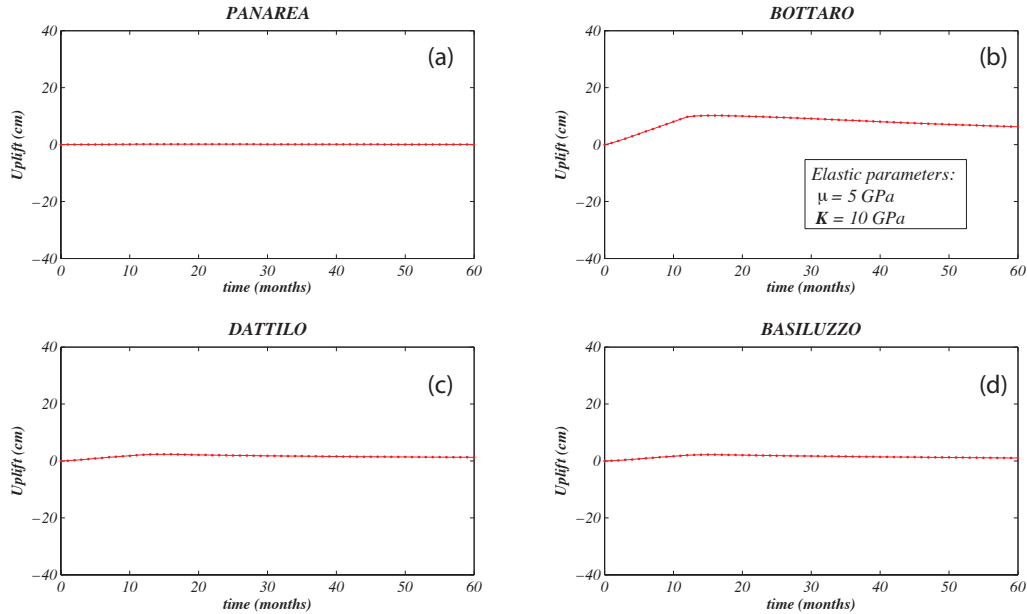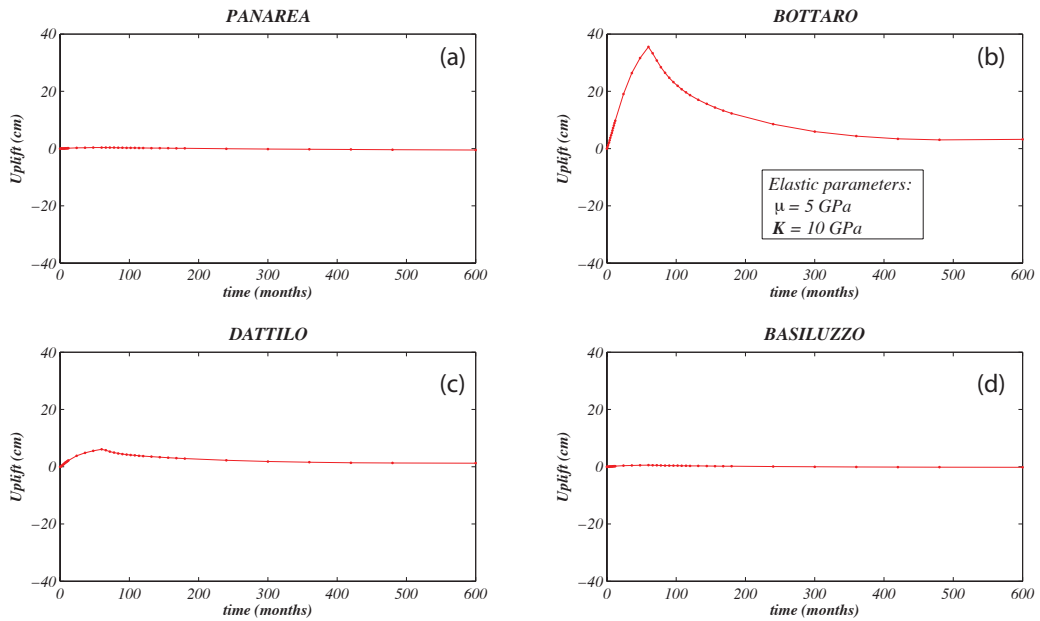
Figure A.11: Vertical displacement computed at different locations for the Case 1. (**a**) Displacement at Panarea island. (**b**) Displacement at Bottaro islet, i.e. at sea level above the inlet of fluids. (**c**) Displacement at Dattilo. (**d**) Displacement at Basiluzzo.

about 10 cm at Bottaro islet (Fig. A.11b), i.e. right above the fluid inlet at surface, at the end of the unrest. When fluxes return to steady state value, we observe a very slow subsidence for the remaining 4 yr of simulation. Displacement computed at different locations do not present remarkable values, with order of magnitude of mm (Fig. A.11a,c,d). This behavior is due to lateral spreading of temperature and pressure changes, which does not change beyond 1 km from the inlet of fluids (Figs. A.9 and A.10). Panarea island, for example, is at about 3 km from Bottaro inlet, then changes in hydrothermal fluid circulation do not affect the domain below the main island.

Case 2 and 3 have the same, long unrest phase (5 yr). Vertical displacement computed for Case 2 and 3 is shown in Figs. A.12 and A.13. The long unrest is able to displace the surface up to ∼40 cm of uplift at Bottaro (Figs. A.12b and A.13b), and small changes (few cm) are observed also at Dattilo islet, which is relatively near (1 km from Bottaro) to the fluid source region (Figs. A.12b and A.13b). Also in this two cases, no remarkable uplift is computed at Panarea and Basiluzzo (Figs. A.12a,d and A.13a,d).

Case 2 and 3, however, have a different pattern of deformation during the quiet period. In Case 2, fluid activity returns to a steady state value, then at Bottaro we observe a general slow pattern of subsidence, and the uplift is almost null at the end of the simulation (Fig.A.12b). In Case 3, we simulate a scenario where no fluid injection is supposed to be present during the quiet period. The absence of fluid

Figure A.12: Vertical displacement computed at different locations for the Case 2. (**a**) Displacement at Panarea island. (**b**) Displacement at Bottaro islet, i.e. at sea level above the inlet of fluids. (**c**) Displacement at Dattilo. (**d**) Displacement at Basiluzzo
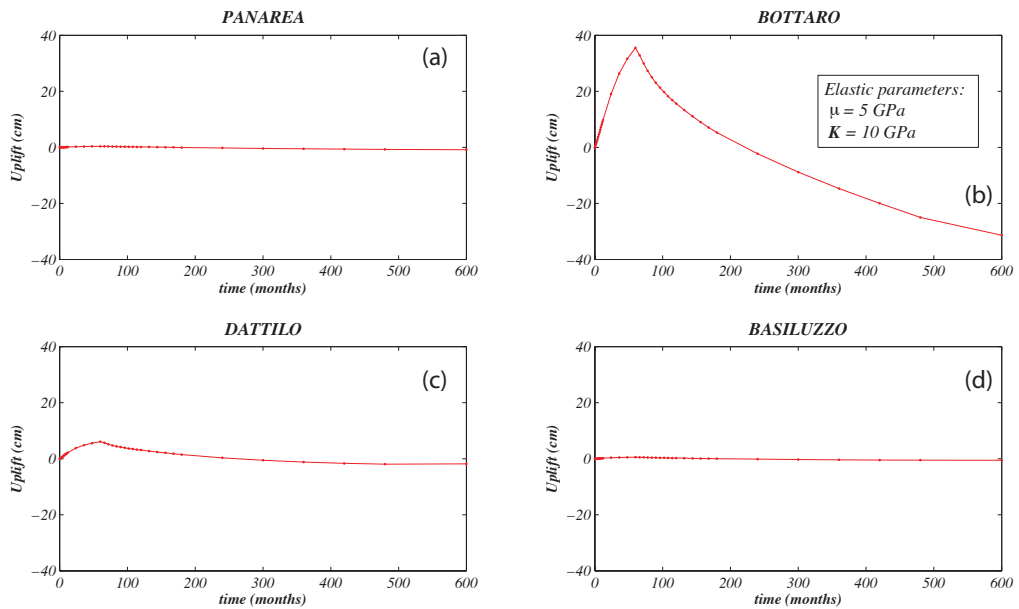
Figure A.13: Vertical displacement computed at different locations for the Case 3. (**a**) Displacement at Panarea island. (**b**) Displacement at Bottaro islet, i.e. at sea level above the inlet of fluids. (**c**) Displacement at Dattilo. (**d**) Displacement at Basiluzzo

injection leads to a high pressure drop of few MPa and high temperature lowering in the fluid source region (Fig. A.10c,f), and resulting then in a subsidence much faster than Case 2 (Fig. A.13b). At the end of simulation, a value of -50 cm is attained, i.e. with a subsidence rate of 2.5 cm per year.

A.5   Conclusion

A first-step modeling of the hydrothermal fluid circulation of the submarine volcano at Panarea has been presented in this chapter. GPS data analysis has shown a vertical ground displacement in correspondence of a gas eruption at islets in November 2002. Starting from our experience in modeling hydrothermal fluid circulation at Campi Flegrei, we have applied here the same conceptual model, taking into account an hydrothermal system fed by a magmatic component of gases injected at the bottom of the domain (Chiodini et al., 2003). The eruption has been modeled as a crisis of the system, taking into account a higher injection of fluid for a period of time. After simulating an unrest period followed by a longer quiet period, we have calculated the arising vertical displacement using a mathematical model of poro-elasticity (Rinaldi et al., 2010)

Higher flow rate at the fluid source causes measurable uplifts at the surface (up to tens of cm) Properties and duration of unrest control the deformation history. Three different scenarios have been simulated. Case 1, which presents the shortest unrest length, produce up to 10 cm of uplift at the end of the crisis. Case 2 and 3, with a much longer unrest period (5 yr), can produce up to 40 cm of deformation. Also the system behavior during the quiet phase may play a big role. In Case 1 and 2, the injection returns to initial value after the unrest period, and these scenarios produce a subsidence which leads the vertical ground displacement to a zero value at the end of simulation. However, when the injection is null during the quiet period, subsidence is much faster (2.5 cm/year), and at the end of simulation ground surface is at a depth much lower than the initial value. In all the simulated scenario, the displacement is almost zero a few km far from the source of fluids.

Present results are not consistent with trends observed on the island of Panarea, because of a few main limitations of the proposed model. Properties and condition of the hydrothermal system are poorly constrained, and we are not able to identify the location of the main bottom source. Recorded displacement at Panarea imply that pressure and temperature anomalies should be greater below the main island, i.e. a greater amount of fluid should characterize the hydrothermal system. Probably a generalized pressure variation at the bottom of the whole system may explain the high displacement registered at Panarea islands without any gas emission. Furthermore, we are simulating a homogeneous system, but heterogeneity are presents in the Panarea archipelago, because of the active tectonic affecting the Aeolian region.

Results from unrest Case 3, highlight as a the total absence of fluid injection may lead to a very fast subsidence. Such subsidence was not observed at Panarea archipelago, indicating that hot fluids are still feeding the hydrothermal system.

References

Altamini, Z., Collilieux, X., Legrand, J., Garayt, B., Boucher, C., 2007. ITRF2005: a new release of the international terrestrial reference frame based on time series of station positions and earth orientation parameters. J. Geophys. Res. 112, B09401. doi:10.1029/2007JB004949.

Anzidei, M., 2000. Rapid bathymetric surveys in marine volcano areas: a case study Panarea area. Phys. Chem. Earth 25, 77–80.

Anzidei, M., Baldi, P., Casula, G., Riguzzi, F., Surace, L., 1995. La rete Tyrgeonet. Suppl. Bol. Geod.Sc. Aff. LIV, 2 Istituto Geografico Militare Italiano.

Anzidei, M., Esposito, A., Bortoluzzi, G., De Giosa, F., 2005. The high resolution bathymetric map of the exhalative area of Panarea Aeolian islands, Italy. Ann. Geophys. 48, 899–921.

Calanchi, N., Capaccioni, B., Martini, M., Tassi, F., Valentini, L., 1995. Submarine gas-emission from Panarea Island Aeolian Archipelago: distribution of inorganic and organic compounds and inferences. Acta Vulcanol. 7, 43–48.

Caliro, S., Caracausi, A., Chiodini, G., Ditta, M., Italiano, F., Longo, M., Minopoli, C., Nucco, P.M., Paonita, A., Rizzo, A., 2004. Evidence of a new magmatic input to the quiescent volcanic edifice of Panarea, Aeolian Islands, Italy. Geophys. Res. Lett. 31, L07619. doi:10.1029/2003GL019359.

Capaccioni, B., Rossi, P.M., Tassi, F., Tedesco, D., Vaselli, O., 2003. Risultati delle osservazioni geochimica presso l'isola di Panarea in seguito all'evento di degassamento sottomarino del 3 novembre 2002. Abstract, GNV General Assembly, p. 17.

Caramanna, G., Carapezza, M.L., Cioni, R., Cardellini, F., Cinti, D., Lelli, M., Pizzino, L., Quattrocchi, F., Voltattorni, N., 2003. Primi sei mesi di monitoraggio elle diverse fasi (solida-liquida e gassosa) presso le esalazioni sottomarine di Panarea a partire dal novembre 2002. Abstract, GNV General Assembly P. 19.

Chiarabba, C., Jovane, J., Di Stefano, R., 2005. A new view of italian seismicity using 20 years of instrumental recordings. Tectonophysics 395, 251–268.

Chiodini, G., Caliro, S., Caramanna, G., Granieri, D., Monopoli, C., Moretti, R., Perotta, L., Ventura, G., 2006. Geochemistry of submarine gaseous emission of Panarea Aeolian Islands, Southern Italy: magmatic vs. hydrothermal origin and implications for volcanic surveillance. Pure Appl. Geophys. 163, 759–780. doi:10.1007/s00024-006-0037-y.

Chiodini, G., Todesco, M., Caliro, S., Del Gaudio, C., Macedonio, G., Russo, M., 2003. Magma degassing as a trigger of bradyseismic events: the case of Phlegrean Fields (Italy). Geophys. Res. Lett. 30(8), 1434–1437. doi:10.1029/2002GL016790.

Dach, R., Hugentobler, U., Fridez, P., Meindl, M., 2007. Bernese GPS software. version 5.0 AIUB .

Dolfi, D., de Rita, D., Cimarelli, C., Mollo, S., Soligo, M., Fabbri, M., 2007. Dome growth rates, eruption frequency and assessment of volcanic hazard: insight from new U/Th dating of the Panarea and Basiluzzo dome lavas and pyroclastics, Aeolian Islands, Italy. Quat. Int. 162-163, 182–194. doi:10.1016/j.quaint.2006.05.035.

Esposito, A., Anzidei, M., Atzori, S., Devoti, R., Giordano, G., Pietrantonio, G., 2010. Modeling ground deformations of Panarea volcano hydrothermal/geothermal system (Aeolian Islands, Italy) from GPS data. Bull. Volcanol. 72(5), 609–621. doi: 10.1007/s00445-010-0346-y.

Esposito, A., Giordano, G., Anzidei, M., 2006. The 2002-2003 submarine eruption a Panarea volcano (Aeolina Islands, Italy): Volcanology of the seafloor and implications for the hazard scenario. Mar. Geol. 227, 119–134.

Faccenna, C., Civetta, L., Funiciello, F., Margheriti, L., Piromallo, C., 2005. Constraints on mantle circulation around deforming calabrian. Geophys. Res. Lett. 32, L06311. doi: 10.1029/2004GL021874.

Favalli, M., Kartson, D., Mazzuoli, R., Pareschi, M.T., Ventura, G., 2005. Volcanic geomorphology and tectonics of the Aeolian archipelago (Southern Italy) based on integrated DEM data. Bull. Volcanol. 168, 157–170.

Italiano, F., Nuccio, P.M., 1991. Geochemical investigations of submarine volcanic exhalations to the east Panarea, Aeolian Islands, Italy. J. Volcanol. Geotherm. Res. 46, 125–141.

Pruess, K., Oldenburg, C.M., Moridis, G., 1999. TOUGH2 User's Guide, Version 2.0. Paper LBNL-43134. Lawrence Berkeley Natl. Lab., Berkeley, CA, USA.

Rinaldi, A.P., Todesco, M., Bonafede, M., 2010. Hydrothermal instability and ground displacement at the Campi Flegrei caldera. Phys. Earth Planet. Int. 178, 155–161. doi: 10.1016/j.pepi.2009.09.005.

Saccorotti, G., Galluzzo, D., La Rocca, M., Del Pezzo, E., Patan, D., 2003. Monitoraggio dell'attività sismica a Panarea. Abstract, GNV General Assembly, Roma, 9–11 June.

Serpelloni, E., Anzidei, M., Baldi, P., Casula, G., Galvani, A., 2005. Crustal velocity and strain-rate fields in Italy and surrounding regions: new results from the analysis pf [ermanent and non-permanent GPS networks. Geophys. J. Int. 161, 861–880. doi: 10.1111/j.1365-246X.2005.02618.x.

Serpelloni, E., Cavaliere, A., Pietrantonio, G., Galvani, A., Esposito, A., Sepe, V., Devoti, R., Riguzzi, F., 2007. Data analysis of permanent GPS sites (RING) Italy. Eos Trans. AGU 88(52).

Tallarico, A., Dragoni, M., Anzidei, M., Esposito, A., 2003. Modeling long-term ground deformation due to the cooling of a magma chamber: case of Basiluzzo island, Aeolian islands, Italy. J. Geophys. Res. 108(B12), 2568. doi:10.1029/2002JB002376.